# UNIVERSITÉ DE STRASBOURG

*ÉCOLE DOCTORALE MSII*

**ICube (UMR 7357)**

# THÈSE présentée par :

## Nicole LEPOUTRE

soutenue le : **07 décembre 2016**

pour obtenir le grade de : **Docteur de l'université de Strasbourg**

Discipline/ Spécialité : Robotique

## Robot-Assisted Bone Cement Injection

**THÈSE dirigée par :**
  [M. BAYLE Bernard]                Professeur, Université de Strasbourg

**RAPPORTEURS :**
  [M. LION Alexander]               Professeur, Universität der Bundeswehr München
  [M. POIGNET Philippe]             Professeur, Université de Montpellier 2

**EXAMINATEURS :**
  [M. CINQUIN Philippe]             Professeur, Université Joseph Fourier Grenoble, CHU de Grenoble
  [Mme MEYLHEUC Laurence]           Maître de conférences, INSA de Strasbourg
  [Mme BARA Gabriela Iuliana]       Maître de conférences, Université de Strasbourg

Für Markus

Aan mijn ouders

À Suz et Flo

# Acknowledgements

## Acknowledgements

Pour se changer les idées, quoi de mieux que de se retrouver autour de la balle orange. Je remercie donc toute l'équipe de l'élec et surtout les anciennes comme Élise, Pauline et Claire.

De grootste dank gaat naar mijn ouders en mijn twee kleine zusjes. Ze zijn er altijd geweest om mij te steunen en te begeleiden in mijn keuzes. Jullie zijn altijd heel trots op mij geweest en ik hope dat dat nog lang zal duren.

Ich möchte meine Danksagung mit dem Besten beschließen, das mir während meiner PhD-Phase passiert ist: Ich habe Markus kennen gelernt. Während dieser beiden letzten Jahre wusste er immer, wie er mich unterstützen, ermutigen, mir Rat geben und mich in schwierigen Zeiten aufmuntern kann. Und darüber hinaus danke ich ihm für all seine Liebe und die wundervollen Augenblicke, die wir miteinander geteilt haben.

# Abstract - Résumé

## Abstract

Percutaneous vertebroplasty is a minimally invasive intervention that involves injecting bone cement, under fluoroscopic guidance, into the vertebral body. It consolidates the fractured vertebra and reduces pain. However, some inconveniences must be considered. The major difficulties are related to the cement that is injected during its curing phase. It is very liquid at the beginning of the injection, which introduces a high risk of leakage outside the vertebra and, thus, potential dramatic complications. During the injection, the reaction progresses and the cement hardens suddenly, leaving a short working phase. Finally, the operator is permanently exposed to harmful X-rays.

This work aims to provide a new teleoperated injection device with haptic feedback that allows a fine supervision of the cement injection by including a viscosity control system. This device will allow the radioprotection of the medical staff, a reduction of the leakage risks and an extended injection phase.

**Key words**: Rheology, Modeling, Control, Medical robotics.

## Résumé

La vertébroplastie percutanée est une intervention non chirurgicale et peu invasive qui consiste à injecter, sous contrôle radioscopique, un ciment orthopédique dans le corps vertébral. Malgré son efficacité, celle-ci présente quelques inconvénients non négligeables. Le premier est dû au ciment orthopédique qui est injecté pendant sa polymérisation. Au début, sa faible viscosité augmente le risque de fuite hors de la vertèbre traitée, ce qui peut provoquer de lourdes complications. Ensuite, la variation rapide de viscosité limite la durée. Le second désagrément concerne le contrôle par fluoroscopie à rayons X qui expose le praticien de manière prolongée.

Ainsi, l'enjeu de ce projet est de proposer aux radiologues un nouveau système d'injection à distance avec retour d'effort sur lequel la viscosité du ciment est régulée pendant l'injection. Le développement de ces aspects permettra la radioprotection des praticiens, une réduction des risques de fuite et une durée d'injection allongée.

**Mots-clés** : Rhéologie, Modélisation, Automatique, Robotique médicale.

# Contents

# Contents

# List of figures

# List of tables

# Nomenclature

**Physical quantities**

| | | |
|---|---|---|
| $\alpha$ | Thermal diffusivity of Osteopal® V | $1.645 \times 10^{-7}$ m$^2 \cdot$s$^{-1}$ |
| $\lambda$ | Thermal conductivity of Osteopal® V | $0.28$ W$\cdot$m$^{-1}\cdot$K$^{-1}$ |
| $\rho$ | Density of Osteopal® V | $1480$ kg$\cdot$m$^{-3}$ |
| $A_c$ | Free convection transfer surface | $4.5902 \times 10^{-3}$ m$^2$ |
| $A_r$ | Forced convection transfer surface | $9.0658 \times 10^{-3}$ m$^2$ |
| $c$ | Specific heat capacity of Osteopal® V | $1150$ J$\cdot$kg$^{-1}\cdot$K$^{-1}$ |
| $c_\kappa$ | Specific heat capacity of the TEM ceramic Al$_3$O$_3$ plate | $795.6$ J$\cdot$kg$^{-1}\cdot$K$^{-1}$ |
| $c_{Cu}$ | Specific heat capacity of the central copper block | $393.5$ J$\cdot$kg$^{-1}\cdot$K$^{-1}$ |
| $c_r$ | Specific heat capacity of the copper heat sink | $393.5$ J$\cdot$kg$^{-1}\cdot$K$^{-1}$ |
| $M_\kappa$ | Mass of one Al$_3$O$_3$ plate of a Peltier module | $0.0025$ kg |
| $M_{Cu}$ | Mass of the central copper block | $0.1726$ kg |
| $M_r$ | Mass of one heat sink | $0.0779$ kg |
| $P_\text{atm}$ | Atmospheric pressure | $10^5$ Pa |
| $R_c$ | Inner radius of the conduit | $1.25 \times 10^{-3}$ m |
| $R_s$ | Inner radius of the syringe | $7.1 \times 10^{-3}$ m |
| $R_\text{gas}$ | Gas constant | $8.314$ J$\cdot$mol$^{-1}\cdot$K$^{-1}$ |

**Variables**

| | | |
|---|---|---|
| $\epsilon$ | Seebeck coefficient of the TEM (V$\cdot$K$^{-1}$) |
| $\dot{\gamma}$ | Shear rate (s$^{-1}$) |
| $\gamma$ | Shear strain (-) |
| $\eta$ | Viscosity (Pa$\cdot$s) |
| $\tau$ | Shear stress (Pa) |

## Nomenclature

$G$      Total thermal conductivity of the TEM ($W \cdot K^{-1}$)

$h_c$      Free convection coefficient between air and the central copper block ($W \cdot m^{-2} \cdot K^{-1}$)

$h_r$      Forced convection coefficient between air and one heat sink ($W \cdot m^{-2} \cdot K^{-1}$)

$I$      DC current of the TEM (A)

$I_{max}$      Current of the TEM at $\Delta T_{max}$ when $\dot{Q}_c = 0$ (A)

$P$      Electric power supplied to the TEM (W)

$q$      Degree of cure (-)

$Q$      Flow rate of the injection ($m^3 \cdot s^{-1}$)

$\dot{Q}_c$      Heat power absorbed at the TEM cold side (W)

$\dot{Q}_h$      Heat power emitted at the TEM hot side (W)

$\dot{Q}_{max}$      Maximum heat power absorbed at the TEM cold side (W)

$R$      Total electric resistance of the TEM ($\Omega$)

$T_a$      Ambient temperature (K)

$T_c$      Temperature of the cold side of the TEM (K)

$T_h$      Temperature of the hot side of the TEM (K)

$\Delta T$      $= T_h - T_c$ (K)

$\Delta T_{max}$      $\Delta T$ at $I_{max}$ when $\dot{Q}_c = 0$ (K)

$V$      Voltage applied to the TEM (V)

$V_{max}$      Voltage of the TEM at $I_{max}$ and $\Delta T_{max}$ (V)

$V_P$      Velocity of the piston ($m \cdot s^{-1}$)

# 1 Problem statement

## Contents

## 1.1 Spine health

### 1.1.1 General spine anatomy

With an articulated bone chain, the spine represents the central pillar of the human's trunk. At the upper end, it must carry the head and allow its movements, while fixed to the pelvis at the lower end. It serves as a fixing strut of hundreds of muscles and plays an important part in the posture and the locomotion. Finally, it ensures protection of the caudal central nervous system: the spinal cord. The whole vertebral column also shows an important vascularity.

Figure 1.1 on the facing page illustrates the spine, showing a sequence of individual rigid vertebrae connected with deformable and elastic intervertebral discs, their form and their respective dimensions. The spine can be divided into two parts: the moving column that corresponds to the articulated part and the fixed column which supports the moving column.

On one hand, strengthening the whole spine, the moving column presents a succession of more or less accentuated physiological curvatures that defines three regions: the cervical, thoracic and lumbar columns. Each of these segments has a specific role. The least accentuated, the cervical lordosis (convex forwards), consists of 7 vertebrae (C1 to C7). It must support the head and allows its orientation in all directions. Mobility is here maximum, especially in rotation. Bones, joints and muscles provide good protection, but this region remains fragile. With 12 vertebrae (T1 to T12), the thoracic kyphosis (convex dorsally) bears the thorax that protects vital organs, the head, and the upper limbs that are very mobile but must also allow respiratory motions. Finally, the lumbar lordosis and its 5 vertebrae (L1 to L5) hold the trunk, and indirectly the head and the upper limbs. Stability and strength are furthered by limiting rotation movements but by encouraging flexion-extension movements. The acquisition of these curves is carried out during the first years of life since, in infants under 6 months, there is only a single curvature, the cervical-thoraco-lumbar curvature. The seating position and the support of the head will match with the development of the cervical curvature. Once the standing position is acquired, the last curve expands in order to adapt to these new constraints. These curvatures are adjusted according to loads they support, but also to shocks they absorb.

On the other hand, the fixed column consists of the sacral kyphosis, or sacrum, which is made up of 5 fused vertebrae, and of the coccyx, the most distal part of the spine, consisting of the fusion of 4 to 5 vertebrae depending on the individuals. The average size of the spine varies from 70 to 75 cm in men and from 60 to 65 cm in women, corresponding to two fifth of the stature [Standring 2008].

**MOVING COLUMN**

Cervical lordosis

Thoracic kyphosis

Vertebral body

Lumbar lordosis

Intervertebral disc

**FIXED COLUMN**

Sacrum

Coccyx
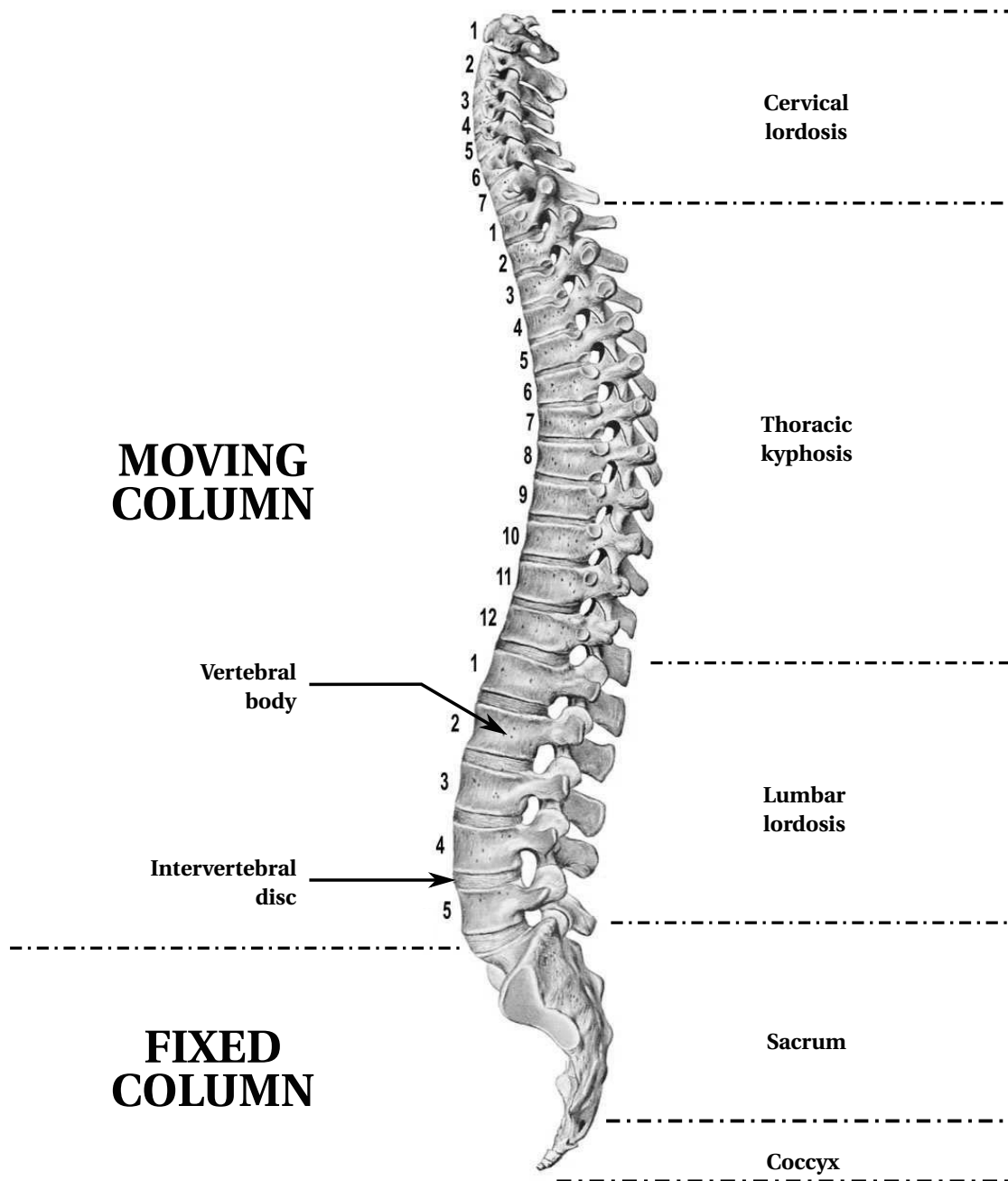
Figure 1.1 – Left lateral view of the spinal column anatomy, adapted from [AnatomyExpert 2016].

Cervical, thoracic and lumbar vertebrae play very different roles and, as illustrated in Figure 1.2, their anatomy is not identical even if some common characteristics can be noticed.

Basically, a vertebra has a solid ventral part, mainly built from the vertebral body, and a hollow dorsal part, which corresponds to the posterior arch. These two parts are connected together by two pedicles. The posterior arch and the vertebral body, also called anterior arch, delimit a protective shell, the spinal canal, through which runs the spinal cord while following the vertebral curves.

**Cervical vertebra**

Spinous process

Lamina

Posterior arch

Spinal canal

Pedicle

Vertebral body

Anterior arch

Transverse process

**Thoracic vertebra**

Spinous process

Lamina

Posterior arch

Transverse process

Pedicle

Anterior arch

Spinal canal

Vertebral body

**Lumbar vertebra**

Spinous process

Lamina

Posterior arch

Transverse process

Pedicle

Anterior arch

Spinal canal

Vertebral body

Figure 1.2 – Superior view of a typical cervical, thoracic and lumbar vertebra, adapted from [Strang 2006].

Within the posterior arch, bone volumes converge towards the median line and are named laminae. These two laminae join to form the spinous process. The lateral spikes extending to the left and to the right are called transverse processes. On the back of the vertebra, laminae, spinous and transverse processes differentiate pipes in which several hundred short muscles are fixed.

The vertebral body consists of cancellous bone tissue surrounded by a thin protective layer of hard, or cortical, bone. Under some circumstances, this vertebral body is likely to collapse as further developed in the following section.

### 1.1.2 Vertebral compression fractures

The stack of vertebrae and intervertebral discs undergoes significant compression efforts. Vertebrae weakness can cause long-term Vertebral Compression Fractures (VCF). They are characterized by a collapse or settling of the vertebral body. This leads to the decrease of the vertebral height but also to a critical modification of the physiological curvatures. These fractures most frequently occur in thoracic and lumbar regions, particularly from T8 to L4 [Mathis 2006]. Severe pain associated with vertebral compression fractures worsens heavily the quality of life and the functional abilities of the victim [Gangi 2006]. The incidence of these fractures increases with age for both sexes while still remaining higher in women than in men [Felsenberg 2002].

Vertebral compression fractures are the most common consequence of osteoporosis. In 2009, the report of the French National Authority for Health estimates that 85% of vertebral fractures are directly due to osteoporosis [HAS 2009]. This disease is characterized by an important bone density loss, which weakens the bones and induces an increased susceptibility to fractures. Figure 1.3 pictures the significant difference between healthy and osteoporotic bone tissue affected by an important bone density loss. To qualify such a loss, a Bone Density Test (BDT) can be performed and results in a T-score. This score is a standard variation that quantifies the bone density variation between the tested patient and a healthy young adult of the same sex. A T-score such that $-1 \leq T \leq 1$ represents a normal bone density while $T \leq -2.5$ indicates that the patient suffers from osteoporosis.



Normal bone                                      Osteoporotic bone
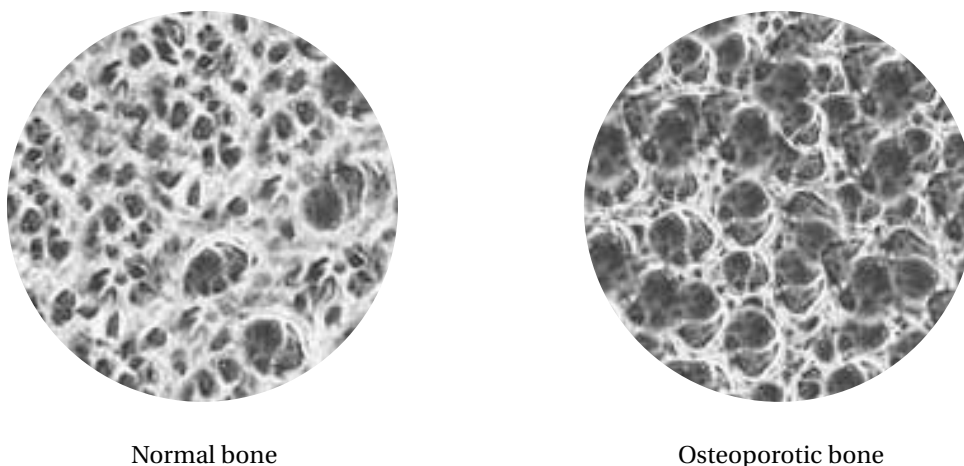
Figure 1.3 – Comparison between normal bone density and reduced bone density due to osteoporosis, adapted from [LPD 2016].

Worldwide, these fractures are often under-diagnosed. According to a report from the International Osteoporosis Foundation [IOF 2010], the overall missed detection rate rises up to 34% . Still, in 2000, estimates show that 1.4 million new osteoporotic vertebral fractures have been diagnosed, including 490 000 in Europe [Johnell 2006]. Osteoporosis occurs predominantly in women. According to [Kanis 2013], nearly one in two women suffer from this affection after their menopause. As the population continues to age, the incidence of vertebral compression fractures is likely to increase. The study proposed by Burge *et al.* projects a growth of these fractures of almost 50% [Burge 2007].

Vertebral fracture can also be the consequence of physical traumas such as falls or car accidents causing one or more vertebrae to collapse. These traumatic fractures account for 14% of the vertebral fractures. Remaining vertebral compression fractures are a consequence of multiple myeloma [Melton 2005] or bone metastasis following breast, lung or prostate cancer [Diamond 2004]. Bone mass of the vertebra is destroyed by the cancer, which weakens the vertebral body and may lead to a vertebral fracture.

### 1.1.3 Proposed treatments

In light of this growing public health problem, various treatments are available starting from simple conservative to surgical solutions. These different medical cares will be detailed and discussed in the following subsections.

#### 1.1.3.1 Conservative treatment

The treatment of vertebral fractures is usually conservative. The patient is strapped into a back brace to ensure the support of the spine and asked to remain in a lying position [Klazen 2010]. Pain is relieved by a drug administration including narcotic analgesics. Physiotherapy sessions and dietary supplements can complete this treatment. Until recently, this option remained the only considered, even if pain could last for months. Because of such a long immobilization, it may also have psychological consequences for the patient.

#### 1.1.3.2 Vertebroplasty and its derivatives

To offer a minimally invasive alternative to conservative treatment, percutaneous vertebroplasty has been introduced in 1984 [Galibert 1987]. It is a non-surgical image-guided intervention that consists in injecting synthetic (acrylic, calcium phosphate, *etc.*) fast hardening bone cement, as highlighted in Figure 1.4. The pathological vertebra is then strengthened. This intervention is greatly appreciated by patients since stabilizing



(a)                                                         (b)
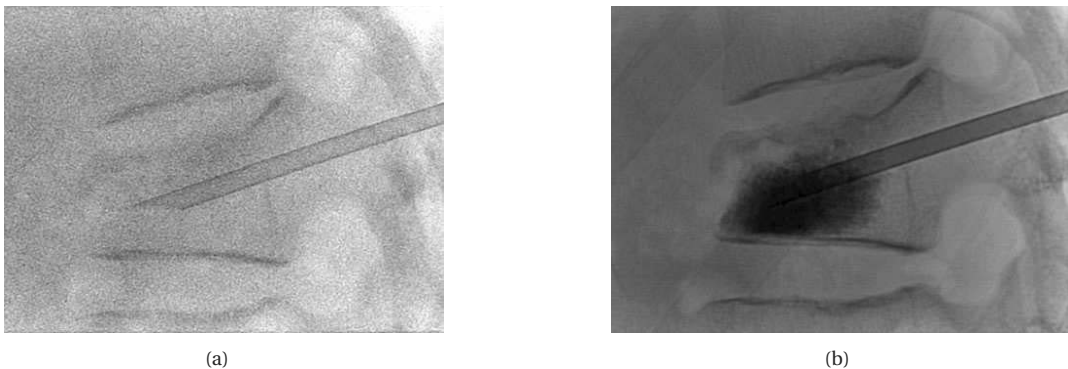
Figure 1.4 – Lateral fluoroscopic images of a vertebroplasty procedure: (a) after the insertion of the trocar; (b) after the injection of bone cement inside the damaged vertebra.

the fractured vertebra decreases immediately and significantly their pain, facilitates their mobility and, thus, their quality of life [Gangi 1994].

Developed in the 1990s, an alternative to vertebroplasty is percutaneous kyphoplasty. Prior to the bone cement injection, a special balloon is introduced inside the vertebral body through the same cannula. By inflating carefully this balloon as illustrated in Figure 1.5, a cavity is created to restore the initial height of the collapsed vertebra [Yan 2011]. The balloon is then deflated to leave an empty cavity behind. The same exercise can be performed on the other side of the vertebral body to ensure uniformity and a reliable correction. This technique also ends with the injection of bone cements.
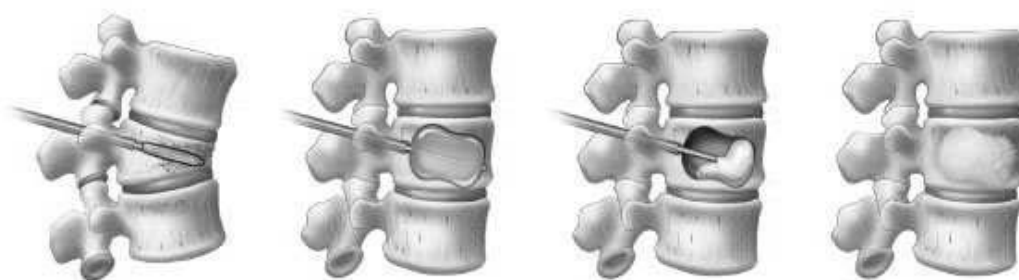
Figure 1.5 – Illustration of a kyphoplasty procedure, from [Center 2015].

During kyphoplasty, the height restoration is arguable since the fragile vertebra could subside again when deflating the balloon. This intervention is still classified as a vertebral augmentation procedure. To ensure the height restoration, a stentoplasty, or more explicitly cemented kyphoplasty with stent, is performed. In this procedure, as its designation suggests, a stent is deployed (Figure 1.6(b)) and cemented (Figure 1.6(c)) inside the vertebral body. It is indicated in traumatic fractures, which are very painful and further cause spine deformation and destabilize the entire stature, with serious consequences for the younger subjects.

While the significant improvement in pain is similar between a vertebroplasty and a kyphoplasty procedure (around 90% according to [Hulme 2006]), the meta-analysis of the literature carried out by Eck *et al.* [Eck 2008] shows a much higher prevalence of cement leakage during vertebroplasty (19.7%) than during kyphoplasty (7%). However, vertebroplasty is less time-consuming [Chang 2015] and less expensive.



(a)                    (b)                    (c)
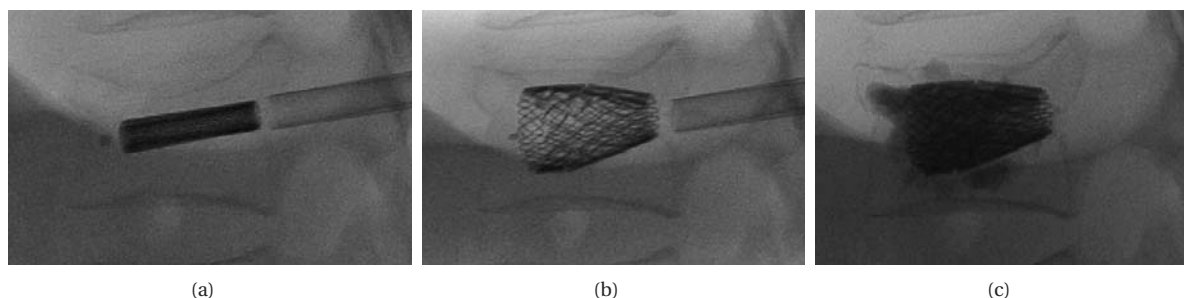
Figure 1.6 – Example of a stentoplasty procedure: (a) insertion of the cannula with a stent; (b) deployment of the stent; (c) bone cement injection.

Finally, Vexim, a recent French company, presents a new concept with the SpineJack® system [Oglaza 2010, Vexim 2016]. It involves the expansion of two implants, similar to jacks, for the reconstruction of vertebral fractures and height restoration. This technique also concludes with a cement injection to seal the treated vertebra with the jacks.

All these procedures are either performed by neurosurgeons, orthopedic surgeon, or interventional radiologists.

### 1.1.3.3 Surgical treatments

Rarely, surgery is required for vertebral compression fractures. Called spinal fusion, this surgical procedure aims to fuse two or more vertebrae using metallic screws or rods as illustrated in Figure 1.7. It makes every motion impossible at the painful segment and leads to the complete fusion of the adjacent vertebrae within a year after surgery.
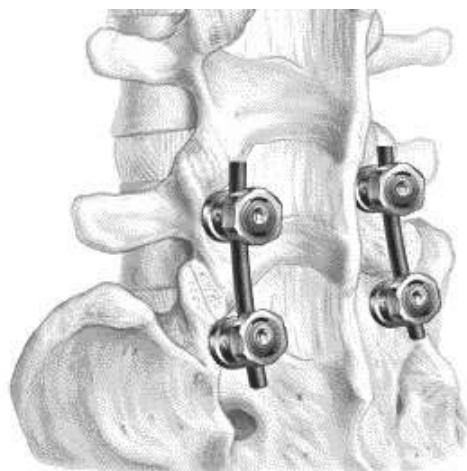
Figure 1.7 – Illustration of a spinal fusion showing pedicle screws, from [Pincus 2016].

This surgical treatment is generally not applicable to older patients due to the stress and the long recovery time caused by such an invasive method. It is important to remark that patients with compression vertebral fractures have an average age of 75 years old [Hulme 2006].

Given their outstanding performance and simplicity, vertebroplasty and its derivatives seem to be excellent approaches. They all end up with bone cement injection inside the diseased vertebra. So, from here on, we will only focus on percutaneous vertebroplasty. All the following reasoning also applies to vertebral augmentation interventions.

## 1.2 Percutaneous vertebroplasty

### 1.2.1 History and current state

Percutaneous vertebroplasty procedure was first reported in 1987 by Prof. Galibert and Prof. Deramond for the percutaneous treatment of an aggressive vertebral hemangioma [Galibert 1987] at the University Hospital of Amiens (France). During the following years, this technique has been improved [Deramond 1998] so that it could be indicated for vertebral metastatic lesions and then for painful osteoporotic fractures. This intervention appears in the United States only in the middle of the 1990s [Jensen 1997].

Nowadays, vertebroplasty and vertebral augmentation procedures are still gaining in popularity to stabilize painful vertebral fractures. This growth is especially confirmed in France as shown in Figure 1.8 that gathers the number of percutaneous vertebroplasty procedures and the number of treated vertebrae over the past years. This graph shows that the number of interventions doubled within the last five years (from 2010 to 2015). Moreover, one can notice that the number of treated vertebra grows faster than the number of interventions. This observation is consistent with the fact practitioners tend to treat several vertebrae during a unique procedure. Unfortunately, worldwide, similar data have not been found but one can imagine they would show an identical trend.
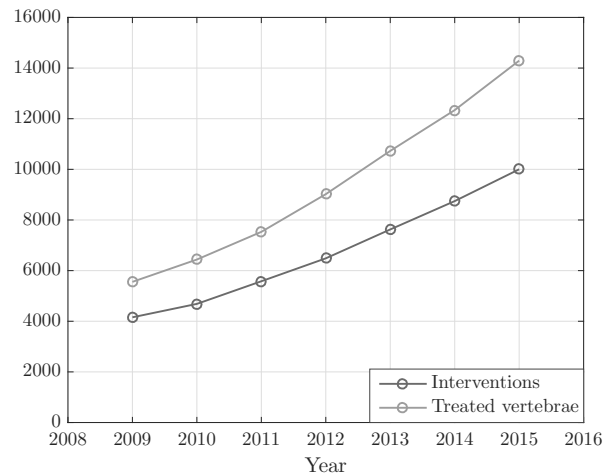
Figure 1.8 – Statistics on percutaneous vertebroplasty procedures in France, retrieved from [ATIH 2016].

This popularity is confirmed by an abundant number of case studies or meta-analysis in the literature. For instance, Figure 1.9 counts, over the past few years, the number of publications in the biomedical archive PubMed dealing with vertebroplasty, kyphoplasty or vertebral augmentation.
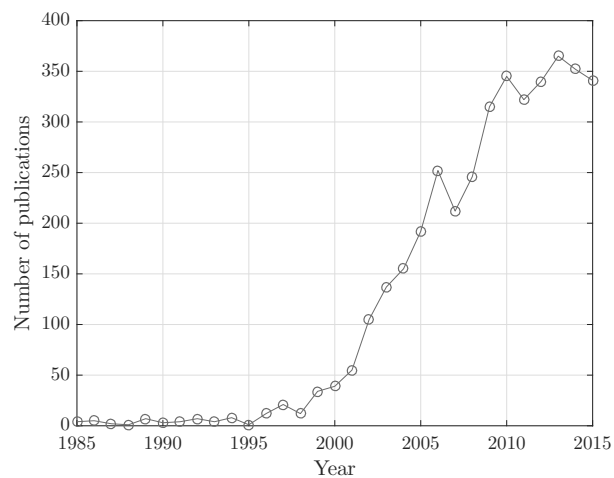


Figure 1.9 – Statistics on literature dealing with vertebroplasty and its derivatives, retrieved from [PubMed 2016].

### 1.2.2 Acrylic bone cements

Almost 100 years ago, from his doctorate thesis on the subject *Polymerization Products of Acrylic Aid* in 1901, Otto Röhm and his staff developed dentures based on methyl methacrylate. To our knowledge, the first artificial hip implantation with an acrylic resin for fixation occurred in 1953, performed by Edward Haboush [Haboush 1953]. Later, from 1958 on, John Charnley, a pioneer in orthopedic surgery, performed total hip replacement surgeries using bone cement [Charnley 1972]. Approved in the 1970s by the U.S. Food and Drug Administration [Vaishya 2013], bone cements are now widely used for the fixation of artificial joints such as hip or knee prostheses.

Among all orthopedic cements, acrylic bone cements are the most employed during percutaneous vertebroplasty procedures. Mostly preferred for young patients, calcium phosphate bone cement is another type of cement that is much less widespread for vertebral fracture reductions. To their advantage, their hardening temperatures are quite low and no monomer can be released in the long term. However, besides their expensive prices, their resorption rate is not always adapted to the bone growth rate of the patient. Their low mechanical strength is another main drawback. So, in what follows, the focus will only be on acrylic bone cements.

### 1.2.2.1  Chemical composition

Acrylic bone cement is a sterile two-component system composed of a polymeric powder and a monomeric liquid. The liquid component consists mainly of Methyl MethAcrylate (MMA) which is an ester of methacrylic acid. Besides MMA, the co-initiator Dimethyl-para-Toluidine (DmpT) is part of the activation triggering the radical polymerization [Kühn 2013]. Finally, to prevent premature polymerization from exposure to light or high temperature during storage, a very small amount of HydroQuinone (HQ) stabilizes the liquid monomer.

In the polymeric powder, the main component is pre-polymerized Poly(Methyl MethAcrylate), abbreviated as PMMA, but, depending on the manufacturer, comes in various compositions: MMA homopolymer, methacrylate copolymer (PMA) and/or MMA-Styrene copolymer (SMMA) [Spierings 2005]. In the same way, as the monomeric liquid incorporates an activator for the radical polymerization reaction, the powder incorporates benzoyl peroxide as initiator, encouraging the polymerization at room temperature. Some PMMA cements include an antibiotic agent inside their composition in order to prevent any infection. Last, since bone cement needs to be visible on fluoroscopic images, a radiopacifier is combined to the polymer, which is either zirconium dioxide ($ZrO_2$) or barium sulphate ($BaSO_4$). Both in the powder and in the liquid, a coloring agent may optionally be added such as chlorophillin E141, giving a green color to the bone cement.

The overall compositions of some commercialized bone cements are summarized in Table 1.1. Even if their composition slightly differs from one PMMA cement to another, they are all based on MMA.

| Bone cement | Overall composition | | Viscosity |
|---|---|---|---|
| (Manufacturer) | Powder | Liquid | |
| Osteopal® V (Heraeus) | PMA-PMMA (14.2 g) BPO (0.1 g) $ZrO_2$ (11.7 g) Coloring E141 (N/D) | MMA (9.2 g) N,N-DmpT (0.2 g) HQ (N/D) Coloring E141 (N/D) | Low |
| SpinePlex® (Stryker) | PMMA-SMMA (14 g) BPO (0.18 g) $BaSO_4$ (6.0 g) | MMA (9.75 mL) N,N-DmpT (0.25 mL) HQ (0.75 mg) | Low |
| CementoFixx-L CementoFixx-M CementoFixx-R (OptiMed) | PMMA (N/D) BPO (N/D) $BaSO_4$ (N/D) Total (19.2 g) | MMA (N/D) N,N-DmpT (N/D) HQ (N/D) Total (10 mL) | Low Medium High |
| Confidence (Teknimed) | PMMA (13.9 g) BPO (0.1 g) $BaSO_4$ (6.02 g) | MMA (9.06 g) N,N-DmpT (0.14 g) HQ (20 ppm) | High |

Table 1.1 – Overall compositions of four commercialized bone cements.

Especially selected for their excellent mechanical strength, acrylic bone cements can show high variable viscosities, depending on their composition. They can be classified into three categories: low-, medium- and high-viscosity PMMA cements. While their different behavior clearly depends on the bone cement composition, manufacturers do not provide any viscosity measurement or quantification. Generally, for vertebroplasty procedures, low-viscosity bone cements are preferred since their mixing and injection are more convenient, even if leakage risks are higher.

#### 1.2.2.2   Handling properties

As soon as both components come into contact, the PMMA evolution follows four successive phases, named as handling phases.

**Mixing phase**   This phase starts as soon as the powder and the liquid monomer are thoroughly mixed using an appropriate tool, triggering the polymerization reaction. The very few and short polymer chains that are formed are very mobile. At the end of this stage, when a homogeneous dough is obtained, the powder is fully dissolved in the liquid and the bone cement is relatively runny. This mixing step will be further detailed in section 1.2.3 where a vertebroplasty procedure is fully described.

**Waiting phase**   Also called doughing time, this phase of one to three minutes is recommended by manufacturers so that the bone cement viscosity increases slowly (formation of polymer chains). When the cement does no longer stick to the surgical glove, the viscosity is suitable for handling. The notion of viscosity, description of the hardening of a fluid or of its ability to flow, will further be developed in Chapter 2.

**Application phase**   During this period, the physician can inject the bone cement inside the damaged vertebra. Viscosity increases and the intervention must be finished by the end of this working phase.

**Setting phase**   This phase starts with the abrupt bone cement hardening. The cement is then too hard to be injected but the curing reaction still goes on. Defined by the ISO 5833:2002 standard [ISO 2002], the setting time represents the time $t_{set}$ when the temperature $T_{set}$ in a $\varnothing 60\,\text{mm} \times 6\,\text{mm}$ polymerizing cement mass is exactly between ambient and maximum temperature $T_{max}$, measured with a thermocouple. This exercise has been performed for three commercial bone cements at an ambient temperature $T_a = 18\,°\text{C}$. While temperature evolution curves are given in Figure 1.10, respective setting times are provided in Table 1.2.

| Bone cement | $T_{max}$ | $T_{set}$ | $t_{set}$ |
|---|---|---|---|
| Osteopal® (Heraeus) | 76.98 °C | 47.49 °C | 17.65 min |
| CementoFixx-R (Optimed) | 104.48 °C | 61.2 °C | 13.52 min |
| CementoFixx-L (Optimed) | 83.01 °C | 50.5 °C | 25.53 min |

Table 1.2 – Typical setting times for different commercial bone cements.
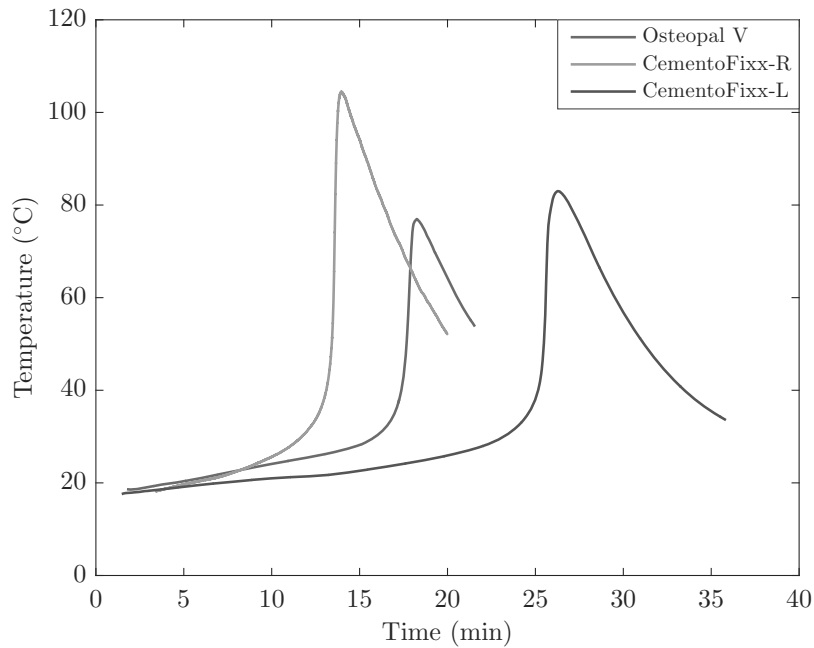
Figure 1.10 – Temperature evolution curves where time zero is the beginning of the mixing phase.

The ISO 5833:2002 standard also mandates the bone cement manufacturer to deliver a detailed representation of the handling properties. Figure 1.11 displays a graphical representation for a bone cement from Heraeus.
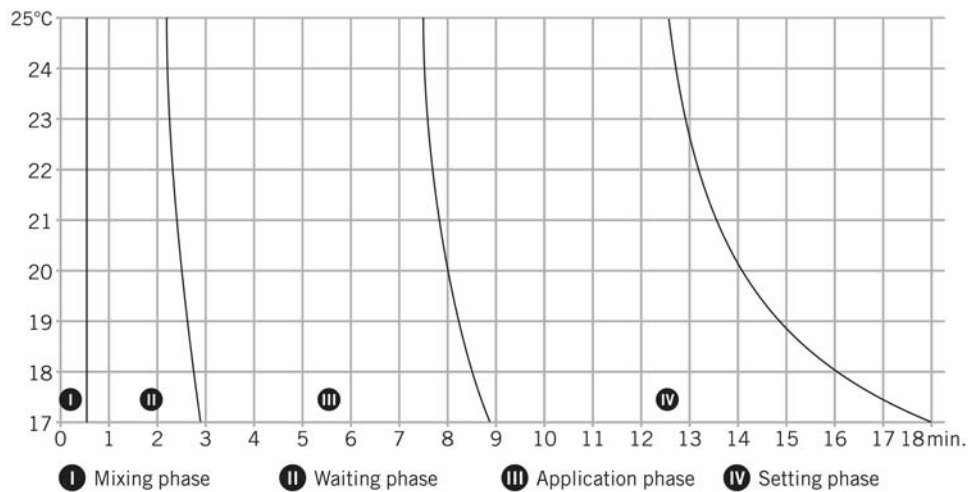


Figure 1.11 – Graph representing the handling properties for Osteopal® V (Heraeus).

The duration of each phase highly depends on the temperature of the bone cement mixture: increasing its temperature accelerates the polymerization reaction. This strong temperature dependency is true for every acrylic bone cement and will be further discussed in section 2.2.2.

### 1.2.3 Procedure

In this section, a usual percutaneous vertebroplasty procedure will be described. Before any intervention, the patient receives a preoperative assessment combining X-ray imaging and magnetic resonance imaging (MRI) [Gangi 2010] in order to have an optimal contrast for both bones and soft tissues.

**Patient setup** The patient is, most of the time, placed in prone position on the table of the imaging device. For cervical fractures only, patients are settled in supine position. Commonly, two imaging devices are combined: a Computed Tomography scanner (CT-scan) for its high spatial resolution and an X-ray fluoroscope which is a mobile radiography equipment that can be rotated around the table [Gangi 1994].

In general, patients receive local anesthesia with mild sedation and analgesia. Only for some personal convenience or for the treatment of several fractures at the same time, general anesthesia is administered.

**Insertion of the trocar(s)** Prior to the intervention, a planning step determines the approach through the vertebra but also the entry point and the insertion line of the trocar, which is a medical tool made up of a hollow tube (cannula) and a solid central stylet. The access path depends on the treated vertebra. At thoracic and lumbar levels, the needle is introduced with a transpedicular approach [Hide 2004] as schematized in Figure 1.12, usually with a bipedicular way to be able to inject bone cement in a uniform manner inside the vertebral body. In order to adapt to the patient's pedicle size, the chosen trocar measures from 10 to 13 G in diameter.



(a)                                             (b)
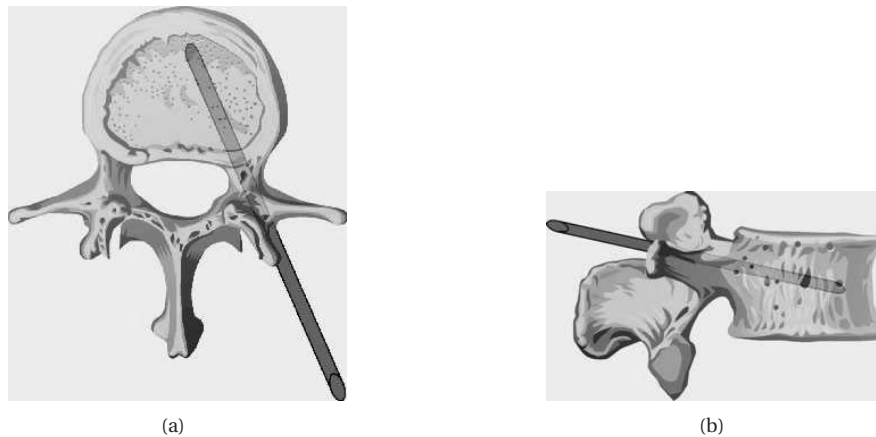
Figure 1.12 – Transpedicular approach for a lumbar vertebra [Guth 2016]: (a) superior view; (b) right lateral view.

Sometimes, an intercostovertebral route is more optimal to access in the thoracic level (see Figure 1.13).
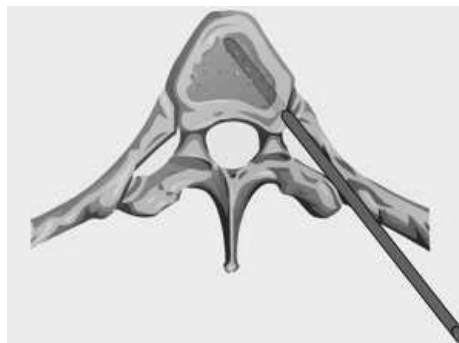


Figure 1.13 – Superior view of an intercostovertebral approach for a thoracic vertebra [Guth 2016].

For the few cervical procedures, a unilateral anterolateral approach is recommended with the use of thinner needles, from 13 to 15G in diameter.

Once the entry point is defined, a small incision is made. The needle is hammered inside the vertebra. The scanner allows the precise guidance of the tool [Gangi 2006] amid the adjacent structures (vascular, neurological and visceral) on the planned trajectory. However, images can only be acquired in a unique plane, potentially slightly inclined. Exposure time to X-rays is relatively low during this stage because the acquisition flow is not continuous and the medical staff can step out the X-ray area when the acquisition of a new image is required.

It is not uncommon that several vertebrae need to be cemented, at least as a preventive measure in the case of osteoporosis. In such a case, all the trocars are inserted before proceeding to the next step which is the preparation of the bone cement to be injected. Figure 1.14 presents a picture where one or two trocars have been inserted in each vertebra that must be addressed. For this patient, a transpedicular approach has systematically been preferred with either a monopedicular or a bipedicular way depending on the treated vertebra.



Figure 1.14 – Multi-level vertebroplasty requiring the insertion of several trocars.

**Bone cement preparation**   Handling characteristics of the bone cement are highly influenced by the procedure conditions, particularly by the temperature. As revealed by Sullivan *et al.*, the cooler the initial temperature of the bone cement, the lower the viscosity [Sullivan 2007] and the longer the setting phase is. Thus, it is a common practice to store the cement kit inside a refrigerator near the operating or interventional radiology room until the immediate start of the injection procedure.

A cement kit contains a sachet of sterile PMMA powder and an ampoule of sterile MMA in a liquid form as highlighted in Figure 1.15(a). Once in the hands of the practitioner, the liquid MMA and the PMMA powder are both poured into a bowl if the mixing is performed manually (Figure 1.15(b)) or into the mechanical, vacuum or centrifugation mixing device. Even if manual mixing is less effective in terms of homogeneity of the mixture, it remains the most common process based on its cost-effectiveness. Mixing by hand takes about 30 s to 1 min and should be achieved with slow and steady motions since the cement polymerization is directly influenced by the mixing method [Baroud 2004a].

Once a homogeneous dough is achieved, the cement should be left to stand. Bone cement manufacturers recommend to let the cement stand briefly so that it attains a certain consistency. The end of this phase, called doughing time, is determined by the doctor's finger test. Indeed, according to ISO 5833-2002 standard [ISO 2002], it is reached when the practitioner can touch the bone cement so that it does not adhere to the glove anymore. This method is highly subjective since it is operator dependent.
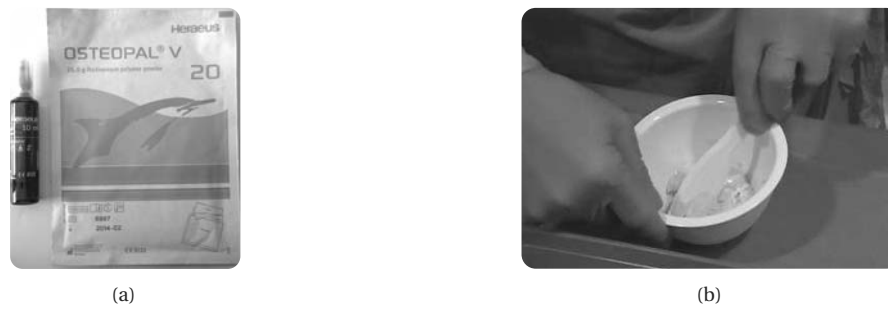
Figure 1.15 – Bone cement mixing: (a) kit of the bone cement Osteopal® V (Heraeus); (b) hand mixing performed by a practitioner.

After this waiting phase, the bone cement is poured (Figure 1.16(a)) or sucked into the injection device (Figure 1.16(b)) and is ready to be injected (Figure 1.16(c)).
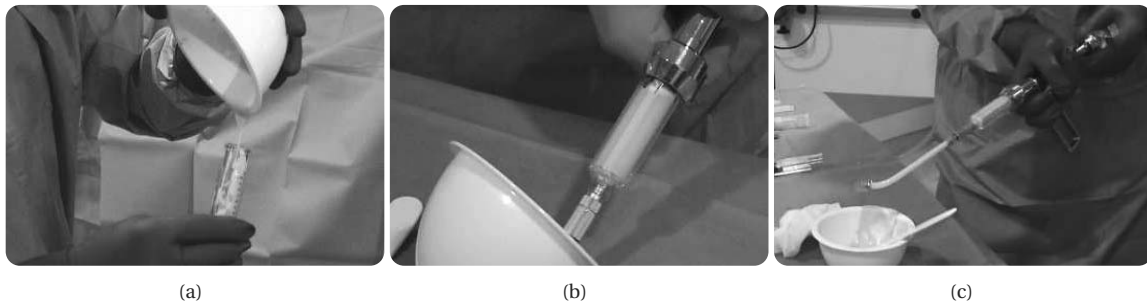


Figure 1.16 – End of the bone cement preparation where (a) bone cement is poured or (b) sucked into (c) the Cemento-MP device (Optimed) ready for the injection.

**Injection of the bone cement**  Once the central needle stylet is removed from the inserted cannula, the injection system is plugged to the trocar either directly or via a connecting hose. The injection can then start. The short hose length allows a better fluid flow and limits product loss by hindering the amount of cement that is necessary to fill the hose and reach the vertebra.

During the injection, continuous fluoroscopy allows to choose the orientation of the image plane, in order to monitor the bone cement diffusion inside the vertebral body. Nevertheless, this imaging modality is highly irradiating [Synowitz 2006]. Yet, the practitioner is forced to stay inside or close to the X-ray area because of the short length of the connecting hose.

Approximately, 30% to 50% of the vertebral body is filled with bone cement, which is equivalent to approximately 3 to 4 mL for a thoracic vertebra and 5 to 7 mL for a lumbar vertebra. The injection has to be completed and the needle has to be removed within 8 to 10 minutes, before the bone cement hardens totally. If the needle is not removed on time, an open surgery is required to withdraw the cannula. Therefore, the practitioner must have a perfect knowledge and control of the used bone cement.

The total procedure lasts between 30 minutes and 2 hours depending on the number of vertebrae to be healed but also on the physician's experience. To validate the good and uniform filling of the vertebral body, a final X-ray imaging step is performed. In Figure 1.17(b), the cemented vertebrae are easily noticeable thanks to the radiopacity of the cement.

(a)                                                (b)
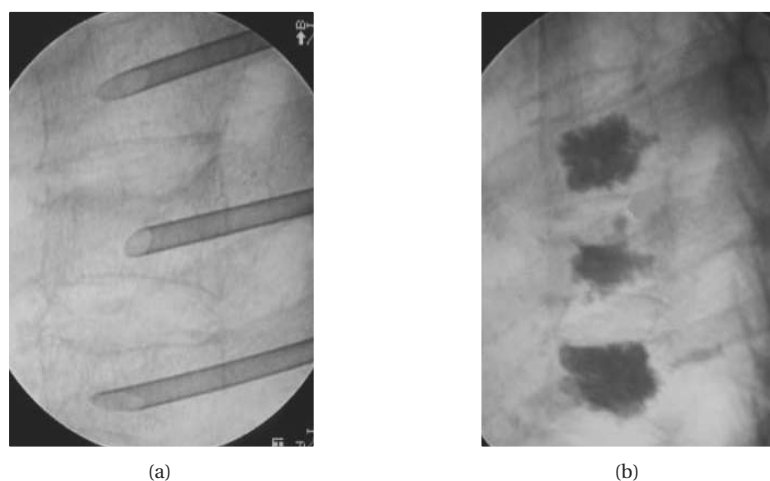
Figure 1.17 – Left lateral fluoroscopic X-ray image of a three-level thoracic vertebroplasty: (a) after the needle insertions; (b) after the cement injection and the removal of the needles, from [Hide 2004].

### 1.2.4 Benefits

The benefits of percutaneous vertebroplasty procedures have been reaffirmed in several large-scale studies such as the one led by Klazen *et al.* [Klazen 2010] and benefits of such an intervention are undeniable. The injection of orthopedic bone cement offers a mechanical action that favors a sustainable stabilization of the healed vertebra [Barr 2000] and a potential height restoration. It is also cost effective. Furthermore, treated patients show increased ambulatory abilities as stated by Mc Graw *et al.* [McGraw 2002]. This is all the more impressive as some patients are too weak to walk before the intervention because of pain but get back on their feet to go home, sometimes the same evening.

Last but not least, studies revealing clinically pain reduction [Anselmetti 2007, McGraw 2002, Barr 2000] are countless. Even partial, this pain relief is a primary benefit of vertebroplasty as demonstrated in 86% of procedures in [Anselmetti 2007] and in 87% in the systematic review of 69 clinical studies conducted by Hulme *et al.* [Hulme 2006]. In terms of pain relief, results are significantly better than those obtained by conservative treatments. However, the analgesic effect of this technique is still poorly explained by doctors. An explanation could lie in the exothermic reaction of cement that causes tissue or nerve necrosis.

### 1.2.5 Complications and drawbacks

#### 1.2.5.1 Complications for the patient

Complications after vertebroplasty interventions are rare but still need to be considered.

**Cement leakage** Most complications are related to cement extrusions. Their detection with imaging devices has been discussed in [Schmidt 2005]. Quality of images using fluoroscopy is usually worse than that of CT-scanner images but C-arm fluoroscopy is the only way to monitor cement leakage during the injection.

Cement leakage outside the treated vertebra is quite critical, up to 20% for vertebroplasty and 7% for kyphoplasty [Heini 2000], but is symptomatic in only around 1.6% of the performed vertebroplasty procedures and 0.7% of the kyphoplasty procedures [Eck 2008]. Cement leaking to the intervertebral disc, into the bloodstream or

the spinal canal may cause complications from a simple lumbar pain to a pulmonary embolism. While poor vision can cause such leakages, this risk is mostly linked to the viscosity of the bone cement since the injection occurs during its ongoing polymerization reaction. Cement viscosity varies strongly between the beginning and the end of the injection. To be injected manually, bone cement must be sufficiently liquid, which increases the risk of leaks. Indeed, at the beginning of the injection, immediately after the mixing phase, the cement has a very low viscosity, which generates a high potential for leakage outside the vertebra. Such leakage might lead to pulmonary embolism. On the contrary, later on during this procedure, the polymerization reaction causes the abrupt hardening of the cement. This requires the radiologist to perform its injection within a time interval of only 10 to 20 min, depending on the cement.

In any case, the estimation of the viscosity during the injection is a key factor in leakage management that remains fully subjective with the hand tools that are currently used in vertebroplasty. Above all, bone cement viscosity control would limit this risk even when the quality of the images is not sufficient.

**New fractures**   The risk of a new fracture either to adjacent or more distant vertebrae is frequent in the months following the intervention. Therefore, some physicians prefer to consolidate preventively adjacent vertebrae, additionally to the pathological one.

As a conclusion, even if this method is very promising, the risks of complications should be limited as much as possible. Moreover, given the recentness of vertebroplasty procedures, long-term data are not yet available to answer questions such as the exothermic heat generation, the effect of monomer emissions or the long-term effect of *a priori* asymptomatic cement leakages.

#### 1.2.5.2   Irradiation of the medical staff

X-ray imaging is harmful to the health of the physician and his medical staff. Current recommendations require the wearing of a leaded apron, thyroid collar and leaded gloves, which may reduce the radiation dose up to 75% [Synowitz 2006, von Wrangel 2009]. However, despite this heavy and uncomfortable equipment, the medical staff is exposed to significant radiation. Under fluoroscopy assistance, percutaneous vertebroplasty requires long beam-on times [Harstall 2005] with an average of $7.97 \pm 1.96$ min per intervention or $2.23 \pm 0.89$ min per treated vertebrae which corresponds to a radiation dose on one practitioner's hand of 0.107 mSv per vertebra. To ensure their safety, the limit of the cumulative radiation dose per practitioner could restrict their number of vertebroplasty procedures, yet so promising.

## 1.3   Available injection tools

### 1.3.1   Manual systems

Currently, most of the commercial systems for bone cement injection work manually. These devices consist of a syringe whose piston is pushed either directly by hand or via a force amplification mechanism, *e.g.* the Cemento-MP device from Optimed [OptiMed 2016] that uses a screw-nut system. Table 1.3 gives a non-exhaustive list of the different manual systems on the market.

Some of these systems have long hoses, *e.g.* X'tens®, which reduce the radiation of the physician, as its magnitude is inversely proportional to the squared distance from the radiation source. A major inconvenient of this example is the internal volume of only 2.5 cm$^3$, forcing the physician to reload the tool several times to treat one single vertebra.
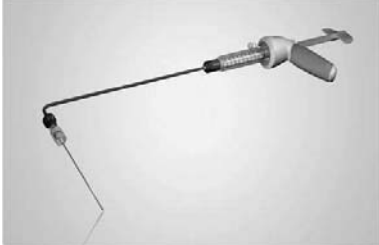
| Product name - Manufacturer | Illustration | Principle |
|---|---|---|
| X'tens® - Thiebaud Biomedical Devices [Thiebaud 2016] |  | Trocar pump pushed directly by hand. |
| Vertecem® II - DePuy Synthes [Synthes 2016b] |  | Syringe pump pushed directly by hand. |
| AVA*max*® PLUS - CareFusion [CareFusion 2016] |  | Syringe pump pushed directly by hand. |
| Precision Cement Delivery (PCD) - Stryker [Stryker 2016] |  | Syringe pump with a screw-nut system. |
| Duro-Ject® - Cook Medical [Medical 2016] |  | Syringe pump with a screw-nut system. |
| Cemento-MP - Optimed [OptiMed 2016] |  | Syringe pump with a screw-nut system allowing high pressure injections. |

Table 1.3 – Overview of some commercial manual delivery systems.

### 1.3.2 Mechatronic systems

Beside a large range of manually operated injection guns, only few robot-assisted systems offer a solution for complications and drawbacks stated in subsection 1.2.5.

#### 1.3.2.1 Radiation protection for medical staff

Radiation exposure during vertebroplasty procedures is a serious problem for the medical staff. As stated previously, leaded protections are required but they are far from being sufficient [Synowitz 2006]. A potential solution could be the extension of the pipes between the trocar and the injection system in order to remove the practitioner's hands from the X-ray beam. Nevertheless, this partial radiation protection solution creates a significant loss of bone cement and a multiplication of efforts required for the injection since the applied forces are proportional to the length of the pipe.

The only way to by-pass the effects associated to radiation is teleoperation. Given the previous exposed issues (material loss and multiplication of efforts), injection systems must be close to the patient and therefore necessarily inside the X-rays area. In order to remove the practitioner from the radiation source, it is imperative to perform the control of the injection remotely. Three remote control solutions either are commercially available or have been presented in the literature.

**Hydraulic control**  Both DePuy Synthes with CONFIDENCE SPINAL CEMENT SYSTEM® [Ferreyro 2015, Synthes 2016a] and Osseon Therapeutics, Inc. [Osseon 2016] with Osseoflex® propose orthopedic cement injection devices with a remote control performed with a hydraulic transmission line filled with sterile water. This allows the medical staff to stay further away (from 50 cm for Osseoflex® up to 1.5 m for Confidence) from the radiation source during the cement delivery. However, such a remote actuator is a source of control failure for the



| (a) | (b) |
|-----|-----|

Figure 1.18 – Commercial hydraulic delivery systems: (a) Confidence from DePuy Synthes [Synthes 2016a]; (b) Osseoflex® CD-H from Osseon [Osseon 2016].

practitioner, which may impede the injection. Hydraulic kinetics adds uncertainty and latency between the control and the action on the system delivery. For instance, since feedback is delayed, it is impossible to stop the injection immediately. So, even if the radiation exposure is reduced, the control of the injection by the physician is more difficult which may increase the risk of leakage.

**Teleoperation**  The StabiliT® system from DFine [DFine 2016] suggests a unilateral teleoperation, illustrated in Figure 1.19. It consists in an injection device which is activated with a simple on/off push-button. The major disadvantage of this option is the complete loss of any tactile feedback representing the hardening bone cement, which is an important control parameter for the physician. In addition, some users complain about small amounts of cement continuing to flow even though the stop has been requested, which is a dangerous behavior

in the leakage context.



Figure 1.19 – StabiliT$^{®}$, the vertebral augmentation system from DFine [DFine 2016].

Paradoxically, the idea of teleoperation with force feedback has not been extensively studied. To our knowledge, the system developed by Loeffel et al. [Loeffel 2007, Loeffel 2009] is the only reference in the field. Contributions of this work are mainly related to the design of the injection device, and its master device with passive force feedback.

#### 1.3.2.2 Viscosity measure and control

To reduce the risk of leakage outside the vertebra, controlling the bone cement viscosity is mandatory. This need has been recognized by Baroud [Baroud 2013a, Baroud 2013b, Baroud 2014] who underlines the convenience of an instrumented injection system including a viscosity measurement to allow the practitioner to start the injection after a minimal viscosity threshold has been exceeded. However, such patents only exhibit bone cement viscosity sensing methods and devices. Key points such as haptic feedback, reduction of the radiation exposure and viscosity control are not addressed.

In an attempt to provide the radiologist with advanced supervision functions, Loeffel et al. [Loeffel 2007, Loeffel 2009] developed an injection device, emphasized in subsection 1.3.2.1 (Figure 1.20), able to deliver cement at higher viscosity than achievable with other devices. This reduces the risk of leakage but, if the viscosity increases too much, the cement does not disperse equally inside the vertebral body and, the injection time is potentially reduced.

As a result of the industrialization of [Truckai 2013], DFine recommends the system StabiliT$^{®}$ [DFine 2016]. This device requires the use of a special low viscosity cement whose curing is handled by applying radiofrequency waves before its injection into the vertebral body, which highly limits the risk of leakage. Although very ingenious, the main reluctance of practitioners comes from the long learning phase and the high cost (from 1000 € to 3000 €) per treated vertebra.

Finally, the manual system patented by Wolf [Wolf 2009] dispenses bone cement and offers temperature control. In its regulation box, a single Peltier module is installed. The fluid flow imposes the cement to, first, pass through the cold face in order to freeze its polymerization reaction and, then, through the hot face to reach a given viscosity. The implementation of this method seems impractical since temperatures of the two faces of the Peltier module, controlled by the same current, are strongly dependent.

(a)                                    (b)
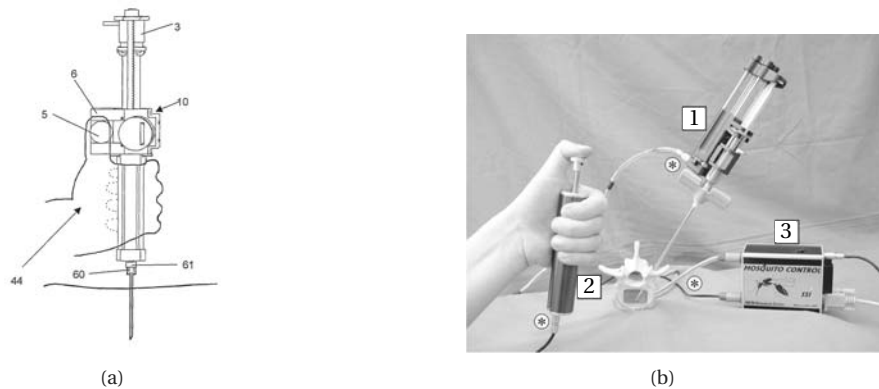
Figure 1.20 – Injection device proposed by Loeffel *et al.*: (a) showing schematically the invention applied to a patient [Loeffel 2009]; (b) with (1) the injection device and (2) the manual actuator powered by (3) the control box [Loeffel 2007].

As a conclusion, few injection devices have emerged from the large number of patents that have been submitted or granted. Among these patents and commercialized systems, some of them claim a temperature and/or a viscosity measurement but none of them combines a satisfactory answer to the following issues:

- reduction of cement leakage risk by controlling its viscosity, and

- radiation protection while preserving the tactile perception.

### 1.3.3 S-Tronic project

In this medical context and based on the above state-of-the-art, a collaboration has been suggested by Prof. Afshin Gangi, head of the Interventional Radiology department at the University Hospital of Strasbourg, and, expert in percutaneous vertebroplasty procedures. Therefore, the S-Tronic project has been submitted and followed up by Prof. Bernard Bayle, funded by Conectus Alsace SATT. The innovation of this project is the development of a new robotic device assisting bone cement injection during vertebroplasty, or potentially kyphoplasty procedures. Such a system allows to get the practitioner out of the X-rays area during the injection phase while controlling the viscosity of the cement in order to facilitate the injection and the filling of the vertebra. This allows to minimize the risk of leakage and to improve the physician's comfort and gesture accuracy. To meet these requirements, the developed injection device features the following characteristics:

- monitoring and control of the bone cement injection,

- online control of the bone cement viscosity, and

- teleoperation with haptic feedback of the injection.

As, in comparison to the injection phase guided by fluoroscopic imaging, the exposure to ionizing radiation of the practitioner is much lower during the positioning and orientation of the trocar, these tasks are assumed to be performed manually. Their automation is thus not within the scope of our project.

## 1.4 Thesis contributions and organization

### 1.4.1 Thesis contributions

The objectives of this thesis differ slightly from those of the project. The first aim of this work was to study the characteristics of the bone cement and to model its behavior in order to determine possible viscosity control parameters, to dimension the injection device and to determine the appropriate instrumentation to measure the bone cement viscosity online. Therefore, a rheological study has been set up to help qualify and quantify parameters influencing the bone cement viscosity. Following the characterization of the bone cement behavior, the next task was to provide quantitative elements required for the design of the new teleoperated injection device with force feedback. Based on this study, a first prototype has concurrently been designed by an engineer from the S-Tronic team. The best control strategy of this device has also been examined. Finally, to control the evolution of bone cement viscosity, an effort has been required to implement a closed-loop temperature control providing adapted performances.

### 1.4.2 Thesis organization

After a short introduction to rheology, chapter 2 presents a rheological study that has been set up to understand and characterize the behavior of the bone cement viscosity during its polymerization phase.

In Chapter 3, this study results in the identification of two models: a well-known rheological model that has been improved by adding a temperature dependency and a new original viscosity model, expressed as a nonlinear differential equation that is exploitable for control purposes.

Chapter 4 develops and justifies the design of a mechatronic injection device in addition to a master interface that is imperative for the remote control. An analysis of the required online measurements leads to the appropriate instrumentation of the device. The system dedicated to the control of the flowing bone cement temperature, validated beforehand by simulations, is also described. Finally, the contradictory properties of the injection show that, in terms of teleoperation with force feedback, the implementation of the rate control strategy is best suited.

To control the online viscosity, our solution focuses on the regulation of bone cement temperature. In Chapter 5, the thermal system has been modeled and identified by considering the flowing bone cement and the emitted heat flux. This allows us to propose a satisfactory temperature control and, thus, viscosity control.

The injection device and its benefits are discussed in the conclusion, along with the prospects of this work. Improvements of the injection device are suggested at different levels.

# 2 Rheology of bone cement

**Contents**

## 2.1 Aspects of rheology

### 2.1.1 Definitions

Rheology describes the deformation of material under the influence of stresses [Bird 1987, Barnes 1989, Osswald 2014]. By measuring internal frictions, viscosity quantifies the resistance to flow. The higher the viscosity, the greater the resistance. In SI units, it is expressed in Pa·s.

The parallel-plates example illustrated in Figure 2.1 can be considered to define parameters involved in the flow. Spaced by a gap of size $h$, the lower plate is fixed while the upper plate with a shear area $A$ moves at a constant
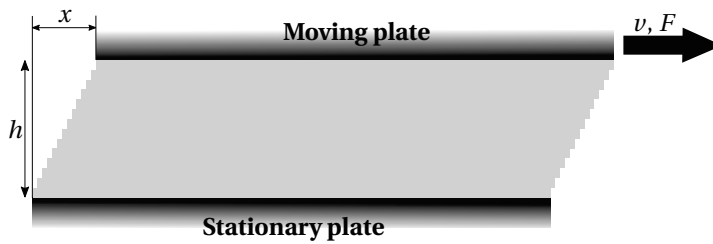


Figure 2.1 – Parallel-plates model showing a flow in layers

speed $v$. Since the fluid adheres to both plates, the displacement of the above plate leads to a flow in layers. Hence, deformation, or shear strain, $\gamma$ can be written as:

$$\gamma = \frac{x}{h} \tag{2.1}$$

and shear rate, rate of the shearing deformation, as:

$$\dot{\gamma} = \frac{d\gamma}{dt} = \frac{v}{h}. \tag{2.2}$$

Controlling the velocity of the moving plate results in a tangential force F. The stress applied at this interface is defined as the tangential force $F$ divided by the cross sectional area $A$. It is named shear stress and can be expressed as:

$$\tau = \frac{F}{A} \tag{2.3}$$

For an incompressible and laminar flow, the simplest constitutive equation expresses the link between shear stress $\tau$ and shear rate $\dot{\gamma}$ as a linear law:

$$\tau = \eta\dot{\gamma} \tag{2.4}$$

where the coefficient of proportionality $\eta$ represents dynamic viscosity. Kinematic viscosity, which is nothing but viscosity per unit density, is also specified. However, from here on, viscosity abusively means dynamic viscosity. Typical viscosity values at 20 °C are given in Table 2.1.

| Material | Dynamic viscosity ($\mathrm{Pa \cdot s}$) |
|---|---|
| Air | $10^{-5}$ |
| Water | $10^{-3}$ |
| Olive oil | $10^{-1}$ |
| Honey | 10 |
| **Bone cement** | **1 to $10^4$** |
| Glass | $10^{40}$ |

Table 2.1 – Typical viscosity values of common materials.

Viscosity is not necessarily a constant function. It can be of very variable complexity, depending on the chemical nature of the product and on the flow conditions. The following section presents a classification of viscosity behavior laws for materials in molten state.

## 2.1.2 Rheological behaviors

### 2.1.2.1 Newtonian fluids

A Newtonian fluid has a constant viscosity that does not depend on flow conditions.

### 2.1.2.2 Non-Newtonian time-independent fluids

As the name implies, non-Newtonian fluids represent all the other fluids that do not meet this characteristic. Viscosity of such fluids evolves as the shear rate changes, and $\tau$ and $\dot{\gamma}$ follow a non-linear relationship. According to the viscosity response to a change of shear rate, a classification of non-Newtonian time-independent fluids can be completed.

**Shear-thinning fluids**  Among non-Newtonian fluids, the most prevalent are described as shear-thinning or pseudoplastic. These materials deform unequally according to the shear rate they are subjected. In particular, their dynamic viscosity decreases as the shear rate rises. Common samples that undergo this behavior are molten polymers, many agro- and food-related or personal care products, or blood. For this last example, blood cells are moving randomly at low shear rates. However, when the flow speed increases, red blood cells are lining up the flow direction and, thus, viscosity of the blood decreases.

**Shear-thickening fluids**  The main feature of these fluids lies in their evolution of viscosity as a function of the flow conditions. Unlike the previous class, a dilatant fluid has a viscosity that increases with the applied stress or shear rate. These fluids are much less common than shear-thinning fluids.

**Plastic fluids**  The distinctive feature of plastic fluids is to not deform below a threshold shear stress named yield stress. Fraction of fluids for which the stress is less than this critical value flows in block or does not flow at all. When shear stress exceeds this yield stress, the material behaves either as a Newtonian (Bingham plastic fluid) or a shear-thinning fluid. Such a result can only be explained by the partial destruction of the component internal structure when the stress becomes sufficiently high. Toothpaste and ketchup provide plastic behaviors. Their yield stress prevents them to flow outside the tube or bottle until they are pushed or shaken.

The previous behaviors are schematized in Figure 2.2 both with a rheogram (shear stress as a function of shear rate) or with viscosity curves (viscosity along shear rate).
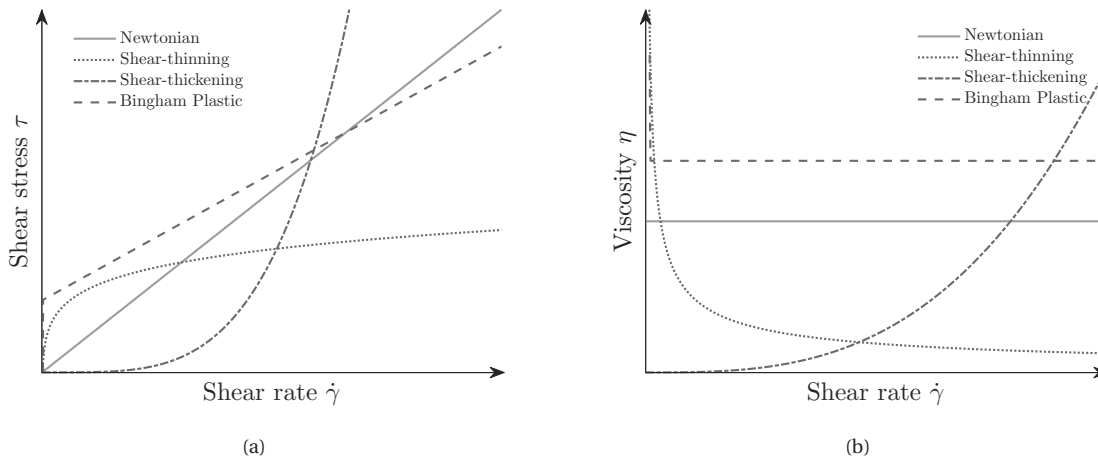
Figure 2.2 – Typical flow behaviors: (a) illustrated with flow curves; (b) illustrated with viscosity curves.

#### 2.1.2.3    Non-Newtonian time-dependent fluids

Studying the influence of shear rate on the stress of a given material is not always sufficient to determine its behavior. The duration of the applied shear stress is sometimes equally important. Materials that have a viscosity which decreases or increases over time, under the influence of a constant stress, or shear rate, are referred to as, respectively, thixotropic or rheopectic fluids. Their initial viscosity is restored after the end of solicitations and sufficient rest time. Thixotropy can be observed in cell biology with the cytoplasm or in cooking with mayonnaise. It can happen that this phenomenon is not reversible, which means that viscosity continues to increase until it reaches a value corresponding to a solid, as for orthopedic bone cement.

#### 2.1.2.4    Viscoelastic fluids

Viscoelastic fluids are unique in their ability to present a variable behavior depending on constraints changes. These materials have both viscous and elastic properties. When the speed of constraints change is low, the internal structure of the material has time to reorganize itself and the material exhibits a liquid behavior. Otherwise, at high load frequencies, the behavior approximates that of a solid. Molten polymers are typical examples of viscoelastic fluids and their behavior can be coupled with one of the previous behaviors.

### 2.1.3    Rheometers

A rheometer is an instrument aiming to specify the behavior of a fluid by shearing the sample and, then, measuring both the stress and strain of the material. Two major classes of rheometers are distinguished: the capillary rheometer and the dynamic or rotational rheometer. Whatever the rheometer and its basic geometry, the fundamental equations always assume the no-slip condition of the fluid at the wall.

#### 2.1.3.1    Capillary rheometer

Introduced by Hagen in 1839 [Hagen 1839] and Poiseuille in 1840 [Poiseuille 1840], the capillary rheometer was the first tool that allowed the measurement of the viscosity of water. Based on a pressure-driven flow, the

geometry of this rheometer is very simple. A capillary tube of radius $R$ and length $L$ with $R << L$ is arranged at the bottom of an upstream reservoir enclosing the sample that needs to be characterized. The material flows through the capillary under the pressure drop either generated by gravity or a mobile piston as schematized in Figure 2.3. Fundamental equations being well established (see Appendix A), the measured flow rate and pressure drop provide a viscosity value. Such a rheometer is employed to measure and identify viscosity at moderate or high shear rates. At a given temperature, several steady-state measurements at different pressures or flow rates are needed to identify a shear-thinning behavior. However, in this flow, the velocity gradient and the viscosity
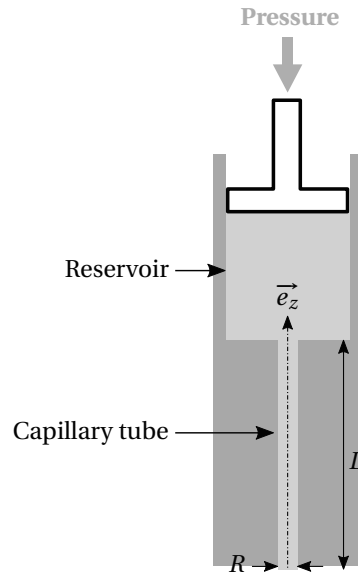
Figure 2.3 – Geometry of the Hagen-Poiseuille flow.

are nonhomogeneous since they both depend on the distance to the central axis. Moreover, the need for a large volume of material prevents temperature regulation for materials with a low thermal diffusivity such as orthopedic bone cement. To characterize curing materials such as bone cement, bench top capillary rheometers are sidelined because they cannot be cleaned out.

### 2.1.3.2 Dynamic rheometer

While a capillary rheometer provides measurements of steady shear functions, small deformations with alternating stress applied by rotational rheometers allow to study the viscoelastic properties of a material and to compute a complex viscosity as later detailed in section 2.3.1. In terms of typology, several geometries can be identified: coaxial cylinder (Couette or Searle systems), parallel disks or cone and plate geometry. The coaxial cylinder geometry being adapted for low viscosity fluids, only parallel plates and cone and plate geometries will be detailed and compared in Table 2.2. Regardless of the selected geometry, two approaches are available: either the stress is controlled and the resulting shear rate measured, or at the contrary, the shear rate is the input and the shear stress is determined. These modes are respectively named controlled-stress (CS) or controlled-rate (CR) rheometers. Contrary to the capillary rheometer, volumes of the tested material are low (around 1 mL), which makes the temperature control possible and easy. Finally, low to moderate shear rates can be investigated.

**Cone and plate**   While the bottom plate is fixed, an upper cone of half-angle $\alpha$ rotates (see Table 2.2). To assume that $\tan \alpha \approx \alpha$, cone angles can vary from 1 deg to 4 deg depending on the size of the particles inside the tested material. This cone and plate geometry ensures the constant shear rate throughout the complete sample

volume. Some experiments have been performed with a 4 deg half-angle and a 10 mm radius but have not been exploited.

**Parallel-plates** Such a rheometer consists of two parallel plates of radius $R$ and spaced by a gap of size $h$, between which a sample of fluid is forced to flow. The bottom plate is fixed while the upper one rotates. This mode enables to reach higher shear rates than the cone and plate geometry by reducing the gap $h$. As further detailed in section 2.3.2.1, an experimental set-up has been designed on such a rheometer with a 10 mm radius and 1 mm gap.

| | Cone and plate | Parallel disks |
|---|---|---|
| Geometry |  |  |
| Benefits | • Homogeneous shear rate<br><br>• Small volume<br><br>• Easy temperature control | • Easy to load<br><br>• Small volume<br><br>• Easy temperature control<br><br>• Possibility to change the gap size $h$, and, thus, the shear rate with the same rotational speed |
| Drawbacks | • Difficult loading<br><br>• Delicate if high particles | • Nonhomogeneous shear rate, depends on position (only for continuous measurements) |

Table 2.2 – Comparison between dynamic rheometers with a cone and plate *vs.* a parallel-plates geometry.

To summarize Table 2.2, shear rate can easily be changed on a parallel-plates rheometer by only adapting the gap $h$ whereas the complete material must be adapted with a cone and plate geometry. Besides its ease of use, the parallel-plates geometry is also recommended for curing or hardening samples with a tridimensional chemical structure [Macosko 1994]. Nevertheless, a cone and plate rheometer provides a constant shear rate in the tested sample, which is convenient to characterize viscosity with a steady flow. For continuous measurements on a parallel-plates rheometer, the strain field is nonhomogeneous and increases with the distance from the rotational axis. While it can be corrected [Macosko 1994], this important drawback does not exist anymore for dynamic measurements. Based on this list of pros and cons, a parallel-plates rheometer with a dynamic testing seems to be the most adapted solution to characterize bone cements.

## 2.2 Acrylic bone cement

### 2.2.1 Chemical aspect

Bringing the monomeric liquid in contact with the powder starts a radical polymerization reaction, which is triggered by the activator inside the liquid and the initiator comprised inside the powder. In a reduction oxidation process, BPO is decomposed by DmpT, forming free radicals. The presence of these radicals ensures the start of the polymerization reaction and the development of a multitude of polymer chains following the chemical equation in Figure 2.4. Without the initiator and activator, the process could start spontaneously only with heat or with other energy sources.
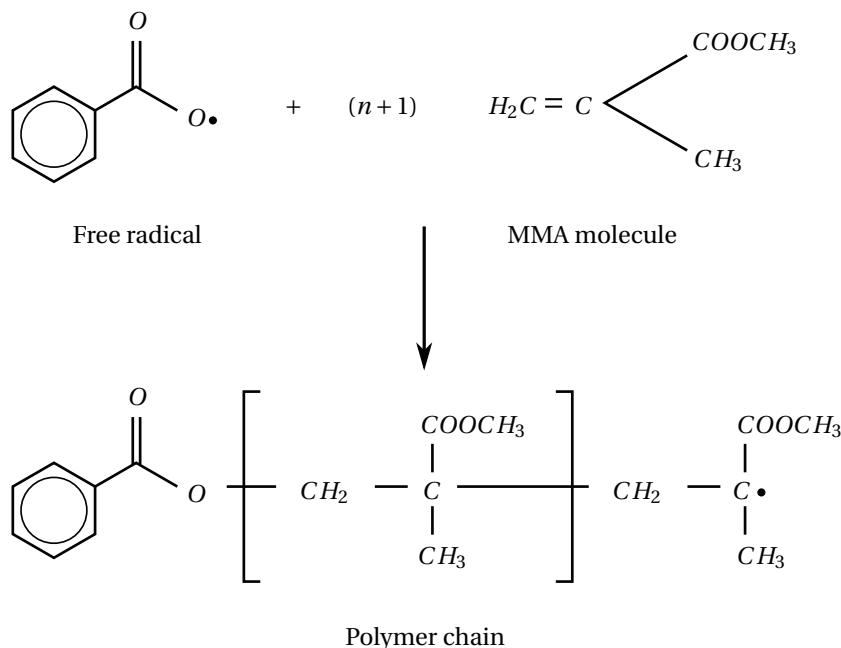


Figure 2.4 – Chemical equation describing the formation of a polymer chain by breaking the C=C double bond of the MMA.

Besides the polymerization reaction, a curing reaction occurs that creates additional cross-links between the polymer chains. For bone cements, the curing level is generally important in order to ensure a higher stiffness. It is such that PMMA bone cements can be compared to thermosetting plastics, and not to thermoplastics as usually for such polymers [Rehman 1996].

This reaction is highly exothermic, which means a considerable amount of heat is released. This exothermic reaction has been investigated on three different commercial bone cements: Osteopal® V from Heraeus and CementoFixx-R and CementoFixx-L from Optimed. Once the powder and liquid have been mixed together, the resulting fluid is poured in a syringe in which a thermistor has previously been installed. Already shown in subsection 1.2.2.2, curves from Figure 2.5 present the evolution of the temperature for these bone cements. In our experiments, the three temperature curves increase slowly until they reach a sharp increase and then, decrease progressively to fall down to room temperature (21.5°C) by natural air convection. The maximum temperature might exceed 100°C. Such high temperatures have never been recorded *in vivo* since vascularization and surrounding tissues dissipate the thermal energy, but temperatures of about 50°C can still be reached [Reckling 1977]. The end of the setting phase for these three different bone cements has been represented with dashed lines in Figure 2.5. It allows to highlight that the sharp rise in temperature concurs with the end of the

29
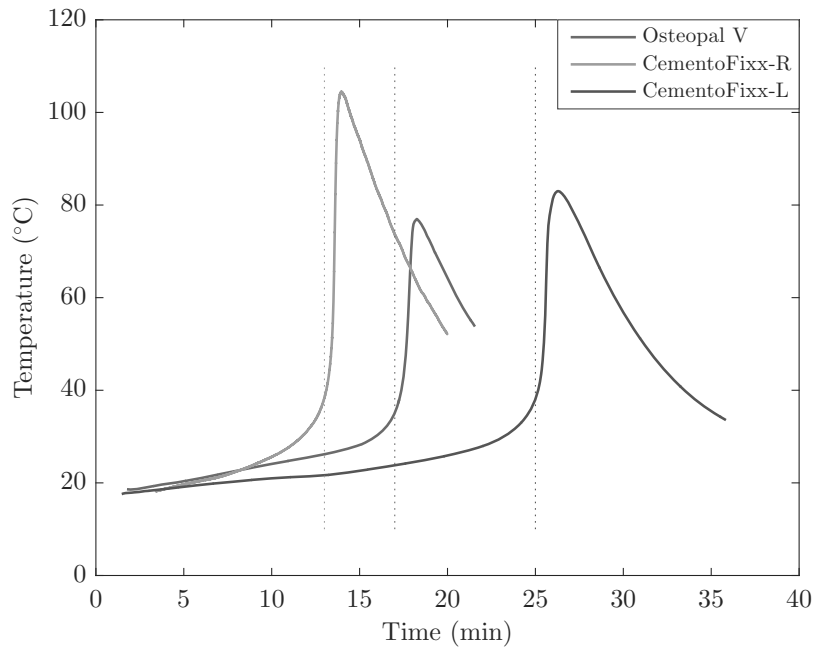
Figure 2.5 – Temperature evolution curves for three bone cements during their curing reaction where time zero is the beginning of the mixing phase.

setting phase and, thus, to the final sudden hardening. So, a temperature control during a rheological study appears to be essential in order to analyze its influence on the bone cement viscosity separately.

## 2.2.2 Bone cement rheological properties

As already mentioned in section 2.1.2, orthopedic bone cement has a highly non-Newtonian behavior. In the literature, studies that outline this behavior are abundant with a preponderance of work on viscosity-time characteristics [Lewis 2011]. An overview of these studies allow to emphasize various parameters influencing the viscosity evolution of bone cement. Since bone cement undergoes a polymerization reaction during the injection, it seems obvious that bone cement is time-dependent. This property has been confirmed by Krause *et al.* [Krause 1982] by using both a cone and plate geometry and a capillary rheometer or by Lewis and Carroll with a cup and plate geometry [Lewis 2002]. In all this research, viscosity is plotted as a function of time and it is easily noticeable that viscosity increases with time until it reaches an almost infinite value, such as a solid. One would describe this behavior as rheopectic, but this time dependency is nothing but the evolution of the polymerization reaction.

Another major influencing factor is temperature. Proved both for calcium phosphate [Sarda 2001, Liu 2006] and acrylic bone cement [Farrar 2001, Nicholas 2007], increasing temperature accelerates the curing reaction and, thus, increases the viscosity. Meanwhile, an analysis developed by Sullivan *et al.* also demonstrates the influence of the initial temperature on the material. A decrease of the initial temperature leads to a decrease in viscosity and an increase of the doughing, setting and working time [Sullivan 2007]. This confirms the efficiency of leaving the cement inside the refrigerator until the very last moment as discussed in the procedure description in subsection 1.2.3.

Even if much less represented in the literature, shear rate is a non-negligible parameter [Kolmeder 2011]. Indeed,

the higher the shear rate is, the lower the viscosity is. This characteristic is also extended during the mixing process. Baroud *et al.* compared a manual mixing with an oscillatory mixing using a rotary shaker on both calcium phosphate and acrylic bone cement. Mixing under oscillations significantly lowers the mean viscosity [Baroud 2004a]. This phenomenon highlights a shear-thinning behavior.

These three main dependencies are illustrated in the following figure.
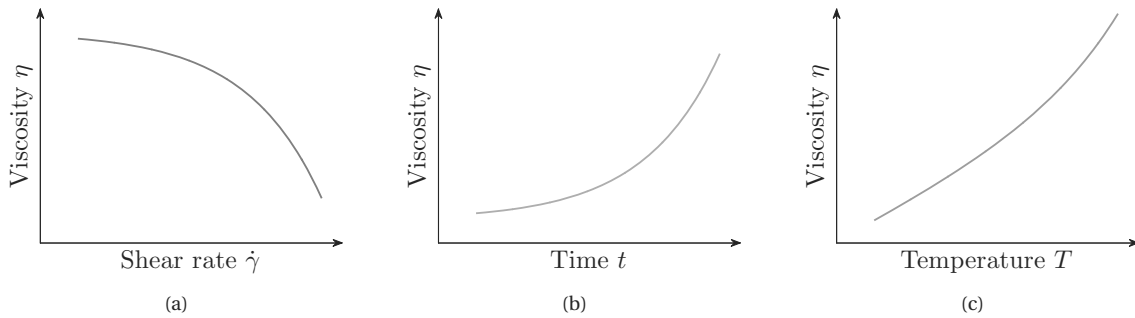


Figure 2.6 – Bone cement viscosity behavior as a function of: (a) shear rate $\dot{\gamma}$ (shear-thinning fluid); (b) time $t$ (rheopectic fluid); (c) temperature $T$ (thermo-dependent fluid).

While there is a sizable literature on the influence of these extrinsic parameters, some intrinsic parameters such as the powder-to-liquid ratio or the size of particles are as essential. On one hand, increasing the powder-to-liquid ratio intensifies the contact among particles, which increases viscosity and shortens the setting time. This property has been exposed in [Sarda 2001, Liu 2006] on calcium phosphate cement but it seems consistent that acrylic bone cement shows the same behavior. On the other hand, the relative amount of small-sized and large-sized PMMA particles strongly influences rheological properties [Lewis 2002]. Indeed, growing the particle size increases the mean viscosity while improving the initial strength [Liu 2006, Hernández 2006].

Hence, it seems imperative to study accurately the influence of both the temperature and the shear rate on viscosity in order to identify a viscosity behavior law that will allow us, on one hand, to size an injection device and, on the other hand, to propose a viscosity control strategy.

### 2.2.3   Viscosity modeling

Several models are exposed in the literature to describe the rheological behavior of bone cement. The first assumption is to consider this fluid to be Newtonian at each time step as pointed out by [Bohner 2003] or [Baroud 2004a]. This remains a rough approximation, since, as explained in subsection 2.2.2, orthopedic bone cement has a shear-thinning behavior.

The most widespread model for characterizing pseudoplastic fluids is the Ostwald-de Waele law [Ostwald 1925], commonly called power law. Illustrated in Figure 2.7, it gives the following relationship between viscosity $\eta$ and shear rate $\dot{\gamma}$:

$$\eta\left(\dot{\gamma}\right) = K\dot{\gamma}^{n-1} \tag{2.5}$$

where $K$ represents the flow consistency in $Pa\cdot s^n$ and $0 < n < 1$ is the flow index of the sample. For fluids with time- and temperature-independent viscosity, $K$ and $n$ are constant parameters. This model also applies to Newtonian fluids when $n = 1$ and to dilatant materials when $n > 1$. The power law describes a shear-thinning behavior for non-zero shear rates. At low shear rates for a shear-thinning fluid (*i.e.* $0 < n < 1$), this model tends

to an infinite viscosity, which does not represent a real fluid. So, this law should only be used for non-low shear rates, for instance higher than $10^{-1}$ s$^{-1}$.
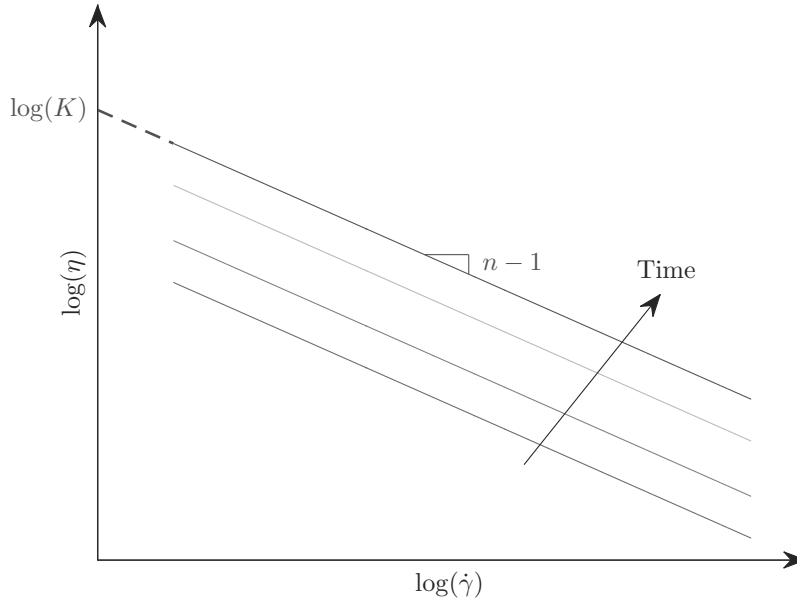


Figure 2.7 – Illustration of the Ostwald-de Waele law.

According to the literature, a valid hypothesis is to assume that acrylic bone cement viscosity follows this well-known law. In order to take into account the time dependency, authors supposed $n$ and $K$ to be functions of time from mixing. For instance, based on experiments on a cone and plane dynamic rheometer for low shear rates and on a capillary rheometer for high shear rates, Krause *et al.* identified $n = at + b$ and $K = c \exp(dt)$ [Krause 1982]. A similar study has been achieved in [Widmer Soyka 2013] on a rotational rheometer with parallel plates and led to the identification of the power law model where both $n$ and $K$ were linear functions *i.e.* $n = at + b$ and $K = ct + d$. Always based on the power law, a slightly different approach has been introduced by [Baroud 2003] and [Lian 2008]. Viscosity is expressed in relation to a characteristic time $t_s$ and shear rate $\dot{\gamma}_s$ such that:

$$\eta(\dot{\gamma}) = K \left( \frac{\dot{\gamma}}{\dot{\gamma}_s} \right)^{n-1} \tag{2.6}$$

where $K = a \left( \dfrac{t}{t_s} \right) + b$ is expressed in Pa·s and $n = c \left( \dfrac{t}{t_s} \right) + d$. This fitting provides satisfactory results only on restrictive time ranges: between 3 and 5 minutes in [Baroud 2003] and between 2 and 8 minutes in [Lian 2008].

Other models characterizing shear-thinning fluids exist like the Carreau law in the form:

$$\eta(\dot{\gamma}) = \eta_0 \left( 1 + \left( \lambda \dot{\gamma} \right)^2 \right)^{\frac{n-1}{2}} \tag{2.7}$$

where $\eta_0$ and $\lambda$ respectively correspond to the viscosity at $\dot{\gamma} = 0$ and a characteristic time (relaxation time). This law differs from the power law by the presence of a Newtonian plateau at low shear rates. Some shear-thinning fluids also have a viscosity which tends asymptotically to a non-zero constant $\eta_\infty$ at infinite shear rate. Improving

the previous law allows to introduce the Carreau-Yasuda law [Carreau 1972, Yasuda 1979]:

$$\frac{\eta(\dot{\gamma}) - \eta_\infty}{\eta_0 - \eta_\infty} = \left(1 + (\lambda\dot{\gamma})^2\right)^{\frac{n-1}{2}}. \tag{2.8}$$

This law found only in [Rusu 2009] is supposed to represent the rheological behavior of bone cement. However, it is all the more useless that maximum shear rates reached in the injection device are such that the infinite threshold will never be reached.

Given that temperature increases simultaneously with the polymerization reaction and, thus, viscosity, it makes sense to express a relationship between time and temperature. Usually, when the viscosity of a polymer depends on temperature, the well-known Arrhenius law allows to describe this relationship [Bird 1987, Dealy 2006]. Once the degree of polymerization is high enough, this law can be applied. For instance, in [Farrar 2001] and, later, in [Boger 2009], authors expressed the bone cement temperature dependence by assuming that the Arrhenius law holds:

$$\frac{1}{t_v} = A\exp\left(\frac{-E}{R_{\text{gas}}T}\right) \tag{2.9}$$

where $t_v$ is the time taken to reach a given viscosity, $R_{\text{gas}}$ the gas constant and $T$ the temperature. Activation energy $E$ and the constant $A$ are parameters that have to be identified as Farrar and Rose achieved thanks to measurements on a CS-rheometer with a parallel plate geometry [Farrar 2001].

Bone cement viscosity is strongly correlated with the progress of the polymerization reaction and, thus, with the degree of cure. Based on the evolution equation of an autocatalytic reaction [Sourour 1976] extended with an empirical diffusion factor [Fournier 1996], Lion *et al.* [Lion 2007] and Kolmeder *et al.* [Kolmeder 2010, Kolmeder 2011] proposed a model describing the degree of cure $q$ of an acrylic bone cement:

$$\frac{dq}{dt} = \left(K_1 + K_2 q^\alpha\right)\left(1 - q\right)^\beta f_D(q) \tag{2.10}$$

where $f_D$ is a diffusion coefficient setting the maximum degree of cure. $K_1$ and $K_2$ model the temperature dependency of the bone cement with an Arrhenius law such that $K_i = A_i \exp\left(-\frac{E_i}{RT}\right)$.

Finally, in [Kolmeder 2013], by introducing an internal variable $p$ that expresses the progress of dissolution as:

$$\frac{dp}{dt} = K_1 + K_2 p^m \quad, \tag{2.11}$$

Kolmeder and Lion combined the dependency on dissolution and the pseudoplastic behavior by improving the power law:

$$\eta = \eta_0(p)l\dot{\gamma}^{n-1} \tag{2.12}$$

The identification of the parameters $A_i$, $E_i$, $l$, $m$ and $n$ leads to the only model, to our knowledge, that gather the shear rate and temperature dependencies.

These different models have been implemented by authors for the purpose of simulations. While Baroud and Yahia identified and incorporated the power law as rheological behavior into a finite element software [Baroud 2004b], many other authors simulated the cement flow inside cancellous bone [Widmer Soyka 2013]. This allows Bohner *et al.* to predict cement extravasation using a theoretical approach [Bohner 2003], even if bone cement has been considered as Newtonian. Teo *et al.* provided a visualization of the PMMA cement flow before a percutaneous vertebroplasty procedure [Teo 2007]. Results of such simulations show a strong relationship between viscosity and the uniformity of the bone cement spreading inside the vertebra [Baroud 2006,

Loeffel 2008]. Last, Landgraf *et al.* proposed a computational fluid dynamics simulation of the bone cement injection while curing *in vivo* [Landgraf 2015].

This state-of-the-art illustrates that a large number of studies has been conducted to characterize and to model the rheological behavior of acrylic bone cement while curing. However, to our knowledge, no model both shows simultaneously the viscosity dependence over the most important parameters (time, shear rate and temperature) and is exploitable for viscosity control purposes. Therefore, in the following section, we will design a rheological study in order to propose a novel bone cement model so that it can be exploited for the future viscosity control.

## 2.3   Rheological study

In the case of the capillary rheometer, there are two issues to deal with. First, the tested material has to flow out of the reservoir through a thin capillary tube at more significant speeds, in order to reach higher shear rates. Since the volume of a bone cement kit lies between 10 and 15 mL, pushing continuously at important speeds would not allow to cover an acceptable time range because the reservoir would empty too quickly. To address this issue, Kolmeder *et al.* interrupted the experiment on certain time intervals and interpolate the data [Kolmeder 2013] which means that they switched between zero and non-zero shear rates. For our study, this solution has been avoided since PMMA also highly depends on this extrinsic parameter. Also, the important volume of material inside the reservoir prevents a satisfactory temperature control, especially since bone cement reveals a small thermal diffusivity. However, given the temperature dependence of this material, temperature regulation is imperative, which eliminates the possibility to use the capillary rheometer. Hence, the dynamic rheometer has been chosen, rheometer that, besides, measures viscoelastic properties. Finally, to not worry about the size of particles in the mixture and to facilitate loading, the parallel-plates geometry has been selected for our rheological study.

### 2.3.1   Viscosity measurement

The controlled rate mode has been preferred since it is the most obvious way to describe the effect of shear rate. Once the sample is loaded, it is subjected to a complex strain $\gamma^*$ or a sinusoidal strain $\gamma$ such that:

$$\gamma^*(t) = \gamma_0 \exp(j\omega t) \quad \text{or} \quad \gamma(t) = \gamma_0 \sin(\omega t) \tag{2.13}$$

with $t$, the time, $\omega$, a constant pulsation, $\gamma_0$, a small amplitude and $j$, the complex number such that $j = \sqrt{-1}$. For low deformations and/or stresses, the linear viscoelastic response results in a complex shear stress $\tau^*$ (or real shear stress $\tau$) that is also sinusoidal at the same pulsation but phase-shifted by an angle $\delta$, also called loss angle, as delineated in Figure 2.8 and expressed as:

$$\tau^*(t) = \tau_0 \exp\left(j(\omega t + \delta)\right) \quad \text{or} \quad \tau(t) = \tau_0 \sin(\omega t + \delta). \tag{2.14}$$
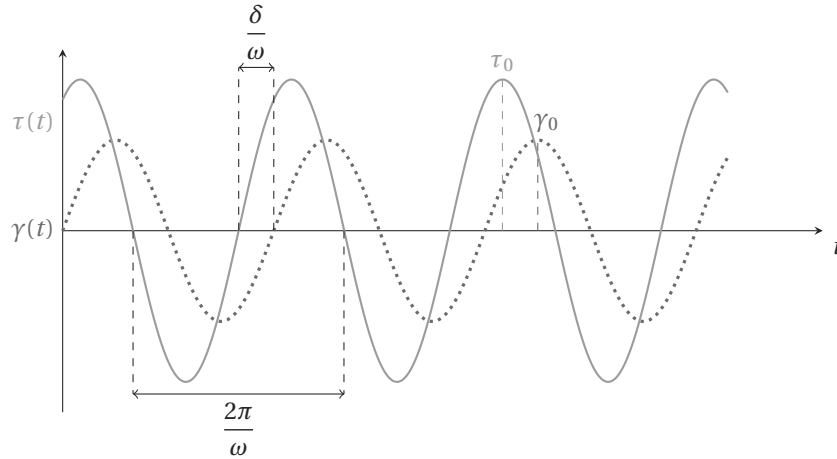
Figure 2.8 – Schematic shear stress response to a sinusoidal strain deformation for a viscoelastic fluid.

From both expressions of strain and shear stress, the complex shear modulus $G^* = \dfrac{\tau^*}{\gamma^*}$ can be written as:

$$G^* = \frac{\tau_0}{\gamma_0} \left( \cos\delta + j \sin\delta \right) \tag{2.15}$$

which is equivalent to:

$$G^*(\omega) = G'(\omega) + j G''(\omega) . \tag{2.16}$$

$G'$ represents the storage modulus which tells us about the energy storage in the flow while the loss modulus $G''$ describes the energy dissipation in the flow. These modules are linked with the mechanical loss factor by:

$$\tan\delta = \frac{G''}{G'}. \tag{2.17}$$

The complex modulus leads to an expression of the resulting shear stress that can be resolved into one component in phase with the strain which coincides with the elastic response, and one component in quadrature phase with the strain which matches with the viscous response. If a material has a purely elastic behavior ($\delta = 0$), the resulting constraint is simplified to $\tau = G'\gamma$ to be in phase with the strain. Conversely, for a purely viscous sample, $\delta = 90°$ and shear stress becomes $\tau = G''\gamma$ to be, this time, in phase quadrature with the deformation.

In a very similar way, the complex viscosity $\eta^*$ is defined as the ratio between shear stress $\tau^*$ and shear rate $\dot{\gamma}^*$:

$$\eta^*(\omega) = \frac{\tau^*}{\dot{\gamma}^*} = \frac{G^*}{j\omega} = \eta'(\omega) - j\eta''(\omega) \tag{2.18}$$

with $\eta'(\omega) = \dfrac{G''}{\omega} = \dfrac{\tau_0}{\gamma_0\omega} \sin\delta$ and $\eta''(\omega) = \dfrac{G'}{\omega} = \dfrac{\tau_0}{\gamma_0\omega} \cos\delta$.

This complex viscosity can directly be compared to the steady-shear viscosity measured as a function of shear rate thanks to the Cox-Merz rule exposed on page 150 in [Bird 1987] and on page 375 in [Dealy 2006]. Scientific works conducted by Cox and Merz are at the root of this rule [Cox 1958]. Found to be valid for most molten polymers, this empirical rule states:

$$|\eta^*(\omega)| = \eta(\dot{\gamma}) \ \text{ for } \ \omega = \dot{\gamma}. \tag{2.19}$$

As many authors in the literature [Al-Hadithi 1992, Lewis 2002, Lian 2008], this law has been assumed to be valid for orthopedic bone cements, especially given that the polymerization reaction is well initiated. Results acquired on the developed injection device will later help to validate the use of this relation (see Figure 5.13).

Such a rheometer allows to characterize the bone cement behavior since both the rotational speed and the temperature can be controlled by the device.

## 2.3.2 Experiments

### 2.3.2.1 Experimental set-up

As already emphasized in section 2.2.2, acrylic bone cement viscosity depends mainly on time $t$, temperature $T$ and shear rate $\dot{\gamma}$. An experimental set-up has been designed to demonstrate and, above all, to model the influence of these parameters on the viscosity evolution of bone cements. As already mentioned, a deformation control has been adopted.

Conditions under which our experiments have been conducted are close to those of any intervention performed at the department of Interventional Radiology at the University Hospital of Strasbourg. Thus, a cement from Heraeus, Osteopal V, has been exploited. The cements kits have all been stored in a refrigerator regulated at 4 °C. Moreover, we have also worked in an air-conditioned room which has been hold at 21 °C, temperature that has been recorded there.

**Hardware** Our tests have been carried out on a rotational rheometer HAAKE[TM] MARS[TM] from ThermoFisher Scientific with a parallel-plates geometry. Radius of both plates has been fixed to $R = 10$ mm while the gap size is $h = 1$ mm. Moreover, in order to separate the influence of each parameter, the sample is temperature-controlled by Peltier modules located below the lower plate of the rheometer. The maximum heating and cooling rate of the controlled chamber is $20\,\text{K}\cdot\text{min}^{-1}$.



(a)                    (b)

Figure 2.9 – Dynamic shear rheometer HAAKE[TM] MARS[TM] from ThermoFisher Scientific: (a) image of the complete device; (b) zoom on the area of interest during an experiment.

**Software** The rheometer is delivered with the software RheoWin 4 that can control the device (see Figure 2.9(a)). Before starting a new test, the exact geometry must be selected. Additionally, the temperature of the sample, the amplitude and the frequency of the deformation must be filled. The amplitude $\gamma_0$ has been set at 0.5 in order to be in the linear viscoelastic domain [Osswald 2014] and has never been changed between experiments. This user-friendly interface allows to complete the rheological testing routine via drag-and-drop icons.

**Course of the experience**   After having zeroed the rheometer, a bone cement kit composed of a powder pack and a liquid ampoule is straight out of the refrigerator. Then, a chronometer is triggered simultaneously with the beginning of the hand-mixing phase of both components in a bowl. This mixing phase continues until a homogeneous paste is obtained, which lasts around 40 s. A small sample of cement is finally loaded on the fixed plate of the rotational rheometer before the rotating shaft is lowered to meet the required gap of size $h$. Oscillations and viscosity computation begin at this point.

The sample analysis is ended either if the viscosity reaches a maximal value ($5.10^5$ Pa·s) or if the device cannot afford the deformation set point anymore.

**Available data**   Throughout the whole experiment, the user can access the raw data. Among others, measurements of the angle and of the torque can be visualized. It allows to evaluate the signal quality in order to make sure viscosity computations are achieved in the linear viscoelastic region. Figure 2.10 shows an example of these measures over a period of 1s.
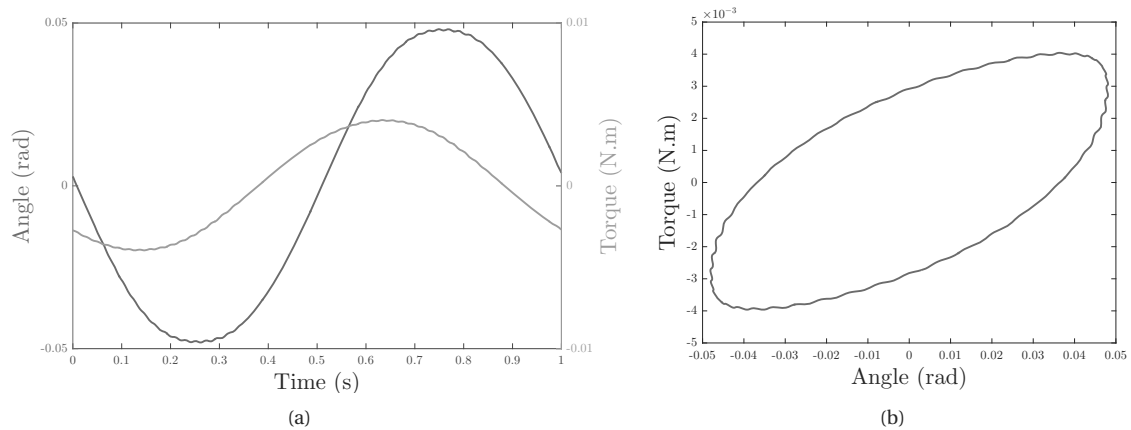


Figure 2.10 – Raw data: (a) angle and torque raw sine waves; (b) torque *vs.* angle Lissajous plot.

Simultaneously, a viscosity curve function of time is updated as torque measurements are available. A new viscosity value is given every 5 to 10 s depending on the tested shear rate. ThermoFisher Scientific rheometers are known for their accuracy. Particularly, the torque resolution is 0.1 nN·m and the normal force resolution is 0.001 N. According to their evaluation on oscillation measurements, the measured deviation of viscosity is less than 1%. Thanks to these high precision sensors, measurements, under the same conditions and by following carefully the experimental protocol, offer a very good repeatability.

### 2.3.2.2   Acquired data

Several series of tests have been run to characterize the effects of both shear rate and temperature.

**Temperature influence**   During the first sequence of tests, shear rate has been fixed for all trials at $\omega = 2\pi f$ with $f = 1$ Hz, *i.e.* $\dot{\gamma} = 2\pi\,\text{s}^{-1}$ according to the Cox-Merz law. Then, the temperature has been incremented between two experiments. Results are given in Figure 2.11 where time zero is when the monomer liquid is added to the polymer powder. The range of investigated temperature goes from 10 °C to 37 °C. The upper limit of temperature, that represents body temperature, originates in the desire of understanding the behavior of bone cement once injected in the treated vertebra. Temperatures behind 10°C have not been explored since a period of 60 min is significantly above the radiologist expectation in terms of injection time.
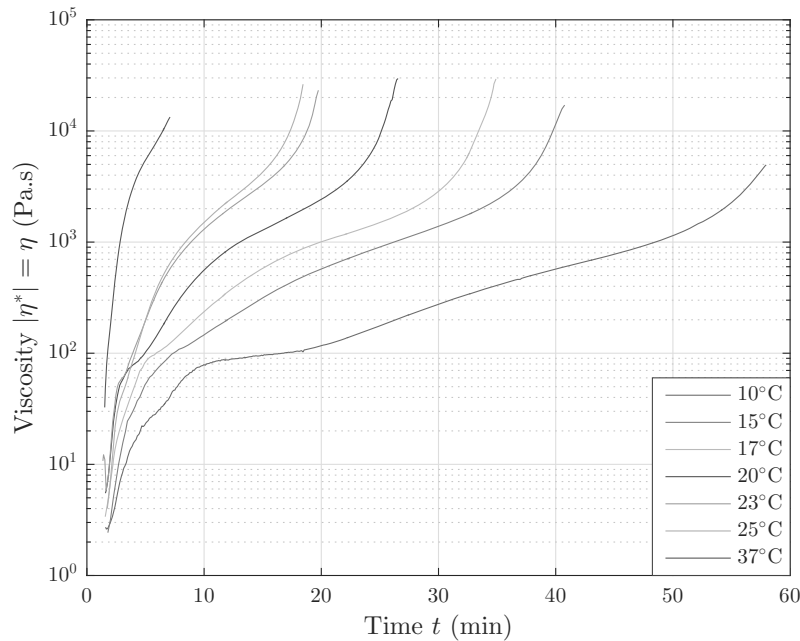
Figure 2.11 – Viscosity evolution along time at $\dot{\gamma} = 2\pi\ \mathrm{s}^{-1}$ for a range of temperature from $10\,°\mathrm{C}$ to $37\,°\mathrm{C}$ for Osteopal® V (Heraeus).

**Shear-thinning behavior** To monitor the effect of pulsation, and thus, shear rate, the rheometer is able to perform a frequency sweep. If bone cement was time-independent, a unique cement kit would be sufficient. Nevertheless, bone cement viscosity evolves over time at an increasingly high rate. If, at the beginning of the experiment, viscosity of the cement can still be considered as time-independent over one cycle, it is not the case when the curing reaction accelerates. In other words, the evolution of the degree of cure is not negligible during a single data acquisition over the frequency range. Therefore, the opposite of the previous exercise has been carried out. This time, it has consisted in imposing a temperature $T_0$ to the sample and varying the angular velocity from one trial to another by adapting frequency $f$ since $\omega = 2\pi f$. In Figures 2.12(a) and 2.12(b), the evolution of viscosity is plotted over time for a range of shear rates at, respectively, $T_0 = 20\,°\mathrm{C}$ and $T_0 = 25\,°\mathrm{C}$.

### 2.3.3 Analysis

As expected, curves from Figure 2.11 show that the cooler the cement is kept, the longer the curing time is. Indeed, at $37\,°\mathrm{C}$, the bone cement Osteopal® V needs less than 5 min to reach $5000\,\mathrm{Pa\cdot s}$, against almost 60 min at $10\,°\mathrm{C}$. Moreover, after 15 min from the start of the mixing phase, a temperature difference of only $6\,°\mathrm{C}$ (between $17\,°\mathrm{C}$ and $23\,°\mathrm{C}$) is enough to almost multiply by four the viscosity value. These observations demonstrate that the bone cement setting time can easily be increased by cooling down the cement of only a few degrees. Also, this justifies again that the bone cement should be cooled inside a refrigerator prior to any percutaneous vertebroplasty to increase as much as possible the setting time. For all the tested temperatures, the speed of the viscosity evolution for Osteopal® V in the last phase of curing (i.e. during the abrupt growth in viscosity) has been computed and is always close to 100 Pa. Similarly, at the beginning of the curing phase, this rate is the same (around 1 Pa) regardless of the temperature. This proves that the setting time can be increased by adjusting temperature.

Regarding Figure 2.12, it can easily be noticed that the higher the shear rate is, the lower the viscosity value is.
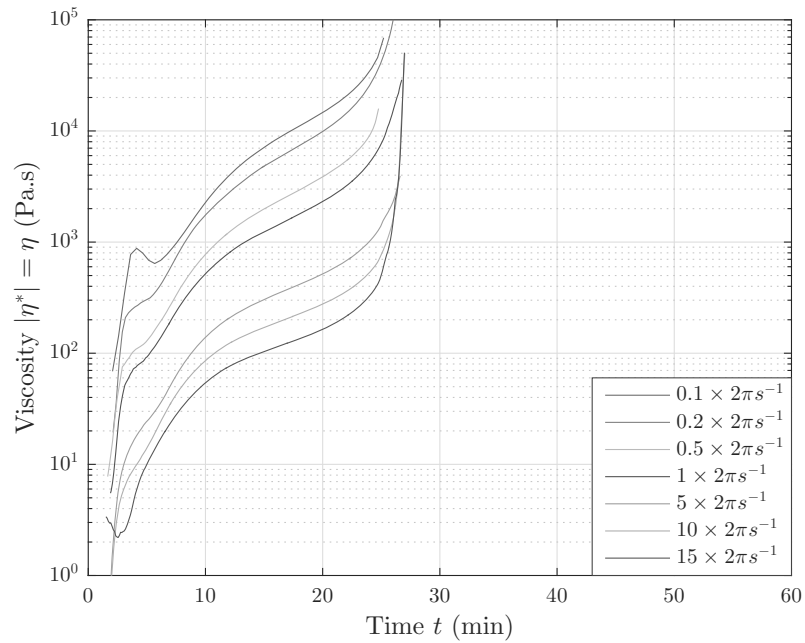
(a)
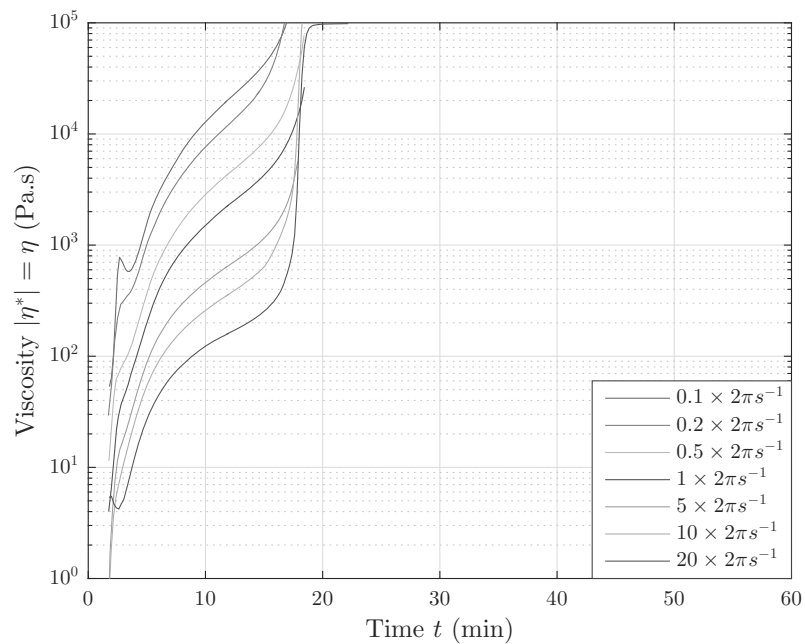


(b)

Figure 2.12 – Evolution of viscosity along time from mixing for several shear rates for Osteopal® V (Heraeus): (a) at $T_0 = 20\,°C$; (b) at $T_0 = 25\,°C$.

For instance, multiplying the shear rate by 10 results in a viscosity difference of almost a decade after 10 min. This confirms the shear-thinning behavior of acrylic bone cement. Moreover, the end of the curing process seems to be superimposed for all frequencies at a given temperature. So, it seems tough to increase the working

39

phase beyond a certain time period (around 27 min at 20 °C and 18 min at 25 °C) even if the sample is highly sheared, for instance at around $\dot{\gamma} = 100\,\mathrm{s}^{-1}$. The curves do not reach the same maximum viscosity value. This phenomenon results from the slippage of the bone cement during the experiments. Indeed, if the adherence between the rotating plate and the cement is not sufficient to transfer the shear stress to the rotor axis, the output measure is insignificant.

While the full study has been completed on the cement Osteopal® V, generously provided by Heraeus, the approach and the results are fully transposable to other bone cements. Indeed, these trends have been confirmed for two other bone cements from Optimed as exposed in Figure 2.13 with plots of viscosity.



(a)

(b)
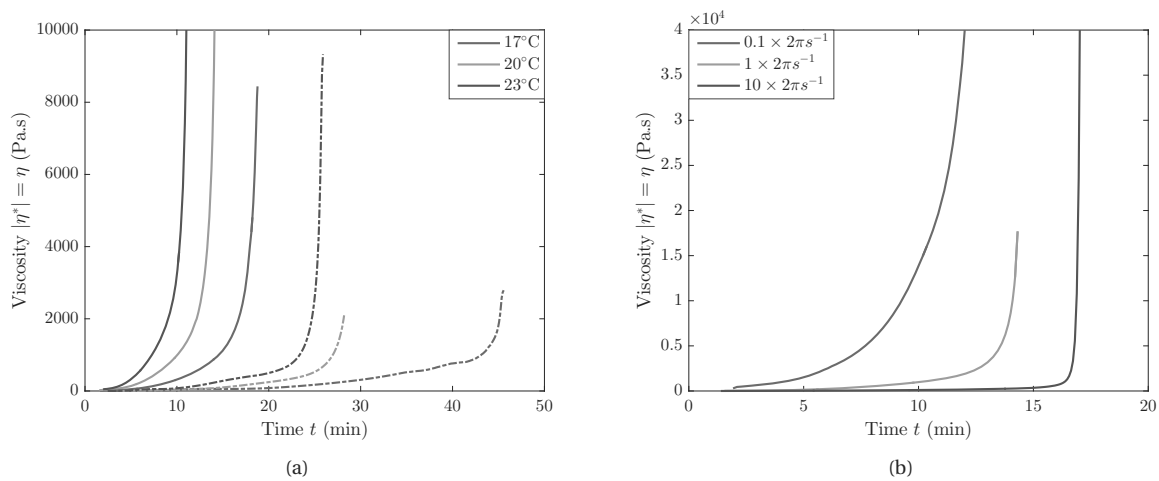
Figure 2.13 – Evolution of viscosity along time from mixing for CementoFixx-R (straight lines) and CementoFixx-M (dashed curves): (a) for a range of temperature at $\dot{\gamma} = 2\pi\,\mathrm{s}^{-1}$; (b) for several shear rates at $T_0 = 20\,°\mathrm{C}$.

In the light of the conducted experiments, viscosity can be adjusted in a controlled way by acting either on the bone cement temperature or on shear rate during the injection. Increasing the shear rate, *i.e.* the bone cement injection speed, of the bone cement decreases its viscosity. Since the injection speed should be left to the decision of the practitioner, it is not possible to play on shear rate. For that reason, we chose to control the cement temperature in order to meet the requirement of both reducing the leakage risk and increasing the working phase. This will be detailed in Chapter 5. This regulation can be achieved by modulating thinly the thermal amplitude, which is recommended to minimize the impact of the viscosity regulation on the surrounding tissues. This control is challenging since the managed fluid is flowing and undergoes an exothermic polymerization reaction.

# 3 Modeling and identification of bone cement viscosity

## Contents

The rheological study that has been carried out in the previous chapter has highlighted how a bone cement behaves depending on extrinsic parameters while curing. However, to meet our goals, among other the control of bone cement viscosity during its injection, a model is required. Experiments led and described in section 2.3.2 provide enough data to identify two models: an algebraic model as common in rheology and another model expressed as a nonlinear differential equation in order to develop a viscosity control strategy further.

## 3.1 Modified Power law

### 3.1.1 Motivation and contributions

Besides a description of the bone cement behavior considering the main extrinsic parameters, this rheological model will serve as a benchmark for online viscosity measurements carried out on the injection device detailed in Chapter 4. Hence, as conceded by many authors in the literature, acrylic bone cement is assumed to follow the power law, already defined in section 2.2.3. While remaining close to the real behavior, this model is elementary since there are only two parameters to identify. Throughout the following chapters, it will be proven that this model is an appropriate choice for the online computation of the viscosity in real time.

With $n < 1$, equation (2.5) describes the pseudo-plastic behavior of acrylic bone cement. However, as detailed in section 2.2.2, this qualification is not sufficient since orthopedic bone cement is also highly time- and temperature dependent. A contribution of this chapter is the identification of parameters $n$ and $K$ of the power law at each time step $t$ in order to define them as mathematical functions of time. In other words:

$$\eta(t,\dot{\gamma}) = K(t)\dot{\gamma}^{n(t)-1} \tag{3.1}$$

Finally, inspired by the time-temperature superposition principle [Bird 1987, Dealy 2006], the influence of temperature will be considered through two shift factors, which will be identified. Based on the idea that a viscosity curve at a given temperature $T$ can be deduced from a viscosity curve at a reference temperature, we will be able to write $\eta$ as a function of time, temperature and shear rate, *i.e.* $\eta(t,T,\dot{\gamma})$.

### 3.1.2 Identification of the functions $n$ and $K$

By applying the logarithmic function to both terms of equation (3.1), the modified power law can also be written as:

$$\log(\eta) = \log(K) + (n-1)\log(\dot{\gamma}) \tag{3.2}$$

For a set of experiments at a fixed temperature, $\log(\eta)$ can be plotted as a function of $\log(\dot{\gamma})$ at each time step. Based on data displayed in Figure 2.12 for Osteopal® V cement, this exercise has been performed for curves at $T_0 = 20\,°C$ (see Figure 3.1(a)) and at $T_0 = 25\,°C$ (see Figure 3.1(a)). The obtained curves feature a linear relationship between $\log(\eta)$ and $\log(\dot{\gamma})$ which validates the use of the power law, at least in this range of shear rate.
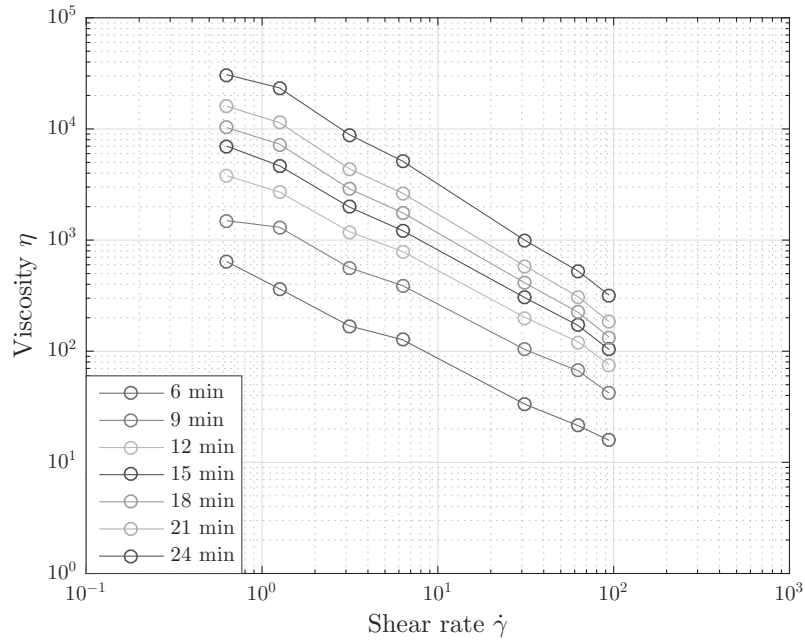
(a)
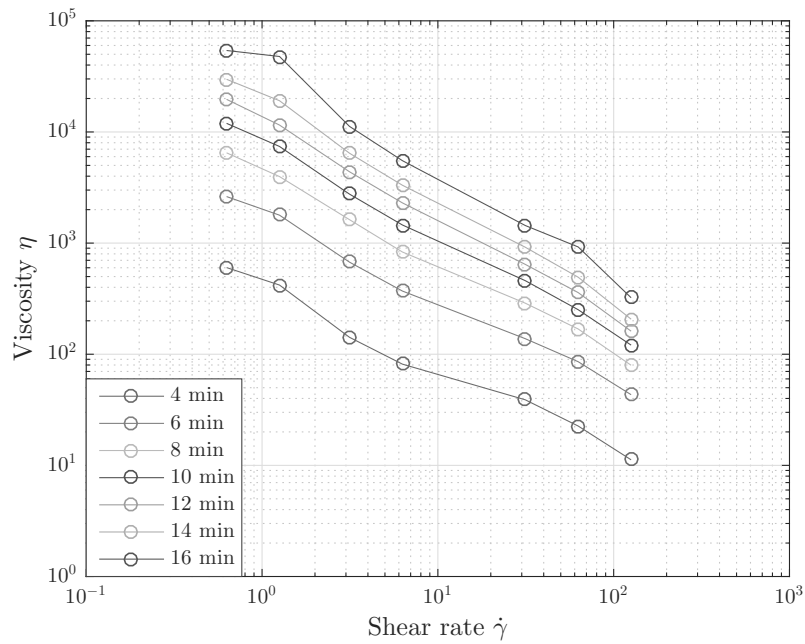


(b)

Figure 3.1 – Viscosity curves in logarithmic scale justifying the application of the power law: (a) at $T_0 = 20\,°\mathrm{C}$; (b) at $T_0 = 25\,°\mathrm{C}$.

In the light of equation (3.2), a linear regression between variables $\log(\eta)$ and $\log(\dot{\gamma})$ estimates parameters $n$ and $K$. The slope determines $n-1$ while $\log(K)$ is evaluated with the y-intercept. Repeating this optimization at different times allows to plot $n$ and $K$ over time. This method has been applied both for experiments at $T_0 = 20\,°\mathrm{C}$

and at $T_0 = 25\,°C$ at time intervals of 5 seconds. With a mean determination coefficient $R_d^2 = 0.9959 \pm 0.0047$ at $T_0 = 20\,°C$ and $R_d^2 = 0.9924 \pm 0.0185$ at $T_0 = 25\,°C$, curves of $n$ and $K$ over time are presented in Figure 3.2.



(a)  (b)
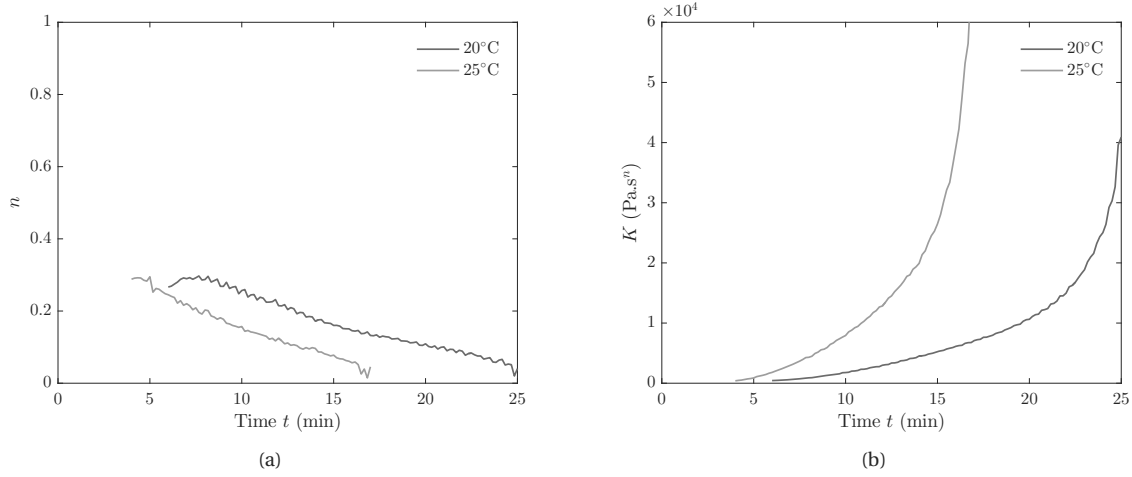
Figure 3.2 – Identification of the parameters $n$ and $K$ of the power law over time at $T_0 = 20\,°C$ (blue curve) and at $T_0 = 25\,°C$ (green curve).

On one side, $n$ decreases slightly over time and is well below 1, which confirms the non-Newtonian, and more particularly the shear-thinning behavior. On the other side, $K$ is the parameter that evolves the most but also influences the most the evolution of viscosity. Indeed, within the time of a vertebroplasty procedure, $K$ is almost multiplied by 5.

It is noticeable that curves representing $n$ and $K$ remind simple mathematical functions. For instance, $n$ looks like a straight line or is slightly exponential while $K$ is clearly exponential or parabolic. In Tables 3.1 and 3.2, the results obtained for $n$ and $K$ identifications are summarized. To remain consistent with the colors in Figure 3.2, results in blue are those at $T_0 = 20\,°C$ and in green those at $T_0 = 25\,°C$.

| $n$ | Identified parameters | | Coefficient of determination |
|---|---|---|---|
| | $a_n$ | $b_n$ | $R_d^2$ |
| Straight line | $-2.3265.10^{-4}$ | 0.3843 | 0.9762 |
| $a_n t + b_n$ | $-3.2735.10^{-4}$ | 0.3594 | 0.9788 |
| Exponential | $-0.1880$ | 1.4406 | 0.9604 |
| $a_n \ln t + b_n$ | $-0.1787$ | 1.2937 | 0.9912 |

Table 3.1 – Results of simple functions fitted to the reconstructed points $n$ over time at two fixed temperatures.

| $K$ | Identified parameters | | | | Coefficient of determination |
| --- | --- | --- | --- | --- | --- |
| | $a_K$ | $b_K$ | $c_K$ | $d_K$ | $R_d^2$ |
| Parabolic | $5.801.10^{-2}$ | $-67.43$ | $1.599.10^4$ | - | 0.6631 |
| $a_K t^2 + b_K t + c_K$ | 0.1213 | $-96.6$ | $1.704.10^4$ | - | 0.7793 |
| Exponential | $4.623.10^{-2}$ | $9.25.10^{-3}$ | - | - | 0.9409 |
| $a_K \exp(b_K t)$ | 12.7 | $8.007.10^{-3}$ | - | - | 0.9347 |
| Power | $4.406.10^{-11}$ | 4.738 | - | - | 0.7628 |
| $a_K t^{b_K}$ | $5.727.10^{-11}$ | 4.956 | - | - | 0.8745 |
| Sum of exponentials | $3.078.10^{-8}$ | $1.791.10^{-2}$ | 429.6 | $2.684.10^{-3}$ | 0.9985 |
| $a_K \exp(b_K t) + c_K \exp(d_K t)$ | $1.404.10^{-10}$ | $3.058.10^{-2}$ | 545.2 | $3.953.10^{-3}$ | 0.9986 |

Table 3.2 – Results of simple functions fitted to the reconstructed points $K$ over time at two fixed temperatures.

Given the determination coefficients in Table 3.1, the straight line is preferred to model the evolution of the index $n$. To parameterize the flow consistency $K$, no simple function stands out among the one tested. However, for both temperatures, fitting the sum of two exponential functions to the data $K$ provides much better results. So, the power law expressed in equation (3.1) can be modeled as:

$$\eta(t, \dot{\gamma}, T) = \left( a_K \exp(b_K t) + c_K \exp(d_K t) \right) \dot{\gamma}^{a_n t + b_n - 1}. \tag{3.3}$$

Parameters $a_n$, $b_n$, $a_K$, $b_K$, $c_K$ and $d_K$ are functions of temperature $T$, which is consistent with the pronounced temperature dependence of $n$ and $K$ in Figure 3.2.

### 3.1.3 Temperature influence

So far, the previous model does not manage the temperature influence. Usually applied for melt polymers [Dealy 2006], the time-temperature superposition principle states that a temperature change for viscosity between a reference temperature $T_{\text{ref}}$ and another temperature $T$ is equivalent to a double shifting thanks to an horizontal translation coefficient $a_{T_{\text{ref}} \to T}$:

$$\eta\left(\dot{\gamma}, T\right) = \frac{1}{a_{T_{\text{ref}} \to T}} \eta\left( \frac{\dot{\gamma}}{a_{T_{\text{ref}} \to T}}, T_{\text{ref}} \right) \tag{3.4}$$

As part of the presented rheological study, it has been confirmed that increasing the cement temperature amounts to accelerating the viscosity rate and, conversely, a decrease in temperature slows down the polymerization reaction and delays the setting time of the cement. This property is equivalent to $a_{T_{\text{ref}} \to T} > 1$ if $T_{\text{ref}} > T$ and $a_{T_{\text{ref}} \to T} < 1$ if $T_{\text{ref}} < T$.

However, applying this time-temperature principle is not possible since data have not been acquired for a large range of shear rates. Therefore, in the following, the principle will be modified in order to move from a viscosity evolution curve at temperature $T_{\text{ref}}$ to another one at $T$ and at a given shear rate $\dot{\gamma}$. As a first approach, the following relationship has been proposed:

$$\eta\left( a_{T_{\text{ref}} \to T} t, T, \dot{\gamma} \right) = \eta\left( t, T_{\text{ref}}, \dot{\gamma} \right) \tag{3.5}$$

From curves acquired at a fixed shear rate but for a range of temperature (see Figure 2.11), this shift factor has

been computed for each temperature $T \in [10; 15; 17; 23; 25; 37] \, °C$ as:

$$a_{T_{\text{ref}} \to T} = \underset{a_T \in \mathbb{R}^+}{\arg\min} \left\| \eta(a_T t, T, \dot{\gamma}) - \eta(t, T_{\text{ref}}, \dot{\gamma}) \right\|_2^2 \tag{3.6}$$

with $T_{\text{ref}} = 20 \, °C$, the reference temperature. Results are reported in Table 3.3. Except on a small range of temper-

| $T(°C)$ | $a_{T_{\text{ref}} \to T}$ | $R_d^2$ |
|---------|---------|---------|
| 10 | 2.75 | 0.6242 |
| 15 | 1.574 | 0.8748 |
| 17 | 1.32 | 0.9822 |
| 23 | 0.749 | 0.9745 |
| 25 | 0.694 | 0.9716 |
| 37 | 0.207 | 0.7656 |

Table 3.3 – Results of the computation of the single shift factor for different temperatures.

atures around the reference temperature, values of determination coefficients $R_d^2$ do not provide satisfactory results.

Looking more closely to the acquired data, we can assume there is a double shift factor. This means that for a temperature change from $T_{\text{ref}}$ to $T$ at a given shear rate, not only the time scale is adjusted but also viscosity is shifted by a vertical translation factor as schematized in Figure 3.3.
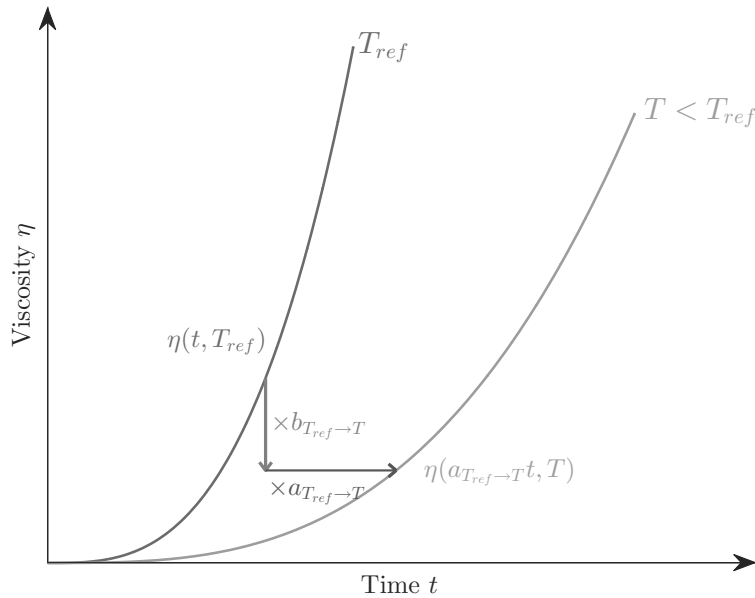


Figure 3.3 – Viscosity curves at $T_{\text{ref}}$ and $T < T_{\text{ref}}$ illustrating the idea of the double shift factor.

In other words,

$$\eta\left(a_{T_{\text{ref}} \to T} t, T, \dot{\gamma}\right) = b_{T_{\text{ref}} \to T} \eta\left(t, T_{\text{ref}}, \dot{\gamma}\right) \tag{3.7}$$

where $a_{T_{\text{ref}}\to T} > 1$ if $T_{\text{ref}} > T$ and $b_{T_{\text{ref}}\to T} < 1$ if $T_{\text{ref}} > T$.

Again, at each temperature $T$ of the interval $[10;15;17;23;25;37]$, parameters $a_{T_{\text{ref}}\to T}$ and $b_{T_{\text{ref}}\to T}$ are identified by solving the following optimization problem:

$$\begin{bmatrix} a_{T_{\text{ref}}\to T} \\ b_{T_{\text{ref}}\to T} \end{bmatrix} = \underset{\substack{a_T \in \mathbb{R}^+ \\ b_T \in \mathbb{R}^+}}{\arg\min} \left\| \eta(a_T t, T, \dot{\gamma}) - b_T \eta(t, T_{\text{ref}}, \dot{\gamma}) \right\|_2^2 \tag{3.8}$$

where $T_{\text{ref}} = 20\,^\circ\text{C}$. With a mean determination coefficient $R_d^2 = 0.9987 \pm 0.002$, computed parameters $a_{T_{\text{ref}}\to T}$ and $b_{T_{\text{ref}}\to T}$ are plotted in Figure 3.4 by circular markers.
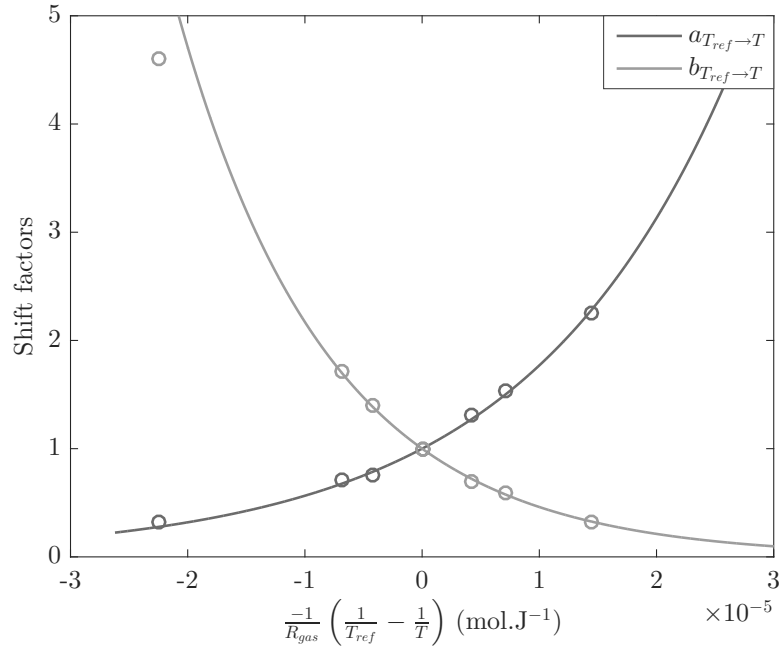


Figure 3.4 – Results of the computation of parameters $a_{T_{\text{ref}}\to T}$ and $b_{T_{\text{ref}}\to T}$ (circular markers) that can both be fitted by an Arrhenius law (continuous lines).

The X-axis represents the quantity $\dfrac{-1}{R_{\text{gas}}} \left( \dfrac{1}{T_{\text{ref}}} - \dfrac{1}{T} \right)$ where the temperatures $T_{\text{ref}}$ and $T$ are expressed in Kelvin. This choice allows to highlight that both shift factors follow an Arrhenius law such that:

$$a_{T_{\text{ref}}\to T} = \exp\left( \frac{-E_a}{R_{\text{gas}}} \left( \frac{1}{T_{\text{ref}}} - \frac{1}{T} \right) \right) \tag{3.9}$$

and

$$b_{T_{\text{ref}}\to T} = \exp\left( \frac{-E_b}{R_{\text{gas}}} \left( \frac{1}{T} - \frac{1}{T_{\text{ref}}} \right) \right). \tag{3.10}$$

These expressions ensure that $a_{T_{\text{ref}}\to T} = 1$ and $b_{T_{\text{ref}}\to T} = 1$ when $T = T_{\text{ref}}$.

Finally, simple linear regressions between $\dfrac{1}{R_{\text{gas}}} \left( \dfrac{1}{T_{\text{ref}}} - \dfrac{1}{T} \right)$ and either $a_{T_{\text{ref}}\to T}$ or $b_{T_{\text{ref}}\to T}$ (see Figure 3.4) lead to

the identification of the activation energies $E_a$ and $E_b$ as summarized in Table 3.4. These identified functions, $a_{T_{\text{ref}} \to T}$ and $b_{T_{\text{ref}} \to T}$, are drawn with straight lines in Figure 3.4.

| Parameters | Values | SI units |
|:---:|:---:|:---:|
| $E_a$ | $5.70 \times 10^4$ | $\text{J} \cdot \text{mol}^{-1}$ |
| $E_b$ | $7.75 \times 10^4$ | $\text{J} \cdot \text{mol}^{-1}$ |

Table 3.4 – Resulting activation energies of the identification of $a_{T_{\text{ref}} \to T}$ and $b_{T_{\text{ref}} \to T}$ as Arrhenius laws.

Combining equations (3.1) and (3.7) provides the following equality:

$$K(a_{T_{\text{ref}} \to T} t, T) \dot{\gamma}^{n(a_{T_{\text{ref}} \to T} t, T) - 1} = b_{T_{\text{ref}} \to T} K(t, T_{\text{ref}}) \dot{\gamma}^{n(t, T_{\text{ref}}) - 1} \,, \tag{3.11}$$

which is equivalent to:

$$K(a_{T_{\text{ref}} \to T} t, T) = b_{T_{\text{ref}} \to T} K(t, T_{\text{ref}}) \tag{3.12}$$

and

$$n(a_{T_{\text{ref}} \to T} t, T) = n(t, T_{\text{ref}}). \tag{3.13}$$

These two last equations show that $K$ also presents this double shift while there is only a time rescaling for $n$. These features are observable in Figure 3.2 where $n$ and $K$ are plotted over time for two different temperatures.

Finally, choosing $T_{\text{ref}} = 20\,°\text{C}$ and referring to the identified values in Tables 3.1 and 3.2, it comes that:

$$a_n = a_n(20\,°\text{C}) = -2.33.10^{-4} \,, \tag{3.14}$$
$$b_n = b_n(20\,°\text{C}) = 0.384 \,, \tag{3.15}$$
$$a_K = a_K(20\,°\text{C}) = 3.08.10^{-8} \,, \tag{3.16}$$
$$b_K = b_K(20\,°\text{C}) = 1.79.10^{-2} \,, \tag{3.17}$$
$$c_K = c_K(20\,°\text{C}) = 430 \,, \tag{3.18}$$
$$d_K = d_K(20\,°\text{C}) = 2.68.10^{-3} \tag{3.19}$$

to finally express the final modified power law as:

$$\eta \left( a_{T_{\text{ref}} \to T} t, T, \dot{\gamma} \right) = b_{T_{\text{ref}} \to T} K(t, T_{\text{ref}}) \dot{\gamma}^{n(t, T_{\text{ref}}) - 1}. \tag{3.20}$$

with $n(t, T_{\text{ref}} = 20°\text{C}) = a_n t + b_n$ and $K(t, T_{\text{ref}} = 20°\text{C}) = a_K \exp(b_K t) + c_K \exp(d_K t)$.

### 3.1.4 Validation

To close the work on this first model, a validation step is fundamental. Therefore, equation (3.20) has been applied for the same temperatures and shear rate than in Figure 2.11. Results of this computation are given in Figure 3.5 with solid lines whereas the dashed lines are the data acquired during our rheological study.
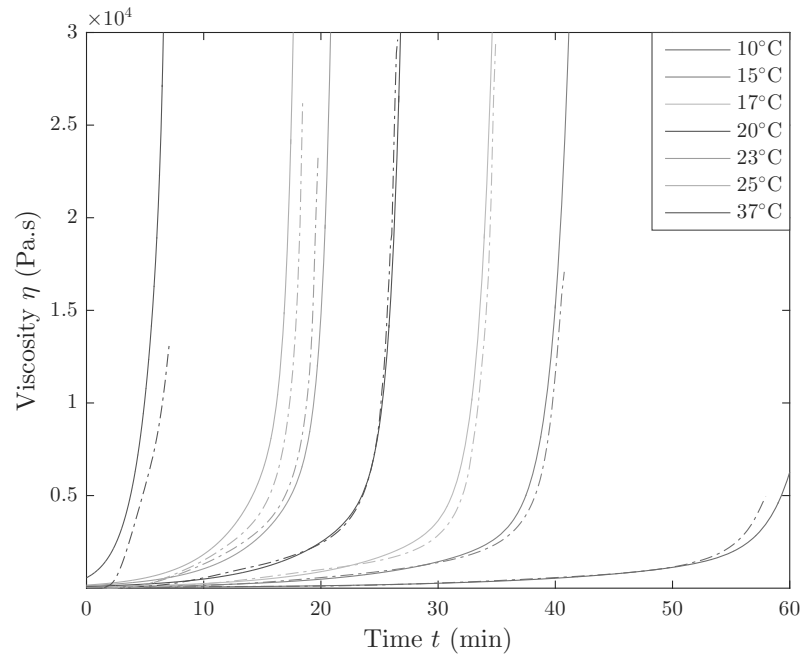


Figure 3.5 – Cross-validation step for the first model where the dashed lines result from the rheological study and the solid lines are the output of the identified model.

On the whole, this first model provides an accurate representation of the bone cement viscosity. Still, some shifts are observable. They are mainly due to the identification errors of the Arrhenius laws $a_T$ and $b_T$ (see Figure 3.4) that fit the experimental data. These errors are reflected and amplified in these final results. We can especially notice that the shift between the experimental data (dashed lines) and the output of the model (solid lines) can be cross-checked against the sign of the error between the experimental data and the fitted curves in Figure 3.4.

## 3.2 Differential equation

### 3.2.1 Motivation and contributions

In the previous section, the algebraic model (2.5) has been improved in order to consider the main parameters influencing the evolution of bone cement viscosity. While results of this identification will further be exploited to validate the ability of computing viscosity online, such a model cannot be applied for control purpose. Indeed, to tune (and simulate) the feedback control of bone cement viscosity, an algebraic relationship is not applicable. A differential equation is preferred to describe viscosity and to perform the system controller synthesis.

However, to our knowledge, there is no such model in the literature. Focusing only on curves obtained at $T_0 = 20\,°\mathrm{C}$ (Figure 2.12(a)) and at $\dot{\gamma} = 2\pi\,\mathrm{s}^{-1}$ (Figure 2.11), a new mathematical expression modeling bone cement viscosity will be identified in the following by developing a phase space identification method.

### 3.2.2 Choice of the model

As already emphasized in the literature and observed in our rheological study, the bone cement viscosity has a nonlinear time behavior. In order to better visualize this nonlinear behavior, we propose a different representation. From now on, our data are displayed as trajectories in the $(\eta, \dot{\eta})$-plane, called phase plane. The viscosity derivative $\dot{\eta}$ is computed via an implicit differentiating scheme. The phase portraits of the data are plotted in Figure 3.6.

Based on both viscosity curves and phase plane trajectories, the future identified model will have to consider the various parameters (time, temperature and shear rate) that affect the viscosity behavior of bone cement. As a first approach, a quite simple model has been selected given the parabolic shape of the curves in the phase plane. It is expressed as:

$$\dot{\eta}(t, \dot{\gamma}, T) = b(\dot{\gamma}, T) + a(\dot{\gamma}, T)\eta^{\alpha}(t, \dot{\gamma}, T) \tag{3.21}$$

where $a$, $b$ and $\alpha$ are parameters to be identified. From Figure 3.6(b), one can notice a strong overlap between the trajectories in spite of the different temperatures at which they were recorded. Hence, one can assume that both parameters $a$ and $b$ do not depend on the temperature parameter but only on $\dot{\gamma}$. The influence of the temperature occurs via the travel speed along the phase plane trajectory and is expressed through an additional parameter $\kappa(T)$. Therefore, equation (3.21) becomes:

$$\dot{\eta}(t, \dot{\gamma}, T) = \kappa(T)\left(b(\dot{\gamma}) + a(\dot{\gamma})\eta^{\alpha}(t, \dot{\gamma}, T)\right). \tag{3.22}$$

Note that the structure of this model presents some similarities with the model proposed by Kolmeder *et al.* [Kolmeder 2011] in equation (2.10).
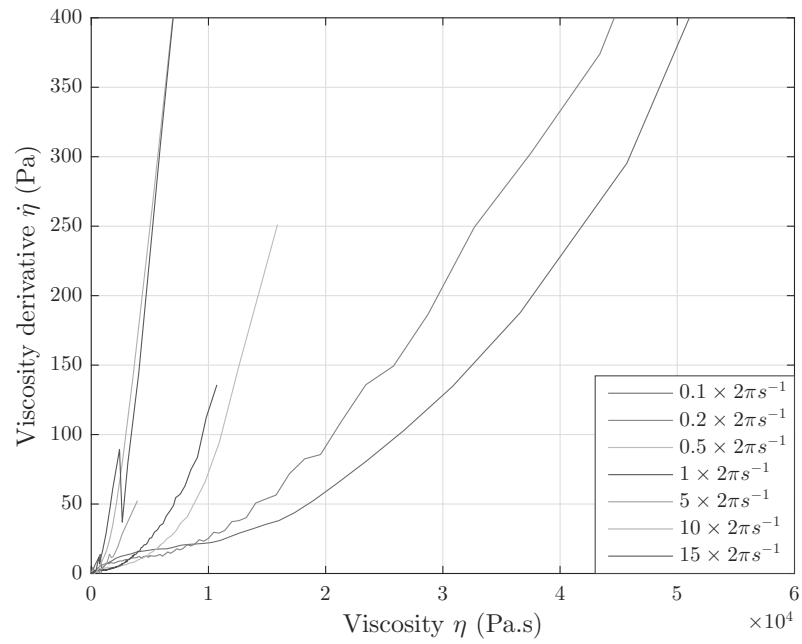
(a)
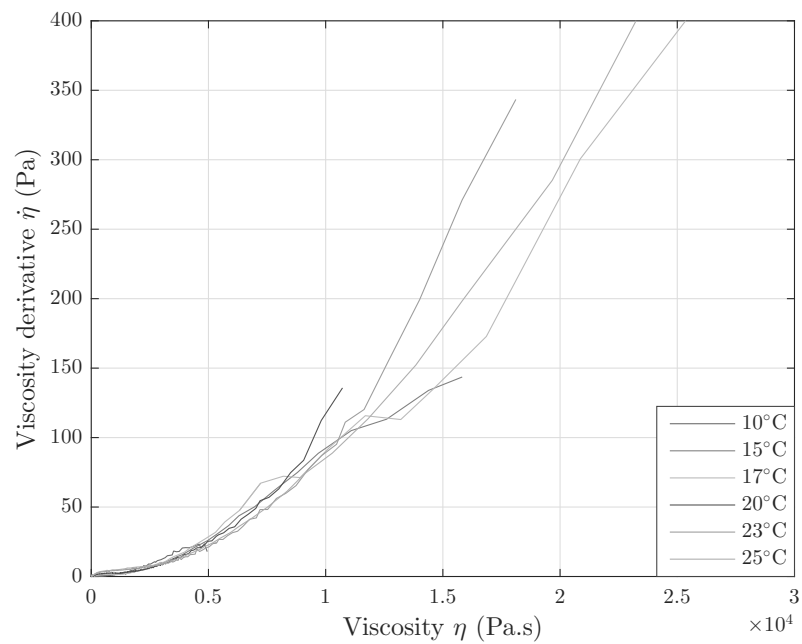


(b)

Figure 3.6 – Trajectories in the phase plan $\dot{\eta} = f(\eta)$: (a) for different shear rates and fixed temperature $T_0 = 20\,°\text{C}$; (b) for a range of temperature at a fixed shear rate $\dot{\gamma} = 2\pi\ \text{s}^{-1}$.

As a second approach, we focus on developing a model that describes the evolution of the viscosity only in the radiologist's area of interest. As further explained in section 4.1.1, the maximal viscosity $\eta_{max}$ during an injection never exceeds 2000 Pa·s. This limit does not result from the capacities of any injection device but rather from possible operative complications. Indeed, the injection of cement with such a high viscosity could generate a new fracture of the treated vertebra. In addition, the radiologist would be unable to withdraw the cannula inserted into the healed vertebra after reaching the viscosity value $\eta_{max}$. However, in order to reach a good identification, this value is raised up to 5000 Pa·s. Hence, our study focuses on the trajectories of Figure 3.7 showing the same curves than those in Figure 3.6(b) but delimited by $\eta_{max}$.
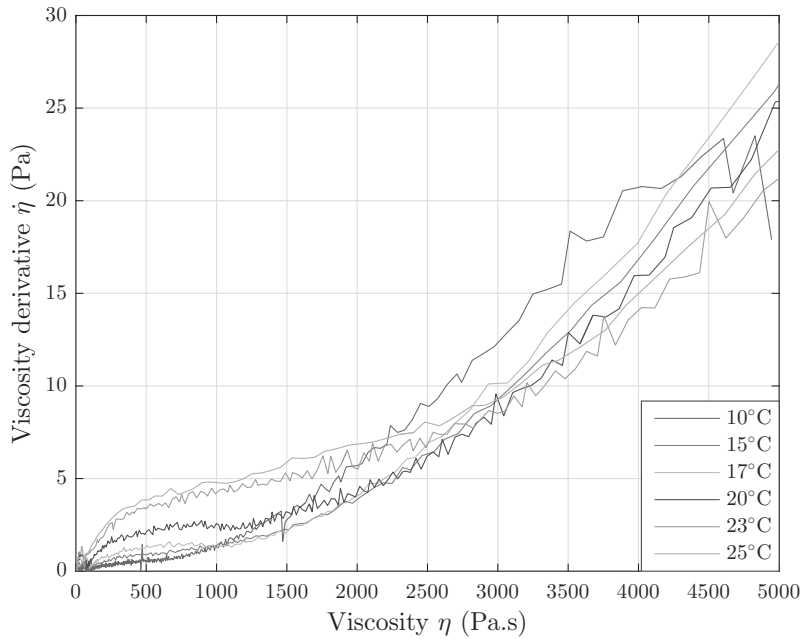


Figure 3.7 – Zoom on trajectories of Figure 3.6(b) in the practitioner's area of interest.

When focusing on the radiologist's area of interest, we cannot assume anymore that the temperature dependency is only expressed through a unique coefficient parameter such as $\kappa(T)$. Even if shear rate and temperature influences are still decoupled, variables $a$ and $b$ are functions of these parameters. In order to better describe the behavior emphasized in Figure 3.7, our model has been made more advanced by adding a second power function:

$$\dot{\eta} = a(\dot{\gamma}, T)\eta^{\alpha} + b(\dot{\gamma}, T)\eta^{\beta} \tag{3.23}$$

where $\alpha$, $\beta$, $a$ and $b$ are the parameters that will be estimated in the following section.

### 3.2.3 Phase space identification

Advanced analysis in phase space is a graphical method mostly aimed at stability studies or singular point research for nonlinear systems. However, identification methods have also been developed in phase space whenever particular characteristics of the systems behavior may be emphasized in the phase plane [Fang 2009, Matcharashvili 2007]. In the following, the state space identification of the model in (3.23) exploits the cement property emphasized in the previous section in particular the fact that the temperature dependence of $a$ and $b$ coefficients can be separated from their shear rate dependence. Therefore, the proposed identification method

is divided into three distinct steps: identifying the parameters $\alpha$ and $\beta$, identifying the influence of temperature on $a$ and $b$ by fixing shear rate and, finally, completing their identification by considering the effect of shear rate.

### 3.2.3.1 Identification of $\alpha$ and $\beta$

Similarly to [Kolmeder 2011], we make the assumption that the parameters $\alpha$ and $\beta$ are constant. In order to determine these parameters, a unique curve has to be find so that it approximates all the curves in Figure 3.6(b) where temperature changes. In fact, as we can notice from Figure 3.6(a), a translation factor allows to move from one shear rate to another.

Identifying these two parameters is equivalent to solve the minimization problem:

$$\begin{bmatrix} \alpha \\ \beta \end{bmatrix} = \underset{\substack{\alpha \in [0,1[ \\ \beta \in [1,+\infty[}}{\arg\min} \left\| \mathbf{F}(\alpha, \beta, a, b, \eta, \dot{\eta}) \right\|_2^2 \tag{3.24}$$

where $\mathbf{F}(\alpha, \beta, a, b, \eta, \dot{\eta})$ is a vector-valued function such that $\mathbf{F} = \begin{bmatrix} F_1 & F_2 & \dots & F_6 \end{bmatrix}$ with:

$$F_i = \sum_{j=1}^{N} \left( \dot{\eta}_{i,j} - a\eta_{i,j}^{\alpha} + b\eta_{i,j}^{\beta} \right)^2. \tag{3.25}$$

The index $i$ represents the $i$-th curve at temperature $T_i$ from Figure 3.6(b) while $j$ symbolizes the $j$-th point of the $i$-th curve. This optimization problem has been formulated using two constraints on $\alpha$ and $\beta$:

- $\alpha$ is limited to the interval $[0,1[$ in order to fit at best with the first part of the curve that shows a slope reduction around $500\,\text{Pa·s}$,

- $\beta$ is such that $\beta \geq 1$ in order to match the diverging part of the curves.

Based on the six temperature curves obtained from $10\,^\circ\text{C}$ to $25\,^\circ\text{C}$, the solution of the nonlinear least-squares problem (3.24) is $\alpha = 0.44$ and $\beta = 3.65$ where a Levenberg-Marquardt algorithm has been executed.

### 3.2.3.2 Temperature dependence

In order to identify the temperature influence on the viscosity evolution, a nonlinear curve-fitting problem in least-squares sense has been solved by exploiting data from Figure 3.6(b). In fact, each curve has been fitted independently to the equation $\dot{\eta} = a\eta^{0.44} + b\eta^{3.65}$ by solving the following optimization problem:

$$\begin{bmatrix} a_i \\ b_i \end{bmatrix} = \underset{\substack{a \in \mathbb{R} \\ b \in \mathbb{R}}}{\arg\min} \left\| \mathbf{G_i}(a, b, \eta_i, \dot{\eta}_i) \right\|_2^2 \tag{3.26}$$

with $G_i = \sum_{j=1}^{N} \left( \dot{\eta}_{i,j} - a\eta_{i,j}^{0.44} + b\eta_{i,j}^{3.65} \right)^2$. The index $i$ represents the $i$-th curve from the right graph in Figure 3.6(b) while $j$ symbolizes the $j$-th point of the $i$-th curve. Results are plotted in Figure 3.8.

Circles indicate parameters $a_i$ (in blue) and $b_i$ (in green), solutions of the optimization problem (3.26) as a function of $\frac{1}{R_{\text{gas}} T}$ where $T$ is the temperature in Kelvin. This representation reveals that parameters $a$ and $b$ follow an Arrhenius behavior and can be formulated as:

$$a = K_\alpha \exp\left( \frac{-E_\alpha}{R_{\text{gas}} T} \right) \quad \text{and} \quad b = K_\beta \exp\left( \frac{E_\beta}{R_{\text{gas}} T} \right). \tag{3.27}$$
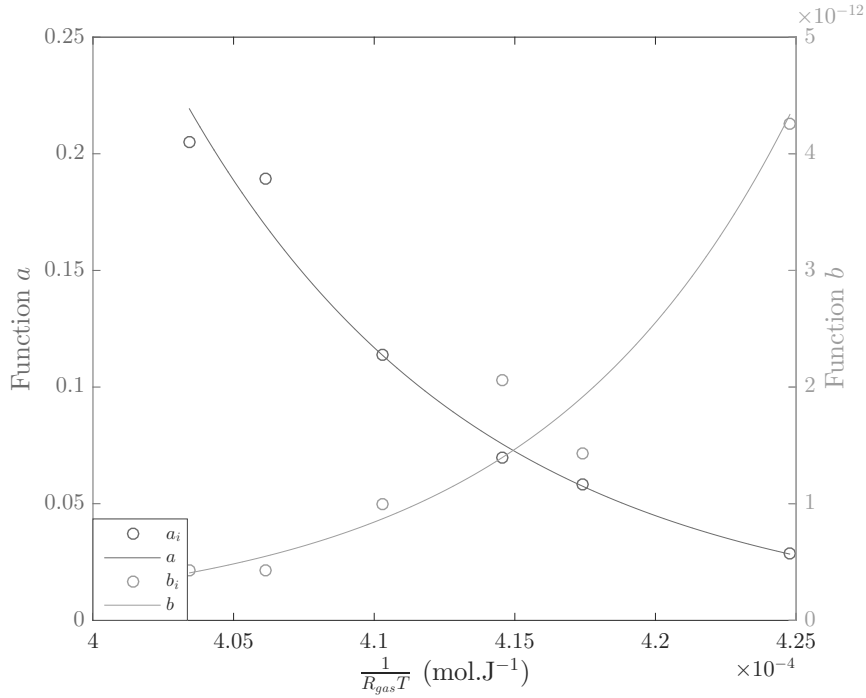
Figure 3.8 – Arrhenius behavior for parameters $a$ (in blue) and $b$ (in green): circular marks represent the solutions of the optimization problem (3.26) and the solid lines describe the identified Arrhenius laws.

From the values $a_i$ and $b_i$, a curve fitting algorithm provides the following best coefficients:

- $K_\alpha = 1.2947.10^{16}\ \mathrm{Pa}^{1-\alpha} \cdot \mathrm{s}^{-\alpha}$ and $E_\alpha = 95722\ \mathrm{J} \cdot \mathrm{mol}^{-1}$ where the coefficient of determination is 0.9916,

- $K_\beta = 1.5470.10^{-32}\ \mathrm{Pa}^{1-\beta} \cdot \mathrm{s}^{-\beta}$ and $E_\beta = 110840\ \mathrm{J} \cdot \mathrm{mol}^{-1}$ where the coefficient of determination is 0.9202.

The model proposed in section 3.2.2 can be improved as:

$$\dot{\eta} = K_\alpha(\dot{\gamma}) \exp\left(\frac{-E_\alpha}{R_{\mathrm{gas}}\,T}\right)\eta^\alpha + K_\beta(\dot{\gamma}) \exp\left(\frac{E_\beta}{R_{\mathrm{gas}}\,T}\right)\eta^\beta \tag{3.28}$$

In this subsection, only $K_\alpha(\dot{\gamma} = 2\pi\ \mathrm{s}^{-1}) = K_\alpha$ and $K_\beta(\dot{\gamma} = 2\pi\ \mathrm{s}^{-1}) = K_\beta$ have been computed since this identification step has been based on the set of data acquired at a fixed shear rate $\dot{\gamma} = 2\pi\ \mathrm{s}^{-1}$.

### 3.2.3.3 Shear rate influence

Functions describing fully the dependence of parameters $K_\alpha$ and $K_\beta$ of the model (3.28) are presented in this section. Formulation of functions $K_\alpha$ and $K_\beta$ is based on the fact that, at a given temperature $T$, there is only a constant translation factor $c$ in the logarithmic scale when changing from one shear rate to another. As a matter of fact, using data from Figure 3.6(a), by computing the difference of two curves with two different shear rates, we get a linear function of time. For two different shear rates $\dot{\gamma}_1$ and $\dot{\gamma}_2$, this means that:

$$\ln(\eta(\dot{\gamma}_2)) = c_{1\to2}\,t + d_{1\to2} + \ln(\eta(\dot{\gamma}_1))\,, \tag{3.29}$$

which is equivalent to:

$$\eta(\dot{\gamma}_2) = \exp(c_{1\to 2}\, t + d_{1\to 2})\eta(\dot{\gamma}_1). \tag{3.30}$$

According to (3.28), for the shear rate $\dot{\gamma}_1 = 2\pi\ \mathrm{s}^{-1}$,

$$\dot{\eta}(\dot{\gamma}_1) = K_\alpha(\dot{\gamma}_1)\exp\left(\frac{-E_\alpha}{R_{\mathrm{gas}}T}\right)\eta(\dot{\gamma}_1)^\alpha + K_\beta(\dot{\gamma}_1)\exp\left(\frac{E_\beta}{R_{\mathrm{gas}}T}\right)\eta(\dot{\gamma}_1)^\beta. \tag{3.31}$$

Hence, differentiating (3.30) leads to:

$$\dot{\eta}(\dot{\gamma}_2) = c_{1\to 2}\exp(c_{1\to 2}\, t + d_{1\to 2})\eta(\dot{\gamma}_1) + \exp(c_{1\to 2}\, t + d_{1\to 2})\dot{\eta}(\dot{\gamma}_1) \tag{3.32}$$

and replacing $\dot{\eta}(\dot{\gamma}_1)$ by its expression in (3.32) to:

$$\dot{\eta}(\dot{\gamma}_2) = c_{1\to 2}\eta(\dot{\gamma}_2) + K_\alpha(\dot{\gamma}_1)\exp(c_{1\to 2}\, t + d_{1\to 2})^{1-\alpha}\exp\left(\frac{-E_\alpha}{R_{\mathrm{gas}}T}\right)\eta(\dot{\gamma}_2)^\alpha +$$
$$K_\beta(\dot{\gamma}_1)\exp(c_{1\to 2}\, t + d_{1\to 2})^{1-\beta}\exp\left(\frac{E_\beta}{R_{\mathrm{gas}}T}\right)\eta(\dot{\gamma}_2)^\beta. \tag{3.33}$$

Therefore, $K_\alpha(\dot{\gamma}_2)$ and $K_\beta(\dot{\gamma}_2)$ can be deduced as:

$$K_\alpha(\dot{\gamma}_2) = K_\alpha(\dot{\gamma}_1)\exp(c_{1\to 2}\, t + d_{1\to 2})^{1-\alpha}, \tag{3.34}$$

and

$$K_\beta(\dot{\gamma}_2) = K_\beta(\dot{\gamma}_1)\exp(c_{1\to 2}\, t + d_{1\to 2})^{1-\beta}. \tag{3.35}$$

In order to compute the values of $K_\alpha$ and $K_\beta$ at any shear rate, a reference shear rate $\dot{\gamma}_{\mathrm{ref}} = \dot{\gamma}_1 = 2\pi\ \mathrm{s}^{-1}$ has been chosen so that:

$$K_\alpha(\dot{\gamma}) = K_\alpha(\dot{\gamma}_{\mathrm{ref}})\exp(c_{\dot{\gamma}_{\mathrm{ref}}\to\dot{\gamma}}\, t + d_{\dot{\gamma}_{\mathrm{ref}}\to\dot{\gamma}})^{1-\alpha}, \tag{3.36}$$

and

$$K_\beta(\dot{\gamma}) = K_\beta(\dot{\gamma}_{\mathrm{ref}})\exp(c_{\dot{\gamma}_{\mathrm{ref}}\to\dot{\gamma}}\, t + d_{\dot{\gamma}_{\mathrm{ref}}\to\dot{\gamma}})^{1-\beta}. \tag{3.37}$$

From this mapping curve, in the logarithmic scale, translation coefficients $c_{\dot{\gamma}_{\mathrm{ref}}\to\dot{\gamma}}$ and $d_{\dot{\gamma}_{\mathrm{ref}}\to\dot{\gamma}}$ allowing to change from $\dot{\gamma}_{\mathrm{ref}}$ to another shear rate $\dot{\gamma}$ are calculated with a standard linear regression based on the least squares method:

$$\begin{bmatrix} c_{\dot{\gamma}_{\mathrm{ref}}\to\dot{\gamma}} \\ d_{\dot{\gamma}_{\mathrm{ref}}\to\dot{\gamma}} \end{bmatrix} = \operatorname*{arg\,min}_{\substack{c\in\mathbb{R} \\ d\in\mathbb{R}}} \sum_{i=1}^{N}(y_i - c\, t_i - d)^2 \tag{3.38}$$

where $y_i = \ln\left(\dfrac{\eta(t_i, \dot{\gamma}, T)}{\eta(t_i, \dot{\gamma}_{\mathrm{ref}}, T)}\right)$.

Considering the linear outcome between the parameters estimation versus the logarithm of shear rate (see circular marks in Figure 3.9), $c_{\dot{\gamma}_{\mathrm{ref}}\to\dot{\gamma}}$ and $d_{\dot{\gamma}_{\mathrm{ref}}\to\dot{\gamma}}$ are determined as:

- $c_{\dot{\gamma}_{\mathrm{ref}}\to\dot{\gamma}} = -0.5209.10^{-3}\log(\dot{\gamma}) + 0.4372.10^{-3}\ \mathrm{s}^{-1}$ with a coefficient of determination of 0.9916,

- $d_{\dot{\gamma}_{\mathrm{ref}}\to\dot{\gamma}} = -1.4681\log(\dot{\gamma}) + 1.0746$ with a coefficient of determination of 0.9964.

For the identification of $c_{\dot{\gamma}_{ref} \to \dot{\gamma}}$, the lowest shear rate has not been considered since a plateau at low shear rates appears.
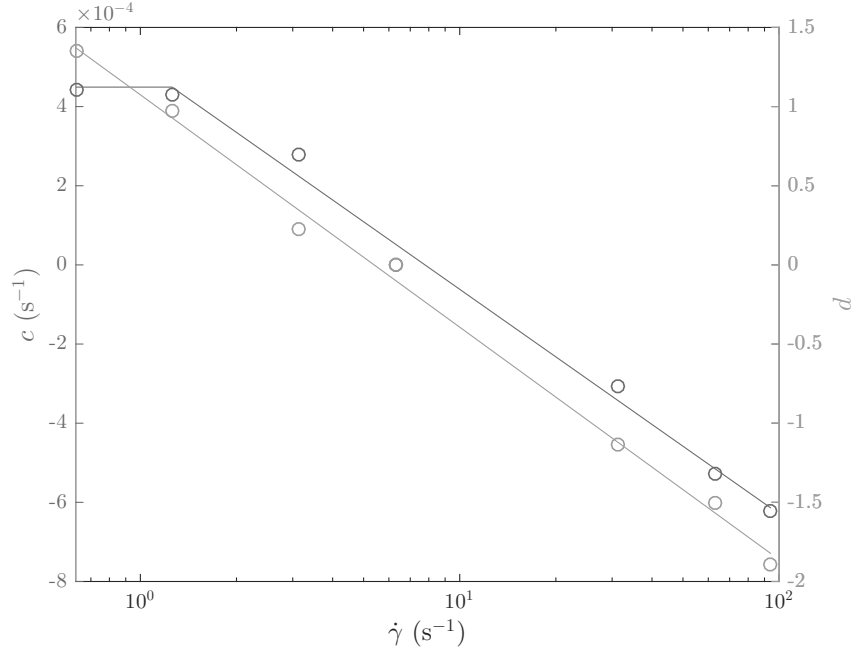


Figure 3.9 – Behavior for parameters $c$ (in blue) and $d$ (in green) where the circles represent the optimization solution for each shear rate and the solid lines describe the identified linear functions.

From the identification process presented above, it follows the final differential equation that models the evolution of viscosity according to temperature and shear rate:

$$\dot{\eta} = c_{\dot{\gamma}_{ref} \to \dot{\gamma}} \eta + K_\alpha \exp\left(\frac{-E_\alpha}{R_{gas} T}\right) \exp(c_{\dot{\gamma}_{ref} \to \dot{\gamma}} t + d_{\dot{\gamma}_{ref} \to \dot{\gamma}})^{1-\alpha} \eta^\alpha + K_\beta \exp\left(\frac{E_\beta}{R_{gas} T}\right) \exp(c_{\dot{\gamma}_{ref} \to \dot{\gamma}} t + d_{\dot{\gamma}_{ref} \to \dot{\gamma}})^{1-\beta} \eta^\beta \quad (3.39)$$

where the values of the parameters are summarized in Table 3.5.

| Parameters | Expression | SI Units |
|:---:|:---:|:---:|
| $K_\alpha$ | $1.2947.10^{16}$ | $Pa^{1-\alpha}s^{-\alpha}$ |
| $K_\beta$ | $1.5470.10^{-32}$ | $Pa^{1-\beta}s^{-\beta}$ |
| $E_\alpha$ | $95722$ | $J.mol^{-1}$ |
| $E_\beta$ | $110840$ | $J.mol^{-1}$ |
| $\alpha$ | $0.44$ | - |
| $\beta$ | $3.65$ | - |
| $c_{\dot{\gamma}_{ref} \to \dot{\gamma}}$ | $-0.5209.10^{-3} \log(\dot{\gamma}) + 0.4372.10^{-3}$ | $s^{-1}$ |
| $d_{\dot{\gamma}_{ref} \to \dot{\gamma}}$ | $-1.4681 \log(\dot{\gamma}) + 1.0746$ | - |

Table 3.5 – Coefficients of the second identified model.

### 3.2.4 Validation

To validate this second model, the evolution of bone cement viscosity estimated by the identified differential equation has been compared to the data acquired on the rotational rheometer. Therefore, at a given shear rate and temperature, the nonlinear Ordinary Differential Equation (ODE) in (3.39) has been solved based on an explicit fourth order Runge-Kutta method with a variable time step. The initial condition of this ODE equation has been taken identical to the first viscosity value of each experimental curve.

The first validation results are those for which shear rate evolved from one experiment to another at a fixed temperature $T_0 = 20\,°C$ (Figure 3.10), and conversely, at an imposed shear rate $\dot{\gamma} = 2\pi\,\mathrm{s}^{-1}$ for a range of temperatures from 10 to 25 °C (Figure 3.11). In both figures, dashed curves are the data acquired during the rheology experiments while solid lines represent the results obtained with the model, by ODE resolutions. Simulated viscosity curves do conveniently fit the experimental data sets. Note that in Figure 3.11, a difference between ODE results and experiments only appears above approximately 5000 Pa·s which is the maximum value considered during the identification process.
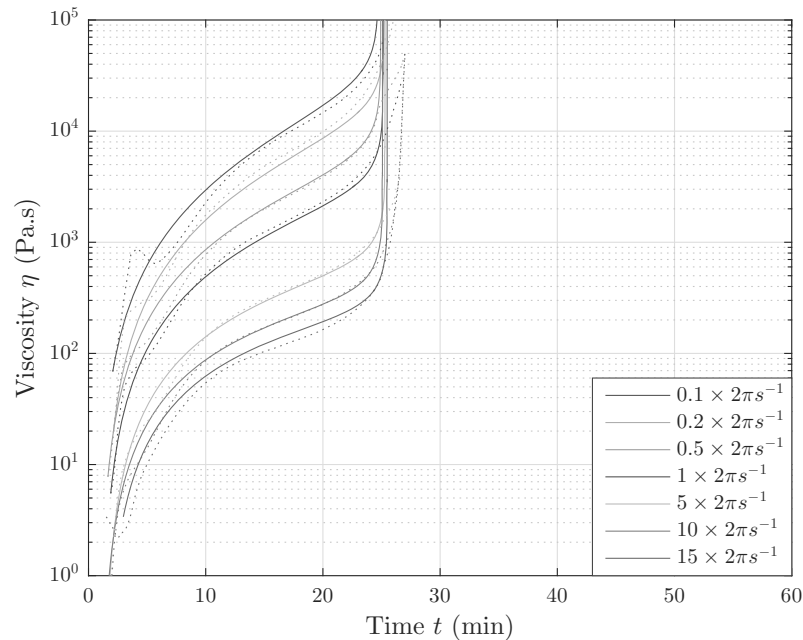


Figure 3.10 – Results obtained with the models, by solving the ODE (solid lines) in comparison with the acquired viscosity data (dashed curves) also presented in Figure 2.12(a).

Based on data different from the ones used for the estimation step, another validation is made. Indeed, new experimental curves have been acquired on the dynamic rheometer. While the experimental protocol detailed in section 2.3.2.1 has carefully been followed with $\dot{\gamma} = 2\pi\,\mathrm{s}^{-1}$ and $T_0 = 25\,°C$, the bone cement sample has been cooled at a given time $t_c$ to reach the temperature $T_0 = 15\,°C$. Then, in Figure 3.12, in order to propose a second validation method, each new acquired curve has been compared to the solution of equation (3.39) for which the shear rate and temperature are identical to the ones used during the experiments.
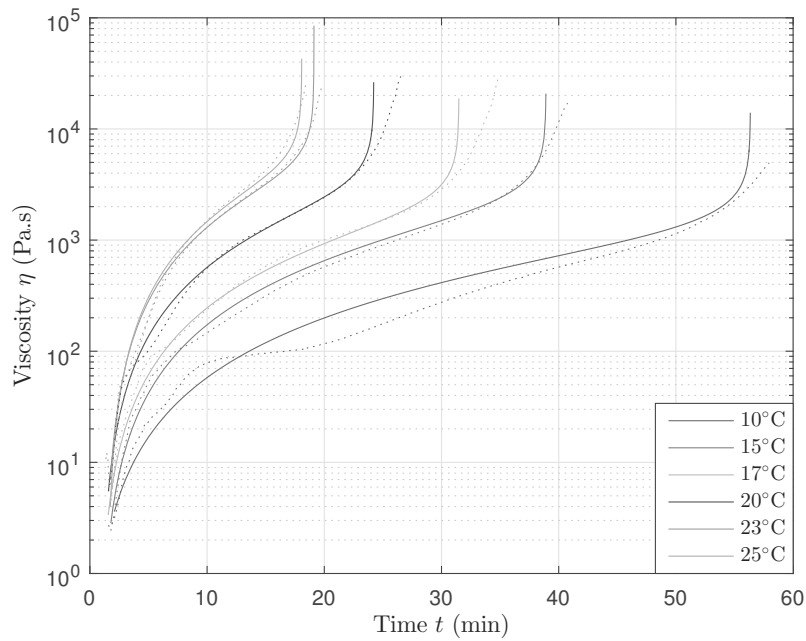
Figure 3.11 – Results obtained with the models, by solving the ODE (solid lines) in comparison with the acquired viscosity data (dashed curves) also presented in Figure 2.11.
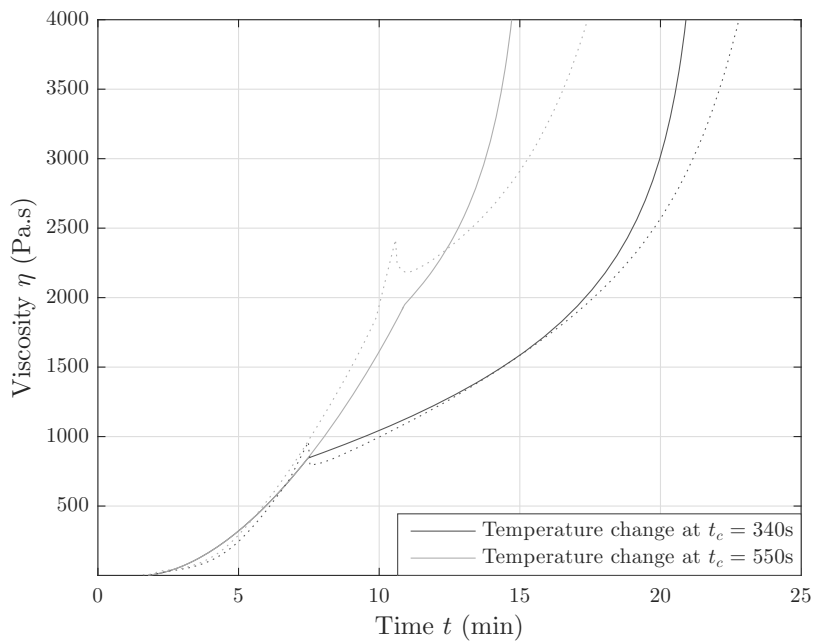


Figure 3.12 – Cross-validation: simulated viscosity versus measured viscosity.

As a conclusion, a shear-thinning model that is thermo-dependent and explicitly dependent in time has first been determined. Then, using a common graphical representation in control, another rheological model has been identified. Since both identifications provide satisfactory outcomes, the first law will be exploited to compute the online viscosity whereas the second model will be handled for future control purposes.

# 4 S-Tronic robot for teleoperated bone cement injection

## Contents

The aim of the S-Tronic project is to help the radiologist to meet the two most important requirements of the vertebroplasty procedure: filling the vertebral body conveniently and preventing cement leakages. To that purpose, a robotic device has been developed, allowing the remote supervision of the cement injection, even at high pressures. In order to assist the practitioner in limiting bone cement leakages, a fine-tuned viscosity control is a key benefit. As a result of the rheological study presented in Chapter 2, a temperature control is an appropriate choice to perform this viscosity control. Then, besides the visual control of the cement delivery via real time fluoroscopic images, the curing state of the cement can be rendered by force feedback on a remote console.

The system proposed in this Chapter combines these features. It includes an injection device that controls the cement flow, a thermal regulation module that controls the fluid temperature, and a master interface that provides the remote force feedback to the operator. Each of these subsystems will be detailed independently in the following sections.

The presented mechatronic systems have been developed in the framework of the S-Tronic project. Mechanical systems have been designed in collaboration with François Schmitt while the software engineering has been completed by Laurent Barbé. Within this chapter, my contributions lie on the dimensioning of the different systems, especially on the thermal regulation module.

# 4.1 Robotic injection device

## 4.1.1 Design and instrumentation

### 4.1.1.1 Dimensioning

Although practitioners understand the concept of viscosity thanks to sensations they experience during injections, they are not able to quantify neither the maximum viscosity threshold at which the injection should be ended nor the minimum viscosity to be reached to avoid leakages. However, viscosity is the parameter that most influences the pressure on the piston of the injection device. This maximum viscosity value is thus a key for the dimensioning of our device.

**Maximum viscosity $\eta_{max}$**   An experiment has been carried out on the rotational rheometer in order to determine this threshold. The experimental protocol described in section 2.3.2.1 has again been followed with Osteopal V$^\circledR$ cement from Heraeus. However, if temperature has not been controlled in order to be consistent with the current practice of vertebroplasty procedures, the shear rate for this experiment must be determined. Bone cement has been proven to be shear-thinning, which means that the lower the shear rate is, the higher the viscosity is. This behavior is valid above a certain shear rate and, at low shear rates, bone cement viscosity shows a Newtonian plateau.For the dimensioning of our injection device, the worst case scenario must be considered. Therefore, the rheological experiment has been performed at $\dot{\gamma} = 0.2 \times 2\pi \text{ s}^{-1}$ since, below this value, almost no viscosity variation can be observed. At this shear rate, it allows to consider a Newtonian plateau. The resulting viscosity evolution is plotted in Figure 4.1.

According to Figure 1.11, the working phase of the tested bone cement does not last more than 9 minutes. From Figure 4.1, the corresponding maximum viscosity equals 1708 Pa·s, which is rounded to $\eta_{max} = 2000$ Pa·s with a safety margin of 15%.
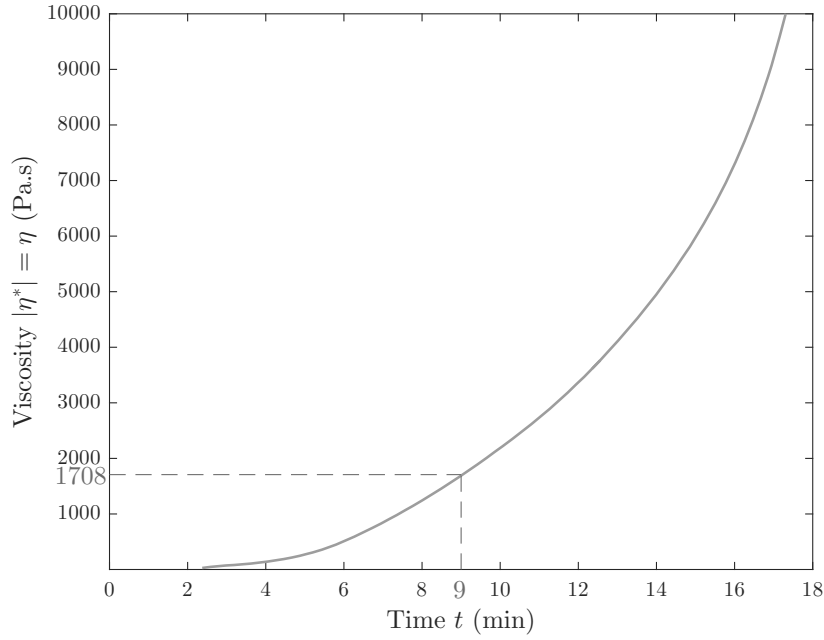
Figure 4.1 – Viscosity obtained with a rotational rheometer, without any temperature control, at $\dot{\gamma} = 0.2 \times 2\pi$ s$^{-1}$.

**Maximum force $F_{\max}$** The bone cement flow in the injection device can be assumed to be a Poiseuille flow, for a constant viscosity $\eta$. As developed in Appendix A, the relationship between the flow rate $Q$ and the pressure drop $\Delta P$ along the pipe of length $L_c$ and of radius $R_c$ is then given by:

$$Q = \frac{\pi R_c^4 \Delta P}{8 \eta L_c} \tag{4.1}$$

Based on recommendations from practitioners, the maximum length of the cannula $(L_c)_{\max}$ can be chosen to be 20 cm. The choice of radius $R_c$ is discussed later, in section 4.1.2.3. From results of measurements in the Interventional Radiology department at Strasbourg University Hospital, the mean flow rate during normal vertebroplasty procedures is $\overline{Q} = 35$ mm$^3 \cdot$s$^{-1}$. Under these conditions, equation (4.1) gives the maximum pressure drop:

$$\Delta P_{\max} = \frac{8 \overline{Q} (L_c)_{\max} \eta_{\max}}{\pi R_c^4} \tag{4.2}$$

which results in $\Delta P_{\max} = 138$ bar. In the current set up, a 10 mL plastic syringe from Ardes (see subsection 4.1.2.1), with an inside diameter of 14.2 mm, is used. This implementation leads to a maximum force of about $F_{\max} = 2200$ N.

#### 4.1.1.2 Description of the injection device

As illustrated in Figure 4.2, the injection device is based on a ball screw linear axis, which transforms the rotation of a high-torque motor into a linear translation, in order to push the piston of the cement-filled syringe with pressures up to 140 bar. The linear axis combines a linear guide and a ball screw from Misumi, with a pitch of 5 mm, a dynamic load of 1830 N and a static load of 2390 N. Notice that the dynamic load value falls below the targeted force $F_{\max}$. However, since injections are very slow, it can be considered that the axis works under
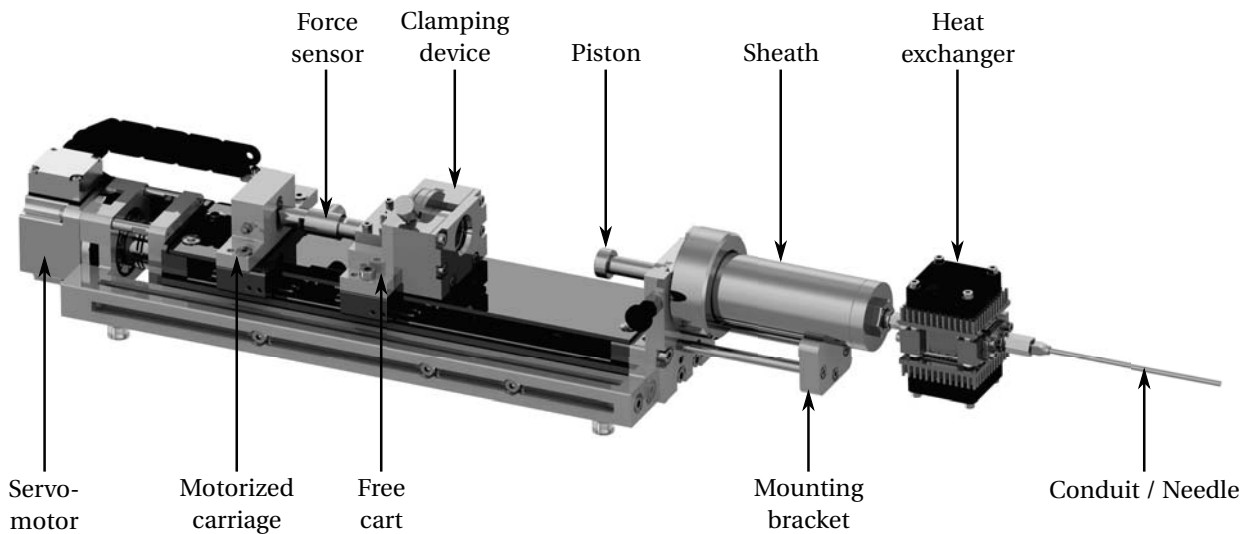
Figure 4.2 – CAD view of the injection device.

static load. The screw itself is motorized by a servo-motor from Harmonic Drive with a 50:1 reduction ratio, providing a nominal torque of about 1.5 N·m. The central track of the device is equipped with two carriages: one is directly mounted on the nut while the second one can move freely along the guide. A manual clamping device with a limit switch has been placed on the free cart to grip the syringe piston. The motorized carriage has been coupled to the free one through a 2 kN uniaxial tension-compression force sensor from Scaime in order to measure the injection force applied to the piston. An additional linear position sensor from Micro-E Systems has also been placed on the free cart in order to provide a direct measurement of the cart position without being affected by a potential backlash of the kinematic chain. Theoretical resolution is below 1 µm for the translation using the motor encoder, and below 0.1 N for the force measurement. Within the context of our application, these resolutions are more than sufficient, and, in section 5.2.1, we will demonstrate that this instrumentation is appropriate to compute bone cement viscosity during the injection.

At the end of the guide, a mounting bracket allows to easily plug and remove the sheath holding the syringe filled beforehand with bone cement. At pressures beyond 100 bar, syringes currently used during vertebroplasty procedures do not always resist and it may happen that these syringes break if bone cement becomes too hard. A specific sheath in which the syringe is embedded limits this problem. This sheath has been machined out of 316L stainless steel in order to provide a high resistance both to pressure and to various chemical products, including biologic fluids and asepsis solutions. It offers a fixation on its back that can interface with the mounting bracket. Thanks to a screw and nut assembly, the disposable syringe can easily be introduced and removed.

Finally, at the outlet of the syringe, a heat exchanger, detailed in section 4.2.3, and a conduit are connected one after another. For more realistic experiments, this straight duct could be replaced by an elbow pipe coupled with a cannula that is, beforehand, inserted inside the vertebra. Even if this geometry has never been tested in practice, simulations proved it would not change anything in future computations.

With the additional cover that has been designed to protect the internal elements (not represented in Figure 4.2), the overall dimension of the system reaches 54 cm×12 cm×10 cm for a mass of approximately 10 kg.

## 4.1.2 Disposable items

Despite the ambition of maximizing the number of items that can be reused for several interventions, some parts can only be disposable.

### 4.1.2.1 Syringe

The syringe is the reservoir that contains the bone cement to be injected. Selected syringes must contain at least 10 mL of cement without exceeding 15 mL to remain consistent with most commercial bone cement kits. A Luer Lock connector is required in order to ensure that the force induced by the cement flowing through the cross-section reduction does not take the conduit apart from the syringe. The outlet is preferred to be centered so that the flow stays axisymmetric. The chosen syringe (see Figure 4.3) is a veterinary syringe that meets the previous requirements. This syringe is well suited to our application as it can be entirely disassembled. Besides, it



Figure 4.3 – Veterinary syringe from Ardes [ARDES 2014].

has been verified that it withstands high pressures, up to 150 bar, thanks to its 1.9 mm thick Premium® polymer walls. Moreover, this type of syringe is also resistant to high temperatures since its sterilization is performed by autoclaving at temperatures between 121 °C and 134 °C [ARDES 2014].

Other syringes have also been considered for their cost effectiveness. However, medical syringes manufactured in polypropylene have been ruled out since they did not resist to the heat produced during the polymerization reaction. Even if much more robust to heat, glass syringes have also been excluded because of their low resistance to forces exceeding 1500 N.

### 4.1.2.2 Piston head

The selected syringes are sold with a piston attached to a brass rod, which does not withstand the required maximum force. From our point of view, the piston rod is not required to be a consumable. Therefore, only disposable piston heads have been produced thanks to rapid prototyping. Their geometry ensures a perfect fitting to the inner wall of the syringe while limiting friction forces. Several tests with varying geometrical parameters such as the piston height, the number and distance of seals have been carried out in order to determine the suited design. Based on measurements of friction forces when pushing the piston inside an empty syringe and the monitoring for any cement leakages, a two-seal geometry has been chosen as highlighted in Figure 4.4. Eventually, apart from the disposable seals, piston heads could be machined out of metal to sustain several interventions in order to avoid their replacement after every single intervention.

### 4.1.2.3 Conduit

Trocars inserted during vertebroplasty procedures have an inner diameter from 10 to 13 G for a length going from 100 mm to 150 mm depending on the pathological vertebra. For needles or catheters, a gauge (G) is a measurement unit corresponding to the number of needles that can be located inside a cylinder of 1 inch in diameter. The higher the gauge is, the thinner the inner part of the needle is. Some conversions from gauge to millimeter are given in Table 4.1.
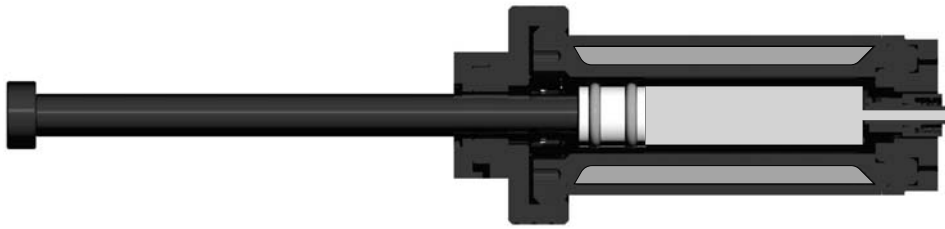
Figure 4.4 – Sheath containing eutectic gel (blue) while holding a syringe filled with bone cement (green) in a longitudinal cross-section view.

| Gauge | Diameter (mm) |
|-------|---------------|
| 1     | 7.35          |
| 5     | 4.62          |
| 10    | 2.59          |
| 13    | 1.83          |
| 15    | 1.45          |
| 20    | 0.81          |
| 30    | 0.29          |

Table 4.1 – Conversions from gauge to the diameter in millimeter.

In the Interventional Radiology department at the University Hospital of Strasbourg, most interventions are performed with a needle of 10 G and 12 cm. For our proof of concept, no vertebroplasty cannulas have been employed. All experiments have been performed with straight non-beveled needles from Unimed, of 11 G and 10 cm. As a first approach, this pipe is sufficient to simulate the bone cement flow to the vertebra. Though the system uses currently this straight conduit, an elbow pipe could be adjusted between the heat exchanger and the cannula that is inserted inside the vertebra.

### 4.1.3   Passive cooling

As specified later in section 4.2, an active temperature system is implemented at the immediate outlet of the syringe in order to control bone cement viscosity. However, since the polymerization reaction that undergoes cement is irreversible, the cement inside the reservoir of the syringe must never reach a viscosity higher than the viscosity set point. Therefore, a passive cooling has been carried out by filling cavities inside the sheath with eutectic gel as illustrated in Figure 4.4. Maintaining the curing bone cement cold in this way allows to increase its setting time. In [Chavali 2003], the authors propose to leave small syringes full of bone cement within ice cubes until they are needed by the practitioner.

The first investigated refrigerant mixture, from Lisotherme, is intended for pharmaceutical logistics or the agri-food sector. It has a melting point of 0 °C and a temperature restitution range from 2 °C to 8 °C. Preliminary tests with the injection device have proven that this temperature range is inappropriate. Indeed, this eutectic gel cools down so much the bone cement inside the syringe that the active temperature control requires to strongly heat the flowing cement all injection long in order to avoid leakages. The second investigated gel (Cryopak Phase 22™) is a material with a phase change point at 22 °C and is appropriate for applications requiring temperatures from 15 °C to 30 °C. Since this working range is quite wide and no indications for use, *e.g.* time and temperature of storage, are specified, a simple experiment has been set up (Figure 4.5) for studying its characteristics. Two syringe holders have been filled with this eutectic fluid. One has been placed in the freezer at −20 °C whereas the second one has been refrigerated at 0 °C, both during 24 hours. Then, a bone cement kit has been prepared
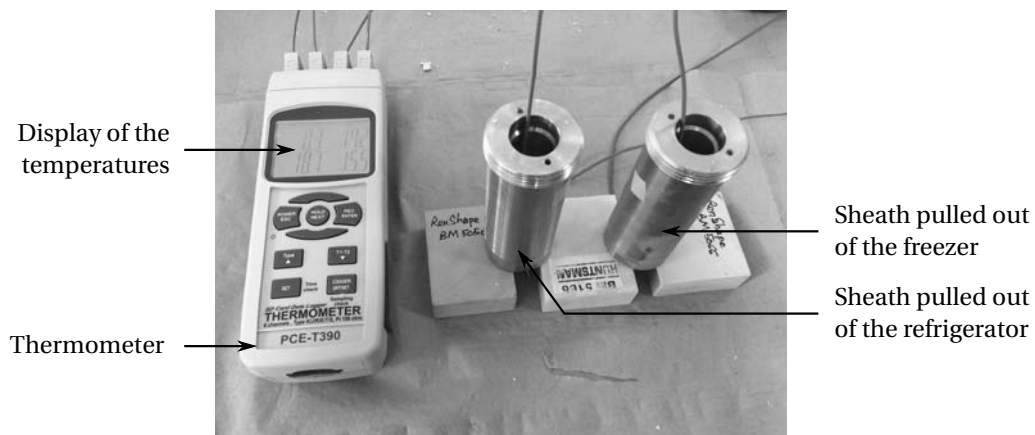
Figure 4.5 – Picture of the experimental set-up to determine the most appropriate usage of the eutectic gel.

and a syringe containing cement has been placed in each sheath. For each set, two thermocouples have been arranged in order to monitor the temperature evolution of both the cement and the inner wall of the sheath. These recordings are plotted in Figure 4.6 where time zero corresponds to the beginning of the mixing process.
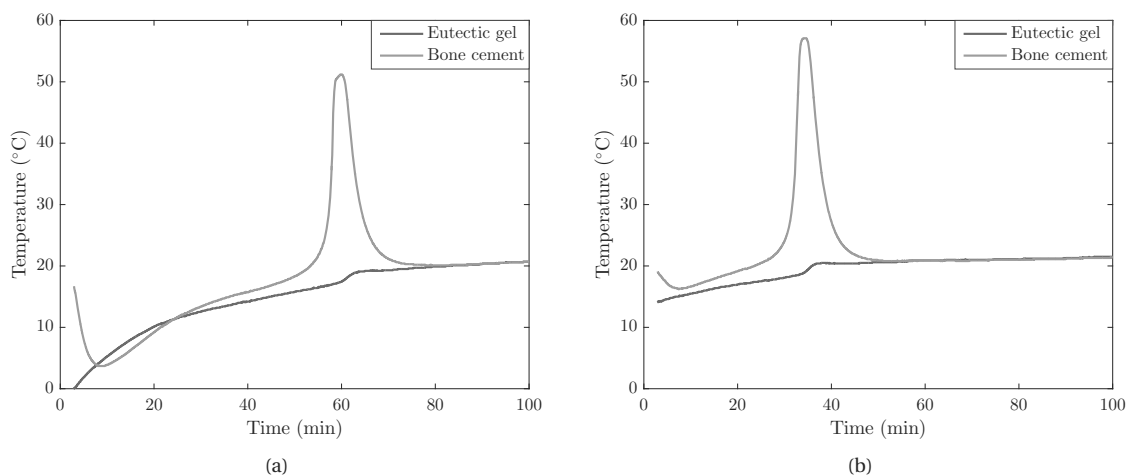


Figure 4.6 – Temperature evolution over time of the bone cement and the eutectic mixture after that the sheath stayed inside: (a) the freezer; (b) the refrigerator.

By leaving the sheath inside the freezer, the cement is very cold (less than 15 °C) for more than 40 minutes. The active regulation would require significant thermal power to control the viscosity of the cold cement. In contrast, with a sheath cooled beforehand in the refrigerator, cement is kept sufficiently cool, *i.e.* at a few degrees below the ambient temperature, to slow down the curing rate. Regarding the cement temperature peak in Figure 4.6(b), this implementation would leave 30 minutes to the practitioner to inject the cement inside the pathological vertebra, which is about three times longer than currently. Thus, in the procedure workflow, the sheath filled with the second eutectic gel is preferred to be left inside the refrigerator until the last moment. This choice is consistent with the current hospital practice. Indeed, by storing the sheath in the fridge with the bone cement kit until the mixture, the medical staff would not need to provide any additional effort.

For a better understanding of the thermal regulation presented hereafter, the following remark is important and should be considered. The polymerization reaction that undergoes the bone cement is irreversible. One could

think that an active temperature control is not possible since bone cement viscosity cannot decrease. However, thanks to this passive cooling, viscosity of the bone cement flowing out the syringe is ensured to be lower than the viscosity set point.

### 4.1.4 Control of the injection device

Numerical and analog I/O modules from Beckhoff interface the sensors and actuators of the system with a master computer via the EtherCAT communication protocol. All the control and instrumentation signals from both the injection and master device are at a sampling frequency of 1000 Hz. For the temperature regulation, a sampling frequency of $F_e = 5$ Hz has been selected, according to the very slow settling times that are in the order of 10 s.

The servo-motor of the injection device is velocity controlled with a simple proportional controller allowing a very stable behavior and satisfactory performance while following a given trajectory, in spite of a small steady state error.

When the practitioner halts the injection, bone cement slightly continues to flow because of its viscoelasticity. To fix this inconvenience, OptiMed proposed the Cemento-MP device with which the physician can disengage the piston and suck some cement. This phenomenon has also been experienced with our injection device and has been identified by halting the injection at different times from the start of the mixing phase. While about 0.3 g (*i.e.* 0.2 mL) of bone cement continues to flow at the very beginning of the injection, it has been noticed that the volume or mass that continues to run out decreases with time until this disagreement ceases. This remark is correlated with the fact that the difference between the viscous modulus $G''$ and the elastic modulus $G'$ decreases until $G'$ becomes greater than $G''$. From the moment when $G' \geq G''$, the bone cement does not flow anymore when the injection is halted. Hence, when the injection is stopped by the radiologist operating the remote console, a re-aspiration of 0.2 mL bone cement has been implemented, which leads to move back the motorized carriage of 1.3 mm at maximum velocity.

## 4.2 Design of a temperature control system

### 4.2.1 Positioning of the temperature exchanger

Ideally, the regulation of the cement temperature should take place the closest to the treated vertebra. Nevertheless, introducing an electric heating element inside the vertebral body is challenging. It is reminded here that the polymerization reaction that undergo acrylic bone cements is irreversible. Whenever the temperature control unit is placed at the end of the cannula, the cement already polymerized upstream in the circuit may form a stopper, making the temperature control useless and the injection impossible. To handle this issue, the thermal control should be performed at the first container of cement that, in our application, is the syringe. However, because of the very small thermal diffusivity of PMMA, its diameter of 14.2 mm imposes a too long thermal settling time at the centerline of the syringe. This statement can be demonstrated by solving the unsteady heat equation for a PMMA cylinder of radius $R_c$ at an initial temperature $T_{\text{init}}$, and with free convection with the environment at temperature $T_\infty$. According to equation (B.6), with a first order approximation, it comes that:

$$\frac{T(0, t) - T_\infty}{T_{\text{init}} - T_\infty} = B_1 \exp\left(\frac{-\omega_1 \alpha t}{R_c^2}\right) \tag{4.3}$$

where $T(0, t)$ represents the temperature at time $t$ on the centerline of the cylinder, and $\alpha$ the thermal diffusivity of the bone cement. $B_1$ and $\omega_1$ are constants defined in Appendix B. Settling time $t_{5\%}$ is defined such that:

$$\frac{T(0, t_{5\%}) - T_\infty}{T_{\text{init}} - T_\infty} = 0.05 \; , \tag{4.4}$$

which in this case leads to:

$$t_{5\%} = \frac{-R_c^2}{\alpha \omega_1} \ln\left(\frac{0.05}{B_1}\right) \; . \tag{4.5}$$

Table 4.2 gives the values of $t_{5\%}$ for a radius $R_c$ either equal to the one of the syringe or of the needle chosen in section 4.1.2.

|  | $R_c$ | $Bi$ | $B_1$ | $\omega_1$ | $t_{5\%}$ |
|---|---|---|---|---|---|
| Trocar | 1.25 mm | 2.23 | 1.34 | 1.60 | 19.5 s |
| Syringe | 7.1 mm | 12.7 | 1.57 | 2.18 | 485 s |

Table 4.2 – Settling time $t_{5\%}$ for two different radii $R_c$.

Previous results have been obtained by considering free convection as boundary condition. To reinforce them, the two-dimensional (2D) axisymmetric heat equation has been solved numerically for a bone cement cylinder of radius $R_c$ and of length $L_e = 45$ mm, initially at $40\,°C$ and with a flow rate $\overline{Q} = 35$ mm$^3 \cdot$s$^{-1}$, order of magnitude for a vertebroplasty procedure. This method has been implemented with MATLAB (see details in Appendix C). Concerning the boundary conditions, the temperature of the circular face representing the inlet of bone cement is set at $T_{\text{in}} = 18\,°C$ while at the outlet, the flow is supposed to be free. Finally, the temperature of the lateral face is set at $T_{\text{imp}} = 10\,°C$, which differs from the previous method. In Figure 4.7, the evolution of the temperature is plotted both for $R_c = 1.25$ mm (needle radius) or $R_c = 7.1$ mm (syringe radius).



(a)



(b)
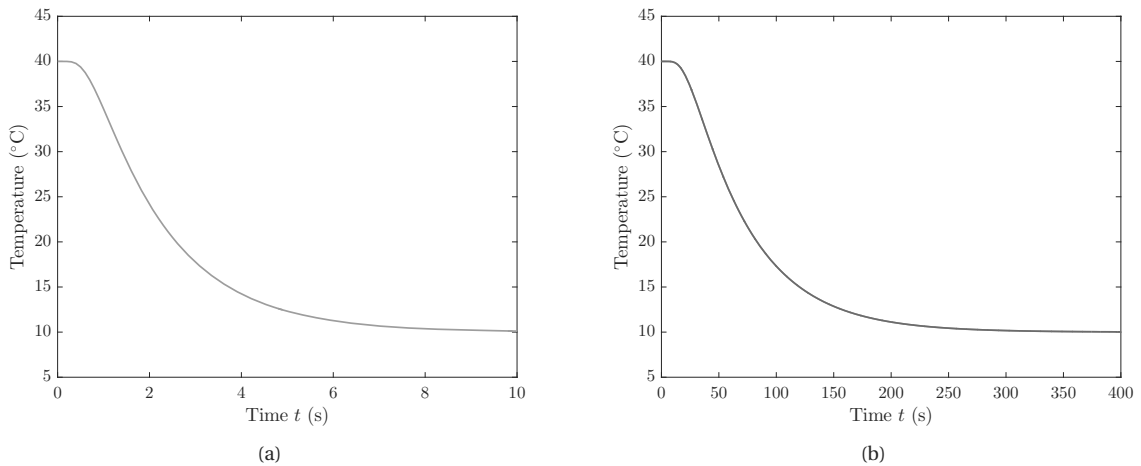
Figure 4.7 – Temperature evolution on the centerline at the outlet of the sample for: (a) $R_c = 1.25$ mm (needle radius); (b) $R_c = 7.1$ mm (syringe radius).

A compromise between issues presented above should be made when choosing the position of the temperature control unit. We have proposed to place the temperature regulation system directly at the output of the syringe because the flow cross section area is around 32 times smaller. As already explained in section 4.1.3, this active

thermal exchange is combined with a passive thermal exchange thanks to the eutectic mixture that slows down the chemical reaction before any active thermal control.

## 4.2.2 Dimensioning of the temperature exchanger

Figure 4.8 displays the previously chosen position of the temperature exchanger. The radius $R_c$ of the pipe on which the temperature control is performed and the length $L_e$ of the thermal exchanger need to be determined in order that the control of the flowing cement affects the center of the fluid stream within an acceptable time. While the optimal solution for $(R_c, L_e)$ would tend towards a zero radius and an infinite length, other issues must be discussed.
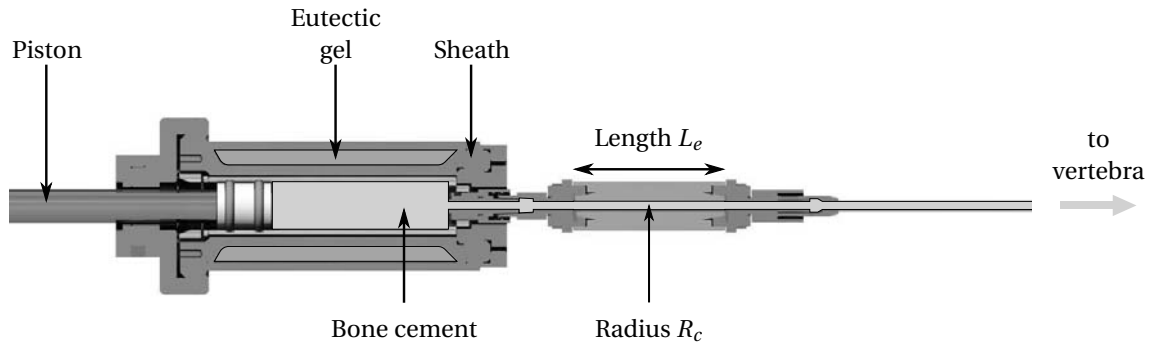


Figure 4.8 – Cutout drawing of the bone cement flow.

### 4.2.2.1 Radius $R_c$

In a cylindrical pipe presenting different cross-section reductions, the major part of the pressure loss happens in the narrower section. This has been confirmed in the project with flow simulations with ANSYS Polyflow software. For instance, Figure 4.9 illustrates the results for bone cement flowing at $\overline{Q}$ from a syringe of radius $R_s = 7.1$ mm through a cannula of length $L_c = 220$ mm and of radius $R_s = 1.25$ mm. The inlet pressure, *i.e.* at $z = 0$, is 5.6 MPa, and the bone cement flows out at atmospheric pressure. In this example, one can compute that, at the cross-section reduction, there is only 3.3 % of the total pressure drop.
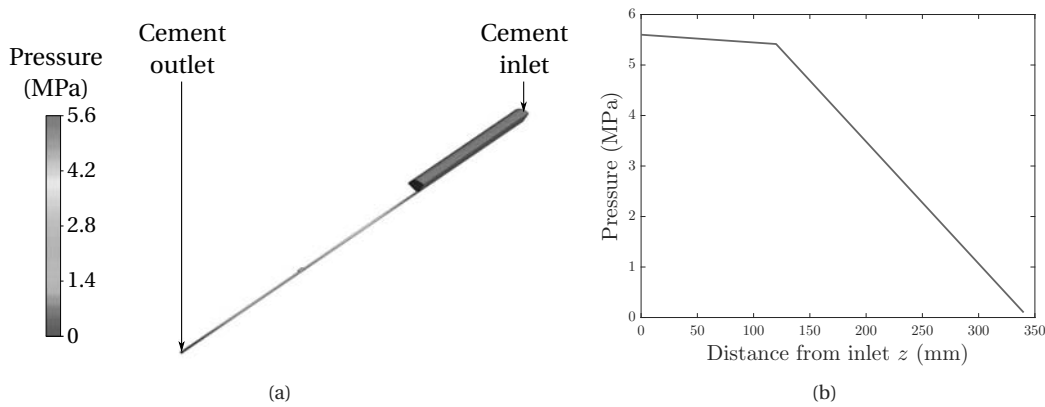


Figure 4.9 – Pressure drop of flowing bone cement: (a) pressure field; (b) pressure evolution on the axis where $z = 0$ is the inlet.

In order to maintain the whole pressure drop in the portion between the syringe and the cannula hammered inside the vertebra, there should ideally not be any cross-section reduction downstream of the syringe exit. Since radiologists work with cannulas ranging from 10 to 13 G, those of 11 G are suitable. The inside radius of the pipe has, hence, been set at $R_c = 1.25$ mm. This section appears very small, resulting in a risk that it becomes clogged prematurely. However, the control of the bone cement viscosity should address this issue.

#### 4.2.2.2 Length $L_e$

By referring to the dimensioning of the injection device, the length $L_e$ over which the bone cement temperature is controlled cannot exceed $(L_c)_{\max} = 20$ cm. Moreover, the transit time $t_{\text{transit}}$ of the cement inside the thermal exchanger has to be longer than the settling time of the thermal exchanger, *i.e.* the time required to impose a temperature at the center of the cement flow. This condition imposes:

$$t_{\text{transit}} \geq t_{5\%} \quad \text{with} \quad t_{\text{transit}} = \frac{\pi R_c^2 L_e}{\overline{Q}}, \tag{4.6}$$

which leads to the minimal length $(L_e)_{\min} = \dfrac{t_{5\%} \overline{Q}}{\pi R_c^2}$.

In order to compute $(L_e)_{\min}$, the heat equation has again been solved numerically (see Appendix C) for a cylinder of length $(L_c)_{\max}$ and radius $R_c$, a cement flow rate $\overline{Q}$ and, initially, at $T_{\text{init}} = 40\,°$C. Boundary conditions are $T_{\text{in}} = 18\,°$C and $T_{\text{imp}} = 10\,°$C in order to consider an extreme case, but realistic. However, instead of monitoring the temperature evolution at the outlet, only a cement particle is considered, that is located on the axis and at the inlet of the cylinder at time zero. From the evolution of this particle in Figure 4.10, the corresponding settling time $t_{5\%}$ and the minimal length can be computed as: $t_{5\%} = 6.5$ s and $(L_e)_{\min} = 4.37$ cm.
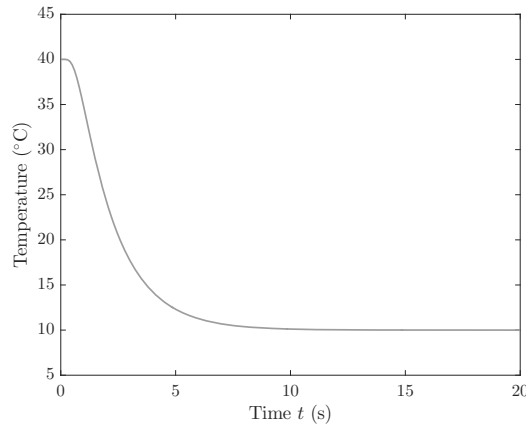


Figure 4.10 – Evolution of the temperature of a cement particle being at the inlet at time zero and moving on the axis of a cylinder.

Finally, the length over which the temperature of the cement is controlled is chosen to be $L_e = 4.5$ cm. This length lies between $(L_e)_{\min}$ and $(L_c)_{\max}$, minimum length to allow the temperature control and maximum length supported by the injection device, respectively. The choice of a value for $L_e$ near $(L_e)_{\min}$ is suitable for a minimal overload and leaves enough space for connectors.

### 4.2.2.3  Peltier modules

In contrast with the Seebeck phenomenon, the Peltier effect found in 1834 occurs when current flows through two different conductors linked at two points. It results in a temperature difference which means that there is a heat absorption at one junction while heat is released at the other point [Peltier 1834]. Exploiting this Peltier effect, thermoelectric modules (TEM), also known as Peltier modules, are solid-state heat exchangers that, under electric current, carry heat through the module from one side to another. The face where heat is absorbed becomes cold while the plate where heat is emitted becomes hot. Since the Peltier phenomenon is reversible, switching the electrical polarity allows to reverse the roles between the hot and the cold plate. Schematized in Figure 4.11, the generic construction of such a module is based on pairs of $n$- and $p$-type of semiconductor columns with a high Seebeck coefficient, that are electrically connected in series and thermally arranged in parallel. The internal connection uses mostly highly conductive materials, both in the electrical and the thermal domains, as copper or silver, whereas the external plates (aluminum ceramics plates) are electro-insulating but thermo-conductive. Modeling and controlling these modules has been an expanding field of research for many years as they are exploited in a wide range of applications. For instance, Choi et al. [Choi 2007] exploited such modules to control the temperature of car seats and Esarte et al. [Esarte 2001] designed a thermoelectric power generator. In any case, a fine modeling is essential for good control performance.
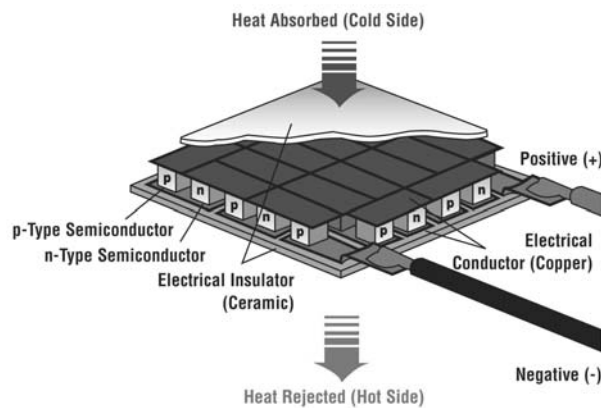


Figure 4.11 – Schematic description of a typical Peltier module, from [Melcor 2006].

Given the complexity of the temperature control for bone cement and also the need of both heating and cooling the fluid, thermoelectric modules prove to be the best compromise. In addition to their small size and light weight, which is imperative to avoid cluttering the interventional field, these modules are heat exchangers that can extract and return a large number of calories with a fast response time in terms of control.

The maximum thermal power $(P_t)_{\max}$ that must be extracted from the bone cement to prevent any exothermic reaction has been evaluated. It has been estimated that the Peltier modules should prevent a temperature increase of about $80\,°\mathrm{C}$. For injections at a flow rate $\overline{Q}$, $(P_t)_{\max}$ can then be computed as $(P_t)_{\max} = 80\rho c\overline{Q}$. Values of $\rho$ and $c$, that respectively represent the density and the specific heat capacity of curing Osteopal $^®$ V cement, have been extracted from [Kolmeder 2010] at a temperature of $20\,°\mathrm{C}$. This gives a thermal power of about $5\,\mathrm{W}$. However, the efficiency of Peltier modules is very poor, from 30% up to 50% depending on the temperature difference between both plates. Therefore, the total electric power should at least reach $20\,\mathrm{W}$. The overview of all the requirements (length $L_e$ and minimal power) has led us to the choice of the TEM QC-63-1.4-8.5M from Quick-Cool with a size of $37\,\mathrm{W}$ for a $40\,\mathrm{mm} \times 20\,\mathrm{mm}$.

### 4.2.3 Technology of the temperature exchanger

The active temperature control system is composed of a central block on which are stacked on both faces a Peltier module and a heat sink followed by a fan, as visible in Figure 4.12.
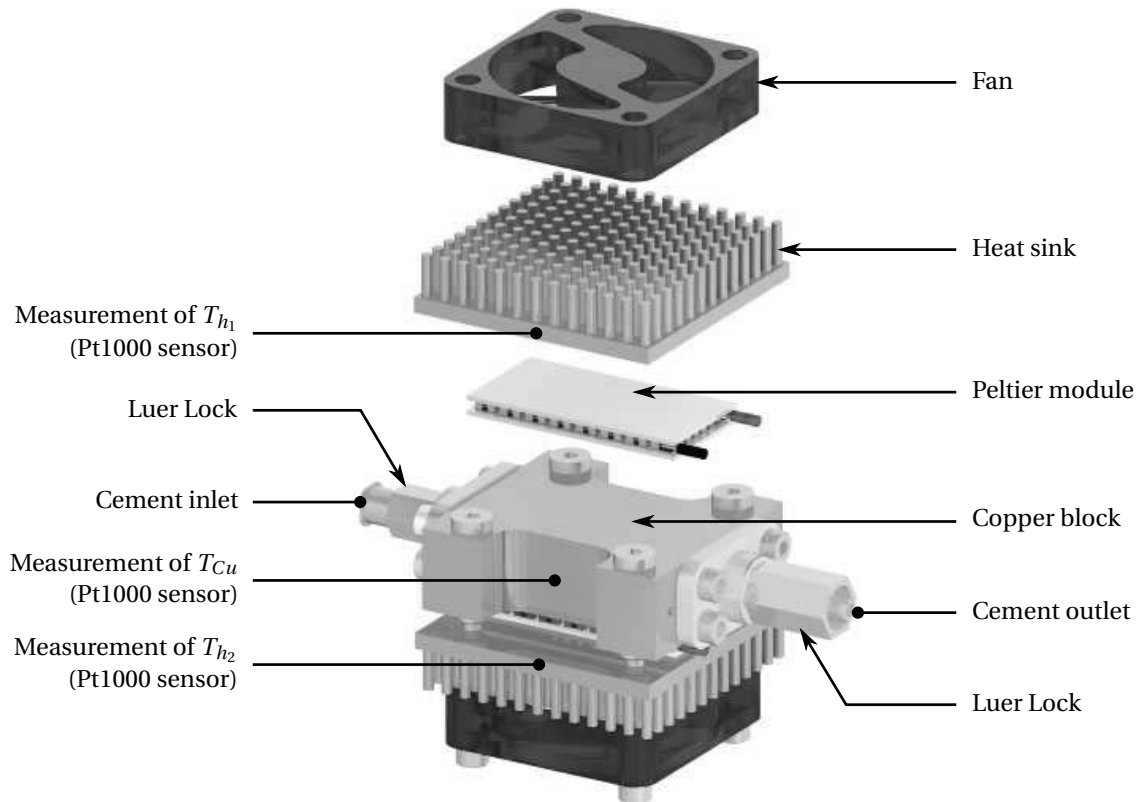


Figure 4.12 – Exploded view of the thermal exchanger block showing the different components and the temperature measurement points.

The central block is made of copper to benefit from its high thermal conductivity and low thermal inertia. This block is crossed by a cylindrical channel through which the bone cement flows. The copper heat sinks and both fans are introduced in order to maximize the thermal efficiency by lowering the temperature difference between the hot and cold side of each TEM. A thermal insulation wrapping the central block has also been added to reduce thermal exchanges with the ambient air. Finally, at each extremity of the channel, a Luer Lock connector makes the interface between the thermal block and the syringe, on one side, and the needle on the other side (see Figure 4.2). The whole thermal block has a size of approximately 45 mm × 45 mm × 60 mm.

Performance of a Peltier module highly depends on the temperature difference between its hot and its cold plate. Fans are essential in order to maintain this temperature difference as low as possible and to ensure their effective functioning. Figure 4.13 illustrates an experiment where a current $I$ has been applied to both Peltier modules but where both fans have been switched off. According to the evolution of $T_{Cu}$, the temperature of the central copper block decreases as soon as the current $I$ becomes non-zero. However, one can notice that, for each TEM, when the temperature difference between the hot and the cold plate reaches 35 °C, their behavior diverge such that both plates start to heat.
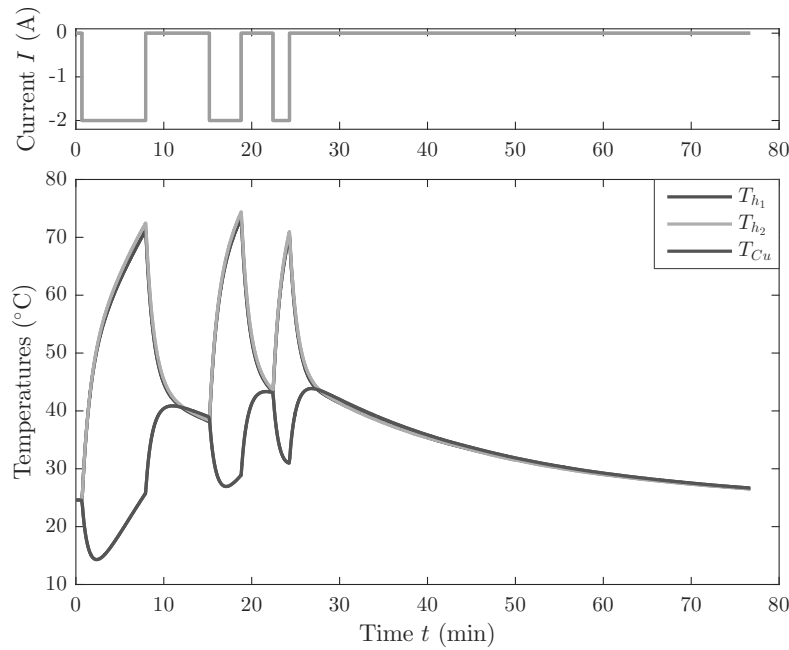
Figure 4.13 – Temperature measures on the thermal exchanger where both TEMs are subject to a current I with both fans turned off.

### 4.2.4   Validation by numerical simulations

Prior to the assembly of the system, FEM simulations with ANSYS Polyflow software have confirmed the choice of these Peltier modules. Especially, the settling time is ensured to be lower than the transit time of the cement in the pipeline. They allow us to estimate the heat transfer capability and, especially, the time delay necessary to equalize the temperature difference between each TEM cold side and the bone cement. Contrary to previous simulations, the exact geometry of the complete thermal exchanger has been considered. Due to its symmetries, simulations have only been carried out on a quarter of the domain (see Figure 4.14(b)). The bone cement rheological behavior has been modeled by the power law with $n = 0.2$ and $K = 7000 \, \text{Pa} \cdot \text{s}^n$. The flowing cement enters with an initial temperature and the cold face of the TEM is set at a constant temperature. For the outer boundaries, the system is subjected to free convective heat exchange with ambient air. By computing the temperature evolution at the outlet of the block, the settling time of the system, the delay to reach the center of the stream and the static gain have been identified. In the example illustrated in Figure 4.14, the cement enters at $18\,^\circ$C and flows at $\overline{Q} = 35 \, \text{mm}^3 \cdot \text{s}^{-1}$. The cold side of the Peltier module is supposed to be at $10\,^\circ$C.

(a)



(b)
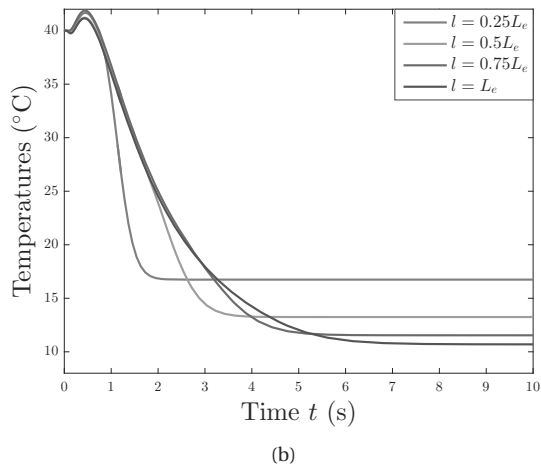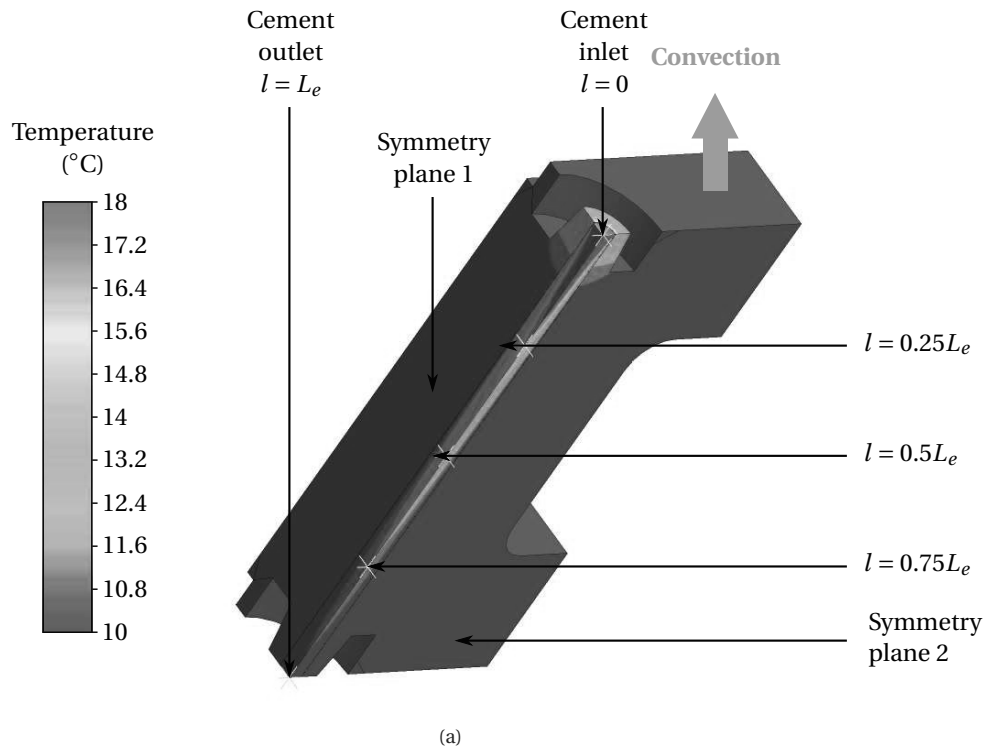
Figure 4.14 – Simulation on the copper block structure with flowing bone cement: (a) temperature field at $t = 10$ s; (b) temperature evolution of the bone cement on the axis at different distances $l$ from the inlet.

As expected, a slight delay is noticeable, which corresponds to the time required to reach the cement in the center of the flow. In these conditions, the simulation confirms the good dimensioning since the settling time is lower than the transit time of the cement in the pipeline.

## 4.3 Teleoperated cement injection

In addition to the collaboration with research engineers, this work has been performed with the participation of Rafael Aleluia Porto, who did his Master thesis in our laboratory.

### 4.3.1 Master device

One of the main objectives of the S-Tronic project is to remove the practitioner from X-ray imaging radiations while still providing enough information about the injection to ensure the safety of the patient. Therefore, a haptic interface has been designed in order to allow the remote control of the injection and to render a force feedback representing the cement hardening to the practitioner.

The interface is built around a cable-driven pulley-capstan transmission (ratio of 10:1), as illustrated in Figure 4.15. It uses a braided stainless steel wire. The capstan is motorized by a brushed DC Maxon motor with a nominal torque of 85.6 N·mm. The end user handle is 43 mm away from the main pulley pin, generating a maximal tangential force of 19.9 N. The workspace of the end-effector ranges from 0 (at rest) to 1 rad.
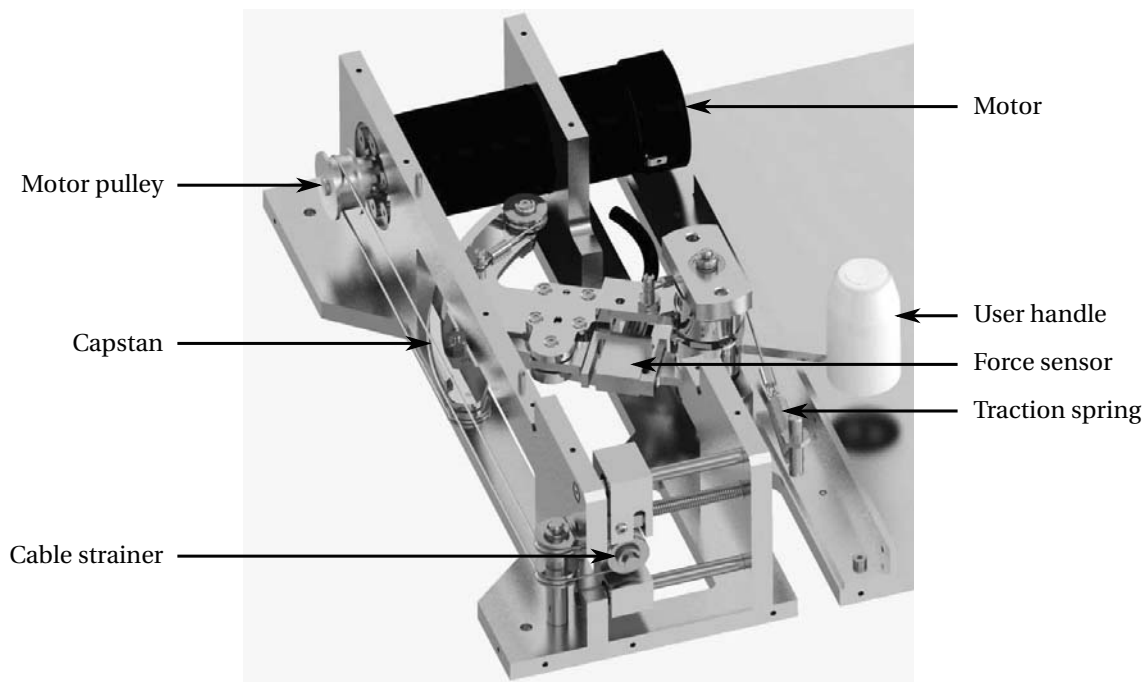


Figure 4.15 – CAD view of the master device mechanism.

The position is measured thanks to the motor encoder, with a theoretical angular resolution lower than 0.01° at the user hand. A 100 N force sensor (Scaime) has been added, providing a measurement ratio of 2.87:1 of the force applied to the user. The resulting resolution of this force measurement is 0.02 N. A return spring can optionally be installed to prevent an accidental release of the handle. The power supply, the motor drive and the force measurement electronics have all been embedded in the interface box, connected to the other control components by an RJ45 socket.

For potential future industrialization, it would be quite interesting to embed this master device prototype into the console of the C-arm, as highlighted in Figure 4.16.

Master     Console of
device     the C-arm
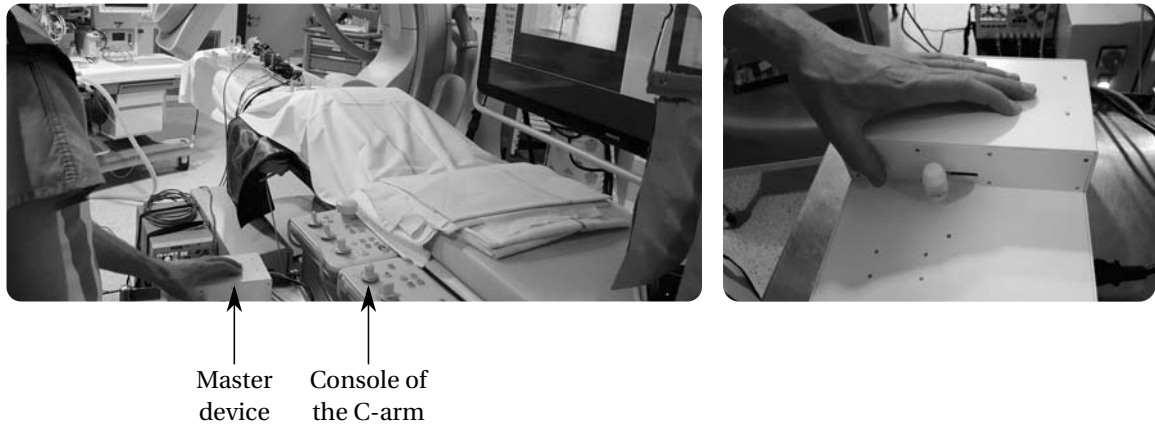
Figure 4.16 – Pictures showing the master device used by a practitioner in an interventional radiology room.

### 4.3.2 Teleoperation background

A master-slave manipulator is always composed of a master interface, a communication network and a slave device as schematized in Figure 4.17. The operator handles the master system while the slave device acts on the environment. Representing such a manipulator using 2-port networks, as proposed in [Raju 1989], relies on the analogy between electrical and mechanical systems. These networks are connected two by two through a velocity signal $V$ (analogy with current) and a force signal $F$ (analogy with voltage). Indexes $h$, $m$, $s$ and $e$ represent the human operator, the master and the slave manipulators and the environment, respectively. $F_h^*$ models the intention of the operator, while $F_e^*$ models external disturbances on the environment, such as those created by physiological motions.
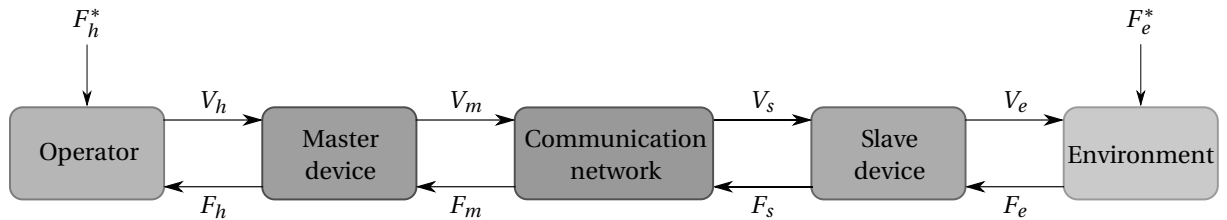


Figure 4.17 – General outline of a master-slave manipulator, adapted from [Bayle 2013].

This linear modeling of the master-slave manipulator by its hybrid representation is written:

$$\begin{bmatrix} F_h(s) \\ -V_e(s) \end{bmatrix} = \underbrace{\begin{bmatrix} h_{11}(s) & h_{12}(s) \\ h_{21}(s) & h_{22}(s) \end{bmatrix}}_{\mathcal{H}(s)} \begin{bmatrix} V_h(s) \\ F_e(s) \end{bmatrix} \tag{4.7}$$

with $\mathcal{H}$ the hybrid matrix.

#### 4.3.2.1 Stability and transparency

The target of bilateral teleoperation control systems is to reach the best compromise between stability and transparency. On one side, it is required to ensure stability independently from both the human and environment behavior, in particular in the medical context where it has an impact on procedures safety.

On the other side, transparency should be optimized in order to allow the best possible immersion of the operator in the remote scene, i.e. the sensation that the user is directly interacting with the environment. It is usually admitted that perfect transparency is obtained when impedance $Z_{th}$ experienced by the operator corresponds to the environment impedance $Z_e$, which is written:

$$Z_{th} = Z_e \tag{4.8}$$

with $Z_{th} = \dfrac{F_h(s)}{V_h(s)}\bigg|_{F_e^* = 0}$ and $Z_e = \dfrac{F_e(s)}{V_e(s)}\bigg|_{F_e^* = 0}$. Thus, it can be shown from equations (4.7) and (4.8) that perfect transparency requires $h_{11} = h_{22} = 0$ and $h_{12}h_{21} = -1$ [Lawrence 1993]. These criteria are applied to design more or less transparent communication channels, according to the modeling compromises that have been made. Based on these choices, stability can be analyzed by applying conservative criterion such as Llewellyn's absolute stability criterion [Bayle 2013].

### 4.3.2.2 Bilateral teleoperation control strategy architectures

Concepts of stability and transparency have been very well stated in different general frameworks. Lawrence generalized first the bilateral teleoperation system as a linear representation, introducing the 4-channel architecture [Lawrence 1993]. In [Hashtrudi-Zaad 1999], the authors proposed the modified 4-channel bilateral teleoperation architecture based on the same structure but with local velocity and force control loops at the master and slave sides. In the 4-channel architecture, signals are exchanged from the master to the slave through four communication channels $C_i$ with $i \in [\![1\,;\,4]\!]$. This generic teleoperation control architecture allows transparency/stability analysis. Deriving the 4-channel architecture provides a framework to analyze simpler structures with only 2 or 3 communication channels. Interestingly, authors of [Hashtrudi-Zaad 2000] show that 3-channel architectures with local force loops can perform perfect transparency, while simplifying practical implementation. Finally, implementations with two channels, in particular the position-position structure and the force-position architectures are simple but still with acceptable performance. As initially proposed in [Hannaford 1989], the position-position system, inspired by the 4-channel architecture, is only based on position measurements of both the slave and the master device.

However, in our application, two important properties have to be emphasized. First, the slave robot is not back drivable, and, therefore, is admittance-type. Second, the interaction force between the slave and the cement is measured. As a result, it is more convenient to select a 2-channel force-position teleoperation architecture. Though it could be interesting to use a local force control loop to increase transparency, the choice has been made to not use force measurement at the master side for control, as it should no longer be used in a future version of the teleoperated cement injection system. Therefore, the master interface force sensor is only used for the characterization of the bilateral teleoperation. Unlike 3- and 4-channel architectures, the perfect conditions for transparency cannot be met for 2-channel architectures and practical considerations have to be considered to reach reasonable performances. While the 4-channel design is based on a highly simplified linear representation, such an architecture can also be used efficiently with some nonlinear environments, as it will be illustrated afterwards.

The implementation of the force-position architecture is represented in Figure 4.18, where $G_m$ and $G_s$ respectively represent the master and slave closed-loop transfer functions.
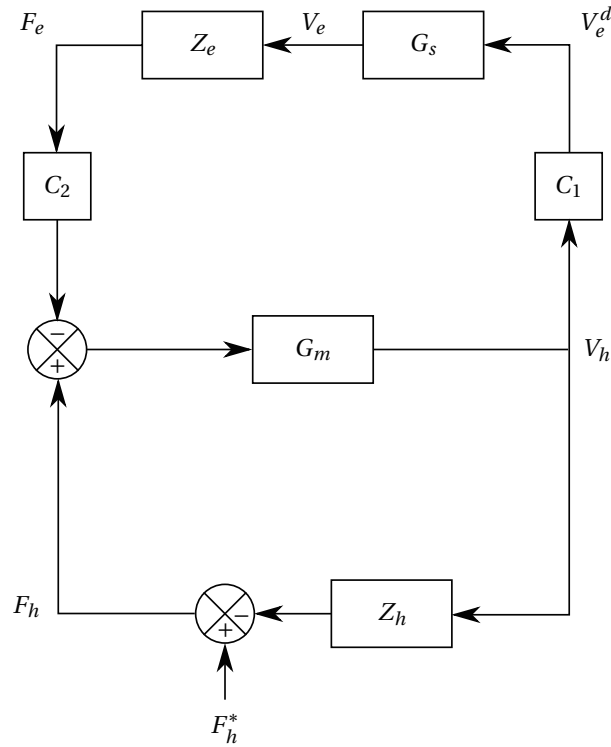
Figure 4.18 – Force-position architecture.

According to Figure 4.18, the following system of equations holds:

$$F_e = C_1 G_s Z_e V_h \tag{4.9a}$$
$$V_h = G_m(F_h - F_e C_2) \tag{4.9b}$$

which leads to the transmitted impedance:

$$Z_{th} = G_m^{-1} + C_1 C_2 G_s Z_e \,. \tag{4.10}$$

As a result, a possible solution to obtain a satisfactory transparency for the system is therefore to make a careful tuning of the slave local loops in order to approach $G_s \approx 1$, and to select:

$$C_2 = C_1^{-1}. \tag{4.11}$$

With this tuning, $Z_{th} = G_m^{-1} + Z_e$, where $G_m^{-1}$, the impedance of the closed-loop control master, has to be minimized to meet the requirement of transparency.

### 4.3.3 Rate control strategy

In the scope of a teleoperated cement injection, the very slow cement flow rate makes the fine control of the injection difficult with the master position. These slow movements would be tiresome for the operator, and, above all, not accurate. Moreover, the master interface has an operation range of 1 radian while the cement injection can last more than 10 minutes.

A different paradigm [Kim 1987], called rate control, is adapted to *slow wide-workspace telemanipulation tasks*, *e.g.* to the remote control of an excavator [Lawrence 1997] or of a mobile platform, as in [Van Quang 2013]. In

very general terms, rate control is a teleoperation mode for which the position of the master interface serves as a velocity reference for the slave system. The architecture used for implementing a teleoperation system under rate control can be derived from the ones employed in the position control, as surveyed in [Mobasser 2008]. Such a control strategy implies a kinematic correspondence between the master position and the slave velocity, that can be written $X_h \equiv V_e^d$. Focusing on the force-position 2-channel architecture (Figure 4.18) that is sufficient in our application, kinematic correspondence is achieved when:

$$C_1 = C_2^{-1} = \frac{\epsilon}{s} \tag{4.12}$$

where $\epsilon$ is a positive scale factor. However, this control cannot be implemented in real time since the derivation operator is non-causal. Appropriately, a filtered derivation transfer function is used such that:

$$C_2 = C_1^{-1} = \frac{\lambda s}{\epsilon(s+\lambda)} \tag{4.13}$$

where $\lambda$ is the cut-off frequency, selected to limit the amplification of the noisy environment force signals. Using this function for the communication channel, the slave velocity reference is expressed as:

$$V_e^d = \epsilon(X_h + \frac{V_h}{\lambda}) \tag{4.14}$$

While this control strategy seems to be the most appropriate in the context of percutaneous vertebroplasty, a critical situation can potentially occur. Indeed, especially when force feedback is insignificant, the practitioner could release the handle, that will stay in a non-zero position. In such a case, the slave device would dangerously continue to inject bone cement without any control from the physician. To address this problem, a return spring (see Figure 4.15) can optionally be installed.

Finally, injection with the master device should also avoid cement leakage, as in section 4.1.4. Therefore, the configuration of the master device, proposed in Figure 4.19, is such that the slave device can inject at a maximum velocity $V_{max}$ by pushing the handle at position $X_{max}$. When the practitioner takes the handle back to $X_0$ ($X_h = 0$ rad and then $V_e^d = 0$), a small amount (0.2 mL) is automatically sucked back.
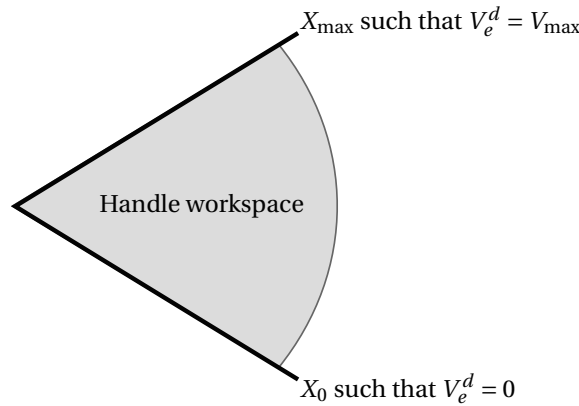


Figure 4.19 – Configuration of the master device.

## 4.4 Experiments

### 4.4.1 Experimental set-up

Coupling the master and slave device using the previous rate control strategy led to experiments aiming at evaluating performances of the teleoperation control that has been implemented. Regarding the adjustment of the gains for the rate control scheme, $\epsilon$ and $\lambda$ have been set at: $\epsilon = 0.91\,\mathrm{mm\cdot s^{-1}}$ and $\lambda = 50\,\mathrm{s^{-1}}$.

Two first experiments have been carried out with the prototype in our laboratory by trying to copy practitioner's gesture. Inspired by many observed vertebroplasty procedures in the Interventional Radiology department at the University Hospital of Strasbourg, each trial starts by preparing a bone cement kit from Heraeus (Osteopal V®). First, hand-mixing is performed until a homogeneous consistency is reached. Once obtained, the cement is poured into the syringe (see Figure 4.20(b)) that is itself inserted into the syringe holder. The latter, to which the thermal exchanger and a needle are plugged with standard Luer-lock connectors, is placed on the slave device. Bone cement is injected inside a L5-phantom vertebra, either hollow or with a cancellous insert.

Another experiment has been completed with an experienced practitioner from the Interventional Radiology department. To practice under realistic conditions, the operator could only watch at the screen showing images from the X-ray imaging device, as in Figure 4.20(c), while pushing the handle of the master system.



|       (a)        |        (b)       |        (c)        |
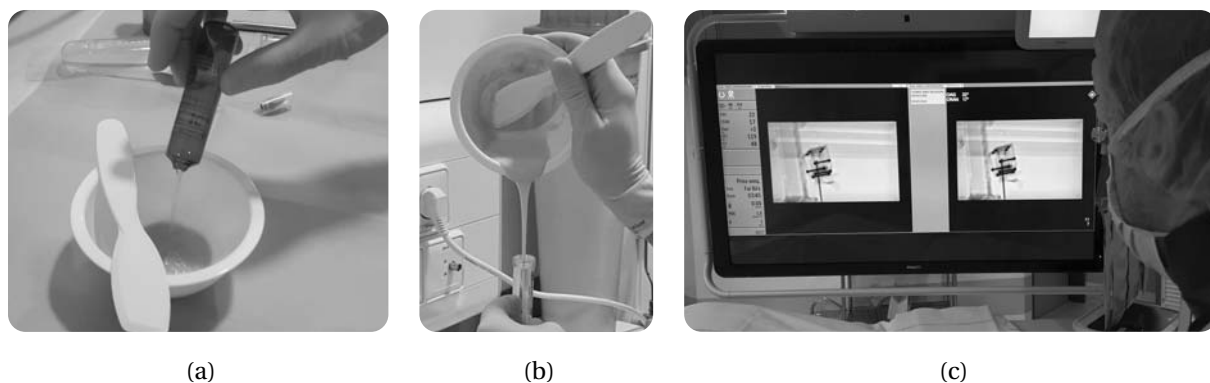
Figure 4.20 – Pictures from an experiment carried out in the Interventional Radiology department at the University Hospital of Strasbourg where: (a) the liquid MMA is poured into the mixing bowl; (b) the homogeneous bone cement is poured into the syringe; (c) the physician observes the control screen while performing the force feedback injection.

### 4.4.2 Experimental results

#### 4.4.2.1 Kinematic correspondence

To illustrate the results, both the position of the master device and the velocity of the slave are superimposed in Figure 4.21 for two experiments conducted in our laboratory and in Figure 4.22 for the first experiment performed at the University Hospital of Strasbourg. Note that $t = 0\,\mathrm{min}$ corresponds to the start of the hand-mixing phase.

One can observe the effects of the quantization on the slave velocity, estimated by differentiating the slave
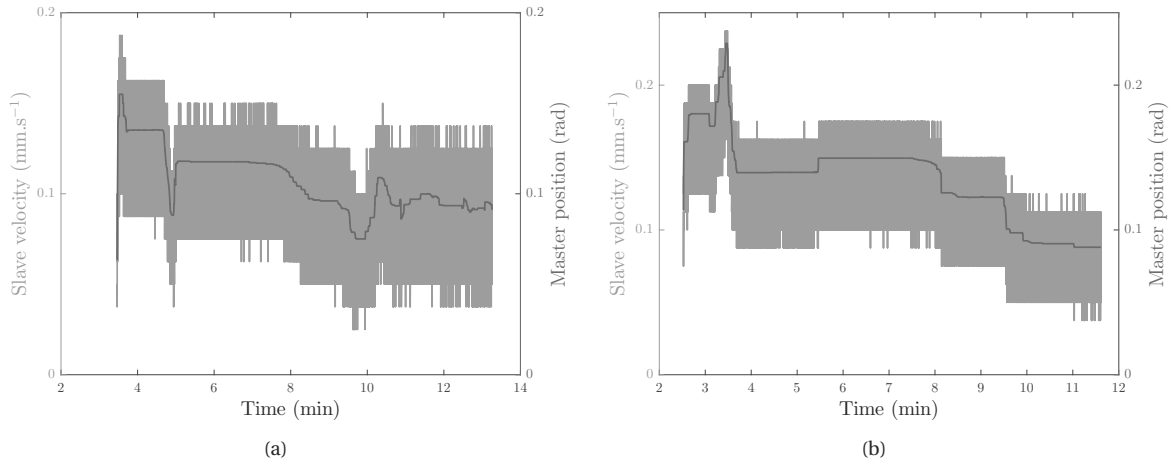
Figure 4.21 – Kinematic correspondence between the master position and the slave velocity (raw data): (a) experiment 1; (b) experiment 2
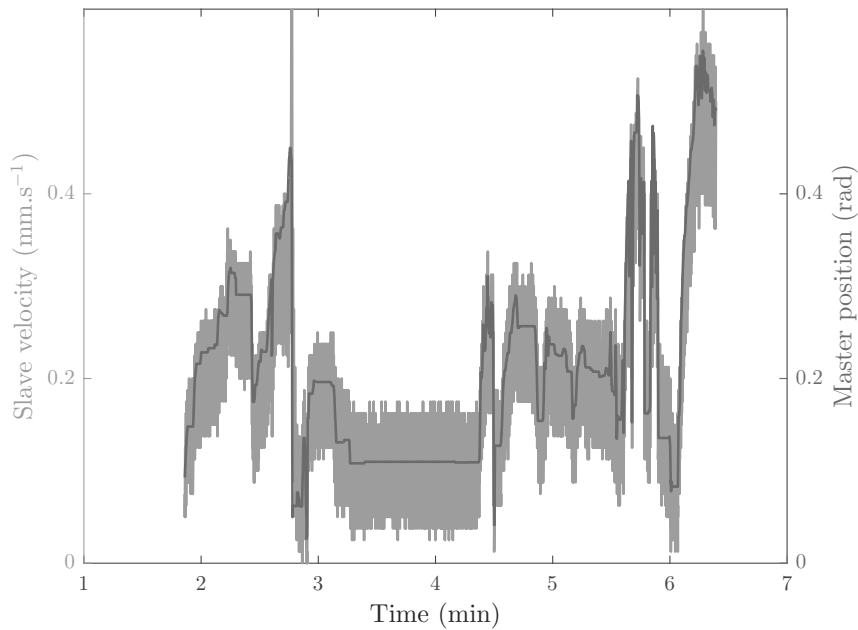


Figure 4.22 – Kinematic correspondence between the master position and the slave velocity (raw data) for the first experiment performed at the hospital.

position measurements. Quantization is significant at such a very low slave velocity. The velocity resolution is $0.012\,\mathrm{mm \cdot s^{-1}}$ while the average velocity is $0.096\,\mathrm{mm \cdot s^{-1}}$ during the experiment of Figure 4.21(a). This has however no effect on the teleoperation performance, since the slave velocity signal is not used in the teleoperation control. Notice that the master velocity, which is used in $C_1$ is also very noisy. However, in our application, the control term proportional to $V_h$ in equation (4.14) is always small (and nearly negligible) since the operator always moves slowly during such an intervention.

#### 4.4.2.2  Transparency and stability

In order to evaluate transparency, the user experienced impedance is compared to the environment impedance, which should be perfectly equal in case of ideal transparency as expressed in equation (4.8). The environment and the user transmitted impedance are simultaneously plotted in Figures 4.23 and 4.24. Data acquired during experiments 1 and 2 will further be exploited for the online viscosity estimation in section 5.2. Among others, the two sharp peaks will be explained.
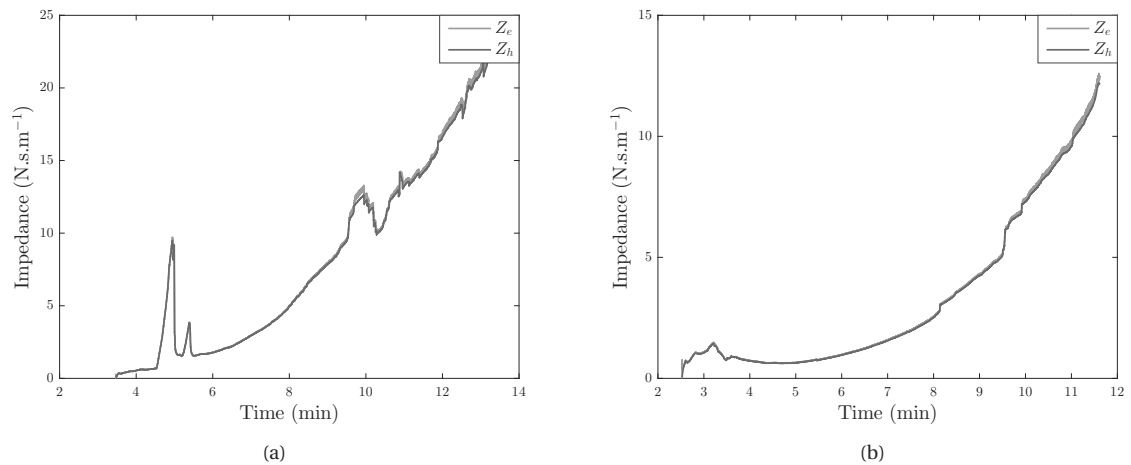


Figure 4.23 – User-transmitted impedance in blue and the environment impedance in green: (a) experiment 1; (b) experiment 2.
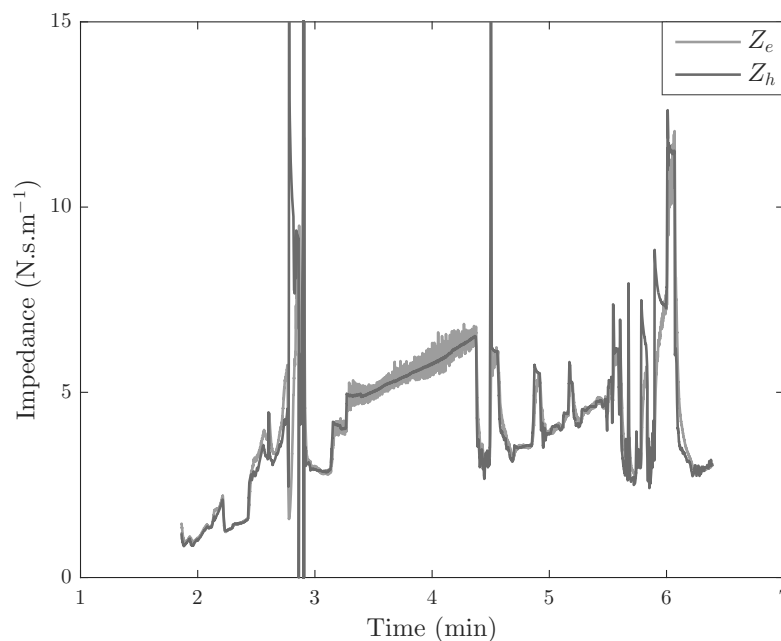


Figure 4.24 – Transparency illustration with the user-transmitted impedance in blue and the environment impedance in green for the first experiment performed at the hospital.

Curves do not represent the raw ratios $Z_{th} = \dfrac{F_h}{V_h}$ and $Z_e = \dfrac{F_e}{V_e}$ since, as explained before, $V_e$ is particularly noisy. As quantization noise is of course not a characteristic of the environment itself, slave velocity measurements have been filtered offline with a low-pass filter prior to the computation of the environment impedance. The correspondence between the environment impedance and the impedance transmitted to the user is very satisfactory, even for high viscosity values. It can also be mentioned that there are no oscillations in the provided data, which shows that the bilateral controller has been properly tuned, using the transparency rules for the communication channels $C_1$ and $C_2$.

In spite of the observation of the practical system stability, it has not been proved theoretically. Tools usually applied in teleoperation are not suitable for an analysis including a realistic model of the environment, that is, in this case, highly nonlinear and strongly dependent on the injection parameters. Stability analysis will deserve further interest in future works, in particular to evaluate the admissible cement viscosity compatible with the teleoperation system stability.

# 5 Online estimation and control of bone cement viscosity

## Contents

To reduce the risk of bone cement leakage outside the vertebral body while extending the setting time, it is proposed in the following to control the cement viscosity all along the injection procedure. The rheological study detailed in Chapter 2 led to the conclusion that the temperature control is the most appropriate way to control the viscosity. In practice, the solution consists in a viscosity closed-loop control with an inner temperature closed-loop control as depicted in Figure 5.1.
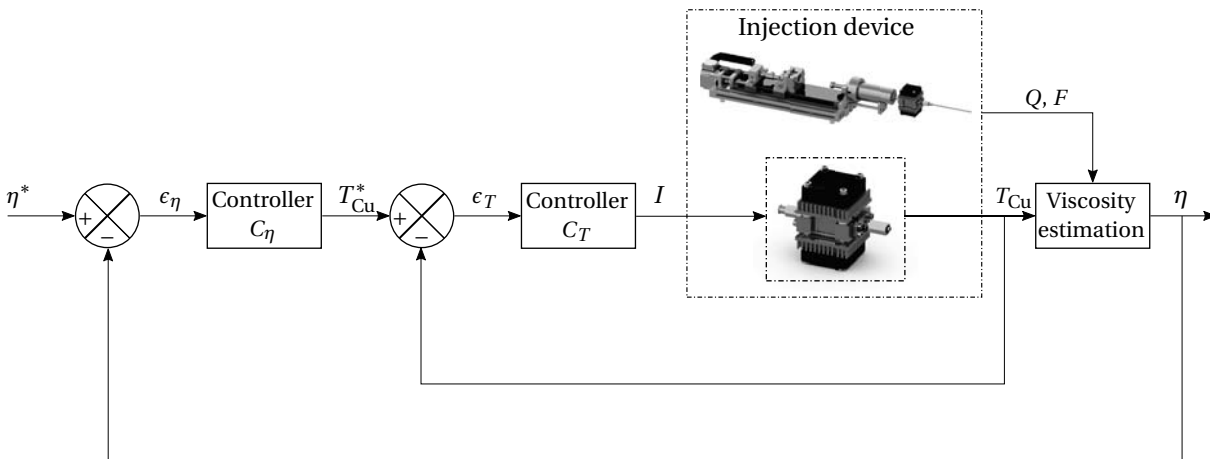


Figure 5.1 – Viscosity closed-loop control

In this chapter, from the modeling and identification of the thermal block, a temperature control strategy will be exposed. Then, the instrumentation of the injection device will be shown to be pertinent for the online viscosity estimation. The viscosity control will finally be proposed.

Variables and parameters denominations employed from now on are all gathered in the nomenclature on page xviii.

## 5.1 Temperature control

Several papers addressed the modeling and control of Peltier modules for temperature control. In [Lineykin 2007], the authors model a TEM and make an analogy between thermal and electrical quantities. Huang et al. [Huang 2000b] linearize the governing equations of an assembly consisting in a Peltier module with a heat sink on its hot side and the object to be cooled on the other side. Based on the linearization of the equations around the operating point, the resulting model is a transfer function with two poles and one zero. The identified gain, zero, and poles vary with the current applied to the module but are averaged for a pseudo-derivative feedback control. In [Shaojing 2010], the same system and its transfer function are taken over. The innovative aspect lies on the design of an adaptive NN-PID controller. Finally, in [Morimitsu 2010], based on a heat disturbance observer, a robust temperature control is proposed to offset parameterization errors, the heat generated by the Joule effect or the external heat flows that disturb the system. The methods proposed in the literature are not directly transferable to our case. Indeed, objects to be cooled have a flat surface so that they can easily be positioned in contact to a Peltier module. In our case, there are more constraints on the system geometry, as it is required to control a flowing fluid in a circular section channel. Still, the proposed models can be adapted to our temperature control objective.

### 5.1.1 Modeling and identification of the thermal block

#### 5.1.1.1 Thermal balance equations of a TEM

The Peltier effect is defined as the cooling or heating effect at the junction of two different semiconducting materials subjected to an electric current. When an electric current flows through the thermocouples of the TEM, a hot and a cold side appear. In an ideal case, the heat power either absorbed at one plate or emitted at the other one would only consider the Peltier effect. However, based on a thermodynamic balance on a single thermoelement [Goldsmid 1986], in addition to the Peltier effect, two other terms in the heat power equation have to be considered in order to model Joule's heating and Fourier's heat diffusion phenomena across each pin. Thus, the heat power $\dot{Q}_c$ absorbed at the cold face and the heat power $\dot{Q}_h$ emitted at the hot side can be expressed as follows:

$$\dot{Q}_c = \epsilon T_c I - \frac{1}{2} R I^2 - G \Delta T \tag{5.1}$$

$$\dot{Q}_h = \epsilon T_h I + \frac{1}{2} R I^2 - G \Delta T \tag{5.2}$$

where $\epsilon$, $R$ and $G$ are respectively the Seebeck coefficient, the total electric resistance and the total thermal conductivity of the TEM. In both equations (5.1) and (5.2), at the right hand side, the consecutive terms represent, respectively, the Peltier's effect, the Joule's effect and the Fourier's heat diffusion. Notice that an insufficient current renders predominant the heat diffusion phenomenon while an excessive current leads to a temperature change imposed by the Joule's effect. The electric power equals the total power that is emitted by the module which yields $P = \dot{Q}_h - \dot{Q}_c = VI$. Hence, the voltage equation writes:

$$V = \epsilon \Delta T + R I. \tag{5.3}$$

Note that $\epsilon$, $R$ and $G$ parameters are specific to each TEM and depend on the current $I$ but also on the temperature difference $\Delta T$ [Huang 2000a]. However, considering the current range that will be employed later on, it is not unfair to consider that the values of these three parameters are constant.

In the literature, several methods have been proposed to estimate the values of these parameters. Among them, Palacios et al. [Palacios 2009] introduce a graphical approach based on equations (5.1) and (5.3) and performance curves provided by the manufacturer. For instance, at a fixed temperature $T_{h_0}$ and for a large set of current values, the heat power absorbed at the cold side $\dot{Q}_c$ and the applied voltage $V$ are plotted as a function of $\Delta T$ as shown in Figure 5.2 for the Peltier modules used by our thermal control system. From equation (5.1) and the non-parallel curves of $\dot{Q}_c$ in Figure 5.2, one can notice that $G$ is not exactly constant with current $I$.

Another approach, presented by Lineykin *et al.* [Lineykin 2007], Luo *et al.* [Luo 2008] and Zhang *et al.* [Zhang 2010], has the advantage to provide analytic solutions. Built on (5.1) and (5.3), their idea is to express $\epsilon$, $R$ and $G$ as functions of $I_{\max}$, $V_{\max}$ and $\Delta T_{\max}$, values given by the manufacturer. In [Luo 2008, Mannella 2014], a similar method has been developed. The only difference lies on the use of $\dot{Q}_{\max}$ instead of $V_{\max}$.
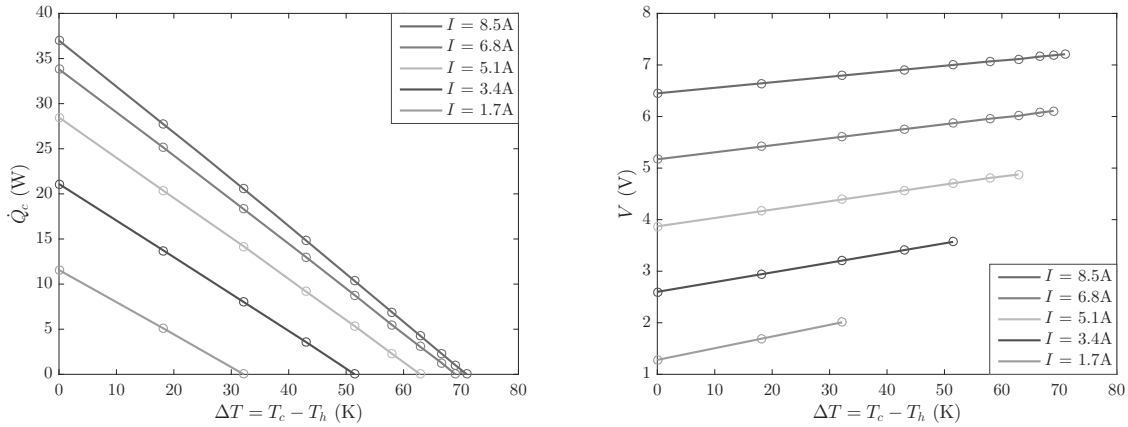
Figure 5.2 – Performances for QC-63-1.4-8.5M (Quick-Cool) at $T_{h_0} = 25\,°\mathrm{C}$.

All these methods have been applied in order to estimate the parameters of the Peltier modules selected for the design of our system. For these TEM, the manufacturer indicates, at $T_h = 25\,°\mathrm{C}$, the following values: $I_{max} = 8.5\,\mathrm{A}$, $V_{max} = 7.6\,\mathrm{V}$, $\Delta T_{max} = 70\,\mathrm{K}$ and $\dot{Q}_{max} = 37\,\mathrm{W}$. The parameters estimation results are presented in Table 5.1. From one method to another, significant differences occur between the estimated values of the

| Parameters | Method in [Palacios 2009] | | Method in [Lineykin 2007] | Method in [Mannella 2014] |
|---|---|---|---|---|
| | $I = 1.7\,\mathrm{A}$ | $I = 8.5\,\mathrm{A}$ | | |
| $\epsilon$ (V.K$^{-1}$) | 0.0226 | 0.0107 | 0.0255 | 0.0236 |
| $R$ ($\Omega$) | 0.7591 | 0.7591 | 0.6842 | 0.6347 |
| $G$ (W.K$^{-1}$) | 0.3208 | 0.3245 | 0.3531 | 0.3276 |

Table 5.1 – Estimated parameters for several methods of the literature.

parameters, specifically up to 15% for $R$. However, to model accurately the control system, and, later on, to design the feedback control, these parameters need to be suitably identified. Therefore, an off-line identification procedure of the temperature control system has been performed.

From here on, parameters and variables indexed by 1 and 2 refer, respectively, to the first and to the second Peltier module of the thermal exchange system, whose design was previously presented in Chapter 4.

### 5.1.1.2 Modeling and identification of the thermal block without bone cement

Aiming to simplify the problem by assuming the two TEMs have an analogous behavior, a first wave of tests have been conducted. We have therefore performed tests for which a profile of current $I$ (sequence of steps of amplitude $I_0$ and of different widths) has been imposed to both TEMs simultaneously so that the central copper block cooled down. Both fans are switched on at their maximal speed. Temperatures $T_{Cu}$, $T_{h_1}$ and $T_{h_2}$ have been collected over time (see Figure 4.12). Because of the configuration of the temperature control device and the influence of the convective exchange with the environment, several orientations of the thermal exchanger have also been alternately investigated. Indeed, the configuration in which both TEMs modules are in a horizontal position (parallel to the floor) could make the behavior of the whole block asymmetric since heat from the lower TEM could rise and disturb the upper TEM functioning. Outcomes of the case where both modules are either in a vertical position (perpendicular to the floor) or in a horizontal position are displayed in Figure 5.3 where $I_0 = -2\mathrm{A}$. Note that dark red, purple and light blue curves represent $T_{Cu}$, $T_{h_1}$ and $T_{h_2}$, respectively.
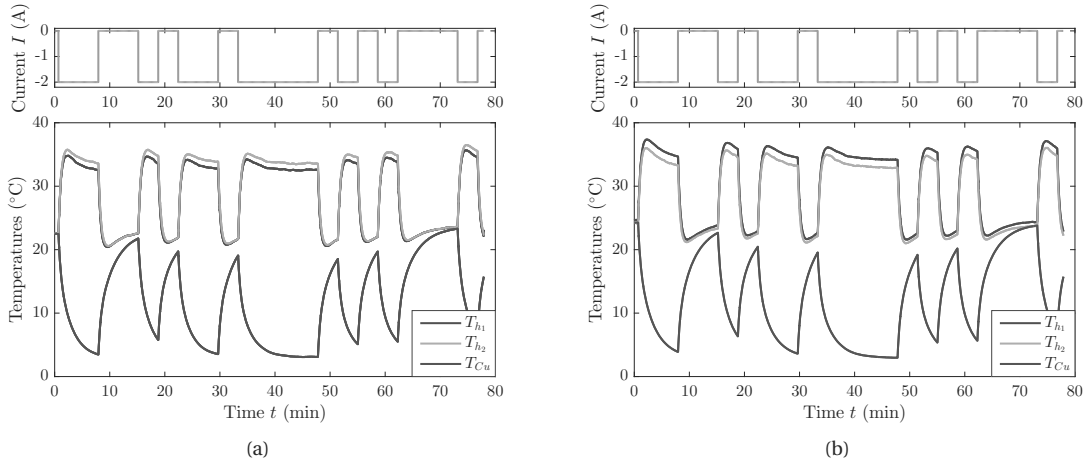
Figure 5.3 – Temperature measurements: (a) in a vertical position; (b) in a horizontal position.

Among the tested configurations, the one in a vertical position (Figure 5.3(a)) seems to be the most suitable, which is consistent with rising heat. However, since a difference is still noticeable between $T_{h_1}$ and $T_{h_2}$, their respective effects need to be separated from each other in the modeling of the whole block.

In the following, the copper block and the plate, made of aluminum oxide, of each Peltier module fixed to the copper are assumed to form a unique set that is uniform in temperature $T_{Cu}$. This hypothesis lies on the high thermal diffusivity of both materials since, for aluminum oxide, $\alpha_{Al_2O_3} = 1.002.10^{-5}$ m$^2 \cdot$s$^{-1}$ and, for the selected copper, $\alpha_{Cu} = 1.078.10^{-4}$ m$^2 \cdot$s$^{-1}$.

The thermal balance of the temperature control system can be expressed by the following three equations (see the nomenclature for the signification of each parameter and variable):

$$(M_{Cu}c_{Cu} + 2M_\kappa c_\kappa)\,\dot{T}_{Cu} = -\dot{Q}_{c_1} - \dot{Q}_{c_2} - h_c A_c (T_{Cu} - T_a) \tag{5.4}$$

$$(M_r c_r + M_\kappa c_\kappa)\,\dot{T}_{h_1} = \dot{Q}_{h_1} - h_{r_1} A_r \left(T_{h_1} - T_a\right) \tag{5.5}$$

$$(M_r c_r + M_\kappa c_\kappa)\,\dot{T}_{h_2} = \dot{Q}_{h_2} - h_{r_2} A_r \left(T_{h_2} - T_a\right). \tag{5.6}$$

Equation (5.4) exhibits the complete thermal balance of the copper block where the two first heat fluxes derive from the heat absorption of each TEM. A 4 mm thick thermal insulating sheet composed of calcium-magnesium silicate surrounds the copper block. However, to consider a potential insulation failure, a small convective exchange has been included through the last term of (5.4). In (5.5) and (5.6), the thermal balance of each heat sink composing a uniform set with the corresponding hot plate is reported with, at the right hand side, the heat emission but also the forced convection (fan). As current $I$ is assumed to be positive to heat the copper block and negative to cool it down, these three last equations become:

$$(M_{Cu}c_{Cu} + 2M_\kappa c_\kappa)\,\dot{T}_{Cu} = (\epsilon_1 + \epsilon_2)\,T_{Cu}I + \frac{1}{2}\,(R_1 + R_2)\,I^2 - G_1\left(T_{Cu} - T_{h_1}\right) - G_2\left(T_{Cu} - T_{h_2}\right) - h_c A_c (T_{Cu} - T_a) \tag{5.7}$$

$$(M_r c_r + M_\kappa c_\kappa)\,\dot{T}_{h_1} = -\epsilon_1\,T_{h_1}\,I + \frac{1}{2}R_1 I^2 - G_1\left(T_{h_1} - T_{Cu}\right) - h_{r_1} A_r \left(T_{h_1} - T_a\right) \tag{5.8}$$

$$(M_r c_r + M_\kappa c_\kappa)\,\dot{T}_{h_2} = -\epsilon_2\,T_{h_2}\,I + \frac{1}{2}R_2 I^2 - G_2\left(T_{h_2} - T_{Cu}\right) - h_{r_2} A_r \left(T_{h_2} - T_a\right) \tag{5.9}$$

From the set of equations (5.7) to (5.9) that models the thermal control block, the following state-space representation can be derived:

$$\dot{X}_1 = A_1(I)X_1 + B_1 U_1 \tag{5.10}$$

$$Y_1 = C_1 X_1 \tag{5.11}$$

where the state vector $X_1 = \begin{bmatrix} T_{Cu} & T_{h_1} & T_{h_2} \end{bmatrix}^T$ and the control vector $U_1 = \begin{bmatrix} I^2 & T_a \end{bmatrix}^T$. The current dependent state matrix $A_1$ is expressed as:

$$A_1 = \begin{bmatrix} M_c^{-1}\left((\epsilon_1 + \epsilon_2)I - (G_1 + G_2) - h_c A_c\right) & M_h^{-1}G_1 & M_h^{-1}G_2 \\ M_c^{-1}G1 & M_h^{-1}\left(-\epsilon_1 I - G_1 - h_{r_1} A_r\right) & 0 \\ M_c^{-1}G_2 & 0 & M_h^{-1}\left(-\epsilon_2 I - G_2 - h_{r_2} A_r\right) \end{bmatrix} \tag{5.12}$$

with $M_c = M_{Cu}c_{Cu} + 2M_\kappa c_\kappa$ and $M_h = M_r c_r + M_\kappa c_\kappa$, while the input matrix $B_1$ and the output matrix $C_1$ are respectively:

$$B_1 = \begin{bmatrix} \dfrac{M_c^{-1}}{2}(R_1 + R_2) & M_c^{-1}h_c A_c \\ \dfrac{M_h^{-1}}{2}R_1 & M_h^{-1}h_{r_1}A_r \\ \dfrac{M_h^{-1}}{2}R_2 & M_h^{-1}h_{r_2}A_r \end{bmatrix} \tag{5.13}$$

and

$$C_1 = \begin{bmatrix} 1 & 0 & 0 \end{bmatrix}. \tag{5.14}$$

The vector of unknown parameters is denoted by $\Theta = [\epsilon_1 \ \epsilon_2 \ R_1 \ R_2 \ G_2 \ G_1 \ h_{r_1} \ h_{r_2} \ h_c]^T$. To achieve their estimation, several Pseudo-Random Binary Sequences (PRBS) have been applied to the thermal block by using the same current value $I_0$ for both Peltier modules and by turning both fans on, at their maximum speed. The range of current $I_0$ that has been experimented is $[-3; 3]$ A with steps of 0.25 A. $T_{Cu}$, $T_{h_1}$ and $T_{h_2}$ have been measured and the Levenberg-Marquardt algorithm applied with a damping factor of 0.1 in order to minimize the following nonlinear multivariable problem:

$$\Theta = \underset{\Theta \in \mathbb{R}^{+9}}{\arg\min} \|\mathbf{H}(\Theta, I, T_{Cu}, T_{h_1}, T_{h_2})\|_2^2 \tag{5.15}$$

where $\mathbf{H} = (H_i)$ with $H_i = \sum_{j=1}^{N_i}(\dot{X}_{1_{i,j}} - A_1 X_{1_{i,j}} - B_1 U_{1_{i,j}})$. The index $i$ represents the $i$-th experiment with an applied current amplitude $I_0(i)$ while $j$ symbolizes the $j$-th temperature measurement point from the $i$-th experiment. Table 5.2 gathers results from the least square regression providing the parameters of the each TEM while $h_c$ is estimated at 52.59 W·m$^{-2}$·K$^{-1}$.

| Estimated parameters | $\epsilon$ (V.K$^{-1}$) | $R$ ($\Omega$) | $G$ (W.K$^{-1}$) | $h_r$ (W.m$^{-2}$.K$^{-1}$) |
|---|---|---|---|---|
| TEM #1 | 0.0213 | 1.348 | 0.228 | 87.83 |
| TEM #2 | 0.0216 | 1.348 | 0.234 | 84.66 |

Table 5.2 – Estimated parameters for each TEM.

### 5.1.1.3  Modeling the flowing bone cement

Since our aim is to control the temperature of the flowing bone cement, the heat transfer between the TEM and the flowing cement has to be considered. Based on the Navier-Stokes equation to compute the velocity profile $\overrightarrow{V}$, the heat equation is given by:

$$\rho c(\frac{\partial T}{\partial t} + \overrightarrow{V} \cdot \overrightarrow{\nabla} T) = \lambda \overrightarrow{\nabla} . \left( \overrightarrow{\nabla} T \right) + \rho \Delta h(T) \frac{\partial q}{\partial t} \tag{5.16}$$

where parameters $\rho$, $c$ and $\lambda$ are those from Osteopal$^{\circledR}$ V (Heraeus), corresponding also to previous simulations and online experiments. $\Delta h$ describes the enthalpy of the polymerization reaction while $q$ is the degree of cure of the reaction. By energy conservation, the four terms involved in this equation represent the temperature evolution, the convective term, the diffusive term and the source term due to the exothermic reaction of the bone cement, respectively. This last term is important since, ex vivo, the temperature of some cements may suddenly rise up above $100\,^{\circ}$C (see example in Figure 2.5). Modeling this heat creation as in equation (5.16) has been proposed by Kolmeder *et al.* [Kolmeder 2011]. However, this sudden peak in temperature is synchronized with a sharp and, at this stage, uncontrollable rise of the cement viscosity. Wishing to carry out the temperature control far beyond the final setting time of the cement, this temperature increase should not be observed in our applications. Hence, the assumption is made that this last term is negligible. Boundary conditions for this equation are the copper temperature $T_{Cu}$ that surrounds the fluid stream and the temperature $T_{\text{in}}$ of the cement that comes out of the syringe and penetrates in the thermal regulation block. At the outlet of the system, the process is supposed in steady state.

Considering the symmetry around the axis of revolution of the pipe, the finite-difference method with a second-order central difference for the space derivative detailed in Appendix C enables to represent the bone cement influence as a state-space representation such that:

$$\dot{X}_2 = A_2(V_P)X_2 + B_2(V_P)U_2 \tag{5.17}$$
$$Y_2 = C_2 X_2. \tag{5.18}$$

$X_2$ is the state vector that includes the temperature at each node of the mesh while $Y_2$ is only the bone cement temperature at the centerline and at the outlet of the thermal block, from here on denoted $T_{BC}$. $T_{\text{in}}$ and $T_{Cu}$ form the input vector $U_2$. The state matrix $A_2$ and the input matrix $B_2$ are both functions of the piston velocity $V_P$.

Bone cement temperature is assumed not to influence the temperature of the copper block because of its limited volume. So, the two proposed state-space representations in series form the complete model of the thermal system, as depicted in Figure 5.4. Remark that the ambient temperature $T_a$ is not a control variable, but accounts for the system operating point. Hence, in the following we will denote $U = I^2$.
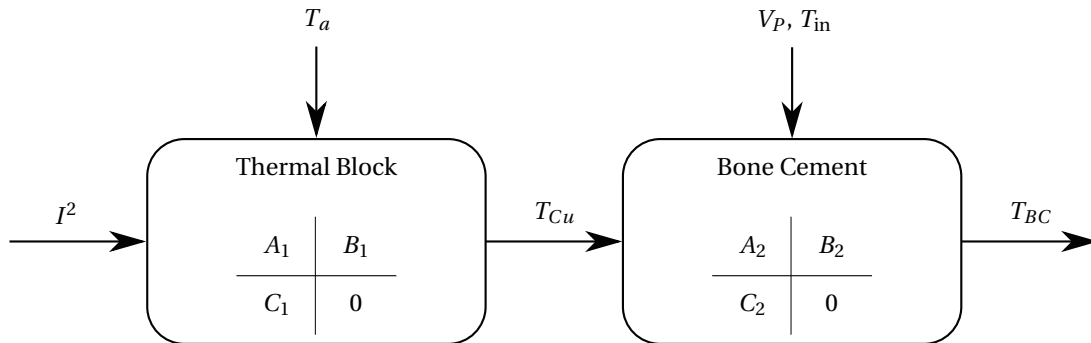


Figure 5.4 – Schematic representation of the thermal system model.

## 5.1.2 Temperature closed-loop control

Based on the previously introduced model, the temperature controller design is presented in the following. The optimal solution would be to directly control the temperature of the bone cement at the system outlet by implementing a feedback control. However, sterility issues during the medical intervention prohibit the use of temperature sensors in contact with the biomaterial. Therefore, since only measurements of $T_{Cu}$ are available through a platinum resistance temperature sensor (Pt1000), the strategy of controlling $T_{Cu}$ has been adopted, which can be represented by the block diagram in Figure 5.5. This scheme represents a classical closed-loop
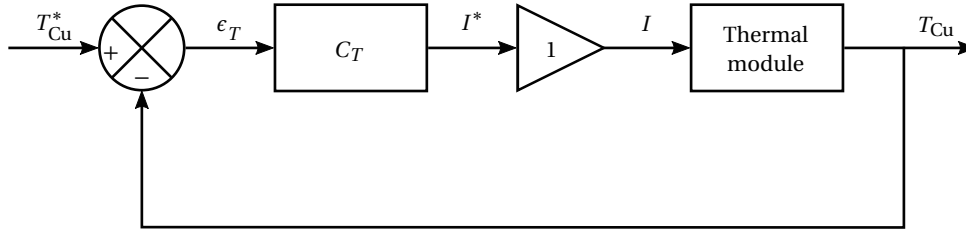


Figure 5.5 – Schematic representation of the temperature closed-loop control.

control scheme where $C_T$ can be a Proportional-Integral-Derivative (PID) controller. Note that even if the chosen TEMs sustain 8.5 A, our programmable power supply (from RIGOL) has a saturation at $\pm 3$ A. The power supply has been considered as a unity gain.

### 5.1.2.1 Lyapunov stability of dynamical systems

In order to deal with stability and performance analysis problems, the Lyapunov theory has been extensively used in modern dynamical systems theory. This theory allows to study systems properties without solving the differential equation describing their behavior by using an energy function usually called Lyapunov function. The positivity of this function and the negativity of its time derivative allow to conclude on system stability. A basic result is stated in the following theorem.

**Theorem 5.1** (Lyapunov stability for LTI systems). *A Linear-Time-Invariant (LTI) system defined by the dynamical equation $\dot{X} = AX$ is quadratically* stable *if and only if there exists a symmetric positive definite matrix P such that the following Lyapunov inequality holds:*

$$A^T P + PA < 0.$$

Note that this inequality is linear in the unknown variable and hence, it can easily be solved by using convex optimization techniques. The feasibility of this Lyapunov inequality with a positive definite Lyapunov matrix $P$ is equivalent to the classical LTI stability result requiring the eigenvalues of matrix $A$ (*i.e.* the system poles) to lie into the left half complex plane. The Lyapunov function guaranteeing the system stability is the quadratic function $X^T P X$.

As emphasized in the previous section, TEM equations (5.10)-(5.11) exhibit the state space representation with a particular structure. Indeed, the state matrix $A_1$ depends affinely on the current $I$ while the control input is $I^2$. This means that the system is bilinear with a quadratic control input. Despite a very rich literature dedicated to the analysis and control of bilinear systems, there are no results, to our knowledge, on the performance analysis and control of bilinear systems with quadratic control input. Therefore, in order to deal with this additional complexity, a simple and very effective approach based on a linear uncertain parameter-dependent reformulation of the dynamic equations (5.10)-(5.11) is presented in the following.

From expression (5.12), it follows that the state matrix $A_1$ can be written as:

$$A_1(I) = A_{10} + A_{20}I \tag{5.19}$$

where

$$A_{10} = \begin{bmatrix} M_c^{-1}\left(-(G_1 + G_2) - h_c A_c\right) & M_h^{-1}G_1 & M_h^{-1}G_2 \\ M_c^{-1}G1 & M_h^{-1}\left(-G_1 - h_{r_1}A_r\right) & 0 \\ M_c^{-1}G_2 & 0 & M_h^{-1}\left(-G_2 - h_{r_2}A_r\right) \end{bmatrix}$$

and

$$A_{20} = \begin{bmatrix} M_c^{-1}(\epsilon_1 + \epsilon_2) & 0 & 0 \\ 0 & -M_h^{-1}\epsilon_1 & 0 \\ 0 & 0 & -M_h^{-1}\epsilon_2 \end{bmatrix}.$$

By considering the current $I$ in equation (5.19) as being an uncertain parameter $\xi$, the system (5.10)-(5.11) is *equivalent* to:

$$\dot{X}_1 = A_1(\xi)X_1 + B_1\,[U\ T_a]^T \tag{5.20}$$
$$Y_1 = C_1 X_1 \tag{5.21}$$

where the state vector is, as previously, $X_1 = \begin{bmatrix} T_{Cu} & T_{h_1} & T_{h_2} \end{bmatrix}^T$. Remark that the input signal is bidimensional. However, the ambient temperature $T_a$ cannot be used for control purposes and therefore, it is considered as on operating point. Hence, the only signal available for control purposes is the input $U = I^2$.

Note that the equivalent reformulation (5.20)-(5.21) is a linear parameter-dependent system with affine parameter dependency and subject to an uncertain time varying parameter. Therefore, the Linear-Parameter-Varying (LPV) techniques may be applied in order to deal with the complexity of the control problem for the initial bilinear model. The stability of a system with structure (5.20)-(5.21) is not guaranteed anymore by the only inclusion of the eigenvalues of the state matrix $A_1(\xi)$ in the left half-plane for all the possible values of the parameter. In fact, when the uncertain parameter $\xi$ is constant, the system stability is equivalent to the left half-plane inclusion of the eigenvalues of $A_1(\xi)$. However, when the uncertain parameter is time-varying, this becomes only a local stability condition which is insufficient to guarantee the global system stability for all the possible parameter trajectories. In order to ensure the global stability, only the Lyapunov theory can be applied. Using the LPV techniques and based on the affine dependency of the state matrix stated in equation (5.19), Theorem 5.1 reformulates as follows.

**Theorem 5.2** (Lyapunov stability for LPV systems). *Parameter-dependent system (5.20)-(5.21) with (5.19) is asymptotically* stable *if there exists a symmetric positive definite matrix P such that the following Lyapunov inequality holds:*

$$A(\xi)^T P + PA(\xi) < 0 \quad \forall \xi \in \mathscr{P}_v$$

*where $\mathscr{P}_v$ is the set of all the vertices of the convex parameter domain $\mathscr{P}$.*

This theorem uses a quadratic Lyapunov function with a constant Lyapunov matrix. This may be very conservative for many applications especially when the parameter domain is very large. It is worth mentioning that less restrictive approaches employing parameter-dependent Lyapunov functions have already been proposed in the literature. However, as shown next, employing a constant Lyapunov matrix is not restrictive for our particular application since the eigenvalues of the state matrix vary slightly over the parameter domain.

The current $I = \xi$ evolves in the interval $\mathscr{P} = [-3;3]$ A. Figure 5.6 shows the evolution of the system poles (eigenvalues of the state matrix) over this parameter domain. A zoom in for each eigenvalue is also drawn in Figure 5.7 in order to better visualize the influence of the current $I$ on the evolution of these poles. For any fixed value of $I$, the system poles have a negative real part which shows the local stability of the system (5.20)-(5.21). The global stability of this system is guaranteed for any variation rate of the uncertain parameter (even for a switching one) whenever the Linear Matrix Inequality (LMI) conditions of Theorem 5.2 are feasible. The implementation of these LMI conditions on the vertices of $\mathscr{P}$ *i.e.* for $\xi \in \{-3, \ 3\}$ provides the following Lyapunov matrix:

$$P = \begin{bmatrix} 1.6314 & -0.2828 & -0.3011 \\ -0.2828 & 2.6906 & -0.1118 \\ -0.3011 & -0.1118 & 2.7016 \end{bmatrix} . \tag{5.22}$$
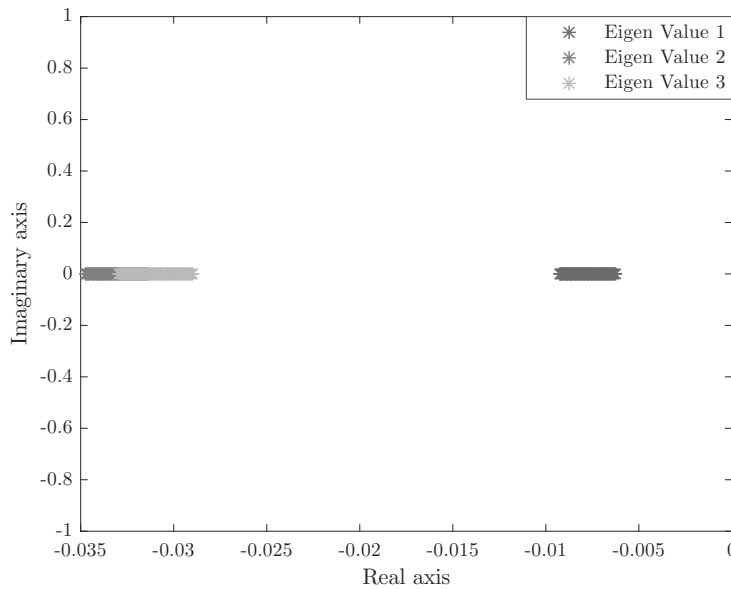


Figure 5.6 – Eigenvalues of $A_1$ for a range of current $I \in [-3;3]$ A.
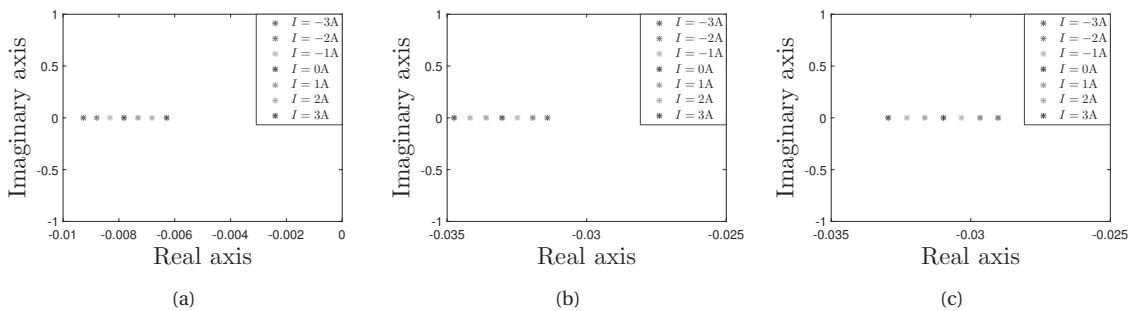


Figure 5.7 – Zoom in on each eigenvalue of $A_1$.

### 5.1.2.2 Design of a PI controller

To design an appropriate controller for the thermal block, a first approach would be to apply the dominant-pole compensation method. Note that such a technique is not robust especially when the state matrix $A_1$ is current-dependent generating time-varying poles as explained in the previous subsection. Therefore, a different design technique has to be applied in order to obtain a controller.

It is important to note that the use of Peltier modules cause an asymmetrical functioning and modeling of the thermal block. This is due to the fact that heating and cooling phases are not governed by the same equations and the commutation from one to the other phase occurs by changing the current sign. Indeed, from equation (5.7) to (5.9), one can remark that the Joule effect expressed as a function of $I^2$ is the source of this asymmetry since, unlike the other terms of these dynamical equations, it does not change its sign according to the current sign. In addition, this can also be remarked using the state-space representation (5.20)-(5.21) since the state-space dynamics change according to the current sign unlike the control input $U$. Therefore, in order to improve the performance of the central copper block closed-loop temperature control, an original control approach has been employed by using two different controllers, one for the heating phase and another for the cooling phase. The commutation between these two controllers depends on the operating phase. Denoting the heating, respectively cooling, controller transfer function as $C_{T_h}$, respectively $C_{T_c}$, the control input $U$ is then computed as:

$$U(s) = C_{T_h}(s)\epsilon_T(s) \quad \text{if } \epsilon_T(t) > 0 \tag{5.23}$$

and

$$U(s) = C_{T_c}(s)\epsilon_T(s) \quad \text{if } \epsilon_T(t) < 0. \tag{5.24}$$

**Synthesis of $C_T$** From system dynamics analysis provided in the previous subsection (see Figure 5.6 and, more particularly, Figure 5.7(a)), the slowest system dynamic corresponds to $I = 3$ A. Therefore, this specific current value has been considered for synthesizing the controller $C_{T_h}$. System (5.20)-(5.21) leads to an LTI model for $\xi = 3$ and the controller has been synthesized using the root locus. This graphical method is proposed within Matlab framework through the SISO Design Tool that plots the poles of the closed-loop system. For instance, Figure 5.8 describes the root locus of the negative feedback control on the above system with a proportional controller $K_P$. Such a controller amplifies the error signal and allows to diminish the rise time. In our application, such a controller is not sufficient since static error increases with $K_P$. Therefore, an integral term $\frac{K_I}{s}$ has been added to improve the controller performance by eliminating residual steady-state errors and rejecting disturbances, generated, for instance, by the exothermic polymerization reaction. This results in adding a pole in zero (red cross in Figure 5.9) and a zero to the controller (red circle in Figure 5.9). Then $K_P$ and $K_I$ gains are adjusted by considering the following design requirements:

- no residual steady-state error is accepted,

- any overshoot is prohibited,

- the settling time should be as fast as possible while keeping in mind the power supply limitations.

Figure 5.9 shows the root locus for the chosen controller providing the best compromise between the previous requirements. Placing the zero of the controller (red circle) at the right side of the slowest pole of the system would force the placement of a closed-loop pole on the slowest branch of the root locus and make the closed-loop system even slower. Therefore, the red circle is placed at its left side. This same reasoning must be applied to currents $I \in [0; 3]$ A. So, the zero of the controller must be smaller than the slowest pole of the system at $I = 0$ A *i.e.* $-0.0078$. Then, to prevent any overshoot, the closed-loop system should only present negative real poles.
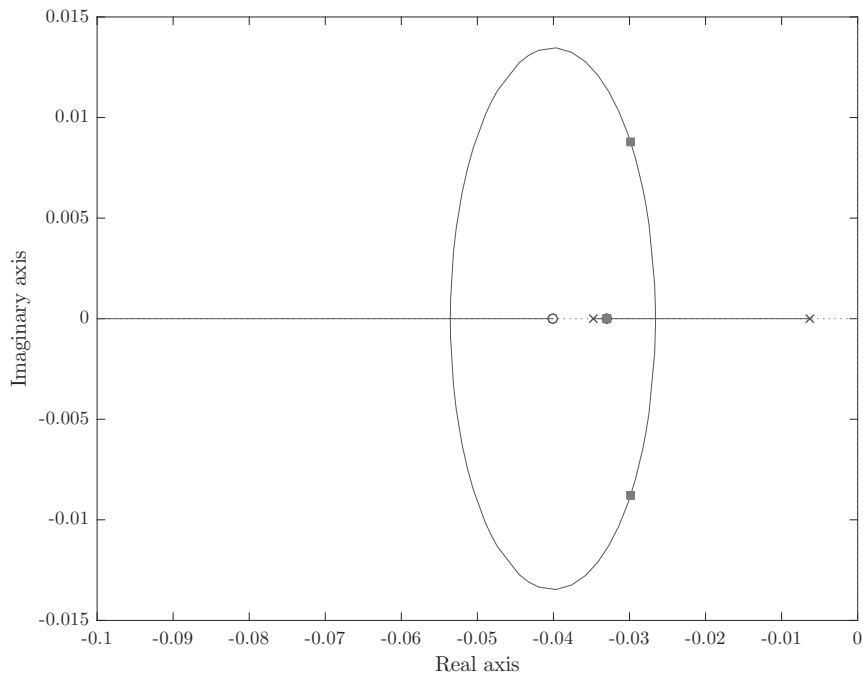
Figure 5.8 – Root locus of the system with proportional control, with the closed-loop poles (pink squares) represented for $K_P = 1\,\mathrm{A}^2 \cdot \mathrm{K}^{-1}$.
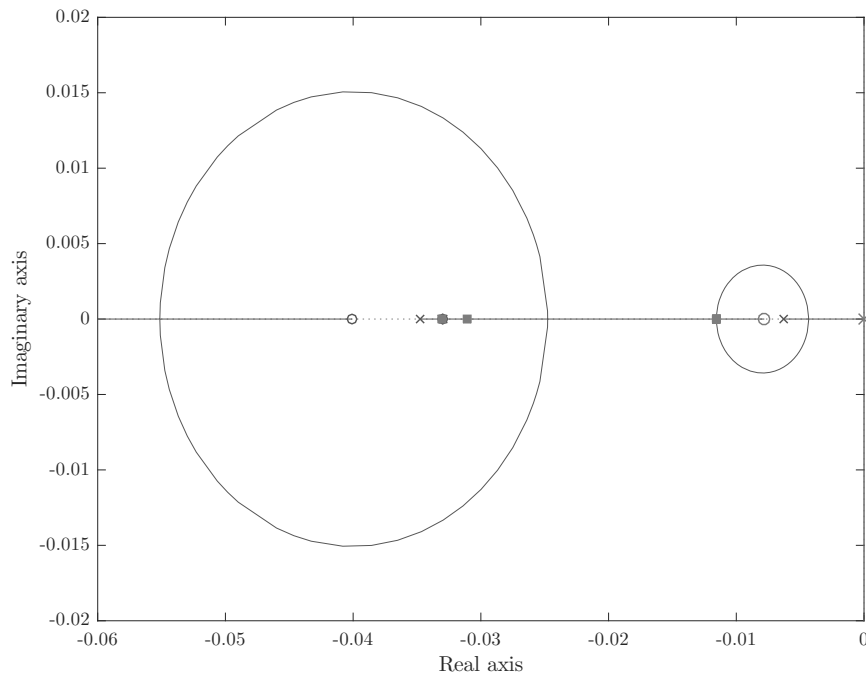


Figure 5.9 – Root locus of the system with proportional integral control, with its closed loop poles represented (pink squares) for: $K_P = 0.72\,\mathrm{A}^2 \cdot \mathrm{K}^{-1}$ and $K_I = 0.00554\,\mathrm{A}^2 \cdot \mathrm{s}^{-1} \cdot \mathrm{K}^{-1}$.

Finally, since current output of the power supply should not be exceeded, the choice of $K_P = 0.72\,\mathrm{A}^2 \cdot \mathrm{K}^{-1}$ and $K_I = 0.00554\,\mathrm{A}^2 \cdot \mathrm{s}^{-1} \cdot \mathrm{K}^{-1}$ is the best compromise between a fast and non-overshooting response.

A derivative term could have been added to the controller structure but it does not provide better performance. Indeed, adding this term to the controller would force to place a pole to the closed-loop system on the slowest branch of the root locus.

The same arguments have been exploited in order to design the second controller $C_{T_c}$ for the cooling part. Again, a PI-controller has been selected with $K_P = 4.55\,\mathrm{A}^2 \cdot \mathrm{K}^{-1}$ and $K_I = 0.0015\,\mathrm{A}^2 \cdot \mathrm{s}^{-1} \cdot \mathrm{K}^{-1}$. This controller is represented in Figure 5.10 where values of $K_P$ and $K_I$ are reminded in Table 5.3 depending on the error sign.
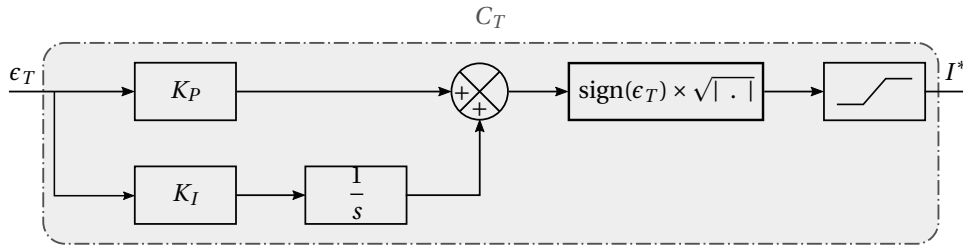


Figure 5.10 – Schematic representation of the complete temperature controller.

| $\mathrm{sign}(\epsilon_T)$ | $K_P$ $(\mathrm{A}^2 \cdot \mathrm{K}^{-1})$ | $K_I$ $(\mathrm{A}^2 \cdot \mathrm{s}^{-1} \cdot \mathrm{K}^{-1})$ |
|:---:|:---:|:---:|
| + | 0.72 | 0.00554 |
| − | 4.55 | 0.0015 |

Table 5.3 – Gains of the temperature controller depending on the sign of the error $\epsilon_T$.

**Stability of the closed-loop control**  A state-space representation of the PI controller can be formulated as follows by using one state-space variable $X_c$:

$$\dot{X}_c = K_I(\sigma)\epsilon_T \tag{5.25}$$

$$U = X_c + K_P(\sigma)\epsilon_T \tag{5.26}$$

where $\sigma$ is the switching function that indicates the commutation from one controller to another according to the strategy given in equations (5.23) and (5.24). This switching function changes its value according to the input signal sign and its codomain is the finite set $\mathscr{I} = \{1,\ 2\}$. Therefore,

$$\sigma = \begin{cases} 1 \text{ if } \epsilon_T \geq 0 \\ 2 \text{ if } \epsilon_T < 0 \end{cases} \quad , \quad K_P(\sigma) = \begin{cases} K_{P_h} \text{ if } \sigma = 1 \\ K_{P_c} \text{ if } \sigma = 2 \end{cases} \quad \text{and} \quad K_I(\sigma) = \begin{cases} K_{I_h} \text{ if } \sigma = 1 \\ K_{I_c} \text{ if } \sigma = 2 \end{cases}.$$

Note that the controller parameters for heating phase are given by the second line of Table 5.3 while the ones for cooling phase are given in the last line of the same table. Using the system representation (5.20)-(5.21) and by neglecting the saturation, it follows that closed-loop state space representation is given by:

$$\dot{X}_{BF} = \begin{bmatrix} A_1(\xi) - B_{10}K_P(\sigma)C_1 & B_{10} \\ -K_I(\sigma)C_1 & 0 \end{bmatrix} X_{BF} + \begin{bmatrix} B_{10}K_P(\sigma) \\ K_I(\sigma) \end{bmatrix} T_{Cu}^* + \begin{bmatrix} B_{11} \\ 0 \end{bmatrix} T_a \tag{5.27}$$

$$Y_{BF} = \begin{bmatrix} C_1 & 0 \end{bmatrix} X_{BF} \tag{5.28}$$

where $X_{BF} = \begin{bmatrix} X_1^T X_c \end{bmatrix}^T$ and $B_{10}$ and $B_{11}$ are the first and, respectively, the second column of matrix $B_1$ in equation(5.13). Note that a sufficient condition for a switching system to be stable is the existence of a common Lyapunov matrix guaranteeing the stability of each mode. Based on this fact and by considering that the uncertain parameter $\xi$ and the switching law are independent, the application of Theorem 5.2 yields that the closed-loop system is stable whenever the following set of LMIs is feasible:

$$P_{BF} = P_{BF}^T > 0$$

$$\begin{bmatrix} A_1(\xi) - B_{10}K_{P_h}C_1 & B_{10} \\ -K_{I_h}C_1 & 0 \end{bmatrix}^T P_{BF} + P_{BF} \begin{bmatrix} A_1(\xi) - B_{10}K_{P_h}C & B_{10} \\ -K_{I_h}C_1 & 0 \end{bmatrix} < 0 \quad \text{for } \xi \in \{0, \ 3\}$$

$$\begin{bmatrix} A_1(\xi) - B_{10}K_{P_c}C_1 & B_{10} \\ -K_{I_c}C_1 & 0 \end{bmatrix}^T P_{BF} + P_{BF} \begin{bmatrix} A_1(\xi) - B_{10}K_{P_c}C_1 & B_{10} \\ -K_{I_c}C_1 & 0 \end{bmatrix} < 0 \quad \text{for } \xi \in \{-3, \ 0\}$$

The Lyapunov matrix $P_{BF}$ ensuring the stability of the closed loop system is:

$$P_{BF} = 10^3 \times \begin{bmatrix} 0.7178 & -0.1731 & -0.1775 & -0.1490 \\ -0.1731 & 0.5492 & -0.1789 & -0.0035 \\ -0.1775 & -0.1789 & 0.5507 & -0.0057 \\ -0.1490 & -0.0035 & -0.0057 & 1.0126 \end{bmatrix}. \tag{5.29}$$

**Experimental validation of the controllers**  An experimental set-up has been designed to validate the efficiency of the tuned controllers. As a first experiment, a temperature reference $T_{Cu}^*$ has been constructed between 15 °C and 30 °C as illustrated by the light blue curve in Figure 5.11. The piston speed $V_P$ is constant at $5\,\text{mm}\cdot\text{min}^{-1}$ in order to allow an injection time of at least 10 min. Increasing the injection speed would not leave enough time to prove the proper functioning of the implemented controllers. Moreover, fans run at full speed since an adjusted control does not seem suitable. Indeed, TEM performs the best for the smallest $\Delta T$, which is always reached for the maximal speed of both fans.

Through this first experiment, we also expected to confirm the ability to regulate the temperature of the flowing bone cement. Working ex vivo, an additional Pt1000 temperature sensor has been installed in direct contact with the bone cement at the outlet of the thermal block. Results are provided in Figure 5.11 where time zero represents the beginning of the bone cement mixing phase.

The control of the copper block is highly satisfactory since the measured temperature $T_{Cu}$ follows the reference signal $T_{Cu}^*$ with the expected properties. Despite the first step at 25 °C, no steady-state error has been observed, which indicates that the integral term of the controller is adapted. The slight error that appears at 25 °C, between 4 and 6 min, may be due to the influence of ambient temperature. However, this error is rejected slowly by our controller. Regarding the rise time of $T_{Cu}$, it is perfectly acceptable. A delay of approximately 5 s is noticeable between $T_{Cu}$ and $T_{Cu}^*$. This is due to the incompressible time required so that the heat diffusion in the copper to reach the temperature sensor placed on the surface of the copper block. At each change in the reference $T_{Cu}^*$, two phases are identifiable in the control curve, *i.e.* the current simultaneously applied to both Peltier modules. There is a very fast and emphasized transient (with a fast rise due to the proportional effect followed by a longer increase of the control due to the integral effect) followed by a steady state to reach the desired temperature and to maintain it. The low integral gain explains the slow linear part between the transient and steady state.

Concerning the bone cement temperature $T_{BC}$, it follows rather well the reference temperature $T_{Cu}^*$. This confirms that the designed temperature exchanger is able to control the centerline temperature of the flowing bone cement. However, there is a static error ranging from 0.1 °C to 0.25 °C. This is due to the fact that the bone cement temperature entering the thermal block at a non-zero speed has a $T_{in}$ temperature different than $T_{Cu}^*$. Moreover, there is no second control loop adjusting the reference $T_{Cu}^*$ to the measured value of the cement
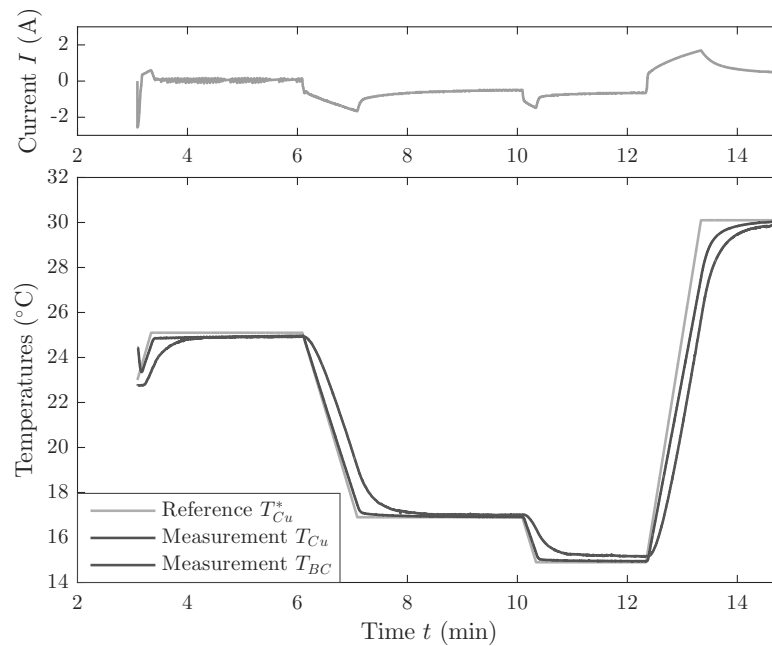
Figure 5.11 – Results of the temperature control at a constant piston speed $V_P = 5\,\mathrm{mm\cdot s^{-1}}$

temperature $T_{BC}$. During an abrupt reference temperature change, the relatively large settling time between $T_{Cu}$ and $T_{BC}$ is a result of the response time of the copper surrounding the bone cement and the offset of the transit time. Indeed, one has to wait at least once the cement transits the control block in order to observe the influence of the temperature control. Analogous experiments with different piston speeds have been led and results are very similar to the reported ones.

### 5.1.3 Effect of temperature changes on the cement mechanical properties

Acrylic bone cements are among others selected by practitioners for their mechanical properties. With the idea of bringing this technology to the market, controlling the cement temperature should however not change its mechanical properties.

Biomechanical requirements for bone cements based on PMMA are standardized according to ISO 5833:2002 [ISO 2002]. It is stipulated that the minimum requirement is 70 MPa for compressive strength, 1800 MPa for bending modulus, and 50 MPa for bending strength. Since the compression forces represent the main load for the vertebral column, only compressive testing has been conducted. To meet this standard in terms of testing, cylindrical samples of the commercial bone cement Osteopal V of $12 \pm 0.1$ mm in height and 6 mm in diameter have been shaped. Indeed, after the usual hand-mixing process, molds made of aluminum provided for that purpose have been filled by the bone cement mixture. To check whether the temperature affects or not the compressive strength, five samples have cured in the fridge at 4.8 °C while five other ones have cured at ambient temperature ($T_a = 21.5$ °C). Since the curing reaction and thus, the mechanical properties, is favored with a heat input, specimens at warm temperatures have not been produced nor tested. Compressive tests have been performed $24 \pm 2$ hours after the samples fabrication. One after the other, each sample was loaded on a testing machine (see Figure 5.12(a)) to apply a constant crosshead speed of $20\,\mathrm{mm\cdot min^{-1}}$ (required to be between 19.8 and $25.4\,\mathrm{mm\cdot min^{-1}}$). From the force measurement, a curve of load against displacement has been obtained, as in Figure 5.12(b), allowing to compute both the compression strength and the Young modulus.
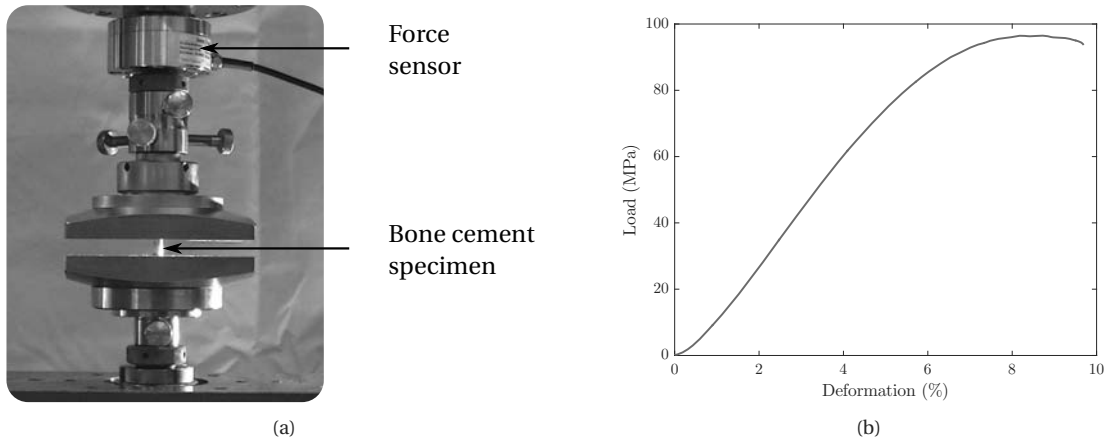
Figure 5.12 – Compressive experiments: (a) set-up; (b) example of an acquired curve.

Each sample went through this compressive testing for five times. Table 5.4 provides the statistical results of the conducted experiments. For all the samples, the Young modulus was computed at a deformation of 2%. In both cases, either at ambient temperature or at 4.8 °C, the overall behavior is very similar and the influence of the temperature change is not discernible. According to the literature, hand-mixing, as performed for our experiment, provides the worst mechanical properties [Dunne 2001, Kühn 2013]. Still, one can notice that, for both temperatures, compressive strength values are well above the one given for the standard.

| Compressive testing | $T_a$ | | $T = 4.8\,°C$ | |
|---|---|---|---|---|
| | Compressive strength (MPa) | Young modulus (GPa) | Compressive strength (MPa) | Young modulus (GPa) |
| Mean | 91.0 | 1.31 | 92.9 | 1.36 |
| Standard deviation | 3.26 | 0.0765 | 2.87 | 0.0510 |

Table 5.4 – Results of the compressive testing for bone cement specimens cured at two different temperatures.

## 5.2  Viscosity estimation and control

The previous section presented the modeling and the identification of the complete thermal block as well as its temperature control. In order to control viscosity, cascade loops are needed. The inner loop is the thermal block control loop developed previously and the outer loop is the viscosity control, presented in the sequel. Since it is impossible to directly measure the viscosity, an online estimation of its value is needed.

### 5.2.1  Online estimation of the bone cement viscosity

Once the bone cement injection starts, the practitioner alternates between injection phases and halting phases needed for check-up throughout the fluoroscopy control screen. This allows him/her to examine if enough bone cement has been injected, to ask for a different viewing angle or to notice a cement leakage. In the following, the

viscosity estimation will differentiate whether the physician injects bone cement or stops it.

### 5.2.1.1 Viscosity estimation during cement injection

The rheological study proposed in Chapter 2 confirms that acrylic bone cement has a shear-thinning behavior, which means that its viscosity decreases when the applied shear rate increases. The power law, defined in section 2.2.3, will be considered to compute the online viscosity. As assumed during the design of the slave device, the flow involved in the injection is assimilated to a Poiseuille flow where the capillary is the conduit of length $L_c$ and of radius $R_c$ (see Figure 4.8). Based on the assumption that the bone cement behavior can be described by the power law, the principle of mass conservation coupled to the resolution of the Navier-Stokes equation provide the following relationship between the pressure drop $\Delta P$ and the flow rate $Q$:

$$Q = \left(\frac{\Delta P}{L_c}\right)^{\frac{1}{n}} \left(\frac{R_c}{2K}\right)^{\frac{1}{n}} \left(\frac{\pi n R_c^3}{3n+1}\right) \tag{5.30}$$

The detailed computation of this relation is given in Appendix A.

In order to compute online the bone cement viscosity, an adapted instrumentation has been included to the injection device as explained in section 4.1.1. The force sensor in the transmission (see Figure 4.2) provides the measurement of the injection force F, which in turn allows to assess the pressure drop as:

$$\Delta P = \frac{F}{\pi R_s} - P_{\text{atm}} \tag{5.31}$$

with $R_s$, the radius of the syringe. This implies two assumptions. On one side, the pressure at the outlet of the syringe is considered equal to the pressure on the plunger. Some of the simulations introduced in section 4.2.2 demonstrate that almost all the pressure drop occurs beyond the last cross-section reduction (see Figure 4.9), which motivates this first hypothesis. On the other side, the pressure at the outlet is supposed to be equal to the atmospheric pressure. A linear position sensor has also been mounted on the carriage, which allows to measure its position and, thus, the bone cement flow rate $Q$.

Despite the measurement of the pressure drop and the flow $Q$, equation (5.30) cannot be applied as it is to compute bone cement viscosity: two unknown parameters ($n$ and $K$) remain to be identified online while there is only one measurement at each time step. According to the identification of the power law in section 3.1, $K$ is by far the parameter that most reflects the viscosity evolution. Hence, for the online viscosity computation, the flow behavior index $n$ is supposed to be constant over time and, based on the rheological characterization, it is chosen to be equal to 0.2. With this hypothesis, equation (5.30) has only a single unknown parameter, which is $K$.

Finally, to reconstruct the viscosity value based on the power law, the shear rate must be computed. According to calculations carried out in Appendix A, the cement shear rate at a distance $r$ from the flow centerline is:

$$\dot{\gamma} = \left(\frac{\Delta P}{2KL_c}\right)^{\frac{1}{n}} r^{\frac{1}{n}} . \tag{5.32}$$

With equation (5.30), it can be written as:

$$\dot{\gamma} = \frac{(3n+1)Q}{\pi n R_c^3} \left(\frac{r}{R_c}\right)^{\frac{1}{n}} . \tag{5.33}$$

As mentioned in Chapter 2, the power law is only valid above a certain shear rate (0.1 Pa·s). To ensure this validity at any non-zero velocity, the highest shear rate is considered, *i.e.* at $r = R_c$, which leads to compute the

shear rate at the wall as:

$$\dot{\gamma} = \frac{(3n+1)Q}{\pi n R_c^3} \ .$$  (5.34)

To summarize the method to enable to compute the online viscosity at each time step, the position (respectively force) sensor provides a flow rate (respectively a pressure drop) measurement. Since $n$ is assumed to be equal to 0.2, parameter $K$ can be computed thanks to equation (5.30). Based on equation (5.34), the shear rate at the wall is estimated in order to estimate the viscosity value according to the power law (2.5).

### 5.2.1.2 Halted injection

A difficulty arises when the physician stops the injection for any of the previously mentioned reasons. While the bone cement viscosity continues to evolve, the power law used by the previous method does not hold anymore since the share rate is null. To pursue an eventual viscosity control, the first approach is to solve online the differential equation identified in section 3.2 by initializing it with the last viscosity value estimated with the previous method.

When the practitioner halts the injection procedure, a viscosity value is less required. However, we must ensure that the cement flowing inside the conduit does not form a plug. Hence, in a second approach, it is preferable either to stop the ongoing viscosity control or to only cool down the bone cement located inside the thermal regulation block.

### 5.2.1.3 Experiments

The online viscosity estimation has been performed during many experiments on the injection device using Osteopal® V cement from Heraeus.

**Experimental set-up** Prior to each experiment, the sheath has been either stored in the freezer or in the refrigerator or just left at ambient temperature $T_a$, at least for 24 h.

Then, to remain consistent with current vertebroplasty procedures, all the experiments have been handled in conditions similar to the ones usually observed in the department of Interventional Radiology at the University Hospital of Strasbourg: the cement kits are refrigerated at 4 °C and the injections are performed at room temperature $T_a = 22$ °C. Each experiment starts when the complete bone cement kit (PMMA powder pack and liquid MMA ampoule) is withdrawn from the refrigerator. A chronometer is triggered once both components come into contact in a bowl. The hand mixing is completed when a homogeneous mixture is obtained. The prepared bone cement is then poured into a 10 mL syringe from Ardes. The fulfilled syringe is then inserted inside the sheath that can be plugged onto the mounting bracket. At this point, the injection can start. Every prepared bone cement has been injected at a piston speed $V_P = 5 \ \mathrm{mm \cdot min^{-1}}$ in order to acquire results for at least 10 min. Bone cement has been injected inside a phantom vertebra from Sawbones, either hollow or filled with a cancellous insert. For some trials, the copper temperature $T_{Cu}$ has been fixed at a given value thanks to the temperature control designed in the previous section.

Seven different experiments have been carried out. Table 5.5 gathers their testing conditions.

| Experiment number | Sheath storage | Copper temperature | Cancellous insert |
|---|---|---|---|
| 1 | $T_a$ | 24 °C | no |
| 2 | $T_a$ | 24 °C | yes |
| 3 | $T_a$ | - | no |
| 4 | Fridge | 10 °C | no |
| 5 | Fridge | - | no |
| 6 | Freezer | 40 °C | no |
| 7 | Fridge | 40 °C | no |

Table 5.5 – Testing conditions of the conducted experiments.

**Results and discussion**  Among the large amount of data acquired for each experiment, only data relevant for the validation of viscosity computation are highlighted. For the two first experiments, the parameter $K$ of the power law has been plotted over time in Figure 5.13. The rheological study described in Chapter 2 has led to
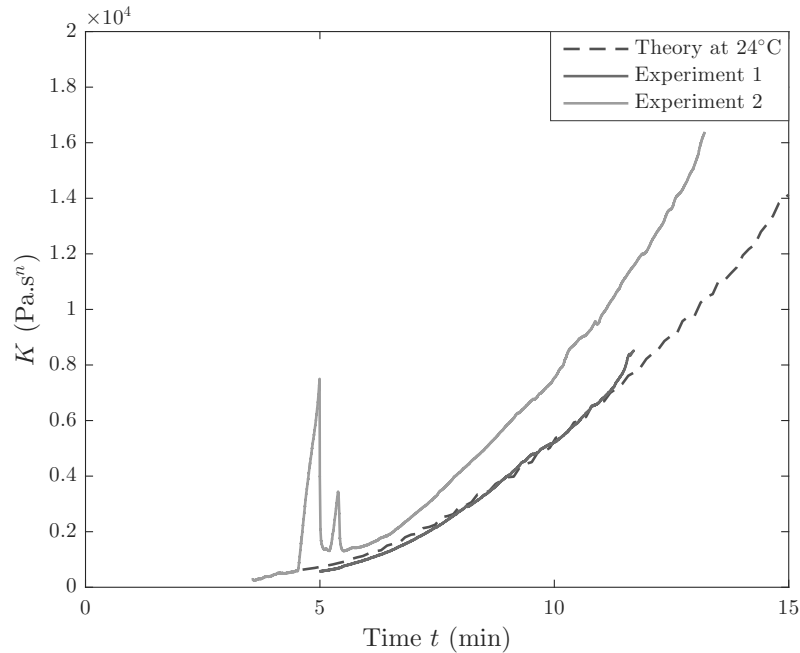


Figure 5.13 – Evolution of the parameter $K$ of the power law for two experiments.

the computation of the parameter $K$ at the reference temperature $T_{ref} = 20$ °C (see Figure 3.2(b)). Based on equation 3.12, the theoretical curve of $K$ at the temperature of the two first experiments, *i.e.* at 24 °C, has been computed and overlaid in Figure 5.13 with a purple dashed line. One can remark that the curve corresponding to Experiment 1 overlaps the theoretical curve. This suggests that the implemented viscosity computation is adequate and that the assumption $n = 0.2$ is correct. Additionally, the overlap of the purple curve obtained through measurements on the dynamic rheometer (in the frequency domain) and the blue curve based on continuous measurements validates *a posteriori* the use of the Cox-Merz rule pointed out in equation (2.19). For the second experiment, two sharp peaks on the curve at instants between 4 and 6 minutes are noticeable. They correspond to the formation of a plug at the end of the needle, which is a common phenomenon occurring during vertebroplasty procedures. Moreover, unlike the first experiment, the bone cement was flowing inside a phantom vertebra filled with a cancellous insert. This foam simulates the interactions that may occur when injecting the bone cement into a real vertebra which renders the cement spread more complex. However, the

bone cement is supposed to flow out of the pipe at atmospheric pressure. The shift between the green and the purple curve may be due to the intravertebral pressure which is different than the atmospheric one and increases during the injection. For now, the intravertebral pressure has not been evaluated, that is why further experiments have been achieved without any cancellous insert.

Besides the validation of the online viscosity computation, some other experiments have been conducted in order to understand the role that each subset of the injection device plays. Therefore, Figure 5.14 gathers the curves of the viscosity estimation for experiments 3 to 7.
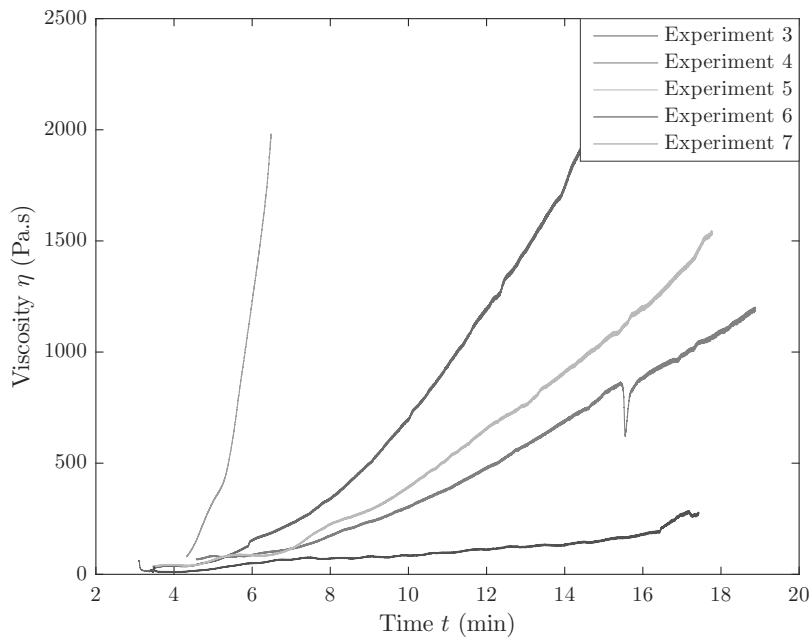


Figure 5.14 – Evolution of the viscosity $\eta$ for five experiments.

Corresponding to experiment 3, the blue curve represents the viscosity evolution without any temperature regulation, neither active nor passive. It can be considered as the reference viscosity curve illustrating the viscosity evolution during a normal percutaneous vertebroplasty procedure. In the curve associated to experiment 4, the sudden drop in viscosity has probably been caused by the flow of an air bubble that was inside the syringe. Despite the fact that the copper block has been set at 10 °C for experiment 4, testing conditions of curves 4 and 5 are very close. In comparison with the reference curve, it allows to demonstrate that a simple passive cooling with the eutectic gel can slow down the polymerization reaction. On top of that, the active temperature control helps to intensify this decrease of the viscosity rate and, thus, of the polymerization rate. However, the passive temperature regulation should not be too excessive. Otherwise, the chemical reaction can almost be frozen and even an important heating with the thermal module would not reactivate the polymerization reaction. This problem can be illustrated through the experiment 6 where the sheath has been stored, prior to the experiment, in a freezer. While the copper block has been set at 40 °C, the viscosity curve does not exceed 200 Pa·s, even after 16 min. This behavior is contrary to the specifications of our project since, with such a low viscosity, the risk of bone cement leakage outside the treated vertebra is extremely high. It also validates *a posteriori* the choice of a more adapted eutectic gel (see subsection 4.1.3). Last but not least, if the syringe holder is stored in a suitable temperature range (as for experiment 7), the polymerization reaction can easily be accelerated and the bone cement viscosity increased by heating it through the active regulation device.

In conclusion, the instrumentation of the injection device is adequate for the online viscosity estimation as

shown by several injection experiments. According to the comparison with the rheological study, this viscosity computation seems to provide reliable results. The hypothesis concerning the pressure at the outlet of the trocar should be further investigated. Indeed, a poor bone cement flow inside a vertebra can lead to the accumulation of cement at the exit of the cannula and to a strong increase in pressure. Finally, both the active and passive temperature control influence the evolution of the viscosity, which proves the possibility of controlling the bone cement viscosity during the injection.

## 5.2.2 Viscosity control

### 5.2.2.1 Constant viscosity reference

Since the online viscosity estimation has been validated, the bone cement viscosity control can be considered. The method followed to control the viscosity differs from the one for the temperature control. Here, the first task is to identify a viscosity reference signal that is appropriate. It has been pointed out in the problem statement of Chapter 1 that the complex behavior of the bone cement can be the cause of severe complications for the patient and difficulties for the practitioner. Indeed, on one hand, the cement has a low viscosity at the beginning of the injection and may then leak outside the pathological vertebra. On the other hand, the physician has to perform the bone cement injection fast enough during the short application phase (about 10 min for instance for Osteopal$^{®}$ V). Based on these remarks, the optimal viscosity reference would be a constant value, defined such that the bone cement leakages are limited and the cement flow inside the treated vertebra stays homogeneous. With such a reference, the practitioner could ideally take as much time as usually needed to perform the injection.

In practice, such an optimal viscosity reference cannot be followed since the ongoing polymerization cannot be stopped and is irreversible. Still, this idea has been implemented and it does not need the design of a specific viscosity controller. Generating the temperature reference of the copper block $T_{Cu}^*$ is then limited to an all-or-none principle. Indeed, the bone cement must be heated until its viscosity reaches the given viscosity reference and then, cooled down in order to slow down the curing reaction and, thus, to increase the working duration. In a first experiment, the temperature reference $T_{Cu}^*$ has therefore been saturated at 5 °C for the cooling phase and at 30 °C for the heating phase. According to the experiment performed at 37 °C on the rotational rheometer (see Figure 2.11) or experiment 7 in the previous subsection (see Figure 5.14), a temperature beyond 30 °C could cause the runaway of the chemical reaction and/or the formation of a plug inside the conduit. Regarding the cooling phase, a temperature reference of 5 °C seems sufficient to decrease the curing rate. Moreover, it would not be appropriate to decrease this cold temperature reference since it should not be acceptable to further reduce performances of the Peltier modules. Remember that their performances are strongly correlated to the temperature difference between their hot and cold plate and only the action of both fans can lower the temperature of the hot plate but not below the room temperature $T_a$.

From the perspective of a potential industrialization, the viscosity threshold could be adjusted to the desires and habits of each practitioner. As part of this thesis, several experiments have been performed by setting the threshold once at different values. In order to be consistent with the complete study, the experimental set-up of subsection 5.2.1.3 has again been used for these trials. The corresponding computed viscosity curve for a threshold at 200 Pa·s is given in Figure 5.15. For all experiments, a more or less sharp evolution in the viscosity is noticeable until the imposed threshold is reached. Once the threshold is exceeded, the viscosity rate is reduced until the end of the experiment. Even if the viscosity rate is slowed down, passed a value of 500 Pa·s, the application phase cannot be considerably increased anymore, due to the irreversibility of the chemical reaction. In Figure 5.15, once the threshold has been reached, one can note that the bone cement viscosity continues to increase with the same rate before it starts to decrease. This phenomenon is related to both the temperature of the copper block that goes from 30 °C to 5 °C and to the discharge of the bone cement inside the
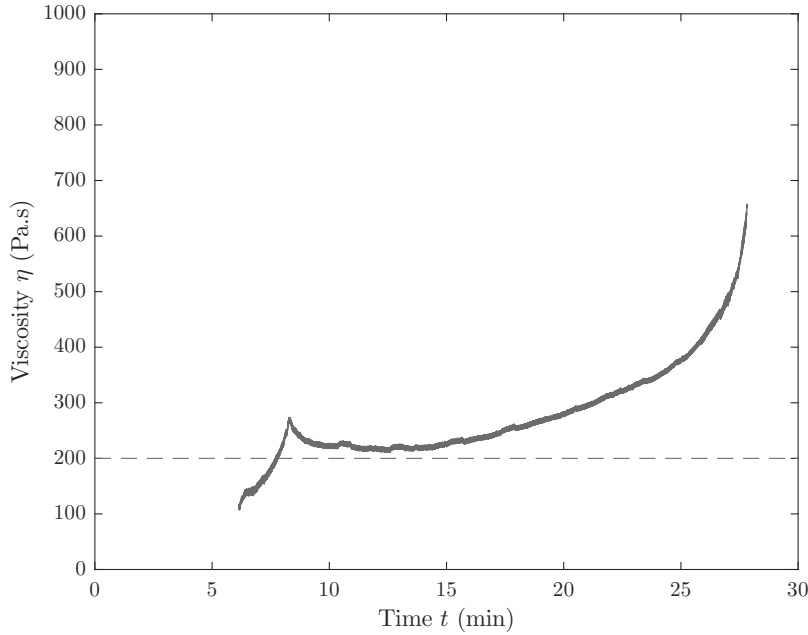
Figure 5.15 – Viscosity control experiments with a constant reference.

conduit when the temperature set point $T_{Cu}^*$ changes. Finally, the viscosity decrease that is observed on both curves could be considered surprising, and contrary to the irreversibility of the polymerization reaction. In fact, the passive cooling with the eutectic mixture makes the viscosity inside the syringe lower than the one inside the conduit, which leads to this deceptive viscosity decrease.

#### 5.2.2.2   Another viscosity reference

Based on the fine modeling and identification of the thermal exchanger and sustained by the results exposed in Figure 5.14, extensive simulation results are presented in the following for a more ambitious viscosity reference. Based on the block diagram in Figure 5.16, these simulations have been implemented within Simulink® (MATLAB). Using a more complex viscosity reference signal $\eta^*$, the viscosity controller $C_\eta$ does not operate on an all-or-none basis anymore. The temperature closed-loop control, including the power supply, is the one schematized in Figure 5.4 where the coefficients of the switching PI controller $C_T$ are gathered in Table 5.3. From the outcome $T_{Cu}$, the bone cement temperature $T_{BC}$ at the centerline and at the outlet of the thermal exchanger is computed by implementing the state-space representation defined by equations (5.17)-(5.18). Finally, the bone cement viscosity is obtained by solving the differential equation identified in Chapter 3.

In order to choose and tune the viscosity controller $C_\eta$, we focused on guaranteeing a minimal viscosity error without any oscillation of $\eta$ around the viscosity reference $\eta^*$. Based on a large number of simulations, a proportional controller computing the copper temperature reference signal relative to the ambient temperature $T_a$ has chosen. This viscosity controller $C_\eta$ is represented in Figure 5.17. The controller gain has been manually tuned and the obtained value is $K_{P_\eta} = 1.8 \, \text{K} \cdot \text{Pa}^{-1} \cdot \text{s}^{-1}$. For the same reasons as exposed in the previous subsection, $T_{Cu}^*$ has also been saturated at 5 °C for the cooling phase and at 30 °C for the heating phase.
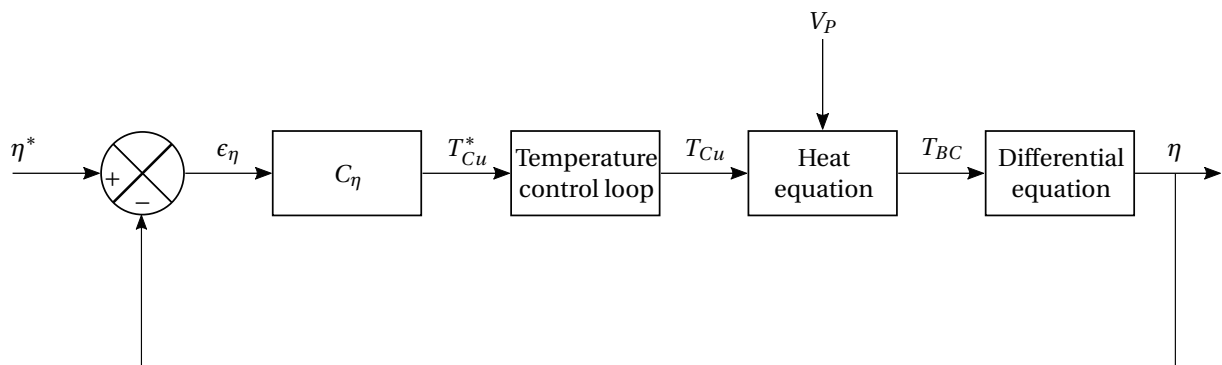
Figure 5.16 – Schematic representation of the viscosity closed-loop control.
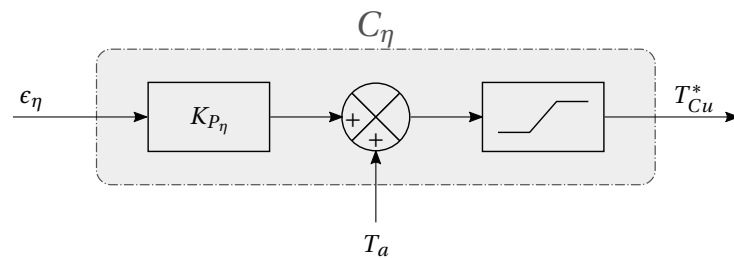


Figure 5.17 – Schematic representation of the viscosity controller.

With this viscosity controller, simulations within Simulink® provides very satisfactory outcomes. For instance, the viscosity reference $\eta^*$, one of the viscosity curves acquired on the dynamic rheometer (see section 2.3.2), and the resulting viscosity $\eta$ are plotted in Figure 5.18(a). Note that, in Figure 5.18(b), for at least 20 min, the viscosity error is quite small (about 10 Pa·s). The copper temperature reference and the obtained temperature $T_{Cu}$ compared to the bone cement temperature $T_{BC}$ as well as the applied current $I$ are reported in 5.18(c) and 5.18(d).

Despite that these simulation results are very promising, they have been achieved by considering some parameters as known. Indeed, in the previous example, the temperature at the inlet of the copper block has been set at $T_{in} = 18\,°\mathrm{C}$ and the bone cement viscosity has been initialized at 10 Pa·s. In addition, the simulation doesn't take into account the evolution of the cement viscosity inside the syringe. In fact, the viscosity of the cement inside the syringe is assumed, at each simulation time step of the cement differential equation, to be identical to the one in the pipe submitted to thermal exchange. Due to these limitations, such excellent simulation results cannot be reached online. Actually, we realize that some measurements are missing on the injection device such as the temperature at the inlet of the thermal exchanger that can be reached by using an additional sensor. Moreover, the viscosity of the cement that resides inside the syringe is unknown and therefore, a way of estimating its value is necessary. In terms of conclusion, even if very satisfactory results have been achieved for a constant viscosity reference, the model of the complete injection device needs be improved by considering additional elements such as the evolution of the viscosity inside the syringe and the temperature at the inlet of the thermal exchanger.
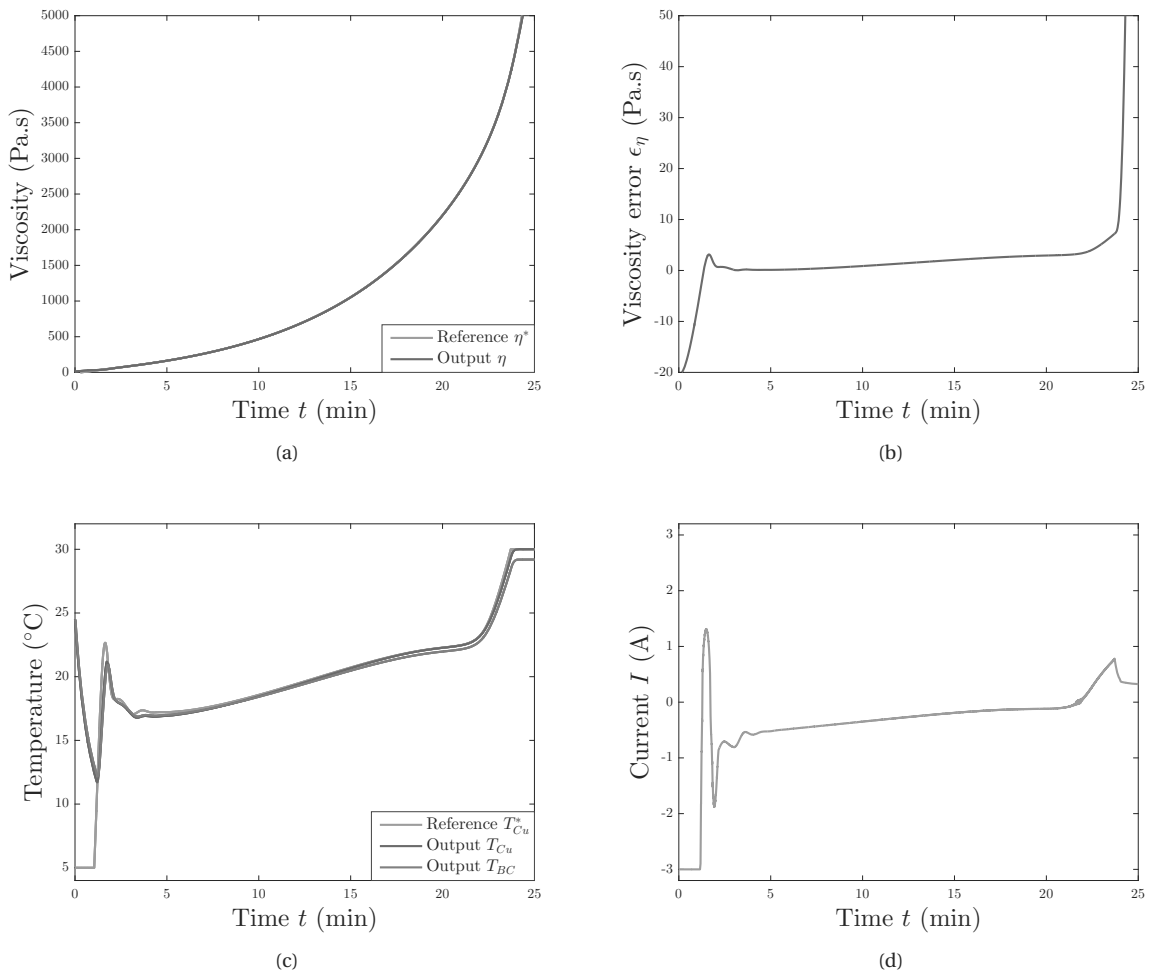
Figure 5.18 – Simulation results within Simulink®: (a) viscosity reference and obtained viscosity; (b) viscosity error; (c) copper temperature reference and obtained temperature $T_{Cu}$ compared to the bone cement temperature $T_{BC}$; (d) applied current $I$.

# 6 Conclusions and perspectives

## 6.1   Conclusions

Percutaneous vertebroplasty involves injecting acrylic or calcium phosphate cement, under fluoroscopic guidance, into a fractured vertebral body. From an extensive literature review proposed in Chapter 1, some major benefits have been distinguished such as long-term consolidation of the pathological vertebra, strong pain relief and short recovery period. Despite significant advantages from the patient's perspective, two major difficulties are directly related to the injected biomaterial. First, the low viscosity of the mixture introduces a high risk of leakage outside the damaged vertebra which might lead to dramatic complications for the patient. In addition, during the injection, the chemical reaction progresses and the bone cement hardens quite suddenly. This leaves only a short application phase to the practitioner. Last but not least, the radiologist is permanently exposed to harmful X-rays: while few CT-scanner images are taken during the trocars insertion, their exposure is worse during the injection time. The practitioner needs a continuous visual feedback to evaluate the volume of cement that has to be injected but also to detect any leakage as soon as possible. In the long term, despite some minimal protections, these harmful radiations prevent from increasing the number of vertebroplasty procedures per practitioner. The work presented in this thesis brings new and original solutions to improve the inconveniences still related currently to this medical procedure.

As a first step, a rheological study has been set up and completed in order to fully understand the general behavior of acrylic bone cements. As already emphasized in the literature, this study has reaffirmed that PMMA bone cements viscosity highly depends on three main parameters that are time, temperature and shear rate. Indeed, its viscosity increases with the evolution of the exothermic curing reaction that undergoes the orthopedic cement. A shear-thinning behavior has also been noticed since viscosity decreases with an increase of shear rate. Moreover, a change in the temperature of the bone cement modifies the evolution of the chemical reaction and, thus, the viscosity: cooling the cement decreases its viscosity while heating leads to an increase of viscosity. From the large number of acquired data, two different models have been identified to describe the evolution of viscosity. Both models consider the influence of time, temperature and shear rate. The first model, named "improved power law" and presented in Chapter 3, is based on the well-known Ostwald-de-Waele law but has been improved by adding the time and temperature dependencies. The second model, expressed as a differential equation, has been designed and identified in a original manner by using a phase plane description. While the first model has been exploited to size the components of the injection device and to provide, when possible, online viscosity estimation, the second one has especially been useful for control purpose. Note that if our

study focused on a particular bone cement, Osteopal® V from Heraeus, our conclusions and approach are fully transposable to any other acrylic bone cement.

In parallel with the characterization of the bone cement behavior, several mechatronic systems have been designed within the S-Tronic project. First, a slave device with the minimum number of disposable items sustains several bone cement injections with forces up to 2000 N. An unconventional sheath has also been added in order to strengthen the syringe that is subject to pressure higher than 100 bar but also to propose passive cooling of the bone cement. Results from the rheological study have supported the choice of a temperature control in order to, later, control the viscosity. Therefore, an adequate thermal exchanger, that can be plugged on the injection device, has been designed using thermoelectic modules. To reduce practitioners' exposure to X-Rays while providing them enough information (force feedback) to ensure the safety of the patient, an haptic interface has been designed that renders the cement hardening. A rate control scheme has been implemented for remote control injections. Such a strategy has proven to be adapted to very slow injection flow rates, allowing to render up to 20 N for a 120 bar injection pressure. In practice, the system is stable and a good kinematic correspondence between the master position and the slave speed has been achieved, which provides the operator with a reliable impedance of the environment.

The usage convenience by the medical staff as well as the full clinical compatibility have been kept in mind, but as secondary concern at this research stage. In the context of the operating room, one could imagine that the injection device is installed on an arm fixed at the operating table while the remote control is integrated to the console of the imaging device.

Although their size and the possibility are important advantages, the functioning of Peltier modules is complex. However, the understanding of their functioning allowed us to propose a fine modeling and identification in order to design a satisfactory temperature controller. However the performance has been limited by the power supply that can only deliver a current of 3 A while the chosen Peltier modules can sustain much more. The purchase of a purposely designed power supply that can provide 7 A will allow to increase the actual performance. With an ideal viscosity reference signal that is constant, the proposed viscosity control allows to meet the specifications: increasing notably the initial low viscosity, in order to reduce bone cement leakages, by accelerating the polymerization reaction until an adequate viscosity threshold is reached while lenghtening the injection phase.

## 6.2 Perspectives

### 6.2.1 Transfer perspectives

S-Tronic is basically an innovation transfer project, including the research effort presented in this thesis. As part of this project, a strategic medico-economic study has been conducted by Alcimed. Among the conclusions, some interesting points have been raised. In particular, about the reimbursements, it was emphasized that the French social security offers such a low reimbursement for percutaneous vertebroplasty procedures (less than 200 €), that some doctors assign patients to stay in the hospital for at least one night in order to recover the costs. These reimbursement rates should not change in the coming years, making thus the French market uninteresting for a device as ours. Conversely, reimbursement rates are much more reasonable both in the United States (from 1200€ to 2200€) and Germany (from 4000€ to 5800€). Our device could be interesting for these markets. Moreover, radiologists, neurosurgeons and orthopedic surgeons from France, Germany and America have been surveyed about their interest of such a device. In Germany and in the United States, users are quite satisfied with existing mechanical devices they use, apart from the exposure to X-rays. They could be, however, particularly interested by the potential low pricing of the device developed by our laboratory. Finally,

according to an orthopedic surgeon from the Hospital for Special Surgery in the United States, *cement leakage during vertebroplasty remains an underestimated problem. It is crucial to control its viscosity.*

This thesis has led to the application for two patents. Given this feedback, they be exploited and enhanced in order to bring our device and the associated methods to the adequate market. Problems and needs faced by practitioners are solved thanks to the device proposed in this project. Still, comments from medical professionals also conduct to several future prospects, some of which are exposed hereafter.

### 6.2.2 Evolution of the temperature control module

An interventional radiologist from Klinikum Bogenhausen in Germany believes that our device is too cumbersome into the operating room. Indeed, the complete system should be redesigned to take up much less space inside the operating room while being less heavy. This design has not yet been initiated. However, we have already considered on another crucial problem for the system industrialization: the design of the thermal exchanger presented in Chapter 4 does not meet the standard requirements of an operating room. The fans, blowing dust, and active thermoelectric elements are currently located in the middle of the surgical field which is prohibited closed to the patient. We are currently working on a second temperature control system that is deported from the patient. This second prototype has already been designed, validated by FEM simulations and manufactured. It is based on a circuit with water that flows thanks to a pump (see Figure 6.1 (a)). Stored inside the tank, the water flows first through a temperature regulation device and then to a water/cement temperature exchanger. The temperature regulation system is similar to the first implemented solution based on a pair of Peltier modules placed on a copper block. Water flows inside this copper through a specific circuit in order to increase the heat-exchange surface. The temperature exchanger is a clamp that can be installed anywhere on the cement channel. However, due to the irreversibility of the polymerization reaction, it should again be placed at the outlet of the syringe as in Figure 6.2(a). This clamping device makes the functioning simpler for the physician and would not be a disposable part of the system.



| (a) | (b) | (c) |
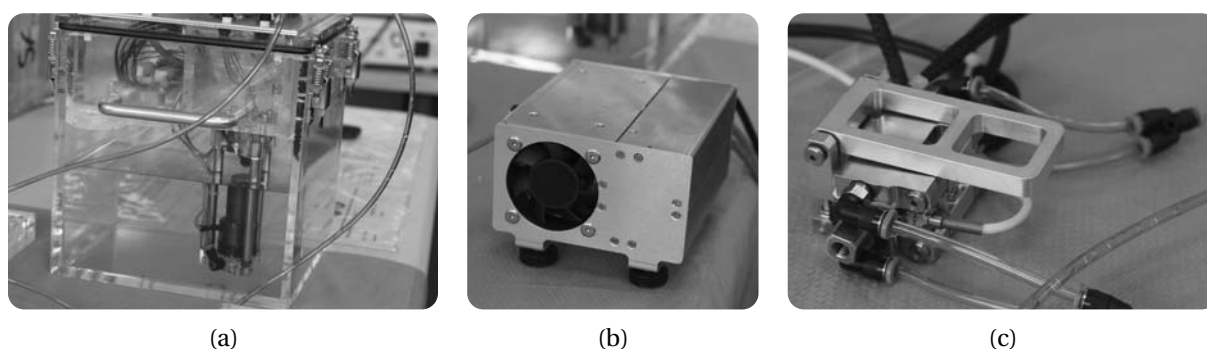
Figure 6.1 – Second prototype for the temperature control: (a) water tank and pump; (b) temperature regulator based on Peltier modules; (c) water/cement thermal exchanger proposed as a clamping device.

Preliminary tests have already been conducted to ensure that the deported system was able to act the bone cement temperature. In a near future, the complete modeling and identification of this second prototype should lead to a new temperature control with better performance, according to the simulations. Still, a delay term, due to the water flow, will have to be considered, as it represents an additional difficulty.

(a)



(b)

Figure 6.2 – CAD views: (a) clamp used as a water/cement thermal exchanger; (b) experimental scenario with the second prototype.

### 6.2.3 Intravertebral pressure

In Chapter 5, the assumption that bone cement flows out of the conduit at atmospheric pressure has been challenged, especially when the cement has been injected into a phantom vertebra including a cancellous insert. In the literature, some studies on cadavers have been carried out in order to picture the intravertebral pressure during a cement injection. Here, thanks to our device and methods, a perspective would be to compute online this intravertebral pressure. On the clamp of the future prototype, a pressure sensor has been installed. The previous online approach to compute viscosity can also lead to the intravertebral pressure $P_{\text{vertebra}}$ for a distance $L_{\text{vertebra}}$ to the vertebra. This sensor is positioned at a known length $L_{\text{sensor}}$ from the outlet of the syringe and on the pipe in which flows the bone cement while bearing $L_{\text{sensor}} \gg R$ as illustrated in figure 6.3.
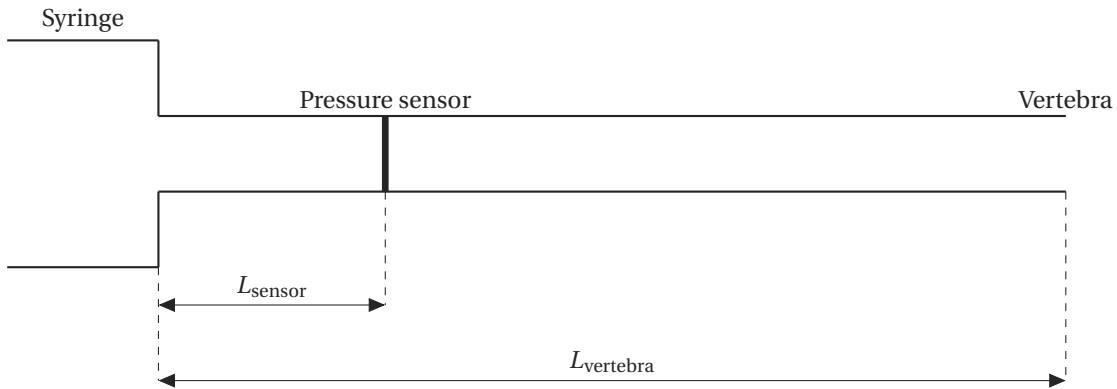


Figure 6.3 – Geometry of the pipe coming out of the syringe and going inside the vertebra.

On both the section of length $L_{\text{sensor}}$ and $L_{\text{vertebra}}$, equation 5.30 could be applied. Assuming that the flow rate is high enough, the cement viscosity at the sensor should be substantially equal to the one at the outlet. Then, knowing that the flow rate is constant in the pipe, the following equality holds:

$$\frac{\Delta P_{\text{sensor}}}{L_{\text{sensor}}} = \frac{\Delta P_{\text{vertebra}}}{L_{\text{vertebra}}} \tag{6.1}$$

where $\Delta P_{\text{sensor}}$ (respectively $\Delta P_{\text{vertebra}}$) represents the pressure drop over $L_{\text{sensor}}$ (respectively $L_{\text{vertebra}}$). Finally, the intravertebral pressure could be accessed as:

$$P_{\text{vertebra}} = \frac{F}{\pi R_s^2}\left(1 - \frac{L_{\text{vertebra}}}{L_{\text{sensor}}}\right) + \frac{L_{\text{vertebra}}}{L_{\text{sensor}}} P_{\text{sensor}}. \tag{6.2}$$

where $F$ is the force applied to the piston and $R_s$ the radius of the syringe.

### 6.2.4 Dielectric measurements

While the ISO 5833-2002 standard recommends the doctor's finger test to checked whether or not the bone cement is ready to be injected [ISO 2002], bone cement manufacturers advise to let the cement stand briefly so that it attains a certain consistency. Both methods are very subjective and Boger *et al.* reported that "time after mixing is not a sufficient measure for determining PMMA viscosity" [Boger 2009] and expressed the urge of developing a solution to compute viscosity during the mixing process. However, usual methods that enable to reach a viscosity value require a controlled flow of the fluid, which is sensitive during the manual or assisted mixing phase.

A collaborative work with the IEF laboratory within S-Tronic project has led to the proof that dielectric measurements reflect the viscosity evolution of bone cement. Hence, based on the idea of interdigitated comb electrodes, an experimental setup has been designed to measure simultaneously dielectric properties and the viscosity of a curing bone cement. As presented in Figure 6.4, it consists in two adapted electronic circuits that have been pasted on the both plates of the dynamic rheometer. While the same experimental protocol than the one for the



Figure 6.4 – Experimental setup for correlating dielectric and rheological properties of curing bone cement.

rheological study (see section 2.3.2.1) enabled to acquire rheological properties, an LCR-meter provided the dielectric properties (capacitance and electric loss angle) of the bone cement. Some preliminary results, given in Figure 6.5, demonstrate that viscosity is correlated with the dielectric properties, particularly the loss angle of the curing cement. Indeed, its decrease is synchronized with the increase in viscosity and once the loss angle becomes constant, the bone cement might be considered as a solid.



(a)

(b)
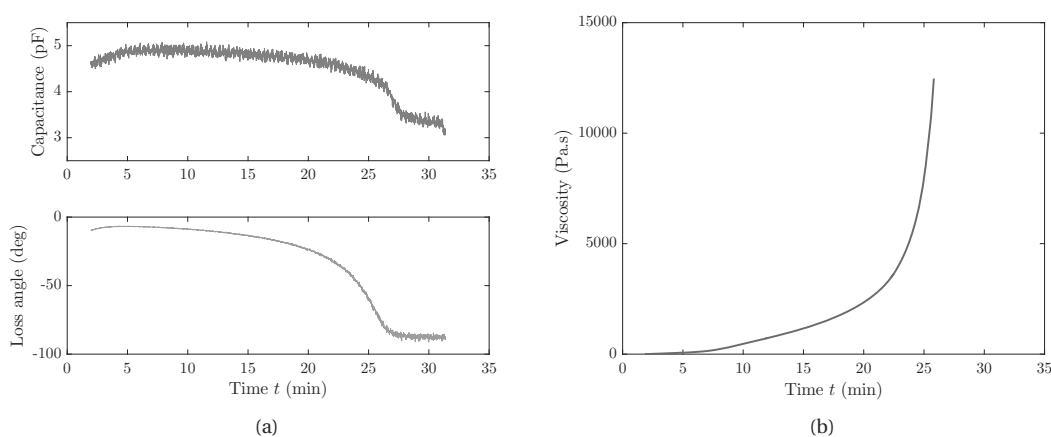
Figure 6.5 – Preliminary results: (a) dielectric properties; (b) viscosity evolution for Osteopal® V bone cement.

Further experiments should be carried out in order to completely understand this correlation. A long study between rheological and electric data could result in a new tool, that could be used during the mixing process, in order to indicate, for instance with an alarm, that a minimum viscosity threshold has been reached. A prototype has already been designed in the form of a spoon as illustrated in Figure 6.6. A similar electronic circuit has been printed on one side of the spatula and a 1 kΩ Negative Temperature Coefficient (NTC) thermistor on the other side.



(a)                      (b)                      (c)
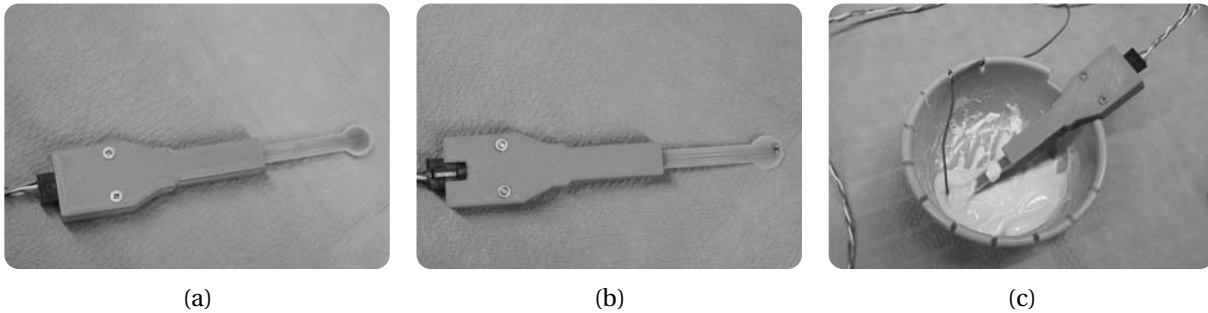
Figure 6.6 – Prototype of a mixing spoon: (a) face to measure dielectric properties; (b) face to measure temperature; (c) realistic mixing scenario.

In addition to provide information during the mixing phase, one could imagine to include a similar sensing system inside syringes, that are disposable items. Indeed, at the end of Chapter 5, it has been concluded that some information are missing in practice for optimal viscosity control, and in particular the cement viscosity value inside the syringe.

# A Hagen-Poiseuille equation

Similar to a capillary rheometer, our injection device is designed such that a piston generates pressure on the bone cement inside the syringe (acting as reservoir) in order to force the cement to flow with a particular speed distribution across a capillary tube of length $L$ and of radius $R$ with $L >> R$ as illustrated in figure A.1. The flow inside the cylindrical tube is identical to a Poiseuille flow.
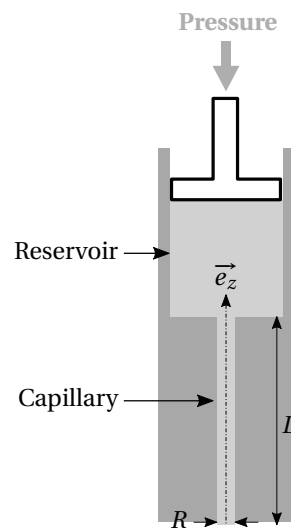


Figure A.1 – Geometry of a Hagen-Poiseuille flow.

A set of assumptions is made:

- the flow is isothermal $\left(\dfrac{\partial}{\partial T} \equiv 0\right)$, axisymmetric $\left(\dfrac{\partial}{\partial \theta} \equiv 0\right)$, stationary $\left(\dfrac{\partial}{\partial t} \equiv 0\right)$, and incompressible (density $\rho$ is constant),
- the no-slip boundary condition is valid which means that the velocity at the wall is zero,
- a pressure gradient is generated in the longitudinal axis $\overrightarrow{e_z}$ which implies liquid layers sliding over each other and thus, velocity, are parallel to $\overrightarrow{e_z}$: $\overrightarrow{V} = V_z(r,z)\overrightarrow{e_z}$,

- the pressure gradient is assumed to be negative when the flow is in the direction of positive $z$.

The symmetric strain rate tensor, defined as $\overline{\overline{\mathbf{D}}} = \dfrac{1}{2}\left(\overline{\overline{\nabla V}} + (\overline{\overline{\nabla V}})^T\right)$, is written in our specific context as follows:

$$\left[\overline{\overline{\mathbf{D}}}\right] = \begin{pmatrix} 0 & 0 & \frac{1}{2}\frac{\partial V_z}{\partial r} \\ 0 & 0 & 0 \\ \frac{1}{2}\frac{\partial V_z}{\partial r} & 0 & \frac{\partial V_z}{\partial z} \end{pmatrix}_{(\vec{e}_r,\vec{e}_\theta,\vec{e}_z)} . \tag{A.1}$$

For a generalized Newtonian flow, the relation between the strain rate tensor and the Cauchy stress tensor is expressed as:

$$\overline{\overline{\sigma}} = -p\overline{\overline{\mathbf{I}}} + 2\eta\overline{\overline{\mathbf{D}}} + \left(\kappa - \frac{2}{3}\eta\right)\vec{\nabla}.\vec{V}\overline{\overline{\mathbf{I}}} \tag{A.2}$$

where:

- $p$ is the applied pressure,

- $\overline{\overline{\mathbf{I}}}$ represents the third-order identity tensor,

- $\eta$ denotes the dynamic viscosity of the fluid,

- $\kappa$ is the bulk viscosity,

- $\dot{\gamma} = \sqrt{2II_{\mathbf{D}}}$ is the magnitude of the strain rate tensor. In the frame of some simple geometries of the flow, $\dot{\gamma}$ designates the shear rate,

- $II_{\mathbf{D}}$, second invariant of $\overline{\overline{\mathbf{D}}}$.

In fluid dynamics, the principle of mass conservation states:

$$\frac{\partial \rho}{\partial t} + \rho\,\vec{\nabla}\cdot\vec{V} = 0 \tag{A.3}$$

Since the assumption is made that the fluid is incompressible, equation (A.3) leads to $\vec{\nabla}\cdot\vec{V} = 0$ which simplifies

- equation (A.2) as:

$$\overline{\overline{\sigma}} = -p\overline{\overline{\mathbf{I}}} + 2\eta(\dot{\gamma})\overline{\overline{\mathbf{D}}} , \tag{A.4}$$

- the last component of $\vec{V}$ as:

$$V_z \equiv V_z(r). \tag{A.5}$$

Considering equation (A.4) and the simplification (A.5), the stress tensor is expressed in the coordinate reference $(\vec{e}_r,\vec{e}_\theta,\vec{e}_z)$ as:

$$\left[\overline{\overline{\sigma}}\right] = \begin{pmatrix} -p & 0 & \eta\frac{\partial V_z}{\partial r} \\ 0 & -p & 0 \\ \eta\frac{\partial V_z}{\partial r} & 0 & -p \end{pmatrix}_{(\vec{e}_r,\vec{e}_\theta,\vec{e}_z)} . \tag{A.6}$$

Governing the motion of fluids, the general Navier-Stokes equation yields:

$$\rho \frac{D\overrightarrow{V}}{Dt} = \overrightarrow{\nabla} \cdot \overline{\overline{\sigma}} + \rho \overrightarrow{g} \tag{A.7}$$

with:

- $\frac{D\overrightarrow{V}}{Dt} = \frac{\partial \overrightarrow{V}}{\partial t} + (\overrightarrow{V} \cdot \overline{\overline{\nabla}})\overrightarrow{V}$, the material derivative of the velocity vector field,
- $\overrightarrow{g}$, the gravitational field.

Given the stationary assumption, we can assess:

$$\frac{\partial \overrightarrow{V}}{\partial t} = \overrightarrow{0} \tag{A.8}$$

Moreover,

$$(\overrightarrow{V} \cdot \overline{\overline{\nabla}})\overrightarrow{V} = V_z \frac{\partial V_z}{\partial z}\overrightarrow{e_z} = \overrightarrow{0} \tag{A.9}$$

Thus, while neglecting gravity, Navier-Stokes equation (equation (A.7)) can be projected in the cylindrical coordinate system and provides:

$$-\frac{\partial p}{\partial r} = 0 \tag{A.10}$$

$$-\frac{1}{r}\frac{\partial p}{\partial \theta} = 0 \tag{A.11}$$

$$-\frac{\partial p}{\partial z} + \frac{1}{r}\frac{\partial r \sigma'_{rz}}{\partial r} = 0 \tag{A.12}$$

where $\overline{\overline{\sigma'}} = 2\eta(\dot{\gamma})\overline{\overline{\mathbf{D}}}$.

From equation (A.12), using the separation of variables, we obtain:

$$\frac{\partial p}{\partial z} = -\frac{\Delta P}{L} \tag{A.13}$$

with $\Delta P = P_{\text{inlet}} - P_{\text{outlet}} > 0$, the pressure drop along the capillary of length $L$.

Then, the integration of equation (A.12) gives:

$$\sigma'_{rz}(r) = -\frac{\Delta P}{L}\frac{r}{2} + \frac{\text{constant}}{r} \tag{A.14}$$

On the symmetry axis, the boundary condition is $\left.\frac{\partial V_z(r)}{\partial r}\right|_{r=0} = 0$, the following relation is achieved:

$$\sigma'_{rz}(r) = -\frac{\Delta P}{L}\frac{r}{2}. \tag{A.15}$$

This relation is valid no matter the behavior law of the dynamic viscosity of the fluid. From here on, the behavior law has to be defined. For bone cement, we can assess that it follows the Ostwald-de Waele law [Ostwald 1925], commonly called Power-law, which is given by :

$$\eta(\dot{\gamma}) = K\dot{\gamma}^{n-1} \tag{A.16}$$

where $K$ represents the consistency in Pa.s$^n$ and $n$ the power law index.

According to equation (A.6), it can be written:

$$\sigma'_{rz} = \eta(\dot{\gamma}) \frac{\partial V_z(r)}{\partial r} \quad \text{with} \quad \dot{\gamma} = -\frac{\partial V_z(r)}{\partial r}. \tag{A.17}$$

From equations (A.16) and (A.17), $\sigma'_{rz}$ is equivalent to:

$$\sigma'_{rz} = -K \left( -\frac{\partial V_z(r)}{\partial r} \right)^n. \tag{A.18}$$

By substituting $\sigma'_{rz}$ with its expression (A.15) and by integrating this last equation, $V_z(r)$ can be computed as:

$$V_z(r) = -\frac{n}{n+1} \left( \frac{\Delta P}{2KL} \right)^{\frac{1}{n}} r^{\frac{n+1}{n}} + \text{constant}. \tag{A.19}$$

Taking into account the no-slip boundary condition, we obtain:

$$V_z(r) = \frac{n}{n+1} \left( \frac{\Delta P}{2KL} \right)^{\frac{1}{n}} \left( R^{\frac{n+1}{n}} - r^{\frac{n+1}{n}} \right). \tag{A.20}$$

Finally, we can compute flow rate $Q$ and shear rate at the wall $\dot{\gamma}_p$:

$$Q = \int_0^R V_z(r) 2\pi r dr = \left( \frac{\Delta P}{L} \right)^{\frac{1}{n}} \left( \frac{R}{2K} \right)^{\frac{1}{n}} \left( \frac{\pi n R^3}{3n+1} \right) \tag{A.21}$$

$$\dot{\gamma}_p = -\frac{\partial V_z(r)}{\partial r} \bigg|_{r=R} = \frac{Q}{\pi R^3} \frac{3n+1}{n}. \tag{A.22}$$

For comparison, for a Newtonian-fluid (i.e. $\eta = \eta_0$), $V_z$, $Q$ and $\dot{\gamma}_p$ are expressed as follows:

$$V_z(r) = \frac{\Delta P}{4\eta_0 L} \left( R^2 - r^2 \right) \tag{A.23}$$

$$Q = \frac{\Delta P \pi R^4}{8\eta_0 L} \tag{A.24}$$

$$\dot{\gamma}_p = \frac{4Q}{\pi R^3}. \tag{A.25}$$

The relationship between flow rate $Q$ and pressure drop $\Delta P$ in (A.21) is called Hagen-Poiseuille equation.

# B Transient convective heat transfer

This appendix aims to present the analytic solution of the transient heat conduction of an infinite cylinder of radius $R$. This problem is axisymmetric and $T(r,t)$ represents the temperature at time $t$ and at a radius $r$ from the centerline. The heat equation yields:

$$\rho c \frac{\partial T}{\partial t} = \lambda \vec{\nabla} \cdot \left( \vec{\nabla} T \right) \tag{B.1}$$

where $\rho$, $c$ and $\lambda$ are the density, the specific heat capacity and the thermal conductivity, respectively. The considered material is not flowing and no terms of heat creation have been added. The initial temperature is such that:

$$T(r,0) = T_{\text{init}} \tag{B.2}$$

At time $t > 0$, the sample is subjected to free convection, with a heat transfer coefficient $h$, with the surrounding environment at $T_\infty$, which writes:

$$-\lambda \frac{\partial T}{\partial r}|_{r=R_c} = h(T - T_\infty) \tag{B.3}$$

Using advanced mathematical methods, the general solution of the transient homogeneous heat conduction can be written in the form of an infinite series as:

$$\frac{T(r,t) - T_\infty}{T_{\text{init}} - T_\infty} = \sum_{j=1}^{\infty} B_j \exp\left(-\omega_j^2 F_0\right) J_0\left(\omega_j \frac{r}{R_c}\right) \tag{B.4}$$

where:

- $B_j = \dfrac{2}{\omega_j} \cdot \dfrac{J_1\left(\omega_j\right)}{J_0^2\left(\omega_j\right) + J_1^2\left(\omega_j\right)}$

- $J_0$ and $J_1$ are the Bessel functions of the first kind, defined as:

$$J_i(x) = \sum_{p=0}^{\infty} \frac{(-1)^p}{p!(n+p)!} \left(\frac{x}{2}\right)^2 p + n \ , \tag{B.5}$$

- $F_0$ is the Fourier number with $F_0 = \dfrac{\alpha t}{R_c^2} = \dfrac{\lambda t}{\rho c R_c^2}$,

- $\omega_j$ are the eigen values of $\omega_j J_1(\omega_j) = Bi J_0(\omega_j)$,

- $Bi$ is the Biot number such that $Bi = \dfrac{h R_c}{2\lambda}$,

Hence, since $J_0(0) = 1$ at the centerline, *i.e.* for $r = 0$, equation (B.4) becomes:

$$\frac{T(0, t) - T_\infty}{T_{\text{init}} - T_\infty} = \sum_{j=1}^{\infty} B_j \exp\left(-\omega_j^2 F_0\right) \tag{B.6}$$

# C Numerical resolution of the heat equation

This appendix explains the method that has been implemented to solve the three-dimensional heat equation for a bone cylinder of length $L$ and of radius $R$. This heat equation becomes then a two-dimensional problem thanks to the axisymmetric problem as represented in Figure C.1.

.
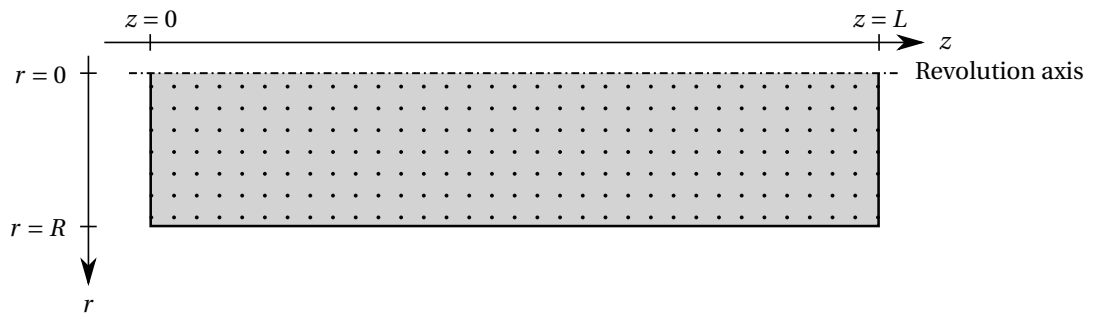


Figure C.1 – Two-dimensional geometry of flowing bone cement where $z = 0$ represents the inlet and $z = L$ the outlet.

A set of assumptions is made:

- the flowing bone cement is considered as a generalized Newtonian fluid,
- the density $\rho$, the specific heat capacity $c$ and the thermal conductivity $\lambda$ are supposed constant,
- the velocity profile does not depend on temperature.

For flowing bone cement, the heat equation writes [Kolmeder 2011]:

$$\rho c \left( \frac{\partial T}{\partial t} + \vec{V} \cdot \vec{\nabla} T \right) = \lambda \Delta T + \rho \Delta h(T) \frac{\partial q}{\partial t} + \eta \dot{\gamma}^2 \tag{C.1}$$

where $q$ represents the degree of cure and can be expressed as:

$$\frac{\partial q}{dt} = (K_1 + K_2 q^\alpha)(1-q)^\beta f_D(q, T) . \tag{C.2}$$

.

According to equation (A.20) in Appendix A, the velocity profile of the bone cement can be explicited as:

$$V_z(r) = \frac{n}{n+1} \left( \frac{\Delta P}{2KL} \right)^{\frac{1}{n}} \left( R^{\frac{n+1}{n}} - r^{\frac{n+1}{n}} \right). \tag{C.3}$$

The bone cement is initially at temperature $T_{\text{init}}$, which means that, at time $t = 0$:

$$\forall r, \forall z, T = T_{\text{init}}. \tag{C.4}$$

As boundary conditions, it has been considered that:

- the geometry is axisymmetric as:

$$\forall z, \left. \frac{\partial T}{\partial r} \right|_{r=0} = 0 \tag{C.5}$$

- the bone cement temperature at the inlet is $T_{\text{in}}$:

$$\forall r, \left. T \right|_{z=0} = T_{\text{in}} \tag{C.6}$$

- the bone cement is free at the outlet:

$$\forall r, \left. \frac{\partial T}{\partial z} \right|_{z=L} = 0 \tag{C.7}$$

- for the lateral face of the cylinder, either

  - the temperature is set at $T_{\text{imp}}$:

$$\forall z, \left. T \right|_{r=R} = T_{\text{imp}} \tag{C.8}$$

  - there is free convection with the environment at $T_\infty$ with a convection coefficient $h$ such that:

$$\lambda \left. \frac{\partial T}{\partial r} \right|_{r=R} = h \left( T_{r=R} - T_\infty \right) \tag{C.9}$$

  - a thermal flux $Q_{th}$ is imposed:

$$\lambda \left. \frac{\partial T}{\partial r} \right|_{r=R} = Q_{th} \tag{C.10}$$

From now on, note that $T_{i,j}^n$ refers to the temperature at time $t_n$, at $r = r_i$ from the centerline and at $z = z_j$ from

the inlet:

$$T_{i,j}^n = T\left(r_i, z_j, t_n\right) \tag{C.11}$$

Based on the finite-difference methods, a space discretization has been performed such that:

$$\left(\frac{\partial T}{\partial r}\right)_{i,j}^n \simeq \frac{T_{i+1,j}^n - T_{i-1,j}^n}{2\Delta r} \tag{C.12}$$

$$\left(\frac{\partial^2 T}{\partial^2 r}\right)_{i,j}^n \simeq \frac{T_{i+1,j}^n - 2T_{i,j}^n + T_{i-1,j}^n}{\Delta r^2} \tag{C.13}$$

$$\left(\frac{\partial T}{\partial z}\right)_{i,j}^n \simeq \frac{T_{i,j+1}^n - T_{i,j-1}^n}{2\Delta z} \tag{C.14}$$

$$\left(\frac{\partial^2 T}{\partial^2 z}\right)_{i,j}^n \simeq \frac{T_{i,j+1}^n - 2T_{i,j}^n + T_{i,j-1}^n}{\Delta z^2} \tag{C.15}$$

After that this spatial finite difference discretization has been achieved, the discretized heat equation can be written as a system of Ordinary Differential Equations (ODE) as:

$$M\begin{bmatrix} \dot{\mathbf{T}} \\ \dot{q} \end{bmatrix} = A\begin{bmatrix} \mathbf{T} \\ q \end{bmatrix} + B \tag{C.16}$$

where $M$ is a mass matrix and $\mathbf{T}$ is the vector that concatenates all temperatures $T_{i,j}$. $A$ is a five-diagonal matrix.

Thanks to the function *ode45* from MATLAB [MathWorks 2016], this system is numerically solved and the evolution of each temperature $T_{i,j}$ can be plotted.

# D Résumé en français

## D.1 Contexte médical

La vertébroplastie percutanée est une intervention non chirurgicale et peu invasive qui consiste à injecter, sous contrôle radioscopique, un ciment orthopédique (PMMA) dans le corps vertébral. Cette technique permet de stabiliser les vertèbres et de réduire les douleurs sévères chez les personnes souffrant principalement d'ostéoporose, mais aussi de métastases ou de fractures traumatiques. Cette approche est particulièrement efficace, puisqu'elle permet de stabiliser la vertèbre fracturée de manière durable. De plus, une amélioration immédiate de la douleur chez les patients et leur lever précoce sont observés.

Malgré son efficacité, cette méthode présente quelques inconvénients non négligeables. Le premier tient au ciment orthopédique, qui est injecté pendant sa phase de polymérisation. Tout d'abord, la faible viscosité du ciment au début de l'injection augmente considérablement le risque de fuite en dehors de la vertèbre traitée, ce qui provoque potentiellement des complications sévères. La prise rapide du ciment limite par ailleurs la durée d'injection à huit à dix minutes maximum, selon le modèle de ciment. Le second inconvénient est lié au contrôle par fluoroscopie à rayons X, qui expose le praticien de manière prolongée.

Pour pallier ces inconvénients, les enjeux de ce travail de thèse étaient :

- la caractérisation du comportement rhéologique du ciment,

- la maîtrise des paramètres influençant sa viscosité, et

- le développement d'un système robotisé télé-opéré avec un retour d'effort.

Actuellement, les systèmes d'injection manuels sont très nombreux sur le marché mais ne répondent aucunement à la problématique de l'exposition des radiologues aux rayons X. Les systèmes télé-opérés sont quant à eux très rares, et à notre connaissance, soit ils n'offrent pas de retour d'effort, soit ils n'éloignent pas le praticien de la source des rayons X. Dans le travail présenté, le développement d'un système d'*injection robotisée de ciment orthopédique* permet la radioprotection des praticiens, une réduction des risques de fuite et une durée d'injection plus longue.

## D.2    Rhéologie des ciments orthopédiques

La viscosité est une propriété rhéologique qui décrit la résistance à l'écoulement du matériau. Afin de mieux comprendre le comportement du ciment et l'évolution de sa viscosité au cours du temps et en fonction son environnement, une étude rhéologique a été menée. Le comportement du ciment orthopédique est régi par un processus complexe puisqu'il subit une réaction de polymérisation exothermique.  En plus des aspects mécanique et temporel, le ciment présente une dépendance en température non négligeable qui doit également être caractérisée. Ces trois principales dépendances sont illustrées dans la figure D.1.
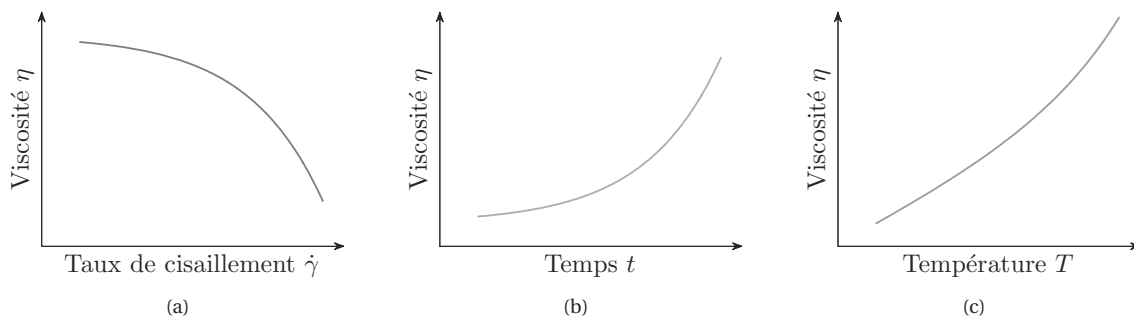


Figure D.1 – Viscosité du ciment orthopédique en fonction : (a) du taux de cisaillement $\dot{\gamma}$ (fluide rhéofluidifiant); (b) du temps $t$ (fluide rhéopectique); (c) de la température $T$ (fluide thermo-dépendant).

Les deux grandes catégories de rhéomètres pour une telle étude sont le rhéomètre capillaire qui utilise un écoulement de Poiseuille à travers un capillaire, et le rhéomètre dynamique, qui quantifie la viscosité en mesurant la déformation de la matière soumise à une sollicitation harmonique. L'important volume de ciment nécessaire lors des essais en rhéométrie capillaire rend une régulation thermique très complexe et peu efficace. Ainsi, l'étude du comportement du ciment acrylique a été menée sur un rhéomètre dynamique (voir figure D.2).



Figure D.2 – Rhéomètre dynamique HAAKE[TM] MARS[TM] de ThermoFisher Scientific : (a) ensemble du dispositif; (b) zoom sur la zone d'intérêt pendant les expériences.

Un tel rhéomètre possède un plateau fixe sur lequel est disposé l'échantillon de ciment à tester, et un plateau oscillant.  Une déformation sinusoïdale est appliquée au ciment et le couple résultant de la déformation est mesuré. Il est aussi sinusoïdal mais déphasé. La consigne et la mesure permettent de remonter à la viscosité complexe, puis l'application de la relation empirique de Cox-Merz permet d'obtenir une mesure de viscosité.

Afin de dissocier les divers paramètres influençant la viscosité du ciment, deux jeux d'essais ont été menés. Le premier ensemble d'expériences a été réalisé en maintenant le ciment à température constante $T_0$ mais en faisant varier le taux de cisaillement $\dot{\gamma}$ d'un essai à l'autre. L'exercice inverse a été exécuté pour la seconde vague de manipulations. Les résultats de ces expériences sont donnés dans les figures D.3 et D.4. Comme prévu, les courbes de la figure D.3 montrent que plus le ciment est froid, plus le temps de prise de ce dernier est long. Ces observations prouvent que le temps de prise peut être augmenté en ajustant la température. En ce qui concerne la figure D.4, nous pouvons facilement remarquer que plus le taux de cisaillement est élevé, plus la viscosité est faible. Ceci confirme le comportement rhéofluidifiant du ciment acrylique. De plus, la fin de la réaction de polymérisation semble être similaire pour toutes les fréquences à une température donnée. Il semble donc difficile d'augmenter la durée d'injection au-delà d'une certaine période.

Tandis que l'étude complète a seulement été conduite sur le ciment Osteopal® V, généreusement fourni par Heraeus, l'approche et les résultats sont entièrement transposables à d'autres ciments osseux. Ces tendances ont notamment été confirmées pour deux autres ciments osseux d'Optimed.

Au vu de ces expériences, la viscosité peut être ajustée de manière contrôlée en agissant soit sur la température du ciment osseux, soit sur son taux de cisaillement pendant l'injection. En augmentant le taux de cisaillement, c'est-à-dire la vitesse d'injection du ciment, sa viscosité diminue. Or, le praticien doit le contrôle de la vitesse d'injection du ciment. Ainsi, dans le cadre de l'application, il n'est pas possible de réguler la viscosité par le biais d'un contrôle du taux de cisaillement. Pour cette raison, nous avons choisi de contrôler la température du ciment afin de répondre à la fois à la réduction du risque de fuite et à l'augmentation du temps d'injection. Cette régulation peut être obtenue en modulant l'amplitude thermique du ciment de façon minime, ce qui est recommandé pour minimiser l'impact de la régulation de viscosité sur les tissus environnants. Ce contrôle reste difficile car le fluide considéré est en écoulement et subit une réaction de polymérisation exothermique.
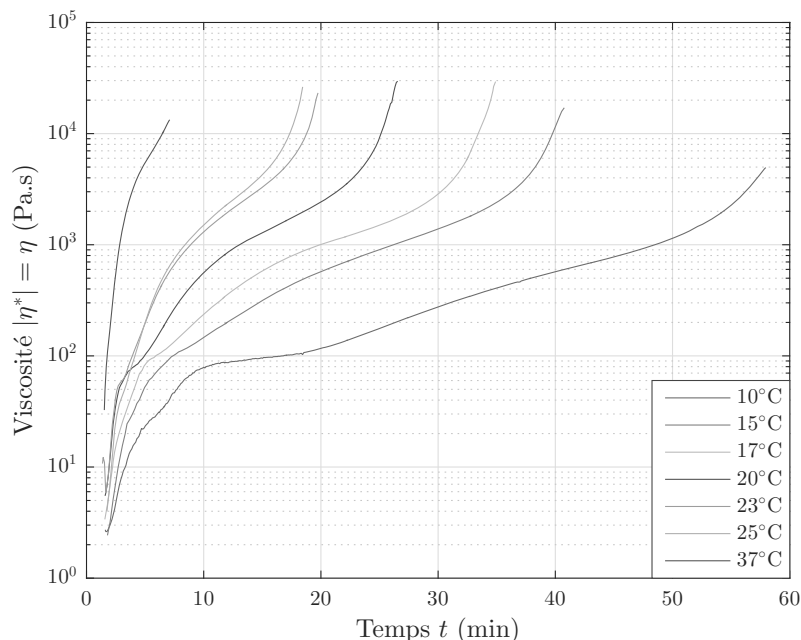


Figure D.3 – Evolution de la viscosité au cours du temps à $\dot{\gamma} = 2\pi$ s$^{-1}$ pour une plage de température allant de 10 °C à 37 °C pour l'Osteopal® V (Heraeus).
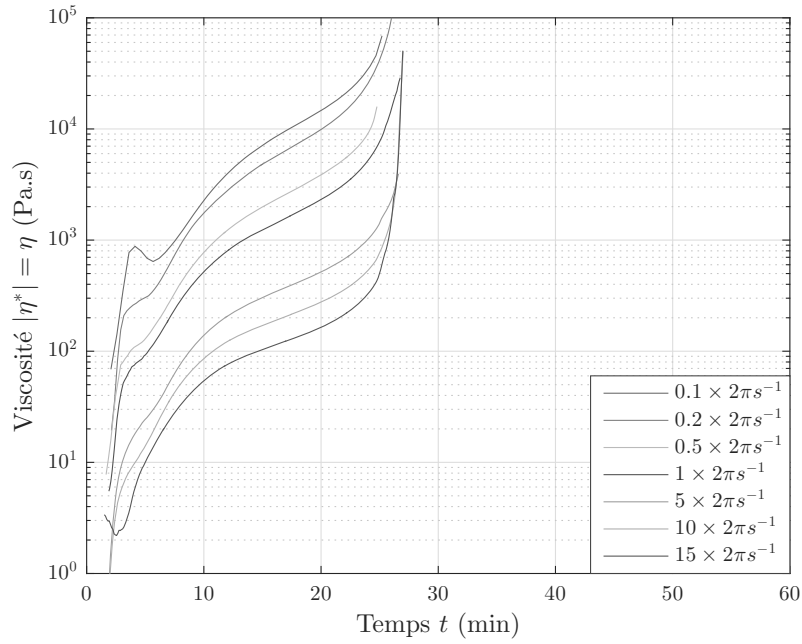
(a)
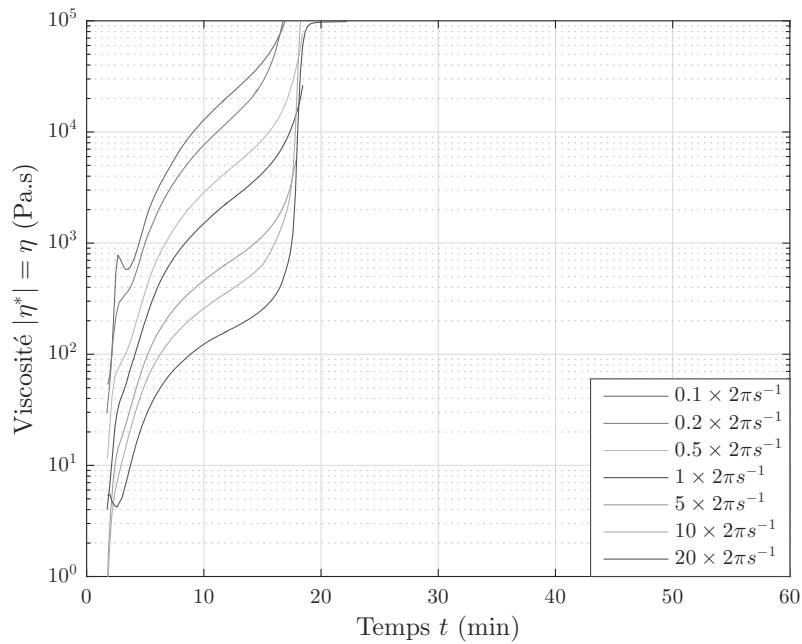


(b)

Figure D.4 – Evolution de la viscosité au cours du temps à partir du mélange pour différents taux de cisaillement pour l'Osteopal® V (Heraeus) : (a) à $T_0 = 20\,°C$; (b) à $T_0 = 25\,°C$.

## D.3 Modélisation et identification de la viscosité du ciment orthopédique

L'étude rhéologique qui a été présentée précédemment a mis en évidence comment les ciments acryliques se comportent en fonction de certains paramètres extrinsèques pendant leur phase de polymérisation. Cependant, pour atteindre nos objectifs, entre autres le contrôle de la viscosité du ciment osseux lors de son injection, un modèle est nécessaire. Les expériences menées fournissent suffisamment de données pour identifier deux modèles: un modèle algébrique commun en rhéologie et un autre modèle exprimé sous forme d'une équation différentielle non linéaire afin de développer une stratégie de contrôle de la viscosité.

### D.3.1 Loi puissance modifiée

#### D.3.1.1 Contributions

Comme le considèrent de nombreux auteurs dans la littérature, le comportement du ciment orthopédique peut être décrit par la loi de puissance déjà définie par :

$$\eta(\dot{\gamma}) = K\dot{\gamma}^{n-1} \,. \tag{D.1}$$

Avec $n < 1$, l'équation (D.1) décrit le comportement rhéofluidifiant du ciment. Cependant, cette qualification n'est pas suffisante puisque ce fluide est également fortement dépendant du temps et de la température. Ainsi, une contribution de cette partie est l'identification des paramètres $n$ et $K$ de la loi puissance à chaque instant $t$ afin de les définir comme des fonctions mathématiques dépendantes du temps. Enfin, inspirée par le principe de superposition temps-température, l'influence de la température sera prise en compte par deux facteurs de translation qui seront identifiés.

#### D.3.1.2 Identification

En appliquant la fonction logarithmique aux deux termes de l'équation (D.1), la loi de puissance peut aussi s'écrire:

$$\log(\eta) = \log(K) + (n-1)\log(\dot{\gamma}) \tag{D.2}$$

Pour l'ensemble de nos données obtenues sur le rhéomètre dynamique, $\log(\eta)$ peut être tracé en fonction de $\log(\dot{\gamma})$ à plusieurs instants $t$ différents comme dans la figure. La linéarité des courbes présentées valide l'utilisation de la loi puissance, u moins dans cette plage de taux de cisaillement. Au vu de l'équation (D.2), une régression linéaire entre $\log(\eta)$ et $\log(\dot{\gamma})$ permet d'estime les paramètres $n$ et $K$ puisque la pente détermine $n-1$ et l'ordonnée à l'origine donne $\log(K)$. En répétant cette optimisation à différents instants, les paramètres $n$ et $K$ ont pu être tracé en fonction du temps dans les figures D.6(a) et D.6(b). Nous pouvons remarquer que les courbes représentant $n$ et $K$ rappellent des fonctions mathématiques simples. Plusieurs identifications de fonctions ont été réalisées. Étant donné les coefficients de détermination obtenus, la droite est préférée pour modéliser l'évolution de $n$. Pour paramétrer $K$, la somme de deux fonctions exponentielles donne les meilleurs résultats. Ainsi, la loi de puissance exprimée dans l'équation (D.1) peut être améliorée comme suit:

$$\eta(t, \dot{\gamma}, T) = K(t)\dot{\gamma}^{n(t)-1}. \tag{D.3}$$

avec $K(t) = \big(a_K \exp(b_K t) + c_K \exp(d_K t)\big)$ et $n(t) = a_n t + b_n$.

(a)

(b)
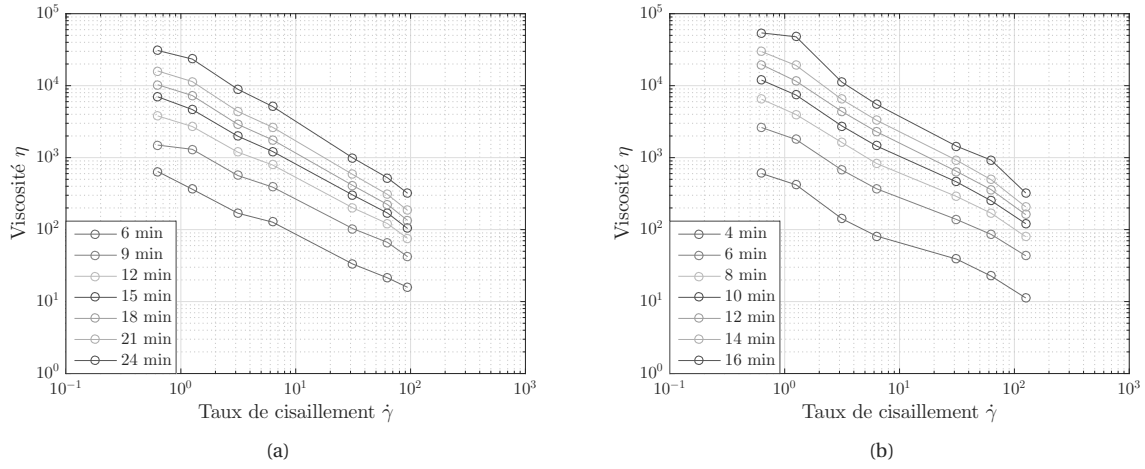
Figure D.5 – Courbes de viscosité représentées sur une échelle logarithmique : (a) à $T_0 = 20\,°\text{C}$; (b) à $T_0 = 25\,°\text{C}$.



(a)

(b)
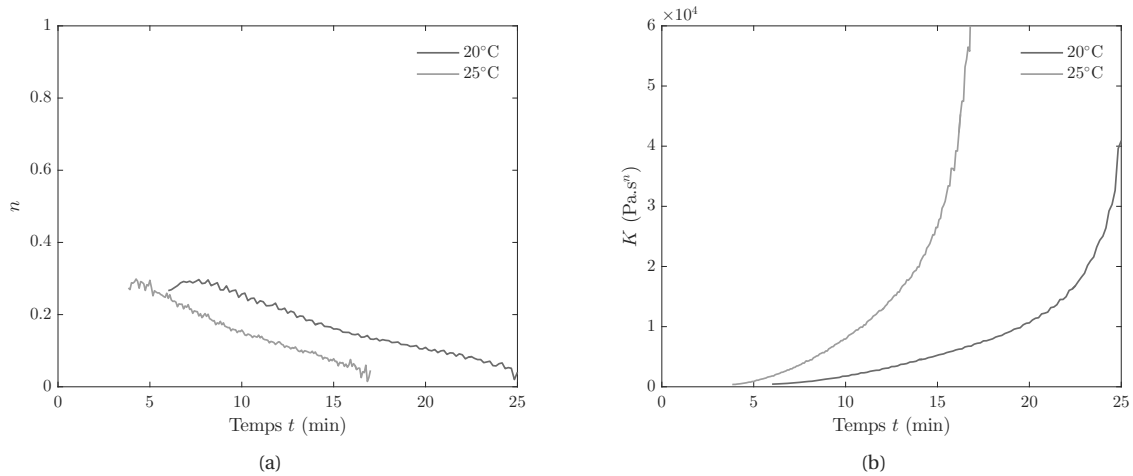
Figure D.6 – Identification des paramètres $n$ et $K$ de la loi puissance en fonction du temps à $T_0 = 20\,°\text{C}$ (courbe bleue) et à $T_0 = 25\,°\text{C}$ (courbe verte).

Jusqu'ici, ce modèle n'intègre pas l'influence de la température. En examinant les données acquises sur le rhéomètre dynamique, il semble qu'un double facteur de translation se dresse. Cela signifie que pour un changement de température de $T_{\text{ref}}$ à $T$ à un taux de cisaillement donné, non seulement l'échelle de temps est ajustée, mais aussi la viscosité est décalée par un facteur de translation vertical. En d'autres termes,

$$\eta\left(a_{T_{\text{ref}}\to T}\,t, T, \dot{\gamma}\right) = b_{T_{\text{ref}}\to T}\,\eta\left(t, T_{\text{ref}}, \dot{\gamma}\right) \tag{D.4}$$

Grâce à une identification précise, ces facteurs de translation ont pu être assimilés à une loi d'Arrhenius telle que:

$$a_{T_{\text{ref}}\to T} = \exp\left(\frac{-E_a}{R_{\text{gas}}}\left(\frac{1}{T_{\text{ref}}} - \frac{1}{T}\right)\right) \quad \text{et} \quad b_{T_{\text{ref}}\to T} = \exp\left(\frac{-E_b}{R_{\text{gas}}}\left(\frac{1}{T} - \frac{1}{T_{\text{ref}}}\right)\right). \tag{D.5}$$

Une phase de validation montre que ce modèle est une représentation précise du comportement du ciment au

cours de sa polymérisation.

## D.3.2 Equation différentielle

### D.3.2.1 Choix du modèle

Comme déjà souligné dans la littérature et observé lors de notre étude rhéologique, la viscosité du ciment orthopédique a un comportement fortement non linéaire. Afin de mieux le visualiser, une représentation différente a été proposée en affichant nos données dans le plan de phase.

En se concentrant sur la zone d'intérêt du praticien, le modèle défini pour décrire au mieux le comportement du ciment est le suivant :

$$\dot{\eta} = a(\dot{\gamma}, T)\eta^{\alpha} + b(\dot{\gamma}, T)\eta^{\beta} \tag{D.6}$$

où $\alpha$, $\beta$, $a$ et $b$ sont les paramètres à estimer.

### D.3.2.2 Identification

L'identification du modèle dans le plan de phase exploite le fait que les dépendances en température et en taux de cisaillement pour les paramètres $a$ et $b$ peuvent être découplées. Par conséquent, la méthode d'identification proposée est divisée en trois étapes distinctes: l'identification des paramètres $\alpha$ et $\beta$, l'identification de l'influence de la température sur $a$ et $b$ en fixant le taux de cisaillement et, finalement, l'identification de l'effet du taux de cisaillement.

Pour la première partie, nous supposons que $\alpha$ et $\beta$ sont des paramètres constants. Afin de déterminer ces paramètres, une courbe unique a été identifiée de telle sorte qu'elle approxime au mieux toutes les courbes où la température change. Sur la base des six courbes obtenues à des températures allant de $10\,°C$ à $25\,°C$, la solution du problème des moindres carrés non linéaires donne $\alpha = 0.44$ et $\beta = 3.65$ où un algorithme de Levenberg-Marquardt a été appliqué.

Afin d'identifier l'influence de la température sur l'évolution de la viscosité, un problème non linéaire d'ajustement de courbes au sens des moindres carrés a été résolu. En fait, chaque courbe a été ajustée indépendamment à l'équation $\dot{\eta} = a\eta^{0.44} + b\eta^{3.65}$ en résolvant un problème d'optimisation. La représentation graphique où les résultats $a_i$ et $b_i$ du problème précédent sont tracés en fonction $\frac{1}{R_{\text{gas}}T}$ révèle que les paramètres $a$ et $b$ suivent également une loi d'Arrhenius et peuvent être formulés comme suit :

$$a = K_{\alpha}\exp\left(\frac{-E_{\alpha}}{R_{\text{gas}}T}\right) \ \text{ and } \ b = K_{\beta}\exp\left(\frac{E_{\beta}}{R_{\text{gas}}T}\right). \tag{D.7}$$

Ainsi, le modèle proposé par l'équation (D.6) peut être amélioré par :

$$\dot{\eta} = K_{\alpha}(\dot{\gamma})\exp\left(\frac{-E_{\alpha}}{R_{\text{gas}}T}\right)\eta^{\alpha} + K_{\beta}(\dot{\gamma})\exp\left(\frac{E_{\beta}}{R_{\text{gas}}T}\right)\eta^{\beta} \tag{D.8}$$

Dans cette partie, seuls $K_{\alpha}(\dot{\gamma} = 2\pi\,\text{s}^{-1}) = K_{\alpha}$ et $K_{\beta}(\dot{\gamma} = 2\pi\,\text{s}^{-1}) = K_{\beta}$ ont été déterminés puisque cette étape d'identification a été basée sur l'ensemble des données acquises à un taux de cisaillement fixe $\dot{\gamma} = 2\pi\,\text{s}^{-1}$.

Il ne reste plus qu'à déterminer la dépendance en taux de cisaillement pour les paramètres $K_{\alpha}$ et $K_{\beta}$. En

calculant la différence de deux courbes avec deux taux de cisaillement différents à la même température en échelle logarithmique, nous obtenons une fonction linéaire du temps. Pour deux taux de cisaillement différents $\dot{\gamma}_1$ et $\dot{\gamma}_2$, cela permet de formuler que:

$$\ln(\eta(\dot{\gamma}_2)) = c_{\dot{\gamma}_1 \to \dot{\gamma}_2} t + d_{\dot{\gamma}_1 \to \dot{\gamma}_2} + \ln(\eta(\dot{\gamma}_1)) \ . \tag{D.9}$$

A partir de cette observation et en choisissant le taux de cisaillement de référence $\dot{\gamma}_{\text{ref}} = 2\pi \, \text{s}^{-1}$, l'équation différentielle finale se met sous la forme suivante :

$$\dot{\eta} = c_{\dot{\gamma}_{\text{ref}} \to \dot{\gamma}} \eta + K_\alpha \exp\left(\frac{-E_\alpha}{R_{\text{gas}} T}\right) \exp(c_{\dot{\gamma}_{\text{ref}} \to \dot{\gamma}} t + d_{\dot{\gamma}_{\text{ref}} \to \dot{\gamma}})^{1-\alpha} \eta^\alpha + K_\beta \exp\left(\frac{E_\beta}{R_{\text{gas}} T}\right) \exp(c_{\dot{\gamma}_{\text{ref}} \to \dot{\gamma}} t + d_{\dot{\gamma}_{\text{ref}} \to \dot{\gamma}})^{1-\beta} \eta^\beta \tag{D.10}$$

où $c_{\dot{\gamma}_{\text{ref}} \to \dot{\gamma}}$ et $d_{\dot{\gamma}_{\text{ref}} \to \dot{\gamma}}$ ont été identifiés comme des fonctions linéaires dépendantes du taux de cisaillement.

Là encore, ce second modèle a été validé. Pour cela, l'évolution de la viscosité du ciment résultant de la résolution de l'équation différentielle (D.10) a été comparée aux données acquises sur le rhéomètre dynamique.

## D.4 Robot S-Tronic pour une injection de ciment télé-opérée

Dans notre contexte médical, le but est de proposer au praticien un dispositif permettant d'injecter du ciment en contrôlant sa viscosité tout en protégeant le personnel des rayons X.

### D.4.1 Dispositif esclave

Au vu de la nature complexe des ciments orthopédiques, un dispositif d'injection spécifique a été développé afin de fournir un système fiable et des conditions d'utilisation réalistes. Pour notre étude, il était impératif de concevoir un dispositif capable d'injecter des ciments ayant une haute viscosité, mais aussi de mesurer tous les paramètres d'injection pour un meilleur contrôle de la viscosité.

Le dispositif d'injection s'inspire d'un pousse-seringue dont la conception est illustrée à la figure D.7. Grâce à



Figure D.7 – Vue CAO du système d'injection.
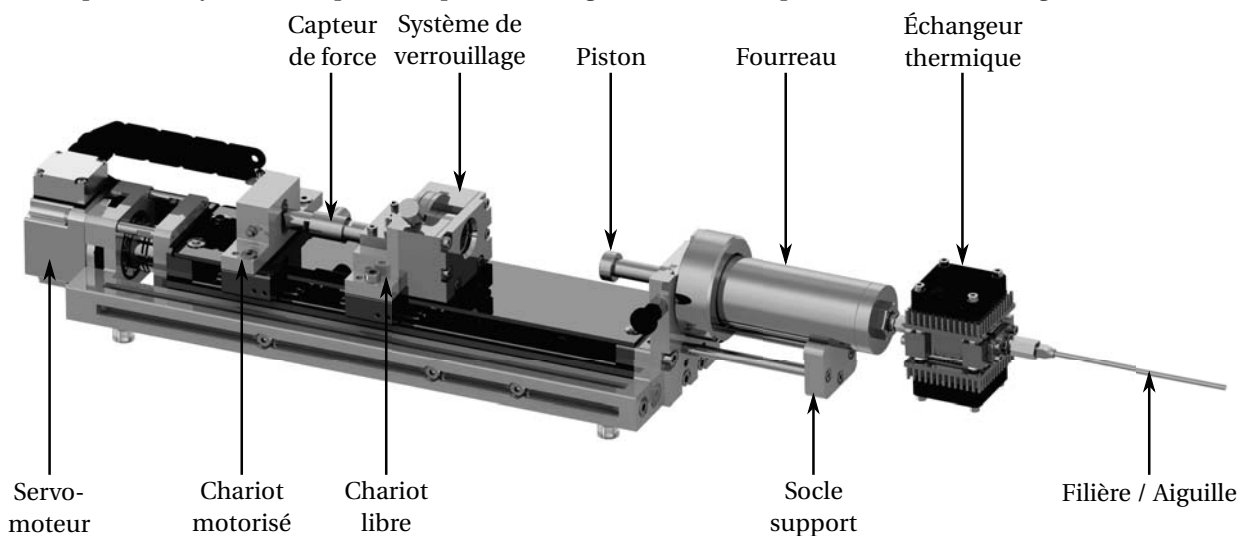
une vis sans fin, la rotation du moteur permet la translation d'un piston coulissant dans une seringue remplie

de ciment, et ceci à des pressions allant jusqu'à 120 bars. La partie mobile est composée de deux chariots sur le même axe, le premier étant lié à la vis, le second étant libre en translation et simplement guidé. Ces deux chariots sont reliés entre eux par l'intermédiaire d'un capteur de force mesurant la force linéaire qui traverse l'ensemble. Un dispositif manuel de serrage est placé sur le chariot libre pour saisir le piston coulissant dans la seringue. La seringue elle-même est située à l'intérieur d'un fourreau en acier inoxydable, doté d'une résistance mécanique élevée.

## D.4.2  Dispositif maître

L'un des objectifs du système est de maintenir le praticien à une distance suffisante des rayons X tout en fournissant suffisamment d'informations sur l'injection pour assurer la sécurité du patient. Par conséquent, une interface haptique a été conçue dans le but de restituer à l'utilisateur une force représentant le durcissement du ciment au praticien. L'interface est construite autour d'un système poulie-cabestan, avec une transmission par câble, comme illustré à la figure D.8.
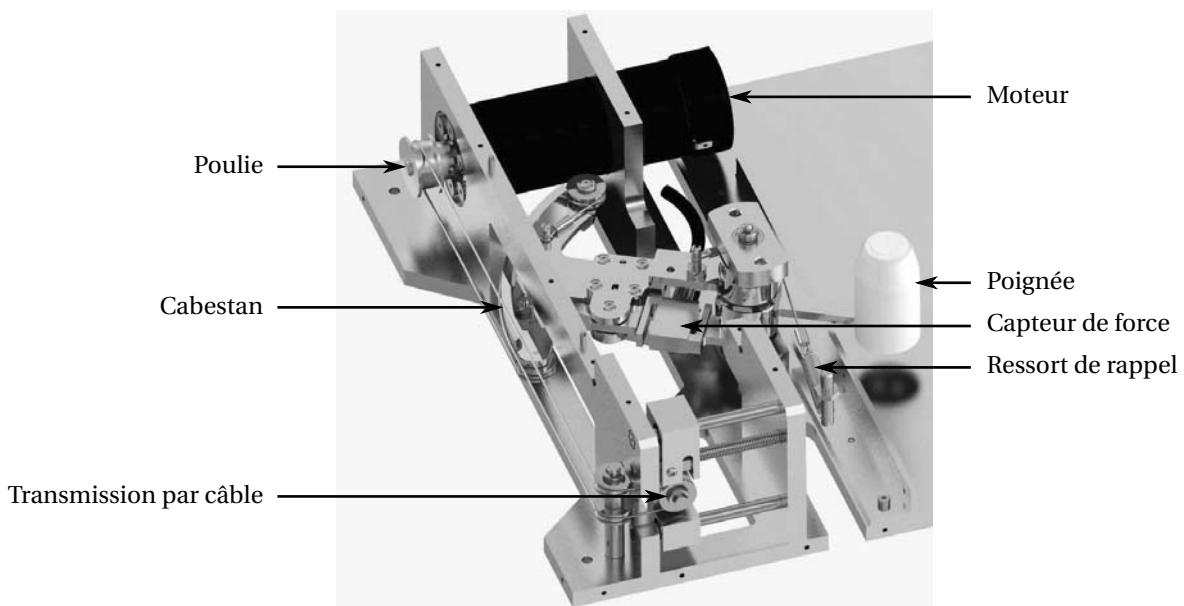


Figure D.8 – Rendue réaliste du mécanisme du dispositif maître.

Contrairement aux schémas classiques de télé-opération, la stratégie implémentée est ici celle dite de *rate control*. La position de l'interface maître impose la vitesse d'injection alors que la force mesurée sur le dispositif esclave est renvoyée sur la poignée tenue par l'utilisateur. Une telle stratégie était incontournable puisque la plage de rotation de l'interface est seulement d'un radian alors que la vitesse d'injection est particulièrement faible et la durée d'injection longue. Cette stratégie étant implémentée, la transparence et la correspondance cinématique ont pu être vérifiées expérimentalement, notamment lors d'essais réalisés dans le service de radiologie interventionnelle au Nouvel Hôpital Civil de Strasbourg.

## D.4.3  Bloc de régulation thermique

La dernière contribution de notre travail porte sur la gestion de la viscosité du ciment. Il s'agit d'allonger le temps d'injection du ciment tout en minimisant le risque de fuite de celui-ci. En se basant sur les résultats

expérimentaux obtenus avec le rhéomètre dynamique, nous avons montré que le paramètre influençant la viscosité du ciment sur lequel il est possible d'agir est la température.

De nombreuses simulations thermiques de l'écoulement de ciment dans le dispositif d'injection ont permis de définir les spécifications de la régulation de température, mais aussi d'apporter des éléments de dimensionnement. Une première version du bloc de régulation thermique réalisé est représentée dans la figure D.9.
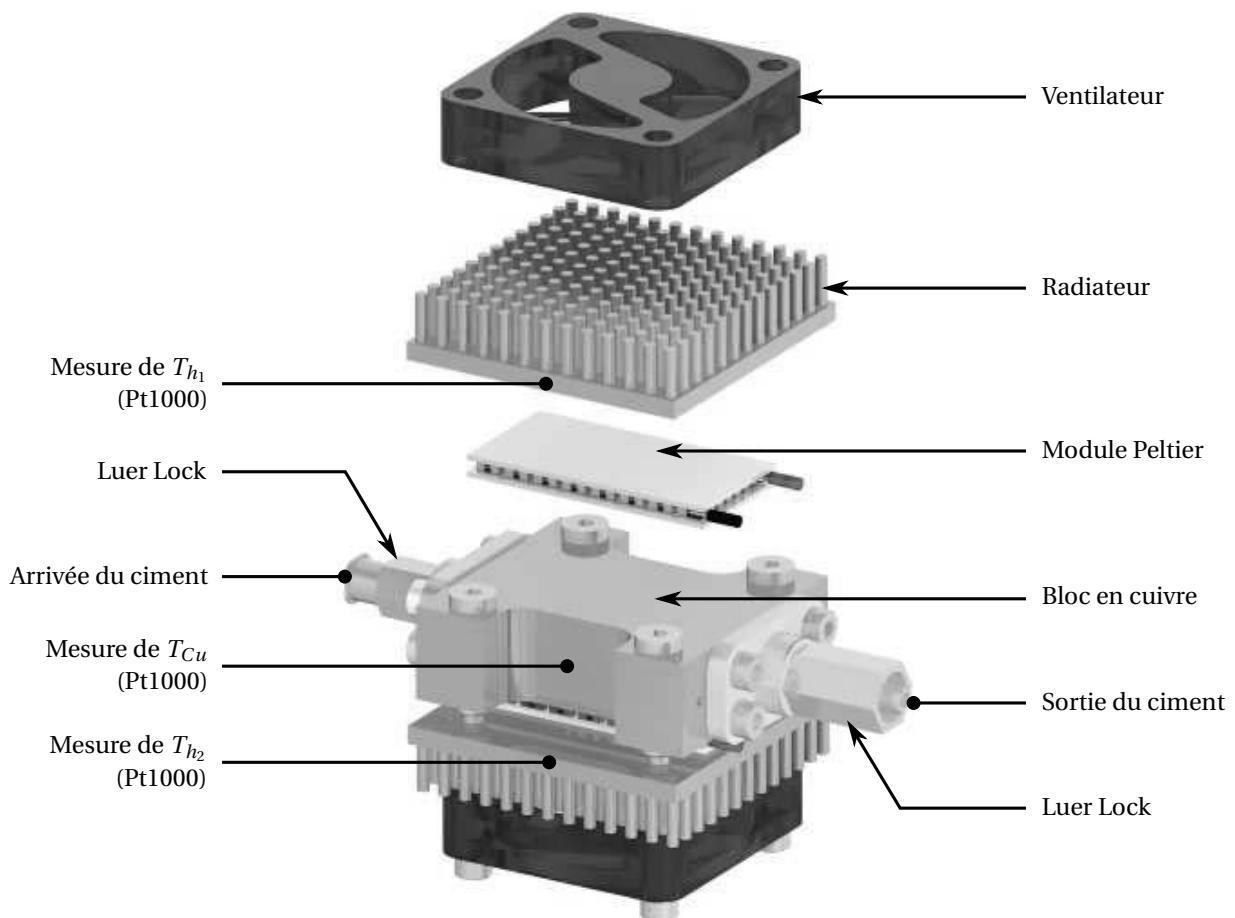


Figure D.9 – Vue explosée de l'échangeur thermique illustrant les différents composants et les mesures de température.

## D.5   Estimation en ligne et contrôle de la viscosité du ciment

La modélisation complète de ce bloc de régulation et l'identification des paramètres clés ont permis d'implémenter une stratégie de contrôle efficace pour la régulation de la viscosité du ciment au cours de l'injection.

### D.5.1 Contrôle de la température

Le bloc de régulation thermique illustré ci-dessus peut être divisé en trois sous-parties et mis en équation de la manière suivante :

$$(M_{Cu} c_{Cu} + 2 M_\kappa c_\kappa) \dot{T}_{Cu} = -\dot{Q}_{c_1} - \dot{Q}_{c_2} - h_c A_c (T_{Cu} - T_a) \tag{D.11}$$

$$(M_r c_r + M_\kappa c_\kappa) \dot{T}_{h_1} = \dot{Q}_{h_1} - h_{r_1} A_r (T_{h_1} - T_a) \tag{D.12}$$

$$(M_r c_r + M_\kappa c_\kappa) \dot{T}_{h_2} = \dot{Q}_{h_2} - h_{r_2} A_r (T_{h_2} - T_a). \tag{D.13}$$

La phase d'identification a permis de remonter aux paramètres propres à chacun des deux modules thermoélectriques mais aussi aux paramètres de convection libre et forcée. Les valeurs de ces paramètres sont rassemblées dans le tableau D.1.

| Paramètres estimés | $\epsilon$ (V.K$^{-1}$) | $R$ ($\Omega$) | $G$ (W.K$^{-1}$) | $h_r$ (W.m$^{-2}$.K$^{-1}$) |
|---|---|---|---|---|
| TEM #1 | 0.0213 | 1.348 | 0.228 | 87.83 |
| TEM #2 | 0.0216 | 1.348 | 0.234 | 84.66 |

Table D.1 – Paramètres estimés pour chaque module thermoélectrique.

La modélisation complète de ce bloc de régulation et l'identification des paramètres clés ont permis d'implémenter une stratégie de contrôle efficace pour la régulation de la température du ciment au cours de l'injection. Il est important de voir que le modèle est asymétrique à cause de l'effet Joule exprimé par un terme en $I^2$. Par conséquent, afin d'améliorer les performances de la régulation de température en boucle fermée du bloc de cuivre, une approche de commande originale a été employée en utilisant deux correcteurs différents, l'un pour la phase de chauffage et l'autre pour la phase de refroidissement. La commutation entre ces deux régulateurs dépend de la phase de fonctionnement. La synthèse du correcteur a permis de montrer qu'un simple correcteur proportionnel-intégral offre des performances suffisantes dans le cadre de notre application. Le choix de ces correcteurs a été validé expérimentalement en suivant une consigne de température tout en effectuant des essais d'injection de ciment.

### D.5.2 Contrôle de la viscosité

Pour contrôler la viscosité, deux boucles d'asservissement imbriquées sont nécessaires. La boucle interne est la boucle de contrôle de bloc thermique développée précédemment et la boucle externe représente le contrôle de la viscosité. Puisqu'il est impossible de mesurer directement la viscosité, une estimation en ligne de sa valeur est nécessaire avant l'implémentation d'une stratégie de commande.

#### D.5.2.1 Estimation en ligne de la viscosité

L'étude rhéologique confirme que le ciment orthopédique a un comportement rhéofluidifiant, ce qui signifie que sa viscosité diminue lorsque le taux de cisaillement appliqué augmente. Pour décrire ce comportement, la loi de puissance est de nouveau considérée pour calculer la viscosité en ligne. L'écoulement impliqué dans l'injection peut être assimilé à un écoulement de Poiseuille où le capillaire est le conduit de longueur $L_c$ et de rayon $R_c$. Ainsi, le principe de conservation de masse couplé à la résolution de l'équation de Navier-Stokes

fournit la relation suivante entre la perte de charge $\Delta P$ et le débit $Q$ :

$$Q = \left(\frac{\Delta P}{L_c}\right)^{\frac{1}{n}} \left(\frac{R_c}{2K}\right)^{\frac{1}{n}} \left(\frac{\pi n R_c^3}{3n+1}\right) \tag{D.14}$$

Afin de calculer en ligne la viscosité du ciment, une instrumentation adaptée a été ajoutée au dispositif d'injection. Le capteur de force dans la transmission fournit une mesure de la force d'injection qui permet à son tour d'évaluer $\Delta P$ alors que le capteur de position permet de calculer le débit $Q$. Ensuite, l'indice $n$ de la loi puissance est supposé être connu, ici constant et égal à 0.2. Avec cette dernière hypothèse, l'équation (D.14) permet d'estimer la valeur de $K$ au cours de l'injection. Enfin, pour reconstruire la valeur de la viscosité, le taux de cisaillement est calculé puis la loi puissance appliquée.

L'estimation en ligne de la viscosité a été implémentée puis expérimentée à plusieurs reprises au cours d'injection avec le système esclave en utilisant du ciment Osteopal® V de Heraeus. Les résultats de ces manipulations ont été comparés au modèle que nous avions identifié grâce à l'étude rhéologique. Cela permet de valider notre estimation de viscosité en ligne.

### D.5.2.2 Contrôle de la viscosité

A partir de cette estimation de viscosité en ligne qui a été validée, le contrôle de la viscosité du ciment osseux peut être considéré. En prenant en compte les remarques des praticiens, la consigne optimale de viscosité serait une valeur constante, définie de telle sorte que les fuites de ciment osseux soient limitées et que l'écoulement de ciment à l'intérieur de la vertèbre traitée reste homogène. Avec une telle référence, le praticien pourrait idéalement prendre autant de temps que nécessaire pour effectuer l'injection. En pratique, une telle consigne ne peut pas être suivie puisque la réaction de polymérisation qui en cours ne peut pas être arrêtée et est irréversible. Néanmoins, cette idée a été mise en œuvre. Dans ce cas, la conception d'un correcteur de viscosité spécifique n'est pas nécessaire puisque la génération de la consigne de température $T_{Cu}^*$ est alors limitée à du tout ou rien. En effet, le ciment osseux doit être chauffé jusqu'à ce que sa viscosité atteigne la consigne de viscosité donnée, puis refroidi afin de ralentir la réaction de polymérisation et donc d'augmenter le temps d'injection. Les premières expériences qui considèrent cette consigne de viscosité sont concluantes.

Ensuite, une consigne de viscosité plus complexe a été considérée. Alors que des résultats de simulations montrent que ce contrôle de viscosité est très prometteur, des résultats identiques n'ont pas encore été obtenus en ligne.

## D.6 Conclusions

Ce travail de thèse a permis, dans un premier temps, de caractériser l'évolution de la viscosité du ciment orthopédique au cours du temps mais aussi en fonction de la température et du taux de cisaillement. Cette caractérisation a abouti à deux modèles et à leur identification. Ensuite, pour répondre à la problématique de protection du praticien, un système d'injection télé-opérée avec retour d'effort a été conçu. Celui-ci permet également de réguler la viscosité du ciment grâce au contrôle précis de sa température. Cette fonctionnalité permet de limiter le risque de fuite, tout en allongeant le temps d'injection, rendant ainsi l'intervention de vertébroplastie plus aisée.

Ce travail, effectué dans le cadre d'un projet financé par la SATT Conectus, a conduit à un prototype fonctionnel avec lequel des essais d'injection dans des vertèbres fantômes ont été réalisés par des praticiens au service de Radiologie Interventionnelle du NHC.

# References

[Al-Hadithi 1992]  T. S. R. Al-Hadithi, H. A. Barnes and K. Walters. *The relationship between the linear (oscillatory) and nonlinear (steady-state) flow properties of a series of polymer and colloidal systems.* Colloid and Polymer Science, vol. 270, no. 1, pages 40–46, 1992. (cited page 36)

[AnatomyExpert 2016]  AnatomyExpert. http://www.anatomyexpert.com/, 2016. (cited pages xiii and 3)

[Anselmetti 2007]  G. C. Anselmetti, G. Corrao, P. Della Monica, V. Tartaglia, A. Manca, H. Eminefendic, F. Russo, I. Tosetti and D. Regge. *Pain Relief Following Percutaneous Vertebroplasty: Results of a Series of 283 Consecutive Patients Treated in a Single Institution.* CardioVascular and Interventional Radiology, vol. 30, no. 3, pages 441–447, June 2007. (cited page 16)

[ARDES 2014]  ARDES. http://www.ardes-group.com/fr/blog/produit/seringue-10cc/, 2014. (cited pages xiv and 63)

[ATIH 2016]  Agence Technique de l'Information sur l'Hospitalisation ATIH. *Formulaire d'interrogation des données.* http://www.scansante.fr/applications/statistiques-activite-MCO-par-GHM, 2016. (cited pages xiii and 9)

[Barnes 1989]  H. A. Barnes, J. F. Hutton and K. Walters. An introduction to rheology, volume 3. Elsevier, 1989. (cited page 24)

[Baroud 2003]  G. Baroud, J. Z. Wu, M. Bohner, S. Sponagel and T. Steffen. *How to determine the permeability for cement infiltration of osteoporotic cancellous bone.* Medical Engineering & Physics, vol. 25, no. 4, pages 283–288, 2003. (cited page 32)

[Baroud 2004a]  G. Baroud, M. Samara and T. Steffen. *Influence of Mixing Method on the Cement Temperature-Mixing Time History and Doughing Time of Three Acrylic Cements for Vertebroplasty.* Journal of Biomedical Materials Research Part B: Applied Biomaterials, vol. 68B, no. 1, pages 112–116, January 2004. (cited pages 14 and 31)

[Baroud 2004b]  G. Baroud and F. B. Yahia. *A finite element rheological model for polymethylmethacrylate flow: Analysis of the cement delivery in vertebroplasty.* Proceedings of the Institution of Mechanical Engineers, Part H: Journal of Engineering in Medicine, vol. 218, no. 5, pages 331–338, Mai 2004. (cited page 33)

[Baroud 2006]  G. Baroud, M. Crookshank and M. Bohner. *High-Viscosity Cement Significantly Enhances Uniformity of Cement Filling in Vertebroplasty: An Experimental Model and Study on Cement Leakage.* Spine, vol. 31, pages 2562–2568, 2006. (cited page 33)

[Baroud 2013a]  G. Baroud. *Bone cement delivery system*, US 20130123790 A1 2013. (cited page 20)

## References

[Baroud 2013b] G. Baroud. *Integrated cement delivery system for bone augmentation procedures and methods,* US 20130190680 A1 2013. (cited page 20)

[Baroud 2014] G. Baroud. *Method and Apparatus for Monitoring and/or Controlling the Curing of Cements used in Medical Procedures*, US 20140009173 A1 2014. (cited page 20)

[Barr 2000] J. D. Barr, M. S. Barr, T. J. Lemley and R. M. McCann. *Percutaneous vertebroplasty for pain relief and spinal stabilization.* Spine, vol. 25, no. 8, pages 923–928, 2000. (cited page 16)

[Bayle 2013] B. Bayle and L. Barbé. Tele-manipulation, chapter 8, pages 269–302. John Wiley & Sons, Inc., 2013. (cited pages xv, 75, and 76)

[Bird 1987] R. Byron Bird, R. C. Amstrong and O. Assager. Dynamics of Polymeric Liquids, Volume 1: Fluid Mechanics. A Wiley-Interscience Publication, John Wiley & Sons, 1987. (cited pages 24, 33, 35, and 42)

[Boger 2009] A. Boger, K. Wheeler, B. Schenk and P. Heini. *Clinical investigations of polymethylmethacrylate cement viscosity during vertebroplasty and related in vitro measurements.* European Spine Journal, vol. 18, pages 1272–1278, 2009. (cited pages 33 and 111)

[Bohner 2003] M. Bohner, B. Gasser, Baroud G. and P. Heini. *Theoretical and experimental model to describe the injection of a polymethylmethacrylate cement into a porous structure.* Biomat, vol. 24, no. 16, pages 2721–2730, July 2003. (cited pages 31 and 33)

[Burge 2007] R. Burge, B. Dawson-Hughes, D. H. Solomon, J. B. Wong, A. King and A. Tosteson. *Incidence and economic burden of osteoporosis-related fractures in the United States, 2005–2025.* Journal of Bone and Mineral Research, vol. 22, no. 3, pages 465–475, 2007. (cited page 5)

[CareFusion 2016] CareFusion. *AVAmax® Advanced Vertebral Augmentation system.* http://www.carefusion. com/documents/brochures/interventional-specialties/IS_AVAmax-Vertebral-Augmentation-System_ BR_EN.pdf, 2016. (cited page 18)

[Carreau 1972] P. J. Carreau. *Rheological Equations from Molecular Network Theories.* Transactions of The Society of Rheology (1957-1977), vol. 16, pages 99–127, January 1972. (cited page 33)

[Center 2015] Garden State Medical Center. *Kyphoplasty/Vertebroplasty.* http://gsmedicalcenter.org/services/ pain-management/minimally-invasive-procedures/kyphoplasty-vertebroplasty/, 2015. (cited pages xiii and 7)

[Chang 2015] X. Chang, Y.-F. Lv, B. Chen, H.-y. Li, X.-b. Han, K. Yang, W. Zhang, Y. Zhou and C.-q. Li. *Vertebroplasty versus kyphoplasty in osteoporotic vertebral compression fracture: a meta-analysis of prospective comparative studies.* International Orthopaedics, vol. 39, no. 3, pages 491–500, March 2015. (cited page 7)

[Charnley 1972] J. Charnley. *The long-term results of low-friction arthroplasty of the hip performed as a primary intervention.* Bone & Joint Journal, vol. 54, no. 1, pages 61–76, 1972. (cited page 9)

[Chavali 2003] R. Chavali, R. Resijek, S. K. Knight and I. Choi. *Extending Polymerization Time of Polymethylmethacrylate Cement in Percutaneous Vertebroplasty with Ice Bath Cooling.* American Journal of Neuroradiology, vol. 24, no. 3, pages 545–546, 2003. (cited page 64)

[Choi 2007] H.-S. Choi, S. Yun and K.-i. Whang. *Development of a temperature-controlled car-seat system utilizing thermoelectric device.* Applied Thermal Engineering, vol. 27, no. 17–18, pages 2841–2849, 2007. (cited page 70)

[Cox 1958] W. P. Cox and E. H. Merz. *Correlation of dynamic and steady flow viscosities.* Journal of Polymer Science, vol. 28, pages 619–622, April 1958. (cited page 35)

[Dealy 2006] J. M. Dealy and R. G. Larson. Structure and rheology of molten polymers. Carl Hanser Verlag GmbH & Co. KG, 2006. (cited pages 33, 35, 42, and 45)

[Deramond 1998] H. Deramond, C. Depriester, P. Galibert and D. Le Gars. *Percutaneous vertebroplasty with polymethylmethacrylate. Technique, indications, and results.* Radiologic Clinics of North America, vol. 36, pages 533–546, May 1998. (cited page 8)

[DFine 2016] DFine. *StabiliT®, A full family of VCF solutions to match the unique needs of every patient.* http://dfineinc.com/stabilit/, 2016. (cited pages xiii, 19, and 20)

[Diamond 2004] T. H. Diamond, J. Bucci, J. H. Kersley, P. Aslan, W. B. Lynch and C. Bryant. *Osteoporosis and spinal fractures in men with prostate cancer: risk factors and effects of androgen deprivation therapy.* Journal of Urology, vol. 172, no. 2, pages 529–532, 2004. (cited page 5)

[Dunne 2001] N.J. Dunne and J.F. Orr. *Influence of mixing techniques on the physical properties of acrylic bone cement.* Biomaterials, vol. 22, no. 13, pages 1819–1826, 2001. (cited page 98)

[Eck 2008] J. C. Eck, D. Nachtigall, S. C. Humphreys and S. D. Hodges. *Comparison of vertebroplasty and balloon kyphoplasty for treatment of vertebral compression fractures: a meta-analysis of the literature.* The Spine Journal, vol. 8, no. 3, pages 488–497, June 2008. (cited pages 7 and 16)

[Esarte 2001] J. Esarte, G. Min and D. M. Rowe. *Modelling heat exchangers for thermoelectric generators.* Journal of Power Sources, vol. 93, no. 1–2, pages 72–76, 2001. (cited page 70)

[Fang 2009] S.-C. Fang and H.-L. Chan. *Human identification by quantifying similarity and dissimilarity in electrocardiogram phase space.* Pattern Recognition, vol. 42, no. 9, pages 1824–1831, 2009. (cited page 52)

[Farrar 2001] D. F. Farrar and J. Rose. *Rheological properties of PMMA bone cements during curing.* Biomaterials, vol. 22, no. 22, pages 3005–3013, 2001. (cited pages 30 and 33)

[Felsenberg 2002] D. Felsenberg, A. J. Silman, M. Lunt, G. Armbrecht, A. A. Ismail, J. D. Finn, W. C. Cockerill, D. Banzer, L. I. Benevolenskaya, A. Bhalla *et al. Incidence of Vertebral Fracture in Europe: Results From the European Prospective Osteoporosis Study (EPOS).* Journal of Bone and Mineral Research, vol. 17, no. 4, pages 716–724, 2002. (cited page 5)

[Ferreyro 2015] R. H. I. Ferreyro and M. M. Miranda. *Hydraulic device for the injection of bone cement in percutaneous vertebroplasty,* US 9186194 B2 2015. (cited page 19)

[Fournier 1996] J. Fournier, G. Williams, C. Duch and G. A. Aldridge. *Changes in molecular dynamics during bulk polymerization of an epoxide-amine system as studied by dielectric relaxation spectroscopy.* Macromolecules, vol. 29, no. 22, pages 7097–7107, 1996. (cited page 33)

[Galibert 1987] P. Galibert, H. Deramond, P. Rosat and D. Le Gars. *Preliminary note on the treatment of vertebral angioma by percutaneous acrylic vertebroplasty.* Neurochirurgie, vol. 33, pages 166–168, 1987. (cited pages 6 and 8)

[Gangi 1994] A. Gangi, B. A. Kastler and J.-L. Dietemann. *Percutaneous Vertebroplasty Guided by a Combination of CT and Fluoroscopy.* American Journal of Neuroradiology, vol. 15, no. 1, pages 83–86, January 1994. (cited pages 6 and 13)

[Gangi 2006] A. Gangi, T. Sabharwal, F. G. Irani, X. Buy, J. P. Morales and A. Adam. *Quality assurance guidelines for percutaneous vertebroplasty.* Cardiovascular and Interventional Radiology, vol. 29, no. 2, pages 173–178, 2006. (cited pages 5 and 14)

[Gangi 2010] A. Gangi and W. A. Clark. *Have Recent Vertebroplasty Trials Changed the Indications for Vertebroplasty?* CardioVascular and Interventional Radiology, vol. 33, no. 4, pages 677–680, June 2010. (cited page 13)

## References

[Goldsmid 1986]  H. J. Goldsmid. *Electronic refrigeration.* Pion, London, 1986. (cited page 85)

[Guth 2016]  S. Guth and A. Gangi. *Interventional Radiology Site : Patient positioning.* http://www.openradiology. org/survey/vertebroplasty/fluoroscopy/Patient%20positioning, 2016. (cited pages xiii and 13)

[Haboush 1953]  E. J. Haboush. *A new operation for arthroplasty of the hip based on biomechanics, photoelasticity, fast-setting dental acrylic, and other considerations.* Bulletin of the Hospital for Joint Diseases, vol. 14, no. 2, pages 242–277, 1953. (cited page 9)

[Hagen 1839]  G. H. L. Hagen. *Ueber die Bewegung des Wassers in engen cylidrischen Rohren.* Annalen der Physik, vol. 46, pages 423–442, 1839. (cited page 26)

[Hannaford 1989]  B. Hannaford. *A design framework for teleoperators with kinesthetic feedback.* IEEE Transactions on Robotics and Automation, vol. 5, no. 4, pages 426–434, Aug 1989. (cited page 76)

[Harstall 2005]  R. Harstall, P. F. Heini, R. L. Mini and R. Orler. *Radiation Exposure to the Surgeon During Fluoroscopically Assisted Percutaneous Vertebroplasty: A Prospective Study.* Spine, vol. 30, no. 16, pages 1893–1898, 2005. (cited page 17)

[HAS 2009]  HAS. *Spondyloplastie par ballonets (Cyphoplastie) - Rapport d'évaluation.* Rapport technique, Haute Autorité de Santé, January 2009. (cited page 5)

[Hashtrudi-Zaad 1999]  K. Hashtrudi-Zaad and S. E. Salcudean. *On the use of local force feedback for transparent teleoperation.* In Robotics and Automation, 1999. Proceedings. 1999 IEEE International Conference on, volume 3, pages 1863–1869, 1999. (cited page 76)

[Hashtrudi-Zaad 2000]  K. Hashtrudi-Zaad. *Design, implementation and evaluation of stable bilateral teleoperation control architectures for enhanced telepresence.* PhD thesis, University of British Columbia, Canada, 2000. (cited page 76)

[Heini 2000]  F. P. Heini, B. Wälchli and U. Berlemann. *Percutaneous transpedicular vertebroplasty with PMMA: operative technique and early results.* European Spine Journal, vol. 9, no. 5, pages 445–450, 2000. (cited page 16)

[Hernández 2006]  L. Hernández, M. Gurruchaga and I. Goñi. *Influence of powder particle size distribution on complex viscosity and other properties of acrylic bone cement for vertebroplasty and kyphoplasty.* Journal of Biomedical Materials Research Part B: Applied Biomaterials, vol. 77B, no. 1, pages 98–103, April 2006. (cited page 31)

[Hide 2004]  I. G Hide and A. Gangi. *Percutaneous vertebroplasty: history, technique and current perspectives.* Clinical Radiology, vol. 59, no. 6, pages 461–467, 2004. (cited pages xiii, 13, and 16)

[Huang 2000a]  B. J. Huang, C. J. Chin and C. L. Duang. *A design method of thermoelectric cooler.* International Journal of Refrigeration, vol. 23, no. 3, pages 208–218, 2000. (cited page 85)

[Huang 2000b]  B. J. Huang and C. L. Duang. *System dynamic model and temperature control of a thermoelectric cooler.* International Journal of Refrigeration, vol. 23, no. 3, pages 197–207, 2000. (cited page 84)

[Hulme 2006]  P. A. Hulme, J. Krebs, S. J. Ferguson and U. Berlemann. *Vertebroplasty and kyphoplasty: a systematic review of 69 clinical studies.* Spine, vol. 31, no. 17, pages 1983–2001, 2006. (cited pages 7, 8, and 16)

[IOF 2010]  International Osteoporosis Foundation IOF. *The Breaking Spine: An IOF Report.* https://www. iofbonehealth.org/sites/default/files/PDFs/WOD%20Reports/2010_the_breaking_spine_en.pdf, 2010. (cited page 5)

[ISO 2002]   International Organization for Standardization ISO. *ISO 5833:2002 Implants for surgery – Acrylic resin cements*, May 2002. (cited pages 11, 14, 97, and 111)

[Jensen 1997]   M. E. Jensen, A. J. Evans, J. M. Mathis, D. F. Kallmes, H. J. Cloft and J. E. Dion. *Percutaneous poly-methylmethacrylate vertebroplasty in the treatment of osteoporotic vertebral body compression fractures: technical aspects.* American Journal of Neuroradiology, vol. 18, no. 10, pages 1897–1904, 1997. (cited page 8)

[Johnell 2006]   O. Johnell and J. A. Kanis. *An estimate of the worldwide prevalence and disability associated with osteoporotic fractures.* Osteoporosis International, vol. 17, no. 12, pages 1726–1733, 2006. (cited page 5)

[Kanis 2013]   J. A. Kanis, E. V. McCloskey, H. Johansson, C. Cooper, R. Rizzoli, J.-Y. Reginster *et al.* *European guidance for the diagnosis and management of osteoporosis in postmenopausal women.* Osteoporosis international, vol. 24, no. 1, pages 23–57, January 2013. (cited page 5)

[Kühn 2013]   K.-D. Kühn. PMMA Cements. Springer Berlin, 2013. (cited pages 10 and 98)

[Kim 1987]   W. S. Kim, F. Tendick, S. R. Ellis and L. W. Stark. *A comparison of position and rate control for telemanipulations with consideration of manipulator system dynamics.* Robotics and Automation, IEEE Journal of, vol. 3, no. 5, pages 426–436, October 1987. (cited page 77)

[Klazen 2010]   C. A. H. Klazen, P. N. M. Lohle, J. de Vries, F. H. Jansen *et al.* *Vertebroplasty versus conservative treatment in acute osteoporotic vertebral compression fractures (Vertos II): an open-label randomised trial.* The Lancet, vol. 376, no. 9746, pages 1085–1092, 2010. (cited pages 6 and 16)

[Kolmeder 2010]   S. Kolmeder and A. Lion. *On the thermomechanical-chemically coupled behavior of acrylic bone cements: experimental characterization of material behavior and modeling approach.* Technische Mechanik, vol. 30, no. 1-3, pages 195–202, 2010. (cited pages 33 and 70)

[Kolmeder 2011]   S. Kolmeder, A. Lion, R. Landgraf and J. Ihlemann. *Thermophysical properties and material modelling of acrylic bone cements used in vertebroplasty.* Journal of Thermal Analysis and Calorimetry, vol. 105, pages 705–718, August 2011. (cited pages 30, 33, 50, 53, 89, and 120)

[Kolmeder 2013]   S. Kolmeder and A. Lion. *Characterisation and modelling rheological properties of acrylic bone cement during application.* Mechanics Research Communications, vol. 48, pages 93–99, March 2013. (cited pages 33 and 34)

[Krause 1982]   W. R. Krause, J. Miller and P. Ng. *The viscosity of acrylic bone cements.* Journal of Biomedical Materials Research, vol. 16, no. 3, pages 219–243, 1982. (cited pages 30 and 32)

[Landgraf 2015]   R. Landgraf, J. Ihlemann, S. Kolmeder, A. Lion, H. Lebsack and C. Kober. *Modelling and simulation of acrylic bone cement injection and curing within the framework of vertebroplasty.* ZAMM - Journal of Applied Mathematics and Mechanics / Zeitschrift für Angewandte Mathematik und Mechanik, vol. 95, no. 12, pages 1530–1547, December 2015. (cited page 34)

[Lawrence 1993]   D. A. Lawrence. *Stability and transparency in bilateral teleoperation.* IEEE Transactions on Robotics and Automation, vol. 9, no. 5, pages 624–637, 1993. (cited page 76)

[Lawrence 1997]   P. D. Lawrence, S. E. Salcudean, N. Sepehri, D. Chan, S. Bachmann, N. Parker, M. Zhu and R. Frenette. Coordinated and force-feedback control of hydraulic excavators, pages 181–194. Springer Berlin Heidelberg, Berlin, Heidelberg, 1997. (cited page 77)

[Lewis 2002]   G. Lewis and M. Carroll. *Rheological properties of acrylic bone cement during curing and the role of the size of the powder particles.* Journal of Biomedical Materials Research, vol. 63, no. 2, pages 191–199, 2002. (cited pages 30, 31, and 36)

## References

[Lewis 2011]  G. Lewis. *Viscoelastic properties of injectable bone cements for orthopaedic applications: State-of-the-art review.* Journal of Biomedical Materials Research Part B: Applied Biomaterials, vol. 98B, no. 1, pages 171–191, 2011. (cited page 30)

[Lian 2008]  Z. Lian, C.-K. Chui and S.-H. Teoh. *A biomechanical model for real-time simulation of PMMA injection with haptics.* Computers in Biology and Medicine, vol. 38, no. 3, pages 304–312, 2008. (cited pages 32 and 36)

[Lineykin 2007]  S. Lineykin and S. Ben-Yaakov. *Modeling and Analysis of Thermoelectric Modules.* Industry Applications, IEEE Transactions on, vol. 43, no. 2, pages 505–512, March 2007. (cited pages 84, 85, and 86)

[Lion 2007]  A. Lion and P. Höfer. *On the phenomenological representation of curing phenomena in continuum mechanics.* Archives of Mechanics, vol. 59, no. 1, pages 59–89, 2007. (cited page 33)

[Liu 2006]  C. Liu, H. Shao, F. Chen and H Zheng. *Rheological properties of concentrated aqueous injectable calcium phosphate cement slurry.* Biomaterials, vol. 27, no. 29, pages 5003–5013, 2006. (cited pages 30 and 31)

[Loeffel 2007]  M. Loeffel, P. F. Heini, N. Bouduban, J. Burger, L.-P. Nolte and J. Kowal. *Development of a Computer-Assisted High-Pressure Injection Device for Vertebroplasty.* Biomedical Engineering, IEEE Transactions on, vol. 54, pages 2051–2056, 2007. (cited pages xiii, 20, and 21)

[Loeffel 2008]  M. Loeffel, S. J. Ferguson, L.-P. Nolte and J. H. Kowal. *Vertebroplasty: experimental characterization of polymethylmethacrylate bone cement spreading as a function of viscosity, bone porosity, and flow rate.* Spine, vol. 33, no. 12, pages 1352–1359, May 2008. (cited page 33)

[Loeffel 2009]  M. Loeffel, I. P. Pappas and L.-P. Nolte. *Injection Device With Haptic Feedback*, US20090216191 A1, August 2009. (cited pages xiii, 20, and 21)

[LPD 2016]  Longmont Pediatric Dentistry LPD. *Osteoporosis & Oral Health.* http://www.longmontkidsdentist.com/library/7728/Osteoporosis%26OralHealth.html, 2016. (cited pages xiii and 5)

[Luo 2008]  Z. Luo. *A simple method to estimate the physical characteristics of a thermoelectric cooler from vendor datasheets.* Electronics cooling, vol. 14, no. 3, pages 22–27, 2008. (cited page 85)

[Macosko 1994]  C. W. Macosko. Rheology: Principles, Measurements, and Applications. Wiley-VCH, Inc., 1994. (cited page 28)

[Mannella 2014]  G. A. Mannella, V. La Carrubba and V. Brucato. *Peltier cells as temperature control elements: Experimental characterization and modeling.* Applied Thermal Engineering, vol. 63, no. 1, pages 234–245, February 2014. (cited pages 85 and 86)

[Matcharashvili 2007]  T. Matcharashvili, T. Chelidze and M. Janiashvili. *Identification of complex processes based on analysis of phase space structures.* In Jim Byrnes, editeur, Imaging for Detection and Identification, NATO Security through Science Series, pages 207–242. Springer Netherlands, 2007. (cited page 52)

[Mathis 2006]  J. M. Mathis, H. Deramond and S. M. Belkoff, editeurs. Percutaneous Vertebroplasty and Kypho-plasty. Springer, 2006. (cited page 5)

[MathWorks 2016]  MathWorks. *ode45.* https://fr.mathworks.com/help/matlab/ref/ode45.html, 2016. (cited page 121)

[McGraw 2002]  J. K. McGraw, J. A. Lippert, K. D. Minkus, P. M. Rami, T. M. Davis and R. F. Budzik. *Prospective Evaluation of Pain Relief in 100 Patients Undergoing Percutaneous Vertebroplasty: Results and Follow-up.* Journal of Vascular and Interventional Radiology, vol. 13, no. 9, Part 1, pages 883–886, September 2002. Part 1. (cited page 16)

140

[Medical 2016]   Cook Medical. *Duro-Ject® Bone Cement Injector Set*. https://www.cookmedical.com/products/ir_duro_webds/, 2016. (cited page 18)

[Melcor 2006]   Melcor. *Thermoelectric Handbook*. https://home.zhaw.ch/~fusa/PSS_VLE_C/CHAPTER_03/CASES/Materials/Melcor_TE_Handbook.pdf, January 2006. (cited pages xv and 70)

[Melton 2005]   L. J. Melton, R. A. Kyle, S. J. Achenbach, A. L. Oberg and S. V. Rajkumar. *Fracture Risk With Multiple Myeloma: A Population-Based Study*. Journal of Bone and Mineral Research, vol. 20, no. 3, pages 487–493, 2005. (cited page 5)

[Mobasser 2008]   F. Mobasser and K. Hashtrudi-Zaad. *Transparent rate mode bilateral teleoperation control*. The International Journal of Robotics Research, vol. 27, no. 1, pages 57–72, January 2008. (cited page 78)

[Morimitsu 2010]   H. Morimitsu and S. Katsura. *A Method to Control a Peltier Device Based on Heat Disturbance Observer*. 36th Annual Conference on IEEE Industrial Electronics Society, pages 1222–1227, November 2010. (cited page 84)

[Nicholas 2007]   M. Nicholas, M. Waters, K. Holford and G. Adusei. *Analysis of rheological properties of bone cements*. Journal of Materials Science: Materials in Medicine, vol. 18, pages 1407–1412, 2007. (cited page 30)

[Oglaza 2010]   J. F. Oglaza, C. Renaud, A. Leonard and G. Huet. *Methods and apparatuses for bone restoration*, US 7846206 B2, December 2010. (cited page 7)

[OptiMed 2016]   OptiMed. *Cemento-MP*. http://www.opti-med.de/nc/en/products/category/spine/product-details/p-kategorie/spine/subkategorie/vertebroplastiesysteme/p-produkt/cemento-mp/, 2016. (cited pages 17 and 18)

[Osseon 2016]   Osseon. *Osseoflex® CD-H hydraulic cement delivery system*. http://www.osseon.com/osseoflex-cd-h-hydraulic-cement-delivery-system/, 2016. (cited pages xiii and 19)

[Osswald 2014]   T. Osswald and N. Rudolph. Polymer Rheology - Fundamentals and Applications. Carl Hanser Verlag GmbH & Co. KG, 2014. (cited pages 24 and 36)

[Ostwald 1925]   W. Ostwald. *Ueber die Geschwindigkeitsfunktion der Viskosität disperser Systeme. I.* Colloid and Polymer Science, vol. 36, pages 99–117, 1925. In German. (cited pages 31 and 115)

[Palacios 2009]   R. Palacios, A. Arenas, R. R. Pecharromán and F. L. Pagola. *Analytical procedure to obtain internal parameters from performance curves of commercial thermoelectric modules*. Applied Thermal Engineering, vol. 29, no. 17–18, pages 3501–3505, 2009. (cited pages 85 and 86)

[Peltier 1834]   J. C. A. Peltier. *Nouvelles Expériences sur la Caloricité des courants électriques*. Annales de chimie et de physique, vol. 56, pages 371–386, 1834. (cited page 70)

[Pincus 2016]   D. Pincus and D. Hoh. *Spinal Cord Injury*. http://neurosurgery.ufl.edu/patient-care/diseases-conditions/spinal-cord-injury/, October 2016. University of Florida Health. (cited pages xiii and 8)

[Poiseuille 1840]   J. L. M. Poiseuille. *Recherches expérimentales sur le mouvement des liquides dans les tubes de très petits diamètres*. Comptes rendus de l'Académie des sciences de Paris, vol. 11, pages 961–967, 1041–1049, 1840. (cited page 26)

[PubMed 2016]   PubMed. *PubMed*. https://www.ncbi.nlm.nih.gov/pubmed, 2016. (cited pages xiii and 9)

[Raju 1989]   G. J. Raju, G. C. Verghese and T. B. Sheridan. *Design issues in 2-port network models of bilateral remote manipulation*. In Robotics and Automation, 1989. Proceedings., 1989 IEEE International Conference on, pages 1316–1321, May 1989. (cited page 75)

# References

[Reckling 1977]  F. W. Reckling. *The bone-cement interface temperature during total joint replacement.* Journal of Bone and Joint Surgery, vol. 59, pages 80–82, January 1977.  (cited page 29)

[Rehman 1996]  I. Rehman, E. J. Harper and W. Bonfield. *In situ analysis of the degree of polymerization of bone cement by using FT-Raman spectroscopy.* Biomaterials, vol. 17, no. 16, pages 1615–1619, 1996. (cited page 29)

[Sarda 2001]  S. Sarda, E. Fernández, J. Llorens, S. Martínez, M. Nilsson and J. A. Planell. *Rheological properties of an apatitic bone cement during initial setting.* Journal of Materials Science: Materials in Medicine, vol. 12, no. 10, pages 905–909, 2001. (cited pages 30 and 31)

[Schmidt 2005]  R. Schmidt, B. Cakir, T. Mattes, M. Wegener, W. Puhl and M. Richter. *Cement leakage during vertebroplasty: an underestimated problem?* European Spine Journal, vol. 14, no. 5, pages 466–473, 2005. (cited page 16)

[Shaojing 2010]  S. Shaojing and Q. Qin. *Temperature Control of Thermoelectric Cooler Based on Adaptive NN-PID.* International Conference on Electrical and Control Engineering, pages 2245–2248, 2010.  (cited page 84)

[Sourour 1976]  S. Sourour and M. R. Kamal. *Differential scanning calorimetry of epoxy cure: isothermal cure kinetics.* Thermochimica Acta, vol. 14, no. 1, pages 41–59, 1976.  (cited page 33)

[Spierings 2005]  P. T. J. Spierings. Testing and Performance of Bone Cements, pages 67–78. Springer Berlin Heidelberg, Berlin, Heidelberg, 2005. (cited page 10)

[Standring 2008]  S. Standring and R. L. M. Newell. Gray's Anatomy: The Anatomical Basis of Clinical Practice, chapter 42 The back, pages 707–748. Churchill Livingstone Elsevier, 2008.  (cited page 2)

[Strang 2006]  C Strang and C Bat. Larousse médical. Paris: Éditions Larousse, 2006.  (cited pages xiii and 4)

[Stryker 2016] Stryker. *PCD: Precision Cement Delivery System.* http://www.stryker.com/en-us/ products/Spine/InterventionalSpine/VertebralAugmentation/CementMixingDeliveryDevice/ PrecisionCementDeliverySystem/index.htm, 2016. (cited page 18)

[Sullivan 2007]  S. J. L. Sullivan and L. D. T. Topoleski. *Influence of Initial Component Temperature on the Apparent Viscosity and Handling Characteristics of Acrylic (PMMA) Bone Cement.* Journal of Biomedical Materials Research Part B: Applied Biomaterials, vol. 81B, no. 1, pages 224–230, April 2007. (cited pages 14 and 30)

[Synowitz 2006]  M. Synowitz and J. Kiwit. *Surgeon's radiation exposure during percutaneous vertebroplasty.* Journal of Neurosurgery: Spine, vol. 4, no. 2, pages 106–109, 2006. (cited pages 15, 17, and 19)

[Synthes 2016a]  DePuy Synthes. *CONFIDENCE SPINAL CEMENT SYSTEM*®. https://www.depuysynthes.com/ hcp/spine/products/qs/CONFIDENCE-SPINAL-CEMENT-SYSTEM, 2016.  (cited pages xiii and 19)

[Synthes 2016b]  DePuy Synthes. *VERTECEM*® *II Bone Cement.* https://www.depuysynthes.com/hcp/spine/ products/qs/vertecem-ii-bone-cement, 2016.  (cited page 18)

[Teo 2007]  J. Teo and S. H. Wang S. C. adn Teoh. *Preliminary study on biomechanics of vertebroplasty: a computational fluid dynamics and solid mechanics combined approach.* Spine, vol. 32, no. 12, pages 1320–1328, May 2007.  (cited page 33)

[Thiebaud 2016]  Thiebaud. *X'tens*®. http://thiebaud-surgical.com/fr/orthopedie/36-xtens.html, 2016.  (cited page 18)

[Truckai 2013]  C. Truckai, R. Luzzi, J. H. Shadduck and R. D. Poser. *Bone treatment systems and methods,* US8523871 B2, September 2013.  (cited page 20)

[Vaishya 2013] R. Vaishya, M. Chauhan and A. Vaish. *Bone cement*. Journal of Clinical Orthopaedics and Trauma, vol. 4, no. 4, pages 157–163, December 2013. (cited page 9)

[Van Quang 2013] Ha Van Quang, Jee-Hwan Ryu and Youngdo Kwon. A Feasibility Study of Rate-Mode Mobile Robot Bilateral Teleoperation with Time Domain Passivity Approach, pages 207–215. Springer Berlin Heidelberg, Berlin, Heidelberg, 2013. (cited page 77)

[Vexim 2016] Vexim. *SpineJack® : restauration anatomique contrôlée*. http://vexim.fr/espace-professionnels/nos-solutions/restauration-anatomique-controlee/, 2016. (cited page 7)

[von Wrangel 2009] A. von Wrangel, Å. Cederblad and M. Rodriguez-Catarino. *Fluoroscopically Guided Percutaneous Vertebroplasty: Assessment of Radiation Doses and Implementation of Procedural Routines to Reduce Operator Exposure*. Acta Radiologica, vol. 50, no. 5, pages 490–496, 2009. (cited page 17)

[Widmer Soyka 2013] R. P. Widmer Soyka, A. López, C. Persson, L Cristofolini and S. J. Ferguson. *Numerical description and experimental validation of a rheology model for non-Newtonian fluid flow in cancellous bone*. Journal of the Mechanical Behavior of Biomedical Materials, vol. 27, pages 43–53, November 2013. (cited pages 32 and 33)

[Wolf 2009] E. W. Wolf. *Apparatus and method for the dispensing of bone cement*, US20090062808 A1, March 2009. (cited page 20)

[Yan 2011] D. Yan, L. Duan, J. Li, C. Soo, H. Zhu and Z. Zhang. *Comparative study of percutaneous vertebroplasty and kyphoplasty in the treatment of osteoporotic vertebral compression fractures*. Archives of Orthopaedic and Trauma Surgery, vol. 131, no. 5, pages 645–650, 2011. (cited page 6)

[Yasuda 1979] K. Yasuda. *Investigation of the analogies between viscometric and linear viscoelastic properties of polystyrene fluids*. phdthesis, Massachusetts Institute of Technology. Department of Chemical Engineering., 1979. (cited page 33)

[Zhang 2010] H. Y. Zhang, Y. C. Mui and M. Tarin. *Analysis of thermoelectric cooler performance for high power electronic packages*. Applied Thermal Engineering, vol. 30, no. 6–7, pages 561–568, 2010. (cited page 85)

# List of publications

## International conferences

- N. Lepoutre, G. Bara, L. Meylheuc, et B. Bayle, *Phase Space Identification Method for Modeling the Viscosity of Bone Cement.* Control Conference (ECC), 2016 European, pp. 2404–2409, Aalborg, June-July 2016.

- N. Lepoutre, R. Aleluia Porto, L. Meylheuc, G. Bara, F. Schmitt, L. Barbé, et B. Bayle, *Robotically Assisted Injection of Orthopedic Cement: System design, Control and Modeling.* Control Conference (ECC), 2016 European, pp. 2127–2132, Aalborg, June-July 2016.

- N. Lepoutre, G.I. Bara, L. Meylheuc, F. Schmitt, L. Barbé et B. Bayle, *Design and control of a thermal device for bone cement injection.* Biomedical Robotics and Biomechatronics (BioRob), 2016 6th IEEE RAS & EMBS International Conference on, pp. 506–513, Singapour, June 2016.

## Patents

- N. Lepoutre, L. Meylheuc, G. Bara, et B. Bayle, *Method for controlling the viscosity of orthopedic bone cement during its curing in percutaneous vertebroplasty*, EP15305975, June 2015.

- F. Schmitt, L. Meylheuc, N. Lepoutre, B. Bayle, E. Lefeuvre, E. Martincic, et A. Valls, *Injection device of bone cement for percutaneous vertebroplasty*, EP15305974, June 2015.

# Nicole LEPOUTRE

# Robot-Assisted Bone Cement Injection

## Résumé

La vertébroplastie percutanée est une intervention non chirurgicale et peu invasive qui consiste à injecter, sous contrôle radioscopique, un ciment orthopédique dans le corps vertébral. Malgré son efficacité, celle-ci présente quelques inconvénients non négligeables. Le premier est dû au ciment orthopédique qui est injecté pendant sa polymérisation. Au début, sa faible viscosité augmente le risque de fuite hors de la vertèbre traitée, ce qui peut provoquer de lourdes complications. Ensuite, la variation rapide de viscosité limite la durée. Le second désagrément concerne le contrôle par fluoroscopie à rayons X qui expose le praticien de manière prolongée.

Ainsi, l'enjeu de ce projet est de proposer aux radiologues un nouveau système d'injection à distance avec retour d'effort sur lequel la viscosité du ciment est régulée pendant l'injection. Le développement de ces aspects permettra la radioprotection des praticiens, une réduction des risques de fuite et une durée d'injection allongée.

**Mots-clés :** Rhéologie, Modélisation, Automatique, Robotique médicale.

## Abstract

Percutaneous vertebroplasty is a minimally invasive intervention that involves injecting bone cement, under fluoroscopic guidance, into the vertebral body. It consolidates the fractured vertebra and reduces pain. However, some inconveniences must be considered. The major difficulties are related to the cement that is injected during its curing phase. It is very liquid at the beginning of the injection, which introduces a high risk of leakage outside the vertebra and, thus, potential dramatic complications. During the injection, the reaction progresses and the cement hardens suddenly, leaving a short working phase. Finally, the operator is permanently exposed to harmful X-rays.

This work aims to provide a new teleoperated injection device with haptic feedback that allows a fine supervision of the cement injection by including a viscosity control system. This device will allow the radioprotection of the medical staff, a reduction of the leakage risks and an extended injection phase.

**Key words:** Rheology, Modeling, Control, Medical robotics.